

PHOTOACOUSTIC SPECTROSCOPY FOR MULTI-GAS SENSING USING NEAR INFRARED LASERS

THÈSE N^o 3670 (2006)

PRÉSENTÉE LE 24 NOVEMBRE 2006

À LA FACULTÉ SCIENCES ET TECHNIQUES DE L'INGÉNIEUR
Laboratoire de nanophotonique et métrologie
SECTION DE GÉNIE ÉLECTRIQUE ET ÉLECTRONIQUE

ÉCOLE POLYTECHNIQUE FÉDÉRALE DE LAUSANNE

POUR L'OBTENTION DU GRADE DE DOCTEUR ÈS SCIENCES

PAR

Jean-Philippe BESSON

ingénieur électricien diplômé EPF
de nationalité suisse et originaire de Engollon (NE)

acceptée sur proposition du jury:

Prof. J. R. Mosig, président du jury
Dr L. Thévenaz, directeur de thèse
Dr S. Schilt, rapporteur
Prof. M. Sigrist, rapporteur
Prof. H. van den Bergh, rapporteur



ÉCOLE POLYTECHNIQUE
FÉDÉRALE DE LAUSANNE

Lausanne, EPFL

2006

A mes parents
A Valérie

Abstract

Photoacoustic spectroscopy is a widely recognised technique to measure trace gases at parts-per-million (ppm) or parts-per-billion (ppb) level using semiconductor laser in the near infrared range. This technique is based on the generation of an acoustic wave in a gas excited by a modulated laser beam at a wavelength corresponding to a absorption line of the gas species, and on the detection of this sound using a sensitive microphone. Various sensors have been developed in the past decades in the field of atmospheric pollution monitoring, in the semiconductor industries, in medical applications and in life science applications.

This work aims at presenting the development of a new sensor for multi-gas detection at sub-ppm level using distributed feedback (DFB) semiconductor lasers developed for the optical telecommunication market in the near infrared range. A novel resonant photoacoustic cell that consists in three resonators was designed and characterised. The sensor was developed to monitor up to three different gases for the monitoring of microclimatic parameters of living organisms and for the manufacturing of the next generation of optical fibres used in the optical telecommunication network application.

The buffer gases used in these two applications are extremely different and have a very important impact on the calibration of the photoacoustic sensor. In particular, effects of the physical gas parameters on the photoacoustic signal are theoretically and experimentally compared. Relaxation effects related to these different buffer gases were observed in particular situations and gave rise to drastic changes in the photoacoustic response. A model is developed and quantitatively compared with experimental data.

Finally, the sensitivity of the sensor is an important parameter, since many applications require detection limits down to ppb levels. The use of an Erbium-doped fibre amplifier made ammonia detection at concentration of 2.4 ppb possible. Ammonia monitoring with typical ambient concentration of water vapour and carbon dioxide at atmospheric pressure could be successfully achieved using an innovative approach.

Keywords

Photoacoustic spectroscopy, molecular relaxation, NIR, semiconductor laser diode, multi-gas sensing

Version abrégée

La spectroscopie photoacoustique est une technique de spectroscopie largement répandue pour la détection de traces de gaz au niveau d'une particule par million (ppm) ou d'une particule par milliard (ppb). L'utilisation des lasers à semi-conducteurs développés récemment et employés en premier lieu dans les télécommunications optiques permet d'obtenir ce type de sensibilité dans le proche infrarouge. La spectroscopie photoacoustique est basée sur la génération d'une onde acoustique dans un gaz créée par la modulation d'un laser dont la longueur d'onde correspond à la longueur d'onde d'absorption du gaz à mesurer. La détection de cette onde acoustique se fait au moyen d'un microphone pourvu d'une sensibilité élevée. Plusieurs capteurs basés sur cette technique ont émergé depuis les années 80 dans les applications telles que la détection de polluants dans l'atmosphère, dans le domaine des sciences de la vie et dans les industries à semi-conducteurs.

Le présent travail vise au développement d'un nouveau capteur multi gaz utilisant des lasers à semi-conducteurs fabriqués pour l'industrie des télécommunications optiques dans l'infrarouge proche. Un nouveau type de cellule comportant trois résonateurs excités dans leur premier mode longitudinal a été conçu et caractérisé. Le capteur développé permet, dans une première application, la mesure de trois différents gaz pour la détection des conditions microclimatiques d'animaux de laboratoire. La deuxième application vise la mesure de composants hydrogénés dans la fabrication de la nouvelle génération de fibres optiques permettant l'utilisation d'une large bande spectrale pour la transmission optique de signaux.

Les gaz porteurs utilisés pour ces deux applications sont de nature très différente et influencent directement la détection du signal photoacoustique. Une investigation théorique et expérimentale détaillée de ces effets sur le signal photoacoustique ainsi que sur les paramètres physiques du gaz est présentée. Les effets de relaxation moléculaire observés dans ces différents gaz porteurs font également l'objet d'une recherche théorique et expérimentale.

Finalement, la limite de détection d'un tel capteur est fondamentale pour certaines applications qui nécessitent des niveaux de détection extrêmes, de l'ordre du ppb. L'utilisation d'un amplificateur optique dopé à l'Erbium permet la détection d'ammoniaque à ces niveaux de sensibilité. Une approche novatrice permet la détection de traces d'ammoniaque à pression atmosphérique incluant les effets du dioxyde de carbone et de la vapeur d'eau comme interférents.

Mots clés

Spectroscopie photoacoustique, relaxation moléculaire, proche infrarouge, laser à semiconducteur, multi-gaz

Remerciements

Ce travail de thèse a été effectué au Laboratoire de Nanophotonique et Métrologie de l'EPFL sous la direction du Dr Luc Thévenaz. Je tiens à le remercier sincèrement de m'avoir fait confiance et de m'avoir intégré dans son équipe. Les discussions scientifiques que nous avons partagées m'ont permis d'avancer et de perfectionner mon approche scientifique.

Je remercie particulièrement le Dr Stéphane Schilt, post-doc dans ce laboratoire pendant plusieurs années chargé de l'activité de spectroscopie. Ces connaissances encyclopédiques en spectroscopie m'ont permis d'appivoiser et de maîtriser le domaine de manière approfondie. Je le remercie également pour son immense disponibilité et ces conseils qui m'ont guidé pendant ces quatre dernières années. Finalement, je le remercie pour la lecture attentive qu'il a porté à ce manuscrit et ses nombreuses propositions d'amélioration.

Mes remerciements vont également aux membres du jury, Prof. M. Sigrist et Prof. H. Van den Bergh pour avoir accepté de juger ce travail et d'avoir pris le temps d'évaluer ce mémoire.

Mes remerciements s'adressent également à la Commission pour la Technologie et l'Innovation ainsi qu'à Omnisens (M. Niklès, F. Sauser, E. Rochat) pour avoir financé en partie ce projet.

J'adresse aussi mes remerciements à M. Gyger pour la fructueuse collaboration concernant les mesures effectuées à l'animalerie de l'EPFL.

Je remercie chaleureusement mes collègues de bureau D. Alasia et M. Mattiello avec qui nous avons partagé, en plus de nombreuses discussions scientifiques, plusieurs excellents moments de détente au travers de pause café et de soupers parfois bien arrosés! J'adresse également un clin d'oeil à mon compagnon de montagne Frédo, qui en plus de ses connaissances en électronique, m'a fait découvrir les joies de terrains inconnus. Merci également à Pascal Morel pour tout le temps consacré au développement et aux dessins techniques destinés à la fabrication des différentes cellules photoacoustiques. Je remercie également mes collègues du groupe, S. Chin, P. Paulou et S. Lamy.

Je remercie sincèrement mes parents qui m'ont encouragé pendant toutes ces années d'étude et de thèse.

Finalement, j'adresse une pensée particulière à Valérie, mon épouse, pour son soutien inconditionnel pendant toutes ces années.

Contents

1	Introduction	1
	Bibliography	5
2	Photoacoustic spectroscopy	7
2.1	Introduction	7
2.2	Absorption spectroscopy	7
2.2.1	Intensity of absorption lines	8
2.2.2	Spectral lineshapes and widths	11
2.3	The photoacoustic effect	15
2.3.1	History of photoacoustics	15
2.3.2	Description of the photoacoustic effect in gases	16
2.4	Photoacoustic signal generation	16
2.4.1	Heat production rate for thermal equilibrium	17
2.4.2	Generation of acoustic waves	18
2.5	Loss mechanisms	26
2.5.1	Quality factor	27
	Bibliography	29
3	Photoacoustic cell design	33
3.1	Introduction	33
3.2	Acoustic resonators	33
3.2.1	Cylindrical cavities	35
3.2.2	Helmholtz resonator	37
3.2.3	Multipass resonant cell	38
3.2.4	Miniature photoacoustic cells	39
3.3	Design of the photoacoustic cell	39
3.3.1	Selection criteria of the photoacoustic cell	39
3.3.2	Selection of an optimal geometry	40
3.4	Modulation schemes applied to spectroscopy	46
3.5	Characterisation of the photoacoustic cell	48
3.5.1	Performance of the cell	48
3.5.2	Improvement of the photoacoustic cell	51
3.6	Resonance frequency tracking and wavelength stabilisation	55
3.6.1	Acoustic resonance frequency tracking	55
3.6.2	Laser wavelength stabilisation	56
	Bibliography	58

4	Trace gas monitoring	63
4.1	Introduction	63
4.2	Description of the applications	63
4.2.1	Life science application	63
4.2.2	Optical fibre manufacturing process application	64
4.3	Laboratory performances	65
4.3.1	Laser selection and characteristics	66
4.3.2	Calibration and detection limits	72
4.3.3	Influence of the buffer gas	78
4.3.4	Conclusion	81
4.4	CO ₂ , NH ₃ and H ₂ O in-situ monitoring: application to life science	81
4.4.1	Sensor architecture	81
4.4.2	Experimental results	84
4.4.3	Conclusion	87
4.5	Multi-hydrogenated compounds monitoring in optical fibre manufacturing process	87
4.5.1	Experimental details	87
4.5.2	Results and discussion	89
4.5.3	Conclusion	94
4.6	Ammonia trace measurements at ppb level	94
4.6.1	Introduction	94
4.6.2	Sensor design	94
4.6.3	Results and discussion	96
4.7	Conclusion	104
	Bibliography	105
5	Molecular relaxation in photoacoustic spectroscopy	109
5.1	Introduction	109
5.2	Molecular collisions	109
5.2.1	Elastic collisions between inert gas molecules	110
5.2.2	Inelastic collisions between diatomic molecules	111
5.3	Vibration-translation energy transfer	113
5.3.1	Intermolecular potentials	113
5.3.2	Transition probabilities	114
5.3.3	Modified theories	116
5.4	Vibration-vibration energy transfer	120
5.4.1	The SSH theory for non-resonant and resonant transfer	120
5.4.2	Intermode transfer in polyatomic gases	121
5.5	Rotation-translation energy transfer	123
5.6	Influence of molecular relaxation in PA spectroscopy	125
5.7	Molecular relaxation in CH ₄ detection	126
5.7.1	Relaxation effects in the CH ₄ -O ₂ system	127
5.7.2	Parabolic response of the sensor with respect to CH ₄ concentration	133
5.7.3	Enhancement of the V-T process rate in CH ₄ -O ₂ mixture using a catalyst	137
5.7.4	Conclusion	139
5.8	Molecular relaxation in HCl detection	140
5.8.1	Relaxation effects in the HCl-He-N ₂ system	144
5.8.2	Relaxation effects in the HCl-He-O ₂ system	147

5.8.3	Improvement of V-T transfers by the use of a catalyst .	148
5.9	Conclusion	149
6	Conclusion	155
A	Modelling molecular relaxation	157
	Bibliography	160
	Nomenclature	163

List of Figures

2.1	Linestrength dependence on temperature for H ₂ O, HCl and CO ₂	9
2.2	Doppler width (HWHM) for CO ₂ , H ₂ O and HCl	12
2.3	Collisional broadening of HCl, CO ₂ and H ₂ O	13
2.4	Comparison of Gaussian and Lorentzian lineshapes with the same HWHM and a Voigt profile	14
2.5	Approximation of the Voigt profile by a Lorentzian distribution for 50 ppm HCl	14
2.6	Discovery of the photoacoustic effect by Alexander Graham Bell with his photophone	15
2.7	First two longitudinal, azimuthal and radial eigenmodes of a both-ended opened cylindrical acoustic cell	23
3.1	Schematic representation of the Helmholtz resonator	38
3.2	Multipass resonant PA cell	38
3.3	Schematic representation of the QEPAS configuration	39
3.4	Theoretical dependence of the resonance frequency	41
3.5	Frequency dependence in air of the first longitudinal mode in function of the length of the resonator.	42
3.6	Quality factor Q	43
3.7	Influence of the resonator radius R_c on the quality factor Q_{100} for different resonator lengths	43
3.8	Theoretical dependence of the cell constant	44
3.9	PA spectrum of methane obtained with an IM-dominant regime	47
3.10	Amplitude of the PA signal of the strong CH ₄ line at 1650.96 nm as a function of the current modulation depth (square modulation)	47
3.11	Schematic representation of the longitudinal PA cell	48
3.12	First longitudinal resonance of the PA cell	49
3.13	Picture of the PA cell	51
3.14	First longitudinal resonance of the gold coated PA cell	52
3.15	Acoustic response of the gold coated PA cell	52
3.16	Acoustic noise as a function of the flow rate	53
3.17	Response time of the PA cell to a change of CH ₄ concentration	53
3.18	Crosstalk between the three resonators	54
3.19	Ratio of the measurement frequency (f_{meas}) and the tracking frequency (f_{track})	56
3.20	Shape of the absorption line measured with the reference and linear cell	56

3.21	Schematic view of the set-up used to actively stabilise the laser wavelength	57
3.22	Frequency drift of a laser diode emitting at 1651 nm	57
4.1	Standard and Low-water-peak fibre spectral attenuation	64
4.2	Linewidth of a laser emitting at 1532 nm	68
4.3	Dependence of the laser wavelength as a function of the injection current and the temperature at 1650 nm	69
4.4	PA spectrum of CH ₄	70
4.5	PA spectrum of CO ₂	70
4.6	PA spectrum of H ₂ O	71
4.7	PA spectrum of NH ₃	71
4.8	PA spectrum of HCl	72
4.9	Scheme of the experimental set-up	72
4.10	Response of the sensor to different CH ₄ concentrations diluted in N ₂	73
4.11	Response of the sensor to different CO ₂ concentrations diluted in air containing 50% of relative humidity	74
4.12	Response of the sensor to different H ₂ O concentrations for the range of ambient humidity levels in air	74
4.13	Response of the sensor to different H ₂ O concentrations diluted in nitrogen	75
4.14	Response of the sensor to different NH ₃ concentrations diluted in nitrogen	76
4.15	Calibration curves for HCl and H ₂ O in a 60% O ₂ -40% He mixture	77
4.16	Variation of the resonance frequency, the quality factor and the cell constant as a function of the gas composition	79
4.17	Calibration curves for CH ₄ in 100% N ₂ , 50% O ₂ -50% He and 90% O ₂ -10%	80
4.18	Schematic representation of the PA sensor for the animal house application	82
4.19	Acoustic resonance of the PA cell	83
4.20	Picture of the installation for <i>in-situ</i> measurements in the animal house	84
4.21	Evolution of ammonia concentration from day 2 (after bedding change) to day 11 in different cages	85
4.22	Evolution of H ₂ O and CO ₂ levels in a selected cage containing 6 mice from day 4 to day 7	85
4.23	CO ₂ accumulation in cages disconnected separately from the ventilation	86
4.24	Measurement of the ventilation flow of an empty cage	86
4.25	Gas distribution system for the preform manufacturing	87
4.26	Typical HCl and H ₂ O concentration measurements over several minutes in the optical manufacturing process	89
4.27	HCl concentration level evolution over 11 days in the optical manufacturing process	90
4.28	H ₂ O concentration level evolution over 11 days in the optical manufacturing process	90
4.29	Attenuation of the low-water-peak fibres	92

4.30	HCl and H ₂ O measurements in a gas mixture of 100 sccm O ₂ saturated with GeCl ₄ , 400 sccm O ₂ and 500 sccm He	93
4.31	HCl and H ₂ O measurements in a gas mixture of 100 sccm O ₂ saturated with SiCl ₄ , 200 sccm O ₂ and 700 sccm He	93
4.32	Scheme of the experimental set-up for ppb ammonia detection .	95
4.33	Residual intensity modulation	97
4.34	PA signal demodulated at $1f$ as a function of ammonia concentration	98
4.35	Amplitude of the NH ₃ and CO ₂ PA signals as a function of the laser current modulation depth in the case of a sinusoidal waveform with $2f$ detection	98
4.36	PA signal demodulated at $2f$ as a function of ammonia concentration	99
4.37	H ₂ O and CO ₂ spectra calculated from the HITRAN database and NH ₃ spectrum obtained from the PNNL database for concentrations of respectively 1.15%, 5000 ppm and 5 ppm and corresponding PA spectra measured using the EDFA and an external chopper for the same compounds concentrations	100
4.38	NH ₃ , CO ₂ and H ₂ O measured spectra at $2f$	101
4.39	Comparison of the simulated $2f$ PA signals for 1 ppm NH ₃ and 4000 ppm CO ₂ at different pressures	103
5.1	The Lennard-Jones intermolecular potential	110
5.2	Collinear collision between a vibrating molecule and a non-vibrating diatomic molecule	111
5.3	Collision between two rotating diatomic molecules	113
5.4	Approximation of the Lennard-Jones potential by two different exponential curves	114
5.5	Energy-level diagram for simultaneous vibrational and rotational transitions	120
5.6	Energy level diagram showing transitions for a molecule with two active vibrational modes	122
5.7	Calculated collision numbers for V-V transitions in CH ₄	123
5.8	Scheme of the experimental set-up used for molecular relaxation effects	127
5.9	Variation of the PA response corresponding to 100 ppm CH ₄ as a function of the O ₂ fraction in N ₂ in the buffer gas	128
5.10	Energy levels diagram of CH ₄ molecule	130
5.11	Variation of the PA signal as a function of the O ₂ concentration in the buffer gas for two different excited CH ₄ transitions . . .	133
5.12	Variation of the PA signal as a function of the CH ₄ concentration for different carrier gases	134
5.13	Dependence of the PA signal corresponding to 20 ppm of CH ₄ as a function of the H ₂ O content in the carrier gas	137
5.14	Variation of the PA signal as a function of the CH ₄ concentration for different carrier gases	139
5.15	Normalisation curves performed in H ₂ O	141
5.16	Simulation of the maximum of the absorption coefficient (IM) and the corresponding $1f$ signal (WM) as a function of the N ₂ fraction in the buffer gas for H ₂ O and HCl	143

5.17	Simulation of the maximum of the absorption coefficient (IM) and the corresponding $1f$ signal (WM) as a function of the O_2 fraction in the buffer gas for H_2O and HCl	143
5.18	Energy level diagram of HCl	144
5.19	Variation of the PA signal amplitude corresponding to 5 ppm HCl as a function of N_2 fraction in He	145
5.20	Simulation of H	146
5.21	Variation of the PA signal amplitude corresponding to 5 ppm HCl as a function of O_2 fraction in He	147
5.22	Amplitude dependence of the PA signal corresponding to 5 ppm HCl as a function of the H_2O content in the carrier gas composed of 50% O_2 and 50% He	148
5.23	Amplitude dependence of the PA signal corresponding to 5 ppm HCl as a function of the H_2O content in the carrier gas composed of 50% N_2 and 50% He	149
A.1	Energy diagram used for modelling molecular relaxation.	157

List of Tables

2.1	Normal vibrational frequencies, rotational frequencies and symmetry factor for CO ₂ , H ₂ O and HCl	10
2.2	Values of $\pi\alpha_{mn}$ for some of the first azimuthal and radial modes of a cylindrical acoustic cavity.	22
3.1	Physical constants of some gases	41
3.2	Comparison of the performances of the PA cells	50
4.1	Characteristics of the lasers used for trace gas monitoring	69
4.2	Detection limits obtained for different gases in various buffer gases	81
4.3	Cages description containing mice	84
4.4	Gas mixtures and chloride concentrations used for HCl and H ₂ O monitoring	88
4.5	Comparison of chlorides, H ₂ O and HCl concentrations between the buffer gas used for PAS measurements and the process gas used in optical fibre manufacturing	88
4.6	Comparison of NH ₃ concentrations calculated from mass-flow controllers (MFC) adjustment and measured with Omnisens' Trace Gas Analyser (TGA)	97
4.7	Parameters of the strongest NH ₃ and CO ₂ lines around 1531.67 nm	102
5.1	Collision parameters used in the Lennard-Jones potential	111
5.2	Examples of some relaxation rates of some vibrational states of CH ₄ with different collisional partners	131
5.3	Parameters of the HCl and H ₂ O line	142
5.4	Examples of some relaxation rates of some vibrational states of HCl	145

Chapter 1

Introduction

Infrared spectroscopy is an efficient method to detect various gaseous species, since many of them absorb in this spectral range. The bases of infrared spectroscopy were theoretically explored by A. Einstein in 1905 and N. Bohr in 1913 who postulated the quantization of the electromagnetic field [1] and the energy levels of atoms [2], respectively. In 1915, Einstein described in details the interaction between light and absorption through the transition probability coefficients between two levels of energy [3]. An important breakthrough was achieved with the contribution of G. Herzberg to the description of molecular transitions [4, 5]. In parallel with theoretical investigations, experimental developments were performed since the beginning of the 20th century. At that time, the developed spectrometers were used with broadband sources in combination with filters to selectively detect the gases of interest. However, the poor selectivity and sensitivity of these sensors made them of rather limited interest.

An important technological breakthrough occurred with the advent of lasers in the early sixties. These sources are particularly well adapted for infrared spectroscopy, since they offer many advantages, such as, for example, high power and monochromatic emission. A wide variety of laser sources currently available (semiconductor lasers, gas lasers, quantum cascade lasers) covers almost the entire infrared spectrum and makes the detection of multiple gas species possible. In particular, distributed feedback laser diodes emitting in the near infrared (NIR) range are excellent light sources, since they present many advantages, such as excellent spectral properties, modulation capabilities through the injection current (intensity or wavelength modulation), long lifetime operation, low cost due to a mass production mainly devoted to the optical telecommunication market.

Infrared spectroscopy is a particular technique for gas traces detection among several other conventional methods like for example, gas chromatography, chemiluminescence or fluorescence. Gas chromatography requires the preparation and the extraction of the gas sample resulting in a long response time and in an impossible continuous measurement. Chemiluminescence is based on a chemical reaction of the gaseous sample, thus modifying the composition of the initial gas which is, for instance, in medical applications not possible. Fluorescence is less adapted to molecular analysis since the cross-sections are weak and thus directly limit the sensitivity of such systems. Laser infrared spectroscopy offers key advantages in comparison to the above mentioned techniques. For instance, short response time, continuous and real-time

trace gas monitoring (from part-per-million (ppm) down to part-per-billion (ppb) range) are with this technique possible. Moreover, the design of portable instruments, particularly well adapted for *in-situ* measurements is achievable.

Laser photoacoustic spectroscopy (LPAS) is a specific technique that differs from conventional optical absorption spectroscopy methods based on the Beer-Lambert law which states the exponential attenuation of the transmitted intensity (Fourier-transform infrared spectroscopy, cavity ring-down spectroscopy, intracavity spectroscopy). Photoacoustic spectroscopy is a calorimetric method, in which the optical energy absorbed in a gaseous species is directly measured through the heating produced in the medium. The conversion from optical energy to heat is induced by molecular absorption of photons at proper wavelength and subsequent non-radiative relaxation of the excited state (collisional relaxation). The small local temperature variation in the sample is associated to a pressure variation. When the deposited optical energy is modulated, a periodic heating is produced, thus generating a modulation of the sample pressure. This results in an acoustic wave, which can be detected using a sensitive miniature microphone.

This technique provides several advantages over standard absorption spectroscopy methods:

- The absorbed energy (not the transmitted energy) in the gas is measured so that no signal is produced in absence of the gas species and thus no background signal is present.
- The detection of the photoacoustic signal is performed using a sensitive microphone and is thus wavelength- independent.
- The response of the system is linear over several order of magnitude with the gas concentration. Theoretically, one calibration point is sufficient to characterise the sensor response.
- A simple sensor configuration makes low (sub-ppm) to extremely low (ppb) detection limits possible.
- The size of the system is kept small, which offers the possibility of portable instruments compatible with industrial environments.

LPAS is a widely recognised method that is applied in many different applications. The most important applications are listed below:

- Environmental pollutants monitoring: ammonia in agricultural environment [6] or in road traffic emission [7, 8], H₂O in atmospheric research [9], contribution of N₂O to the destruction of ozone [10], study of H₂O, CO₂ and C₂H₄ in urban areas [11].
- Medical diagnostics: NO monitoring to analyse vital processes in the human body [12], NH₃ in the human breath [13].
- Industrial process control: NH₃ in the semiconductor industry [14], NO in exhaust system [15] or hydrogenated compounds in the manufacturing of optical fibre process [16].
- Life science field: CH₄, H₂O and CO₂ emission by cockroaches and scarab beetle [17] or microclimate monitoring of living organisms in animal house [18].

-
- Storage et transportation of fruit industry to control the ripening process of different fruits (ethylene monitoring) [19].
 - Detection of gas leaks in hazardous work environment by the use of SF₆ [20].
 - Detection of various doping agents used by athletes [21].

All of these applications require high sensitivity, high selectivity, short response time and transportable instruments, which makes photoacoustic spectroscopy a good candidate to fulfil these needs.

The present work aims at developing a multi-gas sensor using semiconductor lasers emitting in the near infrared range. A first cell prototype based on a single resonator makes multi-gas sensing possible through frequency multiplexing. An improvement of this configuration based on a three resonator set-up is then discussed. Multi-gas sensing is of primary importance to be compliant with the applications that are investigated.

The first application concerns the life science field where microclimate parameters of mice have to be monitored. In particular, CO₂, NH₃ and H₂O are simultaneously recorded. The second application concerns the optical fibre manufacturing process where hydrogenated compounds have to be detected. For this case, CH₄, HCl, and H₂O are monitored in a particular buffer gas specific for the manufacturing of the preform.

The influence of the buffer gas on the PA signal is treated in details, since the conditions between the two applications are very different. This investigation leads to unexpected results due to molecular relaxation. This phenomenon is analysed for CH₄-O₂ and HCl-N₂/O₂ systems resulting in a drastic deterioration of the performance of the system.

Finally, detection of ammonia at ppb level is presented and measurements down to a few ppb are shown. In addition, the interference of CO₂ and H₂O on the ammonia signal is treated.

Organisation of the work

This work mainly consists in four chapters.

- The chapter 2 presents a brief description of the basics of spectroscopy necessary to understand the photoacoustic theory. The second part is dedicated to the theory that describes the heat production rate for thermal equilibrium and the generation of acoustic wave in photoacoustic spectroscopy.
- In chapter 3, a brief review of different acoustic resonators are presented followed by the design of the photoacoustic cell and its characterisation.
- The chapter 4 is mainly dedicated to photoacoustic applications. In particular, a first example in the life science field is described. A second application in the optical fibre manufacturing process is presented with *in-situ* and automated measurements during a period of 11 days. Finally, a sensor design to reach extreme detection limits (in the ppb range) of NH₃ is proposed.

- The chapter 5 deals with molecular relaxation effects in photoacoustic spectroscopy. A brief theory is first given to explain the basics of molecular relaxation. The second part is dedicated to the description of two experimental examples in $\text{CH}_4\text{-O}_2$ mixture and in $\text{HCl-N}_2\text{-O}_2\text{-He}$ mixtures.

Bibliography

- [1] A. Einstein, “Ueber einen die Erzeugung und Verwandlung des Lichtes betreffenden euristischen Gesichtspunkt,” *Annalen der Physik* **17**, 132–148 (1905).
- [2] N. Bohr, “On the constitution of atoms and molecules,” *Philos. mag.* **26**(1), 1–24 (1913).
- [3] A. Einstein, “Ein Satz der Wahrscheinlichkeitsrechnung und seine Anwendung auf die Strahlungstheorie,” *Annalen der Physik* **47**, 879–885 (1915).
- [4] G. Herzberg, *Molecular spectra and molecular structure*, vol. I- Spectra of diatomic molecules (Krieger, Malabar, 1989).
- [5] G. Herzberg, *Molecular spectra and molecular structure*, vol. II- Infrared and Raman spectra of polyatomic molecules (Krieger, Malabar, 1991).
- [6] M. E. Webber, T. MacDonald, M. B. Pushkarsky, C. K. N. Patel, Y. Zhao, N. Marcillac, and F. M. Mitloehner, “Agricultural ammonia sensor using diode lasers and photoacoustic spectroscopy,” *Meas. Sci. Technol.* **16**, 1547–1553 (2005).
- [7] S. Schilt, L. Thévenaz, M. Niklès, L. Emmenegger, and C. Hügli, “Ammonia monitoring at trace level using photoacoustic spectroscopy in industrial and environmental applications,” *Spectrochim. Acta, Part A* **60**(14), 3259–3268 (2004).
- [8] D. Marinov and M. Sigrist, “Monitoring of road-traffic emissions with a mobile photoacoustic system,” *Photochem. Photobiol. Sci.* **2**(7), 774–778 (2003).
- [9] M. Szakall, Z. Bozoki, A. Mohacsi, A. Varga, and G. Szabo, “Diode laser based photoacoustic water vapor detection system for atmospheric research,” *Appl. Spectrosc.* **58**(7), 792–798 (2004).
- [10] M. G. da Silva, A. Miklos, A. Falkenroth, and P. Hess, “Photoacoustic measurement of N₂O concentrations in ambient air with a pulsed optical parametric oscillator,” *Appl. Phys. B* **82**(2), 329–336 (2006).
- [11] P. L. Meyer and M. Sigrist, “Atmospheric pollution monitoring using CO₂- laser photoacoustic spectroscopy and other techniques,” *Rev. Sci. Instrum.* **61**(7), 1779–1807 (1990).
- [12] Y. A. Bakhirkin, A. A. Kosterev, R. F. Curl, F. K. Tittel, D. A. Yarekha, L. Hvozdar, M. Giovannini, and J. Faist, “Sub-ppbv nitric oxide concentration measurements using cw thermoelectrically cooled quantum cascade laser-based integrated cavity output spectroscopy,” *Appl. Phys. B* **82**(1), 149–154 (2006).
- [13] L. R. Narasimhan, W. Goodman, and C. K. N. Patel, “Correlation of breath ammonia with blood urea nitrogen and creatinine during hemodialysis,” *PNAS* **98**(8), 4617–4621 (2001).

-
- [14] S. MacDonald, N. Clecak, R. Wendt, C. G. Willson, C. Snyder, C. Knors, N. Deyoe, J. Maltabes, J. Morrow, A. McGuire, and S. Holmes, "Airborne chemical contamination of chemically amplified resist," Proc SPIE 1466 p. 2 (1991).
- [15] G. Wysocki, A. A. Kosterev, and F. K. Tittel, "Spectroscopic trace-gas sensor with rapidly scanned wavelengths of a pulsed quantum cascade laser for in situ NO monitoring of industrial exhaust systems," Appl. Phys. B **80**, 617–625 (2005).
- [16] J. P. Besson, S. Schilt, F. Sauser, E. Rochat, P. Hamel, F. Sandoz, M. Niklès, and L. Thévenaz, "Multi-hydrogenated compounds monitoring in optical fibre manufacturing process by photoacoustic spectroscopy," Appl. Phys. B **85**, 343–348 (2006).
- [17] F. G. C. Bijnen, F. J. M. Harren, J. H. P. Hackstein, and J. Reuss, "Intracavity CO laser photoacoustic trace gas detection: cyclic CH₄, H₂O and CO₂ emission by cockroaches and scarab beetles," Appl. Opt. **35**(27), 5357–5368 (1996).
- [18] S. Schilt, J. P. Besson, L. Thévenaz, and M. Gyger, "Continuous and simultaneous multigas monitoring using a highly sensitive and selective photoacoustic sensor," in *CLEO/QELS and PhAST* (2005).
- [19] M. da Silva, J. Lima, E. Sthel, E. Marin, C. Gatts, S. Cardoso, E. Campostrini, M. G. Pereira, A. Campos, M. Massunaga, and H. Vargas, "Ethylene and CO₂ emission rates in tropical fruits investigated by infrared absorption techniques," Anal. Sci. **17**, 534–537 (2001).
- [20] M. A. Gondal, A. Dastageer, and M. H. Shwehdi, "Photoacoustic spectrometry for trace gas analysis and leak detection using different cell geometries," Talanta **62**, 131–141 (2004).
- [21] C. Fischer, R. Bartlome, and M. W. Sigrist, "The potential of mid-infrared photoacoustic spectroscopy for the detection of various doping agents used by athletes," Appl. Phys. B **85**, 289–294 (2006).

Chapter 2

Photoacoustic spectroscopy

2.1 Introduction

This first chapter is dedicated to the theory that describes photoacoustic spectroscopy. The first part deals with the fundamentals of absorption spectroscopy, mainly the intensity, the shape and the width of absorption lines. This description is required to the interpretation of the photoacoustic signal. The second part of the chapter is dedicated to the description of photoacoustic spectroscopy through fundamental laws of fluid mechanics and thermodynamics.

2.2 Absorption spectroscopy

The detection of individual gaseous species using optical methods is based on selective interaction processes between radiation and matter. Three main interaction processes can be considered for the detection of gases: Raman scattering, fluorescence emission and absorption processes. Raman scattering offers the advantage that a laser emission at only one wavelength is sufficient for the detection of numerous gases, since the selectivity is given by the characteristic frequency shifts relative to the incident wavelength. The main drawback of this method is the weak scattering cross sections and possible interference with fluorescence. Laser-induced fluorescence is well adapted for the detection of atoms or radicals but is less suitable for the detection of gas species, since the cross sections are small (comparable to Raman scattering [1]).

The most important optical process for spectroscopic detection of gases is based on absorption. The absorption wavelengths and strengths that are specific to each molecule allow the identification of the gaseous compounds and the determination of their concentrations. Absorption cross sections of molecules are typically on the order of 10^{-22} cm² to 10^{-20} cm² in the near infrared (NIR) at atmospheric pressure and thus six to eight orders of magnitude larger than Raman cross sections [2]. This results in a drastic increase in detection sensitivity and absorption spectroscopy is thus the most widely spectroscopic detection scheme used for trace gas monitoring.

2.2.1 Intensity of absorption lines

The fundamental theory governing absorption spectroscopy is embodied by the Beer-Lambert law. The transmitted light intensity through an absorbing media of length l is:

$$I(\tilde{\nu}) = I_0 e^{-a_m} \quad (2.1)$$

where I_0 is the incident light intensity, $\tilde{\nu}$ is the wavenumber in cm^{-1} and a_m is the absorbance of the medium. The wavenumber $\tilde{\nu}$ is defined by:

$$\tilde{\nu} = \frac{\nu}{c} = \frac{E_m - E_n}{hc} \quad (2.2)$$

where ν is the frequency of the lightwave in Hz, c the speed of light in vacuum, h the Planck's constant, E_n is the lower energy level and E_m is the upper energy level.

The absorbance is linked to the absorption coefficient $\alpha(\tilde{\nu})$: $a_m = \alpha(\tilde{\nu})l$. The absorption coefficient is related to the cross section $\sigma(\tilde{\nu})$ of the molecules by:

$$\alpha(\tilde{\nu}) = N\sigma(\tilde{\nu}) = -\frac{1}{l} \ln \left[\frac{I(\tilde{\nu})}{I_0} \right] \quad (2.3)$$

where N is the gas density in (mol/cm^3). The cross section can be represented by a normalised function $g(\tilde{\nu})$, describing the absorption line shape, and by the line intensity S expressed in ($\text{cm}^{-1}/(\text{mol cm}^{-2})$):

$$\sigma(\tilde{\nu}) = Sg(\tilde{\nu}), \quad S = \int_0^{\infty} \sigma(\tilde{\nu}) d\tilde{\nu} \quad (2.4)$$

The measurement of the absorption coefficient allows to obtain the gas density:

$$N = -\frac{1}{lSg(\tilde{\nu})} \ln \left[\frac{I(\tilde{\nu})}{I_0} \right] \quad (2.5)$$

and thus the concentration C of the gas:

$$C = \frac{N}{N_{tot}} \quad (2.6)$$

The total density of molecules at temperature T and pressure p_0 is given by:

$$N_{tot} = N_L \frac{296}{T} p_0 \quad (2.7)$$

where $N_L = 2.479 \cdot 10^{19} \text{ mol cm}^{-3} \text{ atm}^{-1}$ is the Loschmidt number.

The linestrength S of an absorption transition depends on the population N_n in the lower quantum state, which is a function of the Boltzmann distribution, and the probability of the transition (given by the Einstein coefficient B_{nm} ¹) between the upper state m and the lower state n , which depends on the specific spectroscopic constants associated with that molecule's particular transition:

$$S = \frac{1}{N} \frac{h\tilde{\nu}_{nm}}{c} B_{nm} N_n \left[1 - \exp \left(-\frac{hc\tilde{\nu}_{nm}}{kT} \right) \right] \quad (2.8)$$

¹The probability of transition between two states $|m\rangle$ and $|n\rangle$ is $B_{nm} = \frac{8\pi^3}{3h^2c} |\mathbf{R}_{nm}|^2$, where \mathbf{R}_{nm} is the matrix element of the dipolar moment.

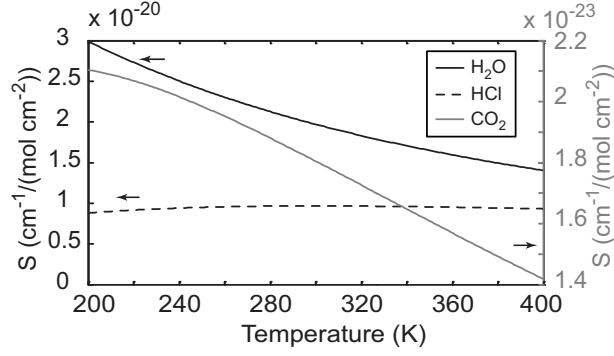


Figure 2.1: Linestrength dependence on temperature for H₂O (*black curve*) at 1369 nm corresponding to the transition (0 0 0)_{2,2} → (1 0 1)_{3,3} [4], for HCl (*dashed curve*) at 1738 nm (line R4) corresponding to the transition (0) → (2) and for CO₂ (*grey curve*) at 1572 nm (line R18), corresponding to the transition (0 0 0) → (2 2⁰ 1).

where k is the Boltzmann constant and the population of the lower state N_n is given by

$$N_n = \frac{N g_n}{Q_{int}} \exp\left(-\frac{hcE_n}{kT}\right), \quad Q_{int} = \sum_n g_n \exp\left(-\frac{hcE_n}{kT}\right) \quad (2.9)$$

Q_{int} is the total internal partition function, E_n is the lower-state energy of the transition and g_n is the degeneracy of the lower state. By combining 2.8 and 2.9, the linestrength at temperature T is obtained:

$$S(T) = \frac{h\tilde{\nu}_{nm}}{c} B_{nm} \frac{g_n}{Q_{int}(T)} \exp\left(-\frac{hcE_n}{kT}\right) \left[1 - \exp\left(-\frac{hc\tilde{\nu}_{nm}}{kT}\right)\right] \quad (2.10)$$

$S(T)$ can be expressed as a function of S_0 obtained at a reference temperature T_{ref} :

$$S(T) = S_0 \frac{Q_{int_0}}{Q_{int}(T)} \frac{T_{ref}}{T} \frac{[1 - \exp(-\frac{hc\tilde{\nu}_{nm}}{kT})]}{[1 - \exp(-\frac{hc\tilde{\nu}_{nm}}{kT_{ref}})]} \exp\left[-\frac{hcE_n}{k} \left(\frac{1}{T} - \frac{1}{T_{ref}}\right)\right] \quad (2.11)$$

The linestrength is usually tabulated at room temperature ($T_{ref} = 296K$) in databases [3]. Equation 2.11 is used to determine line-strengths at different temperatures as far as the partition function Q_{int} is known (see Figure 2.1).

The total internal partition function $Q_{int}(T)$ can be approximated by the product [5]:

$$Q_{int}(T) = Q_n Q_\nu Q_J \quad (2.12)$$

where Q_n is the nuclear, Q_ν the vibrational and Q_J the rotational partition function. For rotational-vibrational transitions only Q_ν and Q_J contribute to the total internal partition function

$$Q_\nu = \sum_\nu g_\nu \exp\left(-\frac{E_\nu}{kT}\right) \quad (2.13a)$$

$$Q_J = \sum_J g_J \exp\left(-\frac{E_J}{kT}\right) \quad (2.13b)$$

	$\tilde{\nu}_1$ (cm ⁻¹)	$\tilde{\nu}_2$ (cm ⁻¹)	$\tilde{\nu}_3$ (cm ⁻¹)	A_m (cm ⁻¹)	B_m (cm ⁻¹)	C_m (cm ⁻¹)	σ_m
CO ₂	1333	667	2349	-	0.39	-	2
H ₂ O	3657	1595	3756	27.88	14.52	9.28	2
HCl	2886	-	-	-	10.59	-	1

Table 2.1: Normal vibrational frequencies ($\tilde{\nu}_1$, $\tilde{\nu}_2$, $\tilde{\nu}_3$), rotational frequencies (A , B , C) and symmetry factor σ for CO₂, H₂O and HCl [5, 7].

By considering the harmonic approximation ², the vibrational partition function is given by:

$$Q_\nu = \left[1 - \exp\left(-\frac{hc\tilde{\nu}_1}{kT}\right) \right]^{-d_1} \left[1 - \exp\left(-\frac{hc\tilde{\nu}_2}{kT}\right) \right]^{-d_2} \dots \quad (2.14)$$

where d_i is the degeneracy of the normal mode $\tilde{\nu}_i$. The rotational partition function depends on the symmetry of the molecule. For linear molecules, a power series valid for $kT \ll hcB_m$ ³ can be obtained

$$Q_J = \frac{1}{\sigma_m} \frac{kT}{hcB_m} \quad (2.15)$$

where σ_m is the symmetry factor given by the symmetry properties of the molecule and B_m the rotational frequency of the molecule. For non-linear molecules, the power series gives:

$$Q_J = \frac{1}{\sigma_m} \sqrt{\frac{\pi}{A_m B_m C_m}} \left(\frac{kT}{hc}\right)^3 \quad (2.16)$$

where A_m , B_m , and C_m are the rotational frequencies in cm⁻¹. The vibrational and rotational fundamental frequencies and the symmetry factor are given in Table 2.1 for some molecules [5, 7]. The total internal partition function given by (2.12) can be written for linear molecules

$$Q_\nu = \frac{1}{\sigma_m} \frac{kT}{hcB_m} \left[1 - \exp\left(-\frac{hc\tilde{\nu}_1}{kT}\right) \right]^{-d_1} \left[1 - \exp\left(-\frac{hc\tilde{\nu}_2}{kT}\right) \right]^{-d_2} \dots \quad (2.17)$$

and for non-linear molecules:

$$Q_\nu = \frac{1}{\sigma_m} \sqrt{\frac{\pi}{A_m B_m C_m}} \left(\frac{kT}{hc}\right)^3 \left[1 - \exp\left(-\frac{hc\tilde{\nu}_1}{kT}\right) \right]^{-d_1} \times \left[1 - \exp\left(-\frac{hc\tilde{\nu}_2}{kT}\right) \right]^{-d_2} \dots \quad (2.18)$$

²The harmonic approximation is obtained by taking the first and second order terms of the power series defined for the central potential linking two molecules [6].

³The rotational energy is given by $E_J = B_m hc J(J+1)$, where B_m is the rotational frequency and J the rotational quantum number.

2.2.2 Spectral lineshapes and widths

In addition to linestrength, lineshapes and widths parameters are important to characterise the absorption line. Broadening of an absorption feature occurs mainly due to three processes: natural line broadening, Doppler broadening and collisional broadening. These three effects are discussed in the next paragraphs.

2.2.2.1 Natural line broadening

Natural line broadening is due to the finite lifetime of the energy levels. Except the fundamental level, all excited levels are characterised by their lifetime [8]:

$$\tau = \frac{1}{A_{nm}} \quad (2.19)$$

where A_{nm} is the Einstein coefficient due to spontaneous emission. It is related to B_{nm} defined in subsection 2.2.1:

$$A_{nm} = 8\pi hc\tilde{\nu}_{nm}^3 B_{nm} = \frac{64\pi^4\tilde{\nu}_{nm}^3}{3h} |\mathbf{R}_{nm}|^2 \quad (2.20)$$

This finite value of the lifetime manifests in a broadening ΔE of the energy level, which is given by the Heisenberg uncertainty relation [9]:

$$\tau\Delta E \geq \hbar \quad (2.21)$$

By combining 2.20 and 2.21, the resulting transition line broadening is:

$$\Delta\tilde{\nu}_{nat} = \frac{\Delta E}{hc} \geq \frac{32\pi^3\tilde{\nu}^3}{3hc} |\mathbf{R}_{nm}|^2 \quad (2.22)$$

The dependence of $\Delta\tilde{\nu}_{nat}$, the frequency spread, on $\tilde{\nu}^3$ results in a much larger value for an excited electronic state, typically $1 \times 10^{-3} \text{ cm}^{-1}$ (30 MHz), than for an excited vibrational state $1 \times 10^{-7} - 6.7 \times 10^{-7} \text{ cm}^{-1}$ (3-20 kHz) or rotational state $3 \times 10^{-14} - 3 \times 10^{-15} \text{ cm}^{-1}$ (10^{-4} - 10^{-5} Hz), because of the much greater $\tilde{\nu}$ for an excited electronic state. Since each atom or molecule behaves identically, natural line broadening is an homogeneous line broadening which results in a characteristic Lorentzian line shape. Natural line broadening is very small for vibrational-rotational transitions and is experimentally not observed in normal conditions, since other processes (Doppler, collisional broadening) result in a much more important broadening.

2.2.2.2 Doppler broadening

When an atom or a molecule has a velocity component v_a in the same direction than the propagation of a beam of light, a shift occurs in the frequency $\tilde{\nu}_a$ at which the photon is absorbed. This effect is called the Doppler shift. The shifted frequency $\tilde{\nu}_a$ can be expressed as a function of the frequency $\tilde{\nu}_0$ of an atom or a molecule at rest:

$$\tilde{\nu}_a = \tilde{\nu}_0 \left(1 \pm \frac{v_a}{c}\right) \quad (2.23)$$

The molecules of any gas are in constant motion and the distribution of their random velocities is described by the Maxwell distribution. The molecules

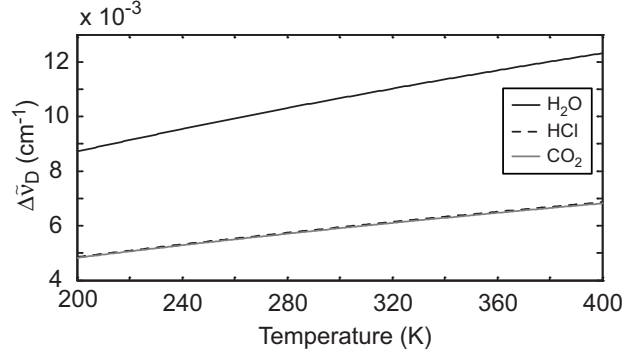


Figure 2.2: Doppler width (HWHM) for CO₂ at 6361.26 cm⁻¹ (1572 nm), for H₂O at 7306.74 cm⁻¹ (1369 nm) and HCl at 5753.97 cm⁻¹ (1738 nm) as a function of temperature.

move in a random way resulting in an inhomogeneous broadening, which is characterised by a Gaussian distribution:

$$g_D(\tilde{\nu}) = \sqrt{\frac{\ln 2}{\pi}} \frac{1}{\Delta\tilde{\nu}_D} \exp\left[-\ln 2 \frac{(\tilde{\nu} - \tilde{\nu}_0)^2}{\Delta\tilde{\nu}_D^2}\right] \quad (2.24)$$

where $\Delta\tilde{\nu}_D$ is the half-width at half-maximum (HWHM):

$$\Delta\tilde{\nu}_D = \frac{\tilde{\nu}_0}{c} \sqrt{\frac{2RT \ln 2}{M}} = \tilde{\nu}_0 (1.132 \times 10^{-8}) \sqrt{\frac{T}{M}} \quad (2.25)$$

where M is the molar mass (kg), T the temperature (K) and R the perfect gas constant (JK⁻¹mol⁻¹). Figure 2.2 illustrates the increasing Doppler width with temperature for CO₂ at 6361.26 cm⁻¹ (1572 nm), for H₂O at 7306.74 cm⁻¹ (1369 nm) and HCl at 5753.97 cm⁻¹ (1738 nm). As can be seen from the figure, Doppler broadening affects H₂O more than CO₂ and HCl due to the lighter molar mass of water vapour. Typical Doppler broadening for molecules of 0.020 to 0.060 kg of 3.3×10^{-3} - 1×10^{-2} cm⁻¹ (100-300 MHz) in the near infrared (NIR) (1.3-2 μm) and 6.7×10^{-4} - 1.3×10^{-3} cm⁻¹ (20-40 MHz) at 10 μm are obtained.

2.2.2.3 Collisional broadening

When collisions occur between gas phase atoms or molecules there is a transfer of energy which leads effectively to a broadening of the energy levels. If τ_{coll} is the mean time between collisions and each collision results in a transition between two states, there is a line broadening $\Delta\tilde{\nu}_L$ of the transition. Using the uncertainty relation of Heisenberg (see equation 2.21):

$$\Delta\tilde{\nu}_L \geq \frac{1}{2\pi\tau_{coll}} \quad (2.26)$$

This process is, like natural broadening, homogeneous and produces a Lorentzian lineshape:

$$g_L(\tilde{\nu}) = \frac{\Delta\tilde{\nu}_L}{\pi} \left[\frac{1}{(\tilde{\nu} - \tilde{\nu}_0)^2 + \Delta\tilde{\nu}_L^2} \right] \quad (2.27)$$

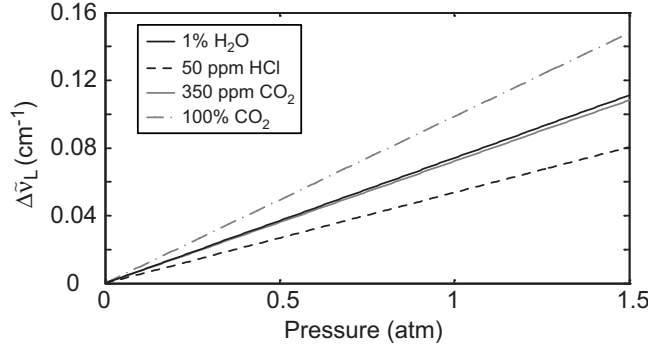


Figure 2.3: Collisional broadening for 50 ppm HCl at 5753.97 cm^{-1} , for pure CO₂ at 6361.26 cm^{-1} , for 1% H₂O at 7306.74 cm^{-1} and 350 ppm CO₂ (at 6361.26 cm^{-1}) diluted in air. Pure and 350 ppm of CO₂ are compared to emphasize the different broadening coefficients (self-broadening coefficient and air broadening coefficient).

Since the probability of collisions increases with pressure and thus the mean free path decreases, the width of the lineshape $\Delta\tilde{\nu}_L$ (HWHM) raises with the total pressure of the gas p_0 through a broadening coefficient g . A small temperature dependence of the half-width also occurs and is characterised by a coefficient n :

$$\Delta\tilde{\nu}_L = gp_0 \left(\frac{T_{ref}}{T} \right)^n \quad (2.28)$$

where T_{ref} is the reference temperature, typically 296 K. The temperature coefficient n is in ranges between 0.5-0.8 [3], whereas the broadening coefficient g depends on the considered transition and on the gas composition. The broadening coefficient includes the self-broadening coefficient g_{self} and the foreign-broadening coefficient, generally due to air-broadening g_{air} . The width of the line shape considering these two parameters and the partial pressure p_{self} of the substance is given by:

$$\Delta\tilde{\nu}_L = [g_{self}p_{self} + g_{air}(p_0 - p_{self})] \left(\frac{T_{ref}}{T} \right)^n \quad (2.29)$$

Figure 2.3 shows the pressure broadening for 50 ppm HCl, pure CO₂, and typical atmospheric concentrations of CO₂ (350 ppm) and H₂O (1%). It can be seen that the broadening is not only dependent on the molecule but also on its concentration since self-broadening and air broadening coefficients are different. At atmospheric pressure and room temperature, the line width is typically of the order of $0.05\text{-}0.1 \text{ cm}^{-1}$ (1.5-3 GHz). The pressure broadening at line center produces an important reduction of the molecule's cross-section, since the product of the molecule's maximum cross-section (σ_{max}) by the width of the line is constant for a Lorentzian distribution:

$$\Delta\tilde{\nu}_L \sigma_{max} = \frac{S}{\pi} \quad (2.30)$$

2.2.2.4 Voigt profile

In the common case for which both Doppler and collisional broadening are significant and none can be neglected, the appropriate lineshape is a combina-

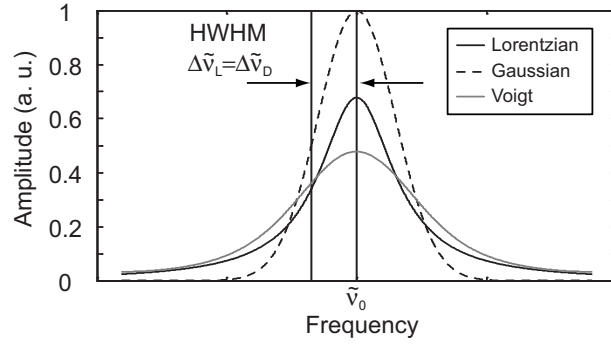


Figure 2.4: Comparison of Gaussian and Lorentzian lineshapes with the same HWHM and a Voigt profile.

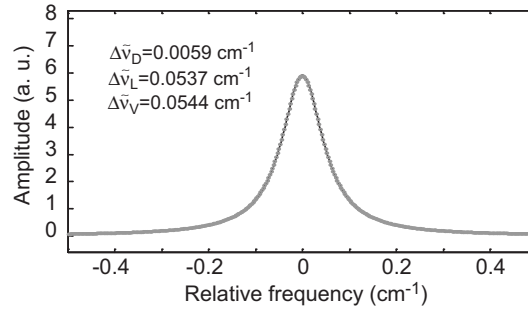


Figure 2.5: Approximation of the Voigt profile by a Lorentzian distribution at standard temperature and pressure conditions ($T=296$ K, $p_0=1$ atm) for 50 ppm of HCl in air at 5753.97 cm^{-1} . Dots represent the Voigt distribution and the solid line the Lorentzian approximation.

tion of the two. This combination of lineshapes leads to a Voigt profile which is the convolution of the Lorentzian and Gaussian distribution, given by:

$$g_V(\tilde{\nu}) = \int_0^{\infty} g_L(\tilde{\nu}') g_D(\tilde{\nu} - \tilde{\nu}') d\tilde{\nu}' \quad (2.31)$$

Figure 2.4 compares a Lorentzian (collisional broadening) and a Gaussian (Doppler broadening) lineshape with the same HWHM. The Gaussian lineshape has a peak value that is about 50% higher than the Lorentzian, but drops off much faster in the wings. A Voigt profile resulting from the convolution of the Gaussian and Lorentzian profiles is also shown. An approximative relation linking the Voigt HWHM $\Delta\tilde{\nu}_V$ to Doppler and collisional broadening can be used:

$$\Delta\tilde{\nu}_V = 0.5346\Delta\tilde{\nu}_L + [0.2166\Delta\tilde{\nu}_L^2 + \Delta\tilde{\nu}_D^2]^{1/2} \quad (2.32)$$

At standard temperature and pressure conditions ($T=296$ K, $p_0=1$ atm), the collisional broadening is approximately one order of magnitude larger than Doppler broadening, so that the Voigt profile is well approximated by a Lorentzian shape (Figure 2.5).



Figure 2.6: Discovery of the photoacoustic effect by Alexander Graham Bell with his photophone.

2.3 The photoacoustic effect

2.3.1 History of photoacoustics

The photoacoustic (PA) effect, also called optoacoustic effect, was discovered in 1880 by A. G. Bell [10], first in solids and then in gases, when he presented his work on the photophone to the American Association for the Advancement of Science. His new instrument (Figure 2.6) consisted in a voice-activated mirror, a selenium cell and an electrical telephone receiver. The rays of the sun were reflected from the voice-activated mirror which modulated the beam through the vibrations of the speaker. The beam was then collected at a distance station by a parabolic reflector, in the focus of which a sensitive selenium cell was placed, connected in a local circuit with a battery and a telephone. Since the resistance of selenium varies with the intensity of light, the voice-modulated sunlight beam resulted in an electrically reproduced telephonic speech.

After the excitement of this discovery, experiments on this effect rapidly ceased, and were abandoned during more than 50 years due to a lack of instrumentation, like suitable light sources, microphone and electronics. In 1938, Viengerov introduced a PA system based on a blackbody infrared source and a microphone in order to evaluate species concentrations in a gas mixture [11]. This first infrared spectrometer based on photoacoustic spectroscopy (PAS) received the name of spectrophone. In the 1960s, an important breakthrough was achieved by the first use of a laser source in PA gas detection [12] and the real development of photoacoustic spectrometry began. In the 1970s and 1980s PA detection boomed as high sensitivities were achieved by using CO and CO₂ lasers [2, 13, 14]. Because of their high power (in the Watt range) and their monochromaticity, these sources turned out to be excellent candidates to reach sub-ppb detection limits. In the 90s, semi-conductor diode lasers operated in the near infrared (NIR) appeared to be excellent sources for PA detection, due to their reliability, tuneability and modulation capabilities [15, 16]. New laser sources such as periodically poled lithium niobate (PPLN) optical parametric oscillators (OPOs) [17, 18] and quantum cascade lasers [19, 20, 21] operating in the fundamental infrared spectral region are currently developed and are expected to break new limits in terms of sensitivity. This sensitivity improvement is possible since fundamental absorption bands occur in the infrared and are therefore several orders of magnitude larger than the overtone bands located in the NIR.

2.3.2 Description of the photoacoustic effect in gases

The photoacoustic effect consists in the generation of sound when a material is illuminated with modulated or pulsed light. The PA effect can be divided in three steps [22]:

- Heat release in the sample material due to relaxation of optical light absorption through molecular collisions
- Acoustic and thermal wave generation due to localised transient heating and expansion
- Detection of the acoustic signal in the PA cell using a microphone

In the first step, photons are absorbed by the material and internal energy levels (rotational, vibrational, electronic) are excited. The initial state is reached after loss of energy by radiation processes (spontaneous or stimulated emission) or by nonradiative deactivation. In the case of vibrational excitation, radiative emissions and chemical reactions do not play an important role, because the radiative lifetimes of vibrational levels are long compared to the time needed for collisional deactivation at pressures commonly used in photoacoustics. Furthermore, the photon energy is too small to induce chemical reactions [23, 24]. Thus, in practice, the absorbed energy is completely thermally released, appearing as translational energy of the gas molecules.

In the second step, sound and thermal wave generation are theoretically described by fluid dynamics and thermodynamics. The governing physical laws are the energy, momentum and mass conservation laws, given through the form of the heat-diffusion, Navier-Stokes and continuity equations, respectively. Details on the solutions of these processes are explained in subsection 2.4.2.

The last step consists in the detection of the generated acoustic wave using a microphone. The solutions of the equations describing the system are strongly dependent on the type and on the geometry of the PA detector. The acoustic properties of the PA cell can be determined independently using acoustic modeling techniques or by measuring them in an acoustic laboratory. Once these acoustic properties are known, the response of the PA cell for any kind of PA excitation can be determined by calculation.

2.4 Photoacoustic signal generation

Photoacoustic signal generation is generally described in two steps. The first one concerns the heat production in the gas sample and the second one the generation of acoustic waves.

The first aspect deals with the absorption processes experienced by a particular gas sample and the subsequent energy transfer from vibrational to translational degrees of freedom ($V - T$ relaxation). The net resulting energy transfer is a heat production rate H . This process is developed in subsection 2.4.1.

The second aspect of PA theory deals with the acoustic wave generation which is directly related to the heat production. This part is treated in subsection 2.4.2.

2.4.1 Heat production rate for thermal equilibrium

Heat production in a gaseous sample excited by an intensity modulated laser beam may be described by the use of molecule population levels [25]. For the simple case where the absorbing gas containing a molecule density N can be modeled by a two-level system consisting in the vibrational ground state of density $(N - N')$ and the excited state with a density N' , the density N' can be calculated by the following rate equation:

$$\frac{dN'}{dt} = (N - N')\sigma\phi - N'\sigma\phi - \frac{N'}{\tau} \quad (2.33)$$

where σ is the absorption cross section and ϕ is the photon flux. The inverse time τ^{-1} can be expressed by the sum of reciprocal time constants of nonradiative and radiative relaxation:

$$\tau^{-1} = \tau_n^{-1} + \tau_r^{-1} \quad (2.34)$$

The first term on the right-hand side of equation (2.33) represents the absorption of the photons at frequency $\tilde{\nu} = (E_1 - E_0)/hc$ (see (2.2)). The second term stands for the stimulated emission of photon while the third one represents the spontaneous emission of photons and the non-radiative relaxation. For typical atmospheric conditions, τ_n is on the order of $10^{-6} - 10^{-9}$ s, while τ_r is between $10^{-1} - 10^{-3}$ s [2]. In consequence, the spontaneous emission of the vibrational levels are long compared to the time needed for a collisional deactivation, and τ can be approximated by τ_n . Thus, the whole absorbed energy in the sample is generally released as heat. However, in some particular situations (for instance, kinetic cooling [2, 26, 27] or methane monitoring in oxygen (see chapter 5)) only part of the absorbed energy is released as heat. For weak absorptions, the excitation rate $\sigma\phi$ is small, so that the density of the excited state is considerably smaller than the total density of molecules ($N' \ll N$). Therefore, the stimulated emission term can be neglected and the rate equation (2.33) reduces to:

$$\frac{dN'}{dt} = N\sigma\phi - \frac{N'}{\tau} \quad (2.35)$$

For a complex harmonic modulation of the incident radiation, the photon flux can be expressed as

$$\phi = \phi_0(1 + e^{i\omega t}) \quad (2.36)$$

where $\omega = 2\pi f$ is the angular modulation frequency. The rate equation is then given by

$$\frac{dN'}{dt} = N\sigma\phi_0(1 + e^{i\omega t}) - \frac{N'}{\tau} \quad (2.37)$$

In equation (2.37), only the time-dependent term with the angular frequency ω contributes to the PA signal. By searching a solution of the type

$$N' = N'_0 e^{i\omega t} \quad (2.38)$$

one obtains

$$N'_0 = \frac{N\sigma\phi_0\tau}{\sqrt{1 + (\omega\tau)^2}} e^{-i\varphi} \quad (2.39)$$

where $\varphi = \arctan(\omega\tau)$ represents the phase lag between the number density N' of the excited state and the photon flux ϕ . The solution of equation (2.37) can finally be written as:

$$N' = \frac{N\sigma\phi_0\tau}{\sqrt{1 + (\omega\tau)^2}} e^{i(\omega t - \varphi)} \quad (2.40)$$

The heat production rate H (by volume and unit time) is related to N' by

$$H = N' \frac{hc\Delta\tilde{\nu}}{\tau_n} \quad (2.41)$$

where $hc\Delta\tilde{\nu}$ is the average thermal energy released due to the nonradiative deexcitation of the excited state. If the deexcitation process results in the conversion of the excited state to the ground state, as assumed with the two-level system, then $\Delta\tilde{\nu} \cong \tilde{\nu}_{laser}$. Taking into account that $\tau_n \cong \tau$ and from equation (2.40), the heat production rate can be expressed as

$$H = N' \frac{hc\tilde{\nu}_{laser}}{\tau} = H_0 e^{i(\omega t - \varphi)} \quad (2.42)$$

with

$$H_0 = \frac{N\sigma I_0}{\sqrt{1 + (\omega\tau)^2}} \quad (2.43)$$

where $I_0 = \phi_0 hc\tilde{\nu}_{laser}$ is the incident light intensity.

For low modulation frequencies $\omega \ll 10^6$, $\omega\tau \ll 1$ (except for the particular cases discussed above), the heat production rate is simplified to obtain

$$H = H_0 e^{i\omega t} \quad (2.44)$$

and

$$H_0 = N\sigma I_0 = \alpha I_0 \quad (2.45)$$

where α is the absorption coefficient of the gas sample. The condition $\omega\tau \ll 1$ is usually satisfied since the modulation frequencies are in the kHz range. In these conditions, since $\phi = 0$, there is no phase lag between the heating of the media and the modulation of the optical intensity. However, in some particular cases, the condition $\omega\tau \ll 1$ is not fulfilled even for modulation frequencies in the kHz range since τ_n^{-1} can be of the same order of magnitude than ω . This particular case is discussed in details in chapter 5.

2.4.2 Generation of acoustic waves

As already mentioned in subsection 2.3.2, sound and thermal waves can be described by classical disciplines of physics such as fluid mechanics and thermodynamics. The physical laws governing the system are the equations of Navier-Stokes, of thermal diffusion, of continuity and a state equation. The physical quantities characterising the PA and photothermal processes are the temperature T , pressure P , density ρ and the three components of the particle velocity vector \mathbf{v} . This complex problem cannot be solved for a general case and some simplifications must be included. For instance, changes of T ,

P and ρ induced by light absorption are usually very small compared to their equilibrium values so that new variables can be introduced:

$$P(\mathbf{r}, t) = p_0 + p(\mathbf{r}, t) \quad (2.46)$$

$$T(\mathbf{r}, t) = T_0 + T_a(\mathbf{r}, t) \quad (2.47)$$

$$\rho(\mathbf{r}, t) = \rho_0 + \rho_a(\mathbf{r}, t) \quad (2.48)$$

where p_0 , T_0 and ρ_0 are the equilibrium value of pressure, temperature and density respectively and p , T_a and ρ_a are the small additional terms arising from the sound. In addition, the fluid is assumed to be at rest except for the motion due to the presence of sound. Considering this assumption, the fluid velocity \mathbf{v} is also one of the "small" quantities. This allows to make the assumption that squares, cross-products and higher order products of the acoustical variables can be neglected. In that sense, a linearised wave equation is derived. To include thermal conduction and friction in the fluid, the linearised Navier-Stokes equation can be used [28]:

$$\frac{\partial \mathbf{v}}{\partial t} = -\frac{1}{\rho_0} \nabla p(\mathbf{r}, t) + D_v \nabla (\nabla \cdot \mathbf{v}_l) \quad (2.49)$$

where $D_v = 4\eta/3\rho_0 + \eta_b/\rho_0$. η represents the coefficient of shear viscosity and is associated with shear motion in the fluid, and η_b is the coefficient of bulk viscosity (also called volume viscosity) and has its origin in relaxation phenomena associated with the compression of the fluid. The velocity vector \mathbf{v} can be separated into a sum of two components, a longitudinal (\mathbf{v}_l) and a transverse (\mathbf{v}_t) component. Only the longitudinal component contributes to the acoustic pressure and therefore the transversal component is neglected⁴.

The fluctuations in sound pressure are accompanied by temperature fluctuations and a thermal diffusivity equation can be derived:

$$\frac{K}{\rho_0 C_p} \nabla^2 T_a(\mathbf{r}, t) = \frac{\partial}{\partial t} \left(T_a(\mathbf{r}, t) - \frac{\gamma - 1}{\gamma \beta_T} \kappa_T p(\mathbf{r}, t) \right) - \frac{H(\mathbf{r}, t)}{\rho_0 C_p} \quad (2.50)$$

where K is the thermal conductivity, C_p is the heat capacity at constant pressure, $\gamma = C_p/C_v$ is the ratio of the specific heat at constant pressure to the specific heat at constant volume, β_T is the coefficient of thermal expansion, κ_T is the isothermal compressibility and H is the density of the deposited heat power (see subsection 2.4.1).

Four equations have been used until now to describe the system (the three components of the Navier-Stokes equation and the diffusivity equation). To complete the model, an equation of mass-density continuity (equation (2.51)) and a thermodynamic equation of state to interrelate the acoustic contributions to the density, pressure and temperature (equation(2.52)) must be given:

$$\frac{\partial \rho_a(\mathbf{r}, t)}{\partial t} + \rho_0 \nabla \cdot \mathbf{v}_l = 0 \quad (2.51)$$

$$\rho_a(\mathbf{r}, t) = \left(\frac{\partial \rho}{\partial P} \right)_{T_0} p(\mathbf{r}, t) + \left(\frac{\partial \rho}{\partial T} \right)_{p_0} T_a(\mathbf{r}, t) = \frac{\gamma}{c_s^2} \left(p(\mathbf{r}, t) - \frac{\beta_T}{\kappa_T} T_a(\mathbf{r}, t) \right) \quad (2.52)$$

⁴Since the transversal component is unrelated to the acoustic pressure it may be neglected in the bulk fluid. However, transverse flow may be important when boundary conditions must be satisfied.

where c_s is the speed of sound defined by:

$$c_s = \sqrt{\frac{\gamma RT}{M}} \quad (2.53)$$

To obtain the modified wave equation, the divergence of equation (2.49) is taken and \mathbf{u} is eliminated by using the equation of mass-density continuity (equation (2.51)):

$$\nabla^2 p_a(\mathbf{r}, t) = \frac{\partial^2 \rho_a(\mathbf{r}, t)}{\partial t^2} - D_v \nabla^2 \frac{\partial \rho_a(\mathbf{r}, t)}{\partial t} \quad (2.54)$$

Finally, $\rho_a(\mathbf{r}, t)$ is eliminated by using the equation of state (2.52):

$$\nabla^2 p_a(\mathbf{r}, t) = \frac{\gamma}{c_s^2} \left[\frac{\partial^2}{\partial t^2} - D_v \nabla^2 \right] \left(p_a(\mathbf{r}, t) - \frac{\beta_T}{\kappa_T} T_a(\mathbf{r}, t) \right) \quad (2.55)$$

Two independent solutions of the coupled equations (2.50) and (2.55) may be derived [22]. The first solution consists in an acoustic wave of a wavelength ranging from a few centimetres to a few metres. The second solution is a strongly damped thermal wave of sub-millimetre wavelength which cannot propagate faraway from the heated region. As the properties of these two waves are very different, their detection can be measured independently. Photothermal detection is a particular technique to measure the thermal wave [29, 30] and is not considered here. Photoacoustic spectroscopy is based on the detection of the acoustic wave using a microphone. The solution of (2.50) and (2.55) can be obtained by assuming that the dimensions of the cell are large compared to the distribution of the thermal wave. As this wave is strongly damped, this condition is usually fulfilled in PAS. In these conditions, the second derivatives of $T_a(\mathbf{r}, t)$ can be neglected. By combining (2.50) and (2.55), a unique pressure equation is obtained.

$$\nabla^2 p(\mathbf{r}, t) - \frac{1}{c_s^2} \frac{\partial^2 p(\mathbf{r}, t)}{\partial t^2} + \frac{1}{c_s^2} D_v \frac{\partial}{\partial t} \nabla^2 p(\mathbf{r}, t) = -\frac{(\gamma - 1)}{c_s^2} \frac{\partial H(\mathbf{r}, t)}{\partial t} \quad (2.56)$$

This equation is a damped wave equation, where the last term of the left-hand side is a viscosity loss term and the part on the right-hand side is a source contribution. The loss term makes this equation impossible to be solved analytically and it is therefore solved by neglecting this part in first approximation. Losses are introduced in a further step as a perturbation of the solution [31]. Thus, the following equation is considered:

$$\nabla^2 p(\mathbf{r}, t) - \frac{1}{c_s^2} \frac{\partial^2 p(\mathbf{r}, t)}{\partial t^2} = -\frac{(\gamma - 1)}{c_s^2} \frac{\partial H(\mathbf{r}, t)}{\partial t} \quad (2.57)$$

Equation (2.57) is an inhomogeneous wave equation that can be solved by taking the time Fourier transform on both sides and expressing the solution $p(\mathbf{r}, t)$ as an infinite series expansion of the normal mode solution $p_j(\mathbf{r}, t)$ of the homogeneous wave equation [23]. Taking the Fourier transform of (2.57), the following expression is obtained:

$$\left(\nabla^2 + \frac{\omega^2}{c_s^2} \right) p(\mathbf{r}, \omega) = \left[\frac{\gamma - 1}{c_s^2} \right] i\omega H(\mathbf{r}, \omega) \quad (2.58)$$

and

$$p(\mathbf{r}, t) = \int_{-\infty}^{\infty} p(\mathbf{r}, \omega) e^{-i\omega t} d\omega \quad (2.59)$$

$$H(\mathbf{r}, t) = \int_{-\infty}^{\infty} H(\mathbf{r}, \omega) e^{-i\omega t} d\omega \quad (2.60)$$

The boundary conditions enable to find the normal modes solution of the homogeneous wave equation. These normal modes are the acoustic modes for a cavity and are described for a cylindrical cavity of radius R_c and length L . Since the walls of the photoacoustic cell are rigid, the component of the acoustic velocity normal to the wall equals zero at $r = R_c$. The acoustic velocity is related to the pressure by (see equation (2.51))

$$\mathbf{v}_l(\mathbf{r}, \omega) = \frac{1}{i\omega\rho_0} \nabla \cdot p(\mathbf{r}, \omega) \quad (2.61)$$

The acoustic wave must satisfy the boundary conditions

$$\nabla_{\perp} p(\mathbf{r}, \omega) |_{r=R_c} = 0 \quad (2.62a)$$

$$\nabla_{\perp} p(\mathbf{r}, \omega) |_{z=0,L} = 0 \quad (2.62b)$$

These boundary conditions determine the normal mode solutions $p_j(\mathbf{r}, \omega)$ of the homogeneous wave equation

$$(\nabla^2 + k_j) p_j(\mathbf{r}, \omega) = 0 \quad (2.63)$$

with

$$k^2 = \frac{\omega^2}{c_s^2} \quad (2.64)$$

For a cylindrical cell, (2.63) can be written in cylindrical coordinates (r, Φ, z)

$$\frac{1}{r} \frac{\partial}{\partial r} \left(r \frac{\partial p_j}{\partial r} \right) + \frac{1}{r^2} \frac{\partial^2 p_j}{\partial \Phi^2} + \frac{\partial^2 p_j}{\partial z^2} + k_j^2 p_j = 0 \quad (2.65)$$

The solutions of this equation are given by [32]

$$p(\mathbf{r}, \omega) = \frac{\cos}{\sin}(m\Phi) [AJ_m(k_r r) + BY_m(k_r r)] [C \sin(k_z z) + D \cos(k_z z)] \quad (2.66)$$

where J_m and Y_m are Bessel functions of the first and second kind, respectively. In order to satisfy the boundary conditions defined in (2.62), the different parameters of (2.66) are given by

$$B = C = 0 \quad (2.67a)$$

$$k_z = k \frac{\pi}{L}, \quad k = 0, 1, 2, \dots \quad (2.67b)$$

$$k_r = \alpha_{mn} \frac{\pi}{R_c}, \quad m = 0, 1, 2, \dots, \quad n = 0, 1, 2, \dots \quad (2.67c)$$

where α_{mn} is the n^{th} root of the equation involving the m^{th} order Bessel function

$$\frac{d}{dr} J_m \left(\frac{\alpha_{mn} \pi r}{R_c} \right) \Big|_{r=R_c} = 0 \quad (2.68)$$

$\pi\alpha_{mn}$	$n=0$	$n=1$	$n=2$	$n=3$
$m=0$	0	3.832	7.016	10.173
$m=1$	1.841	5.331	8.526	11.706
$m=2$	3.054	6.706	9.969	13.170
$m=3$	4.201	8.015	11.346	14.586

Table 2.2: Values of $\pi\alpha_{mn}$ for some of the first azimuthal and radial modes of a cylindrical acoustic cavity.

The first values of $\pi\alpha_{mn}$ are given in table 2.2. The normal modes of the cavity are given by

$$p_j(\mathbf{r}, \omega) = p_j \cos(m\Phi) \cos\left(k\frac{\pi z}{L}\right) J_m\left(\alpha_{mn} \frac{\pi r}{R_c}\right) \quad j = [k, m, n] \quad (2.69)$$

where p_j is a normalization coefficient determined by the orthogonality of the modes:

$$\int p_i^*(\mathbf{r}, \omega) p_j(\mathbf{r}, \omega) dV = V_c \delta_{ij} \quad (2.70)$$

where V_c is the volume of the cell. p_j is given by

$$\frac{1}{p_j} = \frac{1}{\sqrt{\varepsilon_{km}}} \sqrt{1 - \left(\frac{m}{\pi\alpha_{mn}}\right)^2} J_m(\pi\alpha_{mn}) \quad (2.71)$$

where $\varepsilon_{00} = 1$, $\varepsilon_{01} = \varepsilon_{10} = 2$ and $\varepsilon_{km} = 4$ for $k + m > 1$. The boundary conditions given by (2.62) are valid for a cylindrical cavity closed at both ends. For the case of a both-ended opened cavity, the boundary condition at $z = 0$ and $z = L$ changes and the input and output acoustic impedances Z are equal to zero, resulting in boundary conditions for the longitudinal component of $p(\mathbf{r}, \omega)$:

$$p(\mathbf{r}, \omega)|_{z=0,L} = 0 \quad (2.72)$$

In order to satisfy the boundary conditions defined in (2.72), the different parameters of (2.66) are given by

$$B = D = 0 \quad (2.73a)$$

$$k_z = k\frac{\pi}{L}, \quad k = 0, 1, 2, \dots \quad (2.73b)$$

$$k_r = \alpha_{mn} \frac{\pi}{R_c}, \quad m = 0, 1, 2, \dots, \quad n = 0, 1, 2, \dots \quad (2.73c)$$

The normal modes of an open cavity at both ends are given by

$$p_j(\mathbf{r}, \omega) = p_j \cos(m\Phi) \sin\left(k\frac{\pi z}{L}\right) J_m\left(\alpha_{mn} \frac{\pi r}{R_c}\right) \quad j = [k, m, n] \quad (2.74)$$

The eigenfrequencies are the same for an open-open or a close-close cavity and are given by

$$\omega_j = 2\pi f_j = \pi c_s \sqrt{\left(\frac{k}{L}\right)^2 + \left(\frac{\alpha_{mn}}{R_c}\right)^2} \quad (2.75)$$

The eigenvalues (k, m, n) represent the longitudinal, azimuthal and radial indices, respectively. For the normal modes of a cavity, pure longitudinal modes

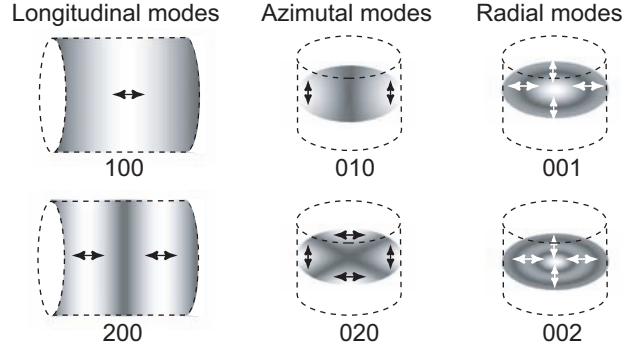


Figure 2.7: First two longitudinal, azimuthal and radial eigenmodes of a both-ended opened cylindrical acoustic cell. Dark gray zones correspond to the nodes of the acoustic waves, and light gray zones to the antinodes of the acoustic wave.

($m = n = 0$), azimuthal modes ($k = n = 0$) and radial modes ($k = m = 0$) are distinguished. The first two modes of each type for an open-open cavity are represented in Figure 2.7. All other eigenvalues stand for mixed modes. The resonant frequencies of the longitudinal modes are overtones of the fundamental mode, $\omega_{k00} = k\pi c_s/L = k\omega_{100}$. The radial and azimuthal modes are described by the Bessel functions and their resonant frequencies are not overtones of the fundamental frequency. Radial modes concentrate the energy along the axis of the resonator, whereas the axis symmetry is broken for azimuthal modes ($n \neq 0$). For example, azimuthal modes with ($k = 1$) tend to concentrate the energy near the walls. The acoustic pressure $p(\mathbf{r}, \omega)$ within the cell is given by the sum over all the normal modes.

$$p(\mathbf{r}, \omega) = \sum_j A_j(\omega) p_j(\mathbf{r}, \omega) \quad (2.76)$$

Substituting equation (2.76) in (2.58) and taking into account that $p_j(\mathbf{r}, \omega)$ is a solution of the homogeneous wave equation, we obtain

$$\sum_j A_j(\omega^2 - \omega_j^2) p_j(\mathbf{r}, \omega) = i\omega(\gamma - 1)H(\mathbf{r}, \omega) \quad (2.77)$$

The amplitude of the mode $p_j(\mathbf{r}, \omega)$ is obtained by multiplying (2.77) by $p_j^*(\mathbf{r}, \omega)$ and integrating this expression over the cell volume. As the eigenstates verify the orthogonality function (2.70), we obtain

$$A_j(\omega) = -\frac{i\omega \gamma - 1}{\omega_j^2} \frac{\int p_j^*(\mathbf{r}, \omega) H(\mathbf{r}, \omega) dV}{V_c \left(1 - \left(\frac{\omega}{\omega_j}\right)^2\right)} \quad (2.78)$$

The integral in the numerator on the right side of equation (2.78) represents the coupling between the heat source $H(\mathbf{r}, \omega)$ and the normal mode $p_j(\mathbf{r}, \omega)$. The denominator represents the mode resonance with $A_j(\omega)$ becoming infinite as ω approaches the resonant frequency ω_j . This physically unreasonable situation is the result of the absence of any loss mechanism in equation (2.57). It may be corrected by modifying equation (2.78) to include a mode damping

described by the quality factor Q_j :

$$A_j(\omega) = -\frac{i\omega}{\omega_j^2} \frac{\gamma - 1}{V_c} \frac{\int p_j^*(\mathbf{r}, \omega) H(\mathbf{r}, \omega) dV}{1 - \left(\frac{\omega}{\omega_j}\right)^2 - \frac{i\omega}{\omega_j Q_j}} \quad (2.79)$$

The method to obtain Q_j is described in details in 2.5.1.

In order to show explicitly the dependence of the acoustic signal on the gas absorption and light intensity, it is necessary to replace $H(\mathbf{r}, \omega)$ in equation (2.79) using equation (2.44) and (2.45). The intensity of the beam is expressed by considering a beam of total power P_0 and of normalised distribution $g(\mathbf{r})$:

$$I_0(r, \omega) = P_0 g(\mathbf{r}) \quad (2.80)$$

Equation (2.79) becomes

$$A_j(\omega) = -\frac{i\omega}{\omega_j^2} \frac{\gamma - 1}{V_c} \frac{\alpha P_0 L}{1 - \left(\frac{\omega}{\omega_j}\right)^2 - \frac{i\omega}{\omega_j Q_j}} \frac{1}{L} \int p_j^*(\mathbf{r}, \omega) g(\mathbf{r}) dV \quad (2.81)$$

The photoacoustic signal is proportional to the absorption coefficient, to the incident optical power and to the length of interaction and is inversely proportional to the modulation frequency and to the cell volume. In the particular case where the optical beam is Gaussian with a radius a ,

$$g(\mathbf{r}) = \frac{2}{\pi a^2} e^{-2\frac{r^2}{a^2}} \quad (2.82)$$

the integral of (2.81) becomes

$$I_j = \frac{1}{L} \int p_j^*(\mathbf{r}, \omega) g(\mathbf{r}) dV = p_j e^{-\mu_j} \quad (2.83)$$

where p_j is the normalisation coefficient defined by (2.71) and $1/\mu_j$ represents the coupling factor between the optical beam and the acoustic mode $p_j(\mathbf{r}, \omega)$. The acoustic energy is proportional to the square of the pressure and is given by [28]

$$E_j(\omega) = \frac{|A_j(\omega)|^2}{\rho c_s^2} = \frac{(\gamma - 1)^2 (\alpha P_0 L p_j e^{-\mu_j})^2}{\rho c_s^2 V_c^2} \frac{\omega^2}{\left(\omega_j^2 - \omega^2\right)^2 + (\omega \omega_j / Q_j)^2} \quad (2.84)$$

Near the resonance ($\omega \cong \omega_j$), the following approximation is done

$$\omega_j^2 - \omega^2 = (\omega_j + \omega)(\omega_j - \omega) \cong 2\omega_j(\omega_j - \omega) \quad (2.85)$$

The acoustic energy is thus given by

$$E_j(\omega) = \frac{1}{4} \frac{(\gamma - 1)^2 (\alpha P_0 L p_j e^{-\mu_j})^2}{\rho c_s^2 V_c^2} \frac{1}{\left(\omega_j^2 - \omega^2\right)^2 + (\omega_j / 2Q_j)^2} \quad (2.86)$$

This equation represents a distribution of Lorentz with half-width at half-maximum given by

$$\Delta\omega_j = \frac{\omega_j}{2Q_j} \quad (2.87)$$

Using equations (2.81) and (2.83), the photoacoustic signal at the resonant frequency becomes

$$A_j(\omega_j) = \frac{Q_j}{\omega_j} \frac{\alpha P_0 (\gamma - 1) p_j L}{V_c} e^{-\mu_j} \quad (2.88)$$

When the modulation frequency is equal to one of the eigenfrequencies of the cavity, the energy from many modulation cycles is accumulated in a standing acoustic wave and the system works as an acoustic amplifier. The final signal amplification is determined by the total losses of the resonator. After an initial transient state, during which energy is accumulated in a standing acoustic wave, a steady state is reached in which the energy lost per cycle due to various dissipation processes is equal to the energy gained per cycle due to the absorption of photons. At resonance, the amplitude is Q_j times larger than the amplitude out of the resonance frequency, i.e. the amplification is equal to the value of the Q factor. The acoustic energy is divided by a factor 2 between the centre of the resonance and $\omega = \omega_j + \Delta\omega_j$, implying a decrease of $\sqrt{2}$ for the photoacoustic signal. The HWHM can also be defined in term of pressure:

$$A_j(\Delta\omega_{p,j}) = \sqrt{E_j(\Delta\omega_{p,j})} = \frac{1}{2} A_j(\omega_j) \quad (2.89)$$

The relation between the pressure and energy line width is obtained:

$$\Delta\omega_{p,j} = \sqrt{3} \Delta\omega_j \quad (2.90)$$

The acoustic mode of order 0 ($k = m = n = 0, \omega_0 = 0$) corresponds to an uniform pressure variation in the cell,

$$p(\mathbf{r}, t) = A_0(\omega) e^{i\omega t} \quad (2.91a)$$

$$A_0(\omega) = \frac{i}{\omega} \frac{\gamma - 1}{V_c} \alpha P_0 L \quad (2.91b)$$

This situation corresponds to a non-resonant system, where the modulation frequency is much smaller than the lowest resonance frequency. In this case, the sound wavelength is much larger than the cell dimension, so that the sound cannot propagate and standing waves cannot be formed. The average pressure in the cavity oscillates with the modulation frequency. Note that this only applies for closed resonators, because in an open resonator the pressure change simply drives gas in or out until the equilibrium pressure is reached [33].

The photoacoustic signal for non-resonant system is proportional to the absorbed power (αP_0) and decreases in $1/\omega$ and $1/V_c$. Advantages of resonant systems over non-resonant configurations can be expressed by comparing the amplitude of the pressure waves given by (2.88) and (2.91). Taking into consideration that the acoustic mode excitation is optimal ($\mu_j \ll 1$) and that ($\alpha P_0/V_c$) is identical for the two cases, we obtain

$$\left| \frac{p_j(\mathbf{r}, \omega_j)}{p_0(\mathbf{r}, \omega)} \right| = \frac{\omega}{\omega_j} p_j Q_j \quad (2.92)$$

The gain obtained from the quality factor Q_j permits the operation of resonant systems at much higher frequencies than non-resonant systems, providing additionally a higher photoacoustic signal. Finally, continuous measurement can be performed with resonant configurations (see also discussion 3.2).

2.5 Loss mechanisms

The energy accumulation attainable in the standing wave of a resonant cavity is many times larger than the energy loss occurring during a single period of an acoustic oscillation. However, the acoustic amplification effect is limited by various dissipation processes. These losses can be divided into surface effects and volumetric effects.

Surface losses are due to the interaction of the standing wave with solid boundaries of the cavity and can be divided into the following categories [34]:

1. Wave reflection losses due to the compliance of the chamber walls
2. Dissipation at the microphone diaphragm
3. Viscous and thermal dissipation inside the boundary layers at the smooth internal surfaces
4. Losses due to wave scattering at surface obstructions such as the gas inlet, microphone and windows.

Reflection losses depend on the density and wave speed of the gas and on the density and wave speed in the reflecting wall and can be determined using acoustic laws [32]. By selecting an appropriately rigid material to build the acoustic resonator, these losses are kept to an insignificant level.

The losses due to the microphone diaphragm require a more careful approach based on energy dissipation considerations, since the energy loss through the microphone and the ability to detect the pressure variations are inter-related. However, since the microphone surface is small (a few mm²), the corresponding energy loss can be neglected [34].

Viscous and thermal dissipation can be described in terms of velocity and temperature gradients near the wall. Throughout the major portion of the resonator volume, the expansion and contraction of the gas occur adiabatically. Near the walls, however, the process becomes isothermal because of the high thermal conductivity of the cell. This leads to heat conduction within a transition region called the thermal boundary layer which is responsible for the thermal dissipation process. In this boundary layer, the expansion of the gas occurs partially adiabatically and isothermally. The thickness of the boundary layer is given by [32]:

$$d_{th,j} = \sqrt{\frac{2KM}{\rho_0\omega_j C_p}} \quad (2.93)$$

where K is the gas thermal conductivity, ρ_0 the density of the gas, C_p the heat capacity at constant pressure and M the molar mass of the gas.

The viscous dissipation can be explained by the boundary conditions imposed by the walls. At the surface, the tangential component of the acoustic velocity is zero due to the viscosity η , whereas in the inner volume of the cavity it is proportional to the gradient of the acoustic pressure (see 2.61). Viscosity losses occur near the transition region, which is called the viscous boundary layer. Similarly to the thermal boundary layer, a thickness of the viscous layer can be obtained [32]:

$$d_{\eta,j} = \sqrt{\frac{2\eta}{\rho_0\omega_j}} \quad (2.94)$$

The thickness of the thermal and viscous layers decreases with the angular resonant frequency ω_j . The thickness of these layers is similar in air at standard temperature and pressure conditions. Pure radial modes ($k = m = 0$) have no viscosity loss on the lateral surfaces since the sound velocity contains only a radial component. Viscosity loss occurs only on the walls situated at the extremity of the PA cell. The total energy loss is thus lower for radial modes than for longitudinal or azimuthal modes, considering a proper design of the resonator. In the case of spherical resonators, no surface viscosity loss occurs for radial modes. Extremely high quality factors ($Q_j \cong 2000 - 10000$) can be achieved for carefully designed spherical resonators [35].

Volumetric or bulk losses are caused by processes that tend to establish equilibrium in the propagating wave [32] and can be divided in the following categories:

1. Free space thermal and viscous dissipation
2. Relaxation losses
3. Diffusion effects
4. Radiation effects

Friction due to compressional motion results in viscous losses, while the volumetric thermal losses are attributable to the transfer of organised energy into dispersed heat due to the resulting temperature gradients in the gas. The combination of these phenomena, termed the Stokes-Kirchhoff losses, can be estimated [32], and amounts to an insignificant source of energy dissipation [34].

Diffusion losses are usually negligible [33] but molecular relaxation in wave propagating through polyatomic gases proves to be much more significant. Losses of this type with finite energy transfer rates between translational-vibrational, vibrational-vibrational, and vibrational-rotational energy states are, however, heavily dependent upon the presence, even in small quantities, of certain polyatomic impurities such as water vapour. Accurate predictions of losses attributable to the relaxation effect therefore depend upon precise knowledge of the characteristic relaxation times of the energy transfer processes among the various compounds of the gas. The determination of these relaxation times is possible from the resulting dispersion frequency and the strong broadening of the acoustic resonance profile [36]. A detailed study of relaxation effects is presented in chapter 5.

Radiation dissipation is negligible for completely closed cavity resonators because of the nearly perfect reflection of the sound at the walls. On the other hand, radiation losses through openings, pipes connecting the resonator to buffer volumes, cannot be neglected. However, the radiation losses can be reduced by increasing the acoustic input impedance of the openings [37] which is achieved by terminating the cavity resonator at the openings with acoustic band-stop filters, which prevent the sound from escaping from the resonator.

2.5.1 Quality factor

The quality factor Q is a key parameter that takes into account the accumulated sound energy and the losses in the photoacoustic system. The physical

definition of the Q factor is

$$Q = \frac{2\pi \text{ accumulated energy}}{\text{energy lost over one period}} \quad (2.95)$$

The contribution of the surface losses to the quality factor for a cylindrical cavity is given by [36]:

$$Q_{surf,j} = \omega_j \frac{\frac{1}{\rho_0 c_s^2} \int |p_j(\mathbf{r}, \omega_j)|^2 dV}{\frac{1}{2} R_{\eta,j} \int |u_{||}(\mathbf{r}, \omega_j)|^2 ds + \frac{1}{2} R_{th,j} \int |p_j(\mathbf{r}, \omega_j)|^2 ds} \quad (2.96)$$

where

$$R_{\eta,j} = \rho_0 \omega_j d_{n,j} \quad (2.97a)$$

$$R_{th,j} = \frac{(\gamma - 1)}{\rho_0 c_s^2} \omega_j d_{th,j} \quad (2.97b)$$

$d_{\eta,j}$ and $d_{th,j}$ are defined in (2.94) and (2.93), respectively.

For pure radial modes, expression (2.96), reduces to

$$Q_{surf,j}^{rad} = \frac{L}{d_{n,j} + (\gamma - 1) d_{th,j} (1 + L/R_c)} \quad (2.98)$$

and for longitudinal modes,

$$Q_{surf,j}^{long} = \frac{R_c}{d_{n,j} + (\gamma - 1) d_{th,j} (1 + 2R_c/L)} \quad (2.99)$$

The volumetric losses also contribute to the quality factor:

$$\frac{1}{Q_{vol,j}} = \frac{\omega_j}{2c_s^2} \left[\frac{4}{3} \frac{\eta}{\rho_0} + (\gamma - 1) \frac{\kappa}{\rho_0 C_p} + \frac{\eta_b}{\rho_0} \right] \quad (2.100)$$

where η_b is an effective viscosity coefficient that contains relaxation losses. The surface losses are dominant in PA systems operated at a pressure higher than 0.1 atm [38] and where relaxation processes are negligible. The quality factor Q containing both surface and volumetric losses is given by:

$$\frac{1}{Q} = \frac{1}{Q_{surf}} + \frac{1}{Q_{vol}} \quad (2.101)$$

Bibliography

- [1] H. Inaba, *Detection of atoms and molecules by Raman scattering and resonance fluorescence*, vol. 14 of *Top. Appl. Phys.* (Springer-Verlag, Berlin, 1976).
- [2] P. L. Meyer and M. Sigrist, "Atmospheric pollution monitoring using CO₂- laser photoacoustic spectroscopy and other techniques," *Rev. Sci. Instrum.* **61**(7), 1779–1807 (1990).
- [3] L. S. Rothman, D. Jacquemart, A. Barbe, D. C. Benner, M. Birk, L. R. Brown, M. R. Carleer, C. Chackerian, K. Chance, L. H. Coudert, V. Dana, V. M. Devi, J. M. Flaud, R. R. Gamache, A. Goldman, J. M. Hartmann, K. W. Jucks, A. G. Maki, J. Y. Mandin, S. T. Massie, J. Orphal, A. Perrin, C. P. Rinsland, M. A. H. Smith, J. Tennyson, R. N. Tolchenov, R. A. Toth, J. Vander Auwera, P. Varanasi, and G. Wagner, "The HITRAN 2004 molecular spectroscopic database," *J. Quant. Spectrosc. Radiat. Transf.* **96**(2), 139–204 (2005).
- [4] R. A. Toth, "Extensive measurements of H₂¹⁶O line frequencies and strengths: 5750 to 7965 cm⁻¹," *Appl. Opt.* **33**(21), 4851–4867 (1994).
- [5] G. Herzberg, *Molecular spectra and molecular structure*, vol. II- Infrared and Raman spectra of polyatomic molecules (Krieger, Malabar, 1991).
- [6] S. Schilt, "Mesure de traces de gaz à l'aide de lasers à semi-conducteur," Ph.D. thesis, Swiss Federal Institute of Technology (2002).
- [7] G. Herzberg, *Molecular spectra and molecular structure*, vol. I- Spectra of diatomic molecules (Krieger, Malabar, 1989).
- [8] J. M. Hollas, *Modern spectroscopy* (John Wiley and Sons, Chichester, 1999).
- [9] W. Heisenberg, "Ueber den anschaulichen Inhalt der quantentheoretischen Kinematik und Mechanik," *Zeitschrift für Physik* **43**, 172–198 (1927).
- [10] A. G. Bell, "On the production and reproduction of sound by light," *Am. J. Sci.* **20**(118), 305–324 (1880).
- [11] M. L. Viengerov, "New method of gas analysis based on Tyndall-Roentgen opto-acoustic effect," *Dokl. Akad. Nauk SSSR* **19**(687) (1938).
- [12] E. L. Kerr and J. G. Atwood, "The laser illuminated absorptivity spectrophone: A method for measurement of weak absorptivity in gases laser wavelength," *Appl. Opt.* **7**(5), 915–922 (1968).
- [13] F. J. M. Harren, J. Reuss, E. J. Woltering, and D. D. Bicanic, "Photoacoustic Measurements of Agriculturally Interesting Gases and Detection of C₂H₄ Below the ppb Level," *Appl. Spectrosc.* **44**(8), 1360–1368 (1990).
- [14] S. Bernegger and M. W. Sigrist, "CO-laser photoacoustic spectroscopy of gases and vapours for trace gas analysis," *Infrared Phys. Technol.* **30**(5), 375–429 (1990).

- [15] A. Miklos and P. Hess, "Modulated and pulsed photoacoustics in trace gas analysis," *Anal. Chem.* **72**(1), 30A–37A (2000).
- [16] Z. Bozoki, J. Sneider, Z. Gingl, A. Mohacsi, M. Szakall, Z. Bor, and G. Szabo, "A high-sensitivity, near-infrared tunable-diode-laser-based photoacoustic water-vapour-detection system for automated operation," *Meas. Sci. Technol.* **10**(11), 999–1003 (1999).
- [17] C.-S. Yu and A. H. Kung, "Grazing-incidence periodically poled LiNbO₃ optical parametric oscillator," *J. Opt. Soc. Am. B-Opt. Phys.* **16**(12), 2233–2238 (1999).
- [18] M. G. da Silva, A. Miklos, A. Falkenroth, and P. Hess, "Photoacoustic measurement of N₂O concentrations in ambient air with a pulsed optical parametric oscillator," *Appl. Phys. B* **82**(2), 329–336 (2006).
- [19] B. A. Paldus, T. G. Spence, R. N. Zare, J. Oomens, F. J. M. Harren, D. H. Parker, C. Gmachl, F. Cappasso, D. L. Sivco, J. N. Baillargeon, A. L. Hutchinson, and A. Y. Cho, "Photoacoustic spectroscopy using quantum-cascade lasers," *Opt. Lett.* **24**(3), 178–180 (1999).
- [20] S. Barbieri, J.-P. Pellaux, E. Studemann, and D. Rosset, "Gas detection with quantum cascade lasers: An adapted photoacoustic sensor based on Helmholtz resonance," *Rev. Sci. Instrum.* **73**(6), 2458–2461 (2002).
- [21] A. A. Kosterev and F. K. Tittel, "Chemical sensors based on quantum cascade lasers," *IEEE J. Quantum Electron.* **38**(6), 582–591 (2002).
- [22] A. Miklos, S. Schäfer, and P. Hess, *Photoacoustic spectroscopy, Theory*, Encyclopedia of spectroscopy and spectrometry (Academic Press, New York, 1999).
- [23] L. B. Kreuzer, *The physics of signal generation and detection*, in optoacoustic spectroscopy and detection, edited by Y-H. Pao (Academic Press, New York, 1977).
- [24] P. Hess, "Resonant Photoacoustic spectroscopy," *Top. Curr. Chem.* **111**, 1–32 (1983).
- [25] A. C. Tam, *Ultra sensitive laser spectroscopy* (Academic press, New York, 1983).
- [26] R. A. Rooth, A. J. L. Verhage, and W. Wouters, "Photoacoustic measurement of ammonia in the atmosphere: influence of water vapor and carbon dioxide," *Appl. Opt.* **29**(25), 3643–3653 (1990).
- [27] M. Hammerich, A. Olafsson, and J. Henningsen, "Photoacoustic study of kinetic cooling," *Chem. Phys.* **163**, 173–178 (1992).
- [28] J. P. M. Trusler, *Physical acoustics and metrology of fluids*, Series in Measurement Science and Technology (Bristol, 1991).
- [29] W. B. Jackson, N. M. Amer, A. C. Boccara, and D. Fournier, "Photothermal deflection spectroscopy and detection," *Appl. Opt.* **20**(8), 1333–1344 (1981).

-
- [30] A. C. Tam, “Applications of photoacoustic sensing techniques,” *Rev. Mod. Phys.* **58**(2), 381–431 (1986).
- [31] A. Rosencwaig, *Photoacoustics and photoacoustic spectroscopy*, vol. 57 (Wiley and sons, J., New York, 1980).
- [32] P. M. Morse and K. U. Ingard, *Theoretical acoustics* (Princeton university press, Princeton, 1968).
- [33] A. Miklos, P. Hess, and Z. Bozoki, “Application of acoustic resonators in photoacoustic trace gas analysis and metrology,” *Rev. Sci. Instrum.* **72**(4), 1937–1955 (2001).
- [34] R. D. Kamm, “Detection of weakly absorbing gases using a resonant optoacoustic method,” *J. Appl. Phys.* **47**(8), 3550–3558 (1976).
- [35] J. B. Mehl and M. R. Moldover, “Precision acoustic measurements with a spherical resonator: Ar and C₂H₄,” *J. Chem. Phys.* **74**(7), 4062–4077 (1981).
- [36] A. Karbach and P. Hess, “High precision acoustic spectroscopy by laser excitation of resonator modes,” *J. Chem. Phys.* **83**(3), 1075–1084 (1985).
- [37] A. Miklos and A. Lörincz, “Windowless resonant acoustic chamber for laser photoacoustic applications,” *Appl. Phys. B* **48**, 213–218 (1989).
- [38] C. F. Dewey Jr, *Design of optoacoustic systems*, in *optoacoustic spectroscopy and detection*, edited by Y-H. Pao (Academic Press, New York, 1977).

Chapter 3

Photoacoustic cell design

3.1 Introduction

This chapter is dedicated to the design and characterisation of a photoacoustic (PA) cell developed for multi-gas sensing. It begins with a description of different PA cell configurations with particular emphasis on cylindrical cavities. The selection of the acoustic cell configuration based on two main applications requirements is described. In addition, the different acoustic modes present in cylindrical resonators are discussed, with a particular attention to the first radial and first longitudinal mode, leading to an optimised cell design.

Different modulation schemes applied to PA spectroscopy are reviewed. An optimum modulation scheme used in combination with the excellent properties of semiconductor lasers results in an optimal PA signal generation.

The characterisation of two cell prototypes is given in section 3.5. A first design enables to find out the best geometric dimension to grant the optimal cell constant, whereas the second cell includes new developments in term of multi-gas sensing, automatic tracking of the resonance frequency and stabilisation of the laser wavelength.

To conclude the chapter, the tracking of the resonance frequency and the stabilisation of the laser wavelength is discussed. These two important points are necessary to secure long-term unattended operation of the sensor.

3.2 Acoustic resonators

PA cells are usually referenced in two categories in literature: resonant and non-resonant cells. This terminology is misleading, since all PA cells can be operated at an acoustic resonance or far away from their resonances [1]. Thus it is preferable to label the system according to the resonant or non-resonant mode of operation.

If the modulation frequency is much smaller than the lowest resonance frequency, the cell is operated in a non-resonant mode [2]. For this kind of operation, the acoustic signal is inversely proportional to the angular modulation frequency (ω) and to the cell volume (V_c), as shown in relation (2.91). Such cells usually have a volume of 1-10 cm³, and the modulation frequency is in the 10-100 Hz range [3]. This kind of cells is generally used in combination with broadband sources, like arc lamps, for which fast modulation is impossible. They also require spectral filtering in order to selectively interrogate

suitable absorption bands. Another drawback of non-resonant systems is the poor isolation from ambient noise due to the low operating frequency and the importance of $1/f$ noise. Finally, no continuous monitoring is possible since a closed resonator is needed to allow a pressure wave to be generated (see discussion at end of subsection 2.4.2). A gas sampling technique is thus needed for non-resonant systems, which consists in introducing the gas in the cell and then hermetically closing it. Only at that time, the photoacoustic signal is produced and can be measured, and, after that, the cell needs to be re-opened to have the gas flowing through. In consequence, non-resonant systems have a long response time and a poor sensitivity for trace gas monitoring. For all these reasons, resonant systems are preferable.

For resonant configurations, the modulation frequency is tuned to one of the eigenresonances of the PA cell ($\omega = \omega_j$). The acoustic wave is amplified by the quality factor Q_j , which can be higher than 700 for some experimental configurations [4, 5]. By combining (2.76) and (2.81), it can be seen that not only the j^{th} but all eigenmodes of the acoustic resonator are excited:

$$p(\mathbf{r}, \omega) = \sum_j -\frac{i\omega}{\omega_j^2} \frac{\gamma - 1}{V_c} \frac{\alpha P_0 L}{1 - \left(\frac{\omega}{\omega_j}\right)^2 - \frac{i\omega}{\omega_j Q_j}} I_j p_j(\mathbf{r}, \omega) \quad (3.1)$$

The amplitude of the considered resonance is proportional to the quality factor Q_j , while the amplitude of the other resonances are reduced by the factor $(\omega_j^2 - \omega^2)$. Therefore, distant resonances are not excited as effectively. If the eigenresonances are well separated and the Q factor of the particular resonance to be used is large enough ($Q_j > 50$), the selected resonance can be excited much more effectively than the others, so that only the resonance frequency at ω_j contributes significantly to the signal (2.88) [1].

When a resonance of frequency ω_j is excited by the laser beam modulated at $\omega = \omega_j$, and the microphone is located at the position $\mathbf{r} = \mathbf{r}_M$, the sound pressure is obtained by combining (2.79) and (2.88):

$$p(\mathbf{r}_M, \omega_j) = -(\gamma - 1) \frac{Q_j}{\omega_j} \frac{L}{V_c} I_j p_j(\mathbf{r}_M, \omega_j) \alpha P_0 \quad (3.2)$$

The quantities in the prefactor of (αP_0) on the right hand side of (3.2) are independent of the light power and the absorption coefficient and can thus be regarded as characteristic quantities of the system. These quantities can be grouped and are defined as the cell constant in literature [1]:

$$C_j(\omega_j) = -(\gamma - 1) \frac{Q_j}{\omega_j} \frac{L}{V_c} I_j p_j(\mathbf{r}_M, \omega_j) \quad (3.3)$$

The PA signal amplitude can be written as

$$S_{PA} = p(\mathbf{r}_M, \omega_j) = C_j(\omega_j) \alpha P_0 \quad (3.4)$$

The cell constant $C_j(\omega_j)$ expressed in (Pa·cm/W) describes the sensitivity of the system at a given resonance frequency. The cell constant is sometimes also expressed in (V·cm/W) which includes the microphone response given in (V/Pa). The cell constant depends on the size of the resonator, the frequency and the quality factor Q of the resonance selected to perform the measurement and the spatial overlap of the laser beam and the acoustic wave. Therefore, the

name cell constant is misleading, since it characterises the whole measurement system (including the acoustic resonator, the microphone position and the laser beam profile with spatial location) rather than the PA cell itself.

The cell constant can be written using the expression for the quality factor (2.87):

$$C_j(\omega_j) = -(\gamma - 1) \frac{1}{2\Delta\omega_j} \frac{L}{V_c} I_j p_j(\mathbf{r}_M, \omega_j) \quad (3.5)$$

Equation (3.5) shows that the cell constant mainly depends on the cavity section (V_c/L) and on the resonance width ($2\Delta\omega$). The way to improve the cell constant is limited. For instance, the overlap integral between the laser beam and the acoustic wave pattern can be optimised for the chosen eigenmode, but is barely higher than one. The only parameter that is possible to modify is the section of the cavity. By reducing the section, the cell constant will increase. Unfortunately, the resonance width is also proportional to the section, which depends on the ratio between the surface and the volume of the cavity. By reducing the section, this ratio increases and the cell constant is reduced. Therefore, it is not possible to have simultaneously a small cross section and a narrow resonance width, so that a trade off has to be found.

Different types of resonant systems were reported in literature. The simple radial, azimuthal or longitudinal resonances occurring in cylindrical cavities are discussed in details in subsection 3.2.1. Advanced configurations based on Helmholtz resonators, multipass resonant cells, intracavity cells and miniature PA resonators are discussed in the next subsections.

3.2.1 Cylindrical cavities

Cylindrical cavities present several advantages, such as the possibility of various mode excitations, the geometric symmetry that coincides well with that of the laser beam propagating along the axis and the simplicity of construction. The resonance frequencies are described by (2.75). The simplest resonances are fundamental modes, whose frequencies are given by (see also Figure 2.7):

$$f_{100} = \frac{c_s}{2L_{eff}} \quad f_{010} = \frac{\alpha_{10}c_s}{2R_c} \quad f_{001} = \frac{\alpha_{01}c_s}{2R_c} \quad (3.6)$$

α_{mn} is the n^{th} root of the equation involving the m^{th} order Bessel function (see Table 2.2 and equation (2.68)), L_{eff} is an effective length that includes a correction factor due to boundary effect at the resonator ends, and is given for a tube open at both ends by [6]:

$$L_{eff} = L + \frac{16}{3\pi} R_c \quad (3.7)$$

The cell constant depends on the selected mode, since the overlap integral between the optical beam and the acoustic mode varies with the cell configuration. The overlap integral (see (2.83)) of a Gaussian beam of radius a (2.82) propagating along the axis and the first radial acoustic mode is given by:

$$I_{001} = \frac{1}{L} \int_0^L dz \int_0^{2\pi} d\Phi \int_0^{R_c} \frac{2}{\pi a^2} e^{-2r^2/a^2} \frac{J_0(\pi\alpha_{01}r/R_c)}{J_0(\pi\alpha_{01})} r dr \quad (3.8)$$

where the normalisation coefficient p_j has been replaced by

$$p_{001} = \frac{1}{J_0(\pi\alpha_{01})} \quad (3.9)$$

Assuming that the beam radius is much smaller than the radius of the cavity ($a \ll R_c$), the overlap integral becomes ¹

$$I_{001} = \frac{1}{J_0(\pi\alpha_{01})} \exp \left[-\frac{1}{2} \left(\frac{\pi\alpha_{01}a}{2R_c} \right)^2 \right] \cong \frac{1}{J_0(\pi\alpha_{01})} \quad (3.10)$$

The amplitude of the first radial eigenmode is determined by using relation (2.69) and (3.9):

$$p_{001}(\mathbf{r}) = \frac{J_0 \left(\alpha_{01} \frac{\pi r}{R_c} \right)}{J_0(\pi\alpha_{01})} \quad (3.11)$$

Finally, the microphone should be placed at the maximum of the acoustic wave ($\mathbf{r} = r_M = 0$):

$$p_{001}(r_M) = -2.48 \quad r_M = 0 \quad (3.12)$$

The location of the microphone at position $r_M = 0$ is in practice not optimum, since it coincides with the cavity axis, and thus with the optical axis. However, it is possible to keep the location of the microphone at this position, if the optical axis is changed using a diagonal excitation. This modification reduces the overlap integral and thus the cell constant (see also subsection 3.3.2). Simulations were performed in the ideal situation (maximum of the overlap integral and maximum of the microphone signal). By combining expressions (3.3), (3.6), (3.10) and (3.12), the cell constant of the first radial mode can be determined:

$$C_{001} = -(\gamma - 1)Q_{001} \frac{L}{V_c} \frac{R_c}{\alpha_{01}c_s\pi} \frac{1}{J_0^2(\pi\alpha_{01})} \quad (3.13)$$

The same procedure can be applied to determine the cell constant of the first longitudinal mode. The overlap integral is given by

$$I_{100} = -\frac{2\sqrt{2}}{\pi} \left(e^{-2R_c^2/a^2} - 1 \right) \cong \frac{2\sqrt{2}}{\pi} \quad (3.14)$$

and the maximum of the acoustic wave is obtained by

$$p_{100}(\mathbf{r}) = \sqrt{2} \sin\left(\frac{\pi z}{L}\right) \quad (3.15a)$$

$$p_{100}(r_M) = \sqrt{2} \quad z = z_M = L/2 \quad (3.15b)$$

Finally, the cell constant is determined

$$C_{100} = -(\gamma - 1)Q_{100} \frac{4}{\pi} \frac{L_{eff}}{V_c} \frac{L_{eff}}{c_s\pi} \quad (3.16)$$

Many works based on cylindrical cavities have been reported in literature. Radial resonances [8, 9, 10, 5] are particularly well adapted when high power

¹When $a \ll R_c$, the integral variable r of expression (3.8) can be extended to infinity, and the following equation is used [7]: $\int_0^\infty r e^{-\chi r^2} J_0(\beta r) dr = 1/(2\chi) e^{-\beta^2/4\chi}$

lasers (such as CO₂ lasers) or high flow rates are used, as window noise and flow noise can be reduced by proper cell design. In addition, radial modes have higher quality factors, since viscous losses are weaker on the cell walls². Configurations based on azimuthal resonances were also reported with DFB lasers [11] or in carbon mass monitoring application [12]. Longitudinal configurations [13, 14, 15, 16] present the principal advantage of being very efficiently excited at resonances in the kHz range. In addition, buffer volumes enable an efficient filtering of window and ambient noise [17].

3.2.2 Helmholtz resonator

The Helmholtz resonator usually consists in two volumes V_1 and V_2 that are connected by a thin duct of radius a and length l (Figure 3.1). It is the acoustic equivalent of a simple mechanical oscillator composed of a mass and a spring. The air in the volume plays the role of the spring, while the air mass in the duct corresponds to the moving mass of the mechanical oscillator. The first volume is illuminated by the laser beam, and the second one contains the detection microphone. This type of resonator does not rely on the generation of standing acoustic modes³, but rather on amplification of the sound from left to right oscillations of the gas volume inside the channel. These oscillations generate a periodical compression and expansion of the gas enclosed in the chamber, which are amplified at the Helmholtz resonance frequency. The response of the Helmholtz cell has been described in details in literature [19, 20] and its resonance frequency is given by

$$f = \frac{c_s}{2\pi} \sqrt{\frac{A_c}{V' l_{eff}}} \quad (3.17)$$

where c_s is the sound velocity, A_c is the cross section of the capillary, l_{eff} is the effective length of the capillary that includes the boundary effects at the resonator ends [6] and V' is an effective volume expressed by

$$\frac{1}{V'} = \frac{1}{V_1} + \frac{1}{V_2} \quad (3.18)$$

The Helmholtz resonator offers several advantages such as the use of small volumes [21] with low resonance frequency and the possibility to increase the signal-to-noise ratio by using differential schemes [22, 23]. The Helmholtz configuration is particularly appropriate in combination with the use of divergent sources, such as quantum cascade lasers (QCL) [24] or semiconductor lasers in the mid-infrared (MIR) range [25], since no overlap integral between the laser source and the acoustic mode appears in the cell constant.

²No viscous losses are present on the lateral cell surfaces, since the particle velocity is composed of pure radial components. Only the extremity surfaces contribute to viscous losses, thus reducing the total viscous losses.

³The design of the resonator must satisfy the condition $\frac{2\pi d}{\Lambda} \gg 1$, where d represents the largest dimension of the resonator and Λ the acoustic wavelength, to avoid any standing wave [18].

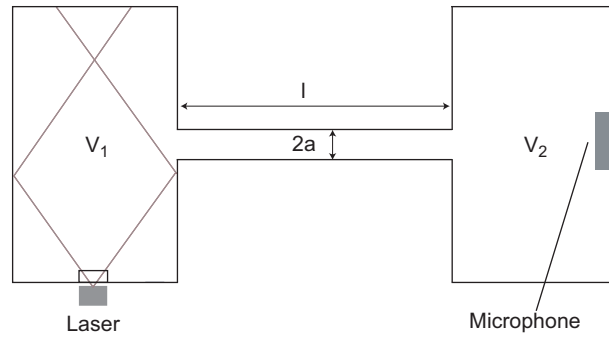


Figure 3.1: Schematic representation of the Helmholtz resonator [25]. The first volume is illuminated by the laser beam without any collimating element. The microphone is placed in the second volume for the detection of the acoustic signal.

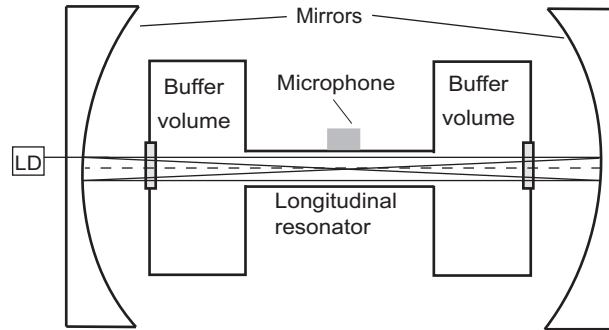


Figure 3.2: Multipass resonant PA cell in a Fabry-Perot configuration. The confocal configuration simplifies the alignment of the cavity [27]. LD: Laser diode.

3.2.3 Multipass resonant cell

Multipass PA cells (Figure 3.2) have found recent developments for specific applications where a very high sensitivity is needed [26]. The increase of power inside the cell is obtained by the use of external mirrors, for instance, in a Fabry-Perot configuration [27] or in a Herriott [28] multipass arrangement [26]. For the former case, a confocal optical cavity is built in order to simplify the alignment of the set-up. A typical finesse of 300 was achieved for this optical cavity, leading to a 100-fold effective gain factor in the optical power. For the latter, an effective power gain of 19 was obtained with 36 passes in a 70 cm cavity, resulting in a total path length of 23.7 m. The increase of power enables excellent detection limits down to ppb levels.

The main drawback of this kind of configurations is the inherent complexity of the system. For example, the length of the optical cavity needs to be actively stabilised to a semi-integer of the laser wavelength in order to stay in resonance. Additionally, this stabilisation needs to be efficient when coupled to the acoustic cavity. Since the PA signal generation requires the incident light to be chopped at an acoustic frequency, it must be checked that this additional modulation does not affect the whole stabilisation. Finally, the mechanical stability of the optical cavity is an important aspect to avoid losing the tracking of the resonance.

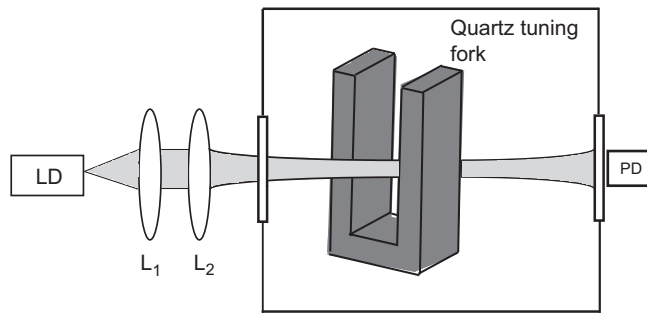


Figure 3.3: Schematic representation of the Quartz-enhanced PAS configuration [30]. LD: Laser diode, L_1 , L_2 : Lenses, PD: photodiode.

3.2.4 Miniature photoacoustic cells

New PA configurations were recently developed in order to miniaturise the PA cell. An original technique based on Quartz-enhanced photoacoustic spectroscopy (QEPAS) was investigated in 2002 by Kosterev et al. [29]. The principle is based on the use of a regular clock-frequency stabilisation element, a quartz tuning fork. This element is used as a resonant transducer for the acoustic signal (see Figure 3.3) [30]. In this case, the accumulated energy is not present in the gas-filled cell, but in the tuning fork. Such an approach removes restrictions imposed to the gas cell by acoustic resonance conditions.

The advantages of such transducers are their very high Q factor ($Q > 10000$ at atmospheric pressure), a virtual immunity to ambient acoustic noise on account of being an acoustic quadrupole, and their very small size (~ 5 mm typical dimensions). Finally, this approach makes a gas cell optional and, if still needed, can be as small as a few cubic millimetres in volume and of arbitrary shape. However, since the resonance frequency of the tuning fork is about 32.8 kHz which is one order of magnitude higher than conventional PA configurations, the system is more sensitive to relaxation processes for several molecules of interest [31]. Finally, QEPAS requires low pressure operation in order to grant a high quality factor.

3.3 Design of the photoacoustic cell

3.3.1 Selection criteria of the photoacoustic cell

The design of the PA cell depends on many parameters mainly given by the requirements of the applications. Two principal applications, one in the life science field and one in the optical fibre manufacturing were investigated in this thesis. In the first application, three different gases (NH_3 , CO_2 and H_2O) were monitored in an animal house containing mice. Water vapour and carbon dioxide were monitored at ambient levels, whereas ammonia had to be measured at sub-ppm level in individually ventilated cages. In the optical fibre manufacturing application, hydrogenated compounds (CH_4 , H_2O and HCl) were monitored in a specific process gas in the sub-ppm range. Monitoring of these gases is of crucial importance for the manufacturing of the novel low-water-peak fibres. A detailed discussion of these *in-situ* measurements are discussed in chapter 4.

The first criterion of choice was based on the use of semiconductor lasers which present excellent properties for trace gas detection (see subsection 4.3.1). Their compactness, reliability, low cost and modulation capabilities make these sources excellent candidates for spectroscopic applications. The small diffraction of the beam in the near infrared (NIR) allows the use a small resonator diameter of a few millimetres. Moreover, the compatibility of these sources with optical fibres offers the possibility to easily align the laser beam into the resonator.

The second important parameter required by the above described applications, is the detection of several species at sub-ppm level using a single PA sensor. This important criterion leads to a particular design of the PA cell. Since the output power of semiconductor lasers is rather low (several milliwatts) in comparison to gas lasers (typically in the Watt range), a PA cell made out of three resonators was built, in order to detect up to three different gases. This geometry offers the possibility to use 100% of each laser output power, thus optimising the detection limit in the sub-ppm range. A single resonator configuration implies the coupling of the different lasers (using standard optical fibre couplers), resulting in a reduced total power, implying a worse sensitivity of the sensor.

Finally, the nature of the detected molecules plays an important role for the design of the PA cell. For instance, NH_3 , H_2O and HCl are polar molecules, which are subject to stick on the cell surface, thus reducing the response time of the cell. In addition, adsorption-desorption processes [3, 32] occur with these molecules, which increases the difficulty to have stable concentrations, especially for sub-ppm levels. In order to reduce these effects, investigations on the appropriate coating were performed. A Teflon coating was deposited on the inner cell surface, which presents excellent properties to minimise adsorption-desorption processes for ammonia detection [33]. A gold coating was used for the detection of H_2O to reduce adsorption-desorption processes. The same gold coating was used for the detection of HCl , which resists to this corrosive molecule. In addition, special care was addressed to the sealing of the cell in order to perform sub-ppm detection of H_2O . Imperfect sealing results in water vapour diffusion inside the cell due to the high ambient H_2O concentration (typically 50% of relative humidity, corresponding to 1.2% of absolute water vapour concentration at room temperature).

3.3.2 Selection of an optimal geometry

In order to determine the best configuration between radial and longitudinal modes, the geometrical dimensions of the cavity (radius R_c and length L) were optimised to obtain the largest cell constant. In addition, the effect on the quality factor and the resonance frequency was also investigated. Azimutal modes were not considered since they need an off-axis beam excitation to be efficient, and thus breaking the symmetry of the cylindrical cavity [34]. Furthermore, azimutal modes present important losses that considerably reduce the sensitivity of the PA cell. The reduction of the losses is nevertheless possible, but requires large cell volumes incompatible with portable instruments.

Since the resonance frequency depends on the length L and radius R_c of the resonator (according to (2.75) and (3.7)), a precise calculation is required to obtain the optimal dimensions of the resonator. A comparison between the

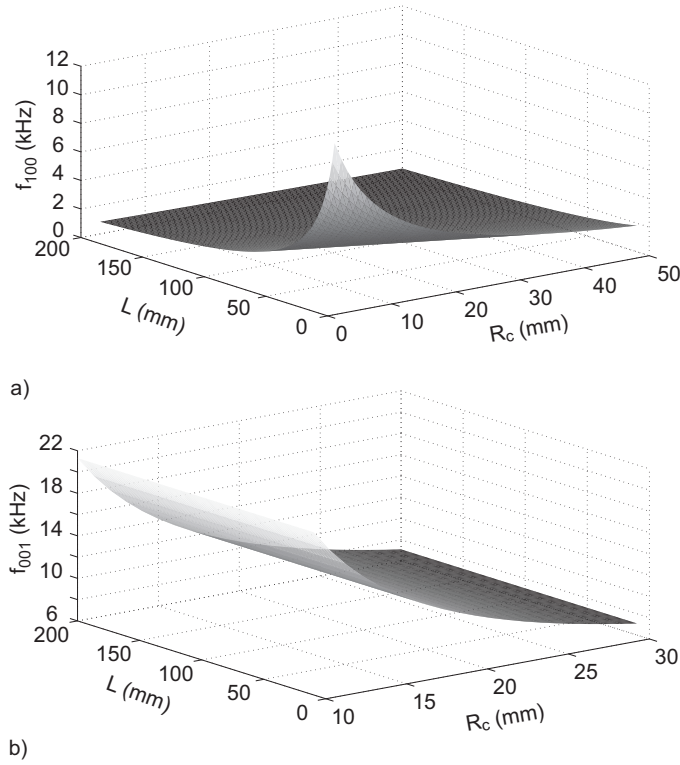


Figure 3.4: Theoretical dependence of the resonance frequency of a) the first longitudinal mode (1 0 0) and b) the first radial mode (0 0 1) as a function of the geometric dimensions (L and R_c) of the resonator.

resonance frequencies of the first longitudinal mode and the first radial mode as a function of R_c and L is shown in Figure 3.4. The considered gas medium for calculations is nitrogen (N_2). Some physical constants of several gases also useful for these simulations are given in Table 3.1.

The resonance frequency range is mainly restricted to several kHz owing to two reasons. The lower boundary is limited by the $1/f$ electronic and ambient acoustic noise. In practice, a frequency of about 1 kHz can be considered as the lower tolerable limit. The upper frequency boundary is limited by the bandwidth of the microphone. Sensitive microphones usually operate at up to 10-15 kHz, which thus corresponds to the maximum of the resonance frequency. These two frequency limits have direct consequences on the dimen-

Substance	ρ_0 (kg/m ³)	γ	M (kg/mol)	η (Pa·s)	K (W/mK)	C_p (J/(mol·K))
He	0.178	1.63	0.0040	$2 \cdot 10^{-5}{}^a$	$152 \cdot 10^{-3}$	20.9
N_2	1.25	1.401	0.0280	$1.75 \cdot 10^{-5}$	$26 \cdot 10^{-3}{}^b$	29.1
O_2	1.43	1.398	0.0320	$2 \cdot 10^{-5}$	$26.7 \cdot 10^{-3}$	29.3
Air	1.293	1.402	0.0288	$1.8 \cdot 10^{-5}$	$25 \cdot 10^{-3}$	29.1
CO_2	1.98	1.293	0.0440	$1.38 \cdot 10^{-5}$	$0.71 \cdot 10^{-3}$	36.8

Table 3.1: Physical constants of some gases at 20°C and 1 atm.

^aat 27°C

^bat 25°C

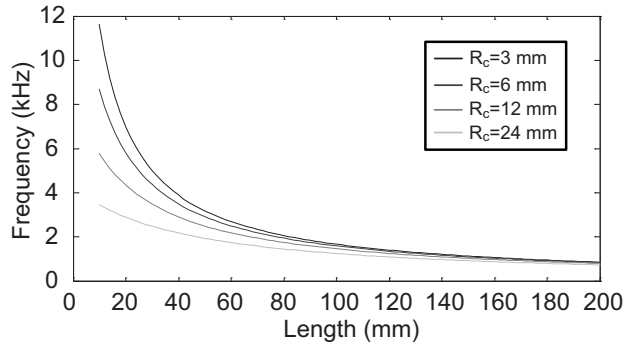


Figure 3.5: Frequency dependence in air of the first longitudinal mode in function of the length of the resonator.

sions of the resonator, which have to be considered to determine the optimal length and radius of the cavity. For the first radial mode, a radius of 15 mm corresponds to a frequency of 14.2 kHz, thus being the lower size limit. The length of the tube is indifferent, since it does not contribute to the value of the resonance frequency. Considering the first longitudinal mode, the maximum length of the resonator is 170 mm, corresponding to a frequency of about 1 kHz. Longer cavities would lead to inferior frequencies and thus increase the $1/f$ noise. Finally, it is useful to represent the dependence of the first longitudinal resonance frequency as a function of the length of the resonator for different resonator radii (Figure 3.5). This figure shows that the influence of the correction factor (3.7) decreases with length and can be neglected for tubes longer than 200 mm.

The comparison of the optimal quality factor expected for the two above described modes is presented in Figure 3.6. The quality factor of the (0 0 1) mode is much larger than for the (1 0 0) mode due to a smaller surface losses contribution (see also subsection 3.2.1). Long resonators increase the cell volume without adding any supplementary friction effects, thus slightly increasing the quality factor. For the first longitudinal mode, Figure 3.6 shows that the quality factor increases with the radius R_c of the resonator and is less sensitive to the length L_c , considering that the length of the resonator is longer than 50 mm. The influence of the radius R_c on the quality factor of mode (1 0 0) is presented in Figure 3.7. Since the thickness of the thermal and viscous boundary layers do only slightly vary with the radius⁴, the main contribution comes from R_c in the numerator of (2.99). Referring to equation (2.101), the quality factor is composed of surface and volume losses. For the case of the longitudinal resonator, the volumetric losses are two orders of magnitude lower and can thus be neglected, so that the total quality factor is given by the surface quality factor (see also Figure 3.7).

The calculation of the cell constant as a function of the dimensions of the resonator for the first radial and first longitudinal mode is presented in Figure 3.8. The maximum cell constant for both modes is obtained for small radius dimensions and for long resonators. However, the radius cannot be much smaller than 15 mm (given by the resonance frequency condition), resulting

⁴The thickness of the thermal and boundary layers for longitudinal modes is principally influenced by the length of the resonator. The thickness decreases for shorter resonators.

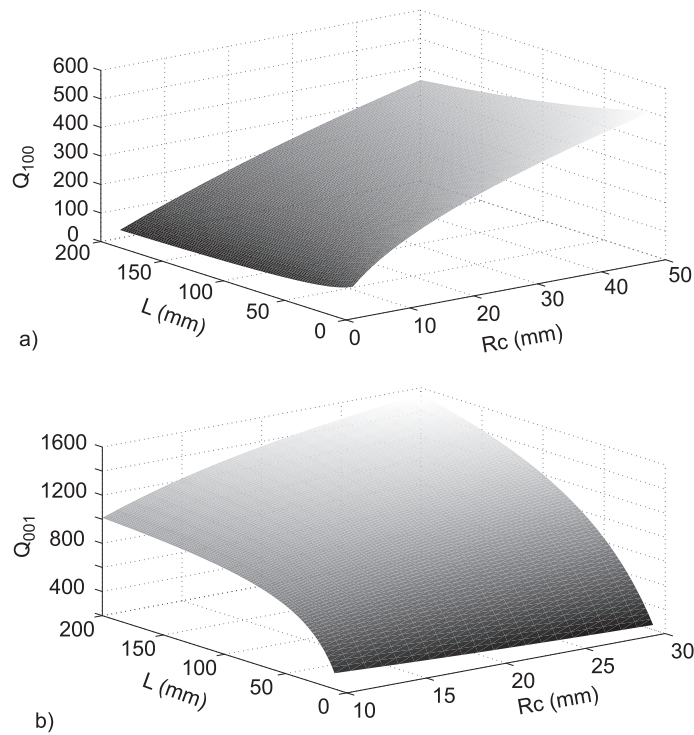


Figure 3.6: Quality factor Q of a) the first longitudinal mode (1 0 0) and b) the first radial mode (0 0 1) as a function of the geometric dimensions (L and R_c) of the resonator.

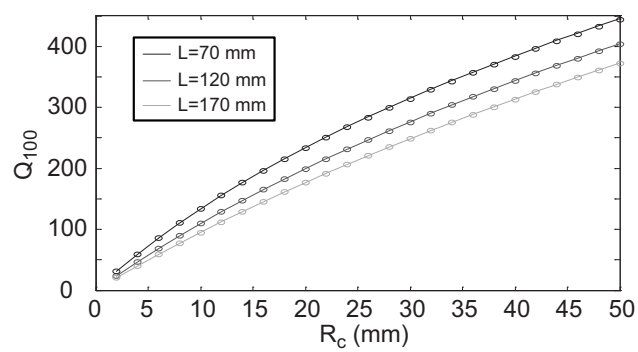


Figure 3.7: Influence of the resonator radius R_c on the quality factor Q_{100} for different resonator lengths. The *circles* represent the total quality factor Q_{tot} and the *solid line* the approximation by the quality factor Q_{surf} due to surface losses.

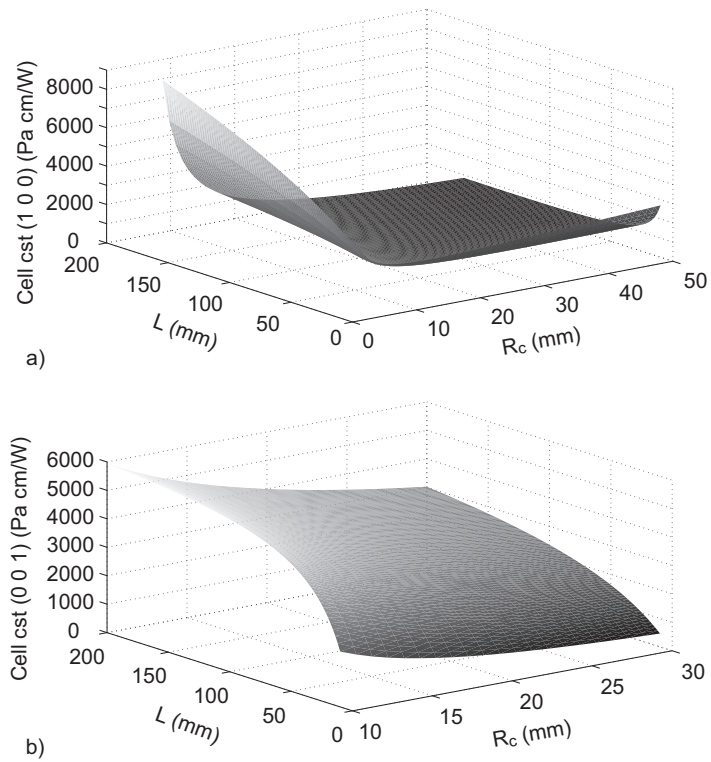


Figure 3.8: Theoretical dependence of the cell constant of a) the first longitudinal mode (1 0 0) and b) the first radial mode (0 0 1) as a function of the geometric dimensions (L and R_c) of the resonator.

in a cell constant of 4760 Pa·cm/W for a 200 mm long resonator. Doubling the length of the resonator results in a cell constant of 5170 Pa·cm/W, thus increasing only slightly the sensitivity. Furthermore, these ideal cell constants values have been calculated by considering that the microphone was placed in the centre of the output flange ($R_c = 0$) and with an axial laser excitation. This is in practice rather not possible, since the optical beam propagates along the resonator axis and passes through a window fixed on the centre of the outer flange. A diagonal excitation or an off-axis microphone detection is however possible, but results in a decrease of the cell constant. For instance, a diagonal excitation with an angle of 12° results in an overlap integral reduction of 40% in comparison with an axial excitation [35]. If the microphone is placed on the circumference of the resonator, the reduction of the detected pressure is 60%.

For the first longitudinal mode, the dimensions of the cavity influence the cell constant by different ways:

1. The signal varies in $L/V_c = 1/\pi R_c^2$, so that a small radius contributes positively to the cell constant.
2. The frequency decreases with L , so that a longer length is preferable since the signal varies in $1/f$.
3. The quality factor is mainly influenced by R_c and according to (2.99), Q increases with R_c .

By taking into account all these conditions, it turns out that the optimised cell constant is achieved for infinite long tube and for infinite small radius. However, the length is limited by the frequency condition that should not be smaller than 1 kHz. This results in a length of 170 mm. The size of the radius is limited by practical building constraints and must allow the beam passing through the resonator without touching the wall in order to avoid wall noise. Thus, the ideal radius of the tube is found to be 3 mm.

Finally, it must be pointed that the calculations made above are valid for a resonator opened at both ends. Longitudinal modes excited with an axial or diagonal optical beam cannot be formed in a resonator closed at both ends, since the overlap integral in such a configuration vanishes for symmetry reasons.

The geometric dimensions defined above result in a frequency of the first longitudinal mode of 997 Hz in pure N_2 , in a quality factor of 30 and a cell constant of 8900 Pa·cm·W⁻¹ (calculations obtained from equations (2.75), (2.99) and (3.3), respectively). The cell constant is improved by a factor 1.9 in comparison to the first radial mode (for dimensions of $L_c = 200$ mm and $R_c = 15$ mm) with axial excitation and with the microphone placed at $R_c = 0$.

3.4 Modulation schemes applied to spectroscopy

Different modulation schemes can be used for the generation of the PA signal. Two different categories can be defined. The first one consists in the modulation of the laser radiation, directly through the injection current or by using an external mechanical chopper, an acousto-optic modulator or an electro-optic modulator. The second technique consists in modulating the absorption of the gas itself by means of the Stark effect [36, 37, 38, 39] or Zeeman effect [40]. This method is valid only for molecules that are sensitive to these effects, for instance NH_3 , H_2CO or NO_2 for the Stark effect [41] and NO for the Zeeman effect. An electric field (Stark effect) or a magnetic field (Zeeman effect) is modulated at the resonance frequency of the cell and produces a periodic molecular absorption due to a change in the molecules energy levels. This technique presents the main advantage of being very selective, since only the active molecule contributes to the PA signal. The other molecules do not interfere with the interrogated species even though their presence is important. Finally, an intensity modulation at frequency f_1 in combination with an absorption modulation at frequency f_2 with a signal detection at the sum or the difference of the two frequencies was successfully performed for the detection of ammonia among water vapour and carbon dioxide [39].

Modulation of the laser radiation is however the most widely used technique since this method is simple, very efficient and can be applied to all molecules. In addition, the modulation of semiconductor lasers is possible by modulating their injection current (see subsection 4.3.1). Two principal regimes are obtained depending on the modulation depth. Either intensity modulation (IM) or wavelength modulation (WM) may be predominant depending on the modulation conditions of the laser injection current. In general, current modulation produces combined IM-WM [35], but two extreme situations may be observed in which one type of modulation is strongly dominant. When the laser is square modulated from threshold to a large current, an on-off modulation of the optical power is achieved and IM is dominant. An example of a methane spectrum recorded around 1651 nm with IM is presented in Figure 3.9. In a WM-dominated regime obtained using a small current modulation on a large DC current, the PA signal directly depends on the modulation depth and an optimum value may be determined (Figure 3.10). In this latter case, a residual IM is always nevertheless observed but has a small influence compared to WM. When IM is applied, the PA signal is proportional to the profile of the absorption line and the spectrum is directly observed (see Figure 3.9). In a WM-dominated regime, the PA signal detected at the modulation frequency f (first harmonic detection) looks like the first derivative of the absorption line profile [43]. Detection of the PA signal at a higher harmonic nf (for instance $2f$, $3f$ detection) is also possible and leads to a signal similar to the n^{th} derivative of the lineshape [44]. In that case, since the detection frequency must correspond to the resonance frequency of the resonator, the modulation frequency f_{mod} corresponds to

$$f_{mod} = \frac{f_{res}}{n} \quad (3.19)$$

In this work, the WM-dominated regime with the optimised modulation depth is considered for trace gas monitoring if not otherwise specified.

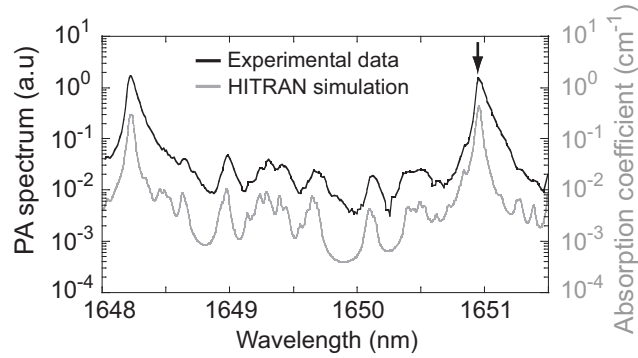


Figure 3.9: PA spectrum of methane obtained with an IM-dominant regime. The wavelength is tuned by changing the laser temperature. The *black curve* is the experimental data and the *grey curve* represents the corresponding absorption coefficient calculated from the HITRAN database [42]. The arrow shows the selected absorption line for CH_4 monitoring.

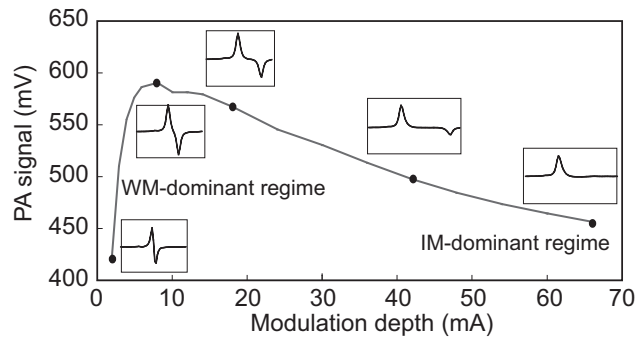


Figure 3.10: Amplitude of the PA signal of the strong CH_4 line at 1650.96 nm as a function of the current modulation depth (square modulation). The shape of the PA signal obtained when the laser is swept through the absorption feature is also shown for some modulation depths indicated by circles on the curve. The WM- and IM-dominated regimes are clearly distinguished by the shape of the PA signal.

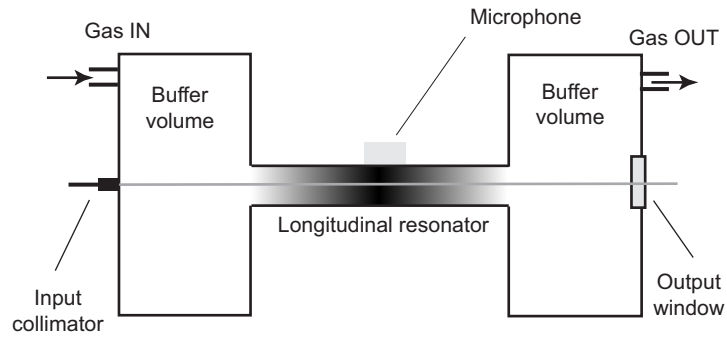


Figure 3.11: Schematic representation of the longitudinal PA cell. The input collimator is fibre-pigtailed and makes an easy connection with semi-conductor lasers possible. The first longitudinal mode is represented inside the resonator in a grey gradation. The darker zone represents the antinode of the acoustic wave. The microphone is located at the centre of the resonator where the maximum of the standing acoustic wave occurs.

3.5 Characterisation of the photoacoustic cell

3.5.1 Performance of the cell

A PA cell operated in its first longitudinal mode based on the calculations developed in section 3.3 was built. The cell is made out of a central stainless steel tube acting as an acoustic resonator (see Figure 3.11). This central tube has a fixed length of 170 mm and a radius of either 3 mm or 6 mm. Two different radii were studied in order to validate the simulations performed in section 3.3. A larger volume of each side of the resonator was designed to act as efficient acoustic notch filters. The length of the volumes can be easily adjusted by the way of a moving piston. The influence of the volumes length on the coupling between the ambient acoustic noise and the resonator was investigated, in order to find the most favourable geometry. The ideal volume length corresponded to a quarter wavelength ($L = 85$ mm), in agreement with previous publications [17]. The diameter of the volumes was chosen in order to ensure a high acoustic impedance mismatch between the resonator and the volumes [45] to achieve an efficient reflection of the acoustic wave at the opened ends. Additionally, the diameter must be large enough to place the gas inlet and windows. For this configuration, the diameter of the buffer volumes was 100 mm. A sensitive electret microphone is located in the centre of the resonator, where the maximum of the acoustic wave occurs (see the first longitudinal mode pattern in Figure 2.7). A 1 mm diameter hole was drilled through the resonator and the surface of the microphone (22 mm^2) was mounted flush with the resonator wall to efficiently detect the acoustic wave. The PA signal was then amplified by a low noise pre-amplifier (gain $G = 200$) and measured using a lock-in amplifier with a time constant set to 10 s. An optical fibre terminated by a built-in collimator is fixed on the first flange of the cell, enabling an easy alignment of the laser beam and the output flange is equipped with an anti-reflection coated window.

The characterisation of the PA cell was performed by measuring its first longitudinal resonance using a certified gas mixture of 5000 ppm of methane (CH_4) buffered in nitrogen. The two different resonators of length $L = 170$

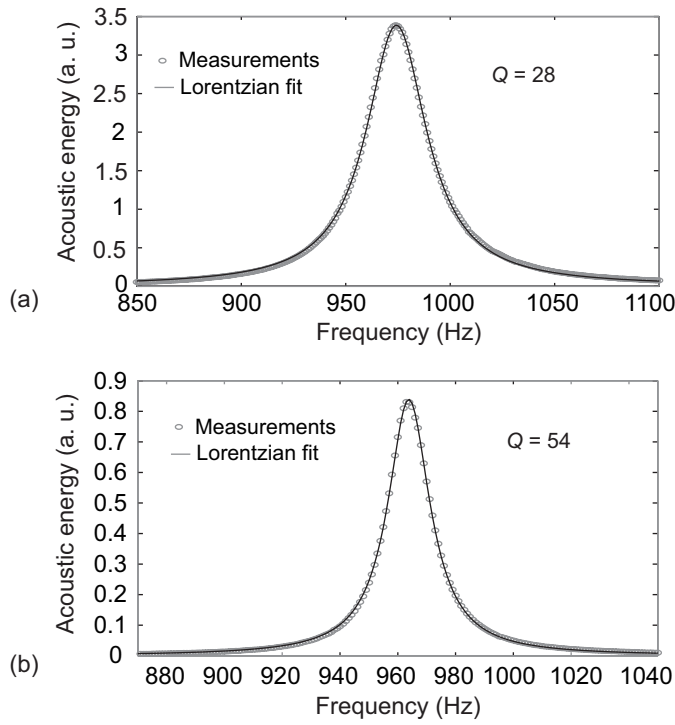


Figure 3.12: First longitudinal resonance of the PA cell with two different resonators of length $L = 170$ mm and radius (a) $R_c = 3$ mm and (b) $R_c = 6$ mm. Circles are experimental points and the curves are the result of a Lorentzian distribution fit. The quality factor corresponds to the ratio of the half width at half maximum of the PA signal to the resonance frequency.

mm and radii $R_c = 3$ mm and 6 mm have been investigated. The parameters of the resonance (central frequency, quality factor) have been extracted from a fitting procedure of the experimental data. The PA energy (square of the PA amplitude) was fitted by a Lorentzian distribution in order to determine the quality factor and the resonance frequency of the PA cell. These results are shown in Figure 3.12. A comparison between the measurements and the theoretical values calculated from equations (3.3), (2.75) and (2.99) was established and is summarised in Table 3.2. A good qualitative agreement is obtained between calculation and measurements. In particular, the experimental quality factors are less than 10% smaller than the calculated values, which indicates a good quality of the internal surface of the resonators. The difference between the calculation and the experiment is in agreement with previously published values [46, 14]. It can also be seen that the resonance frequencies are situated around 1 kHz, which fulfils the condition discussed in subsection 3.3.2. As expected from the simulations, the smaller radius resonator ($R_c = 3$ mm) has demonstrated the best performances. The experimental cell constant can be derived from expression (3.4) by measuring the PA signal obtained in well-controlled conditions, i.e. with a certified concentration of a gas of known absorption and by measuring also the laser power P_0 . With the typical sensitivity of the microphone of 10 mV/Pa and taking into account the gain ($G = 200$) of its preamplifier, a cell constant of 13232 ($\text{Pa}\cdot\text{cm}\cdot\text{W}^{-1}$) is obtained with the 3 mm radius resonator and 6552 ($\text{Pa}\cdot\text{cm}\cdot\text{W}^{-1}$) with the 6

Geometric parameters			Simulation			Experimental results		
Radius (mm)	Length (mm)	Volume (ml)	Freq. (Hz)	Q	Cell constant (Pa·cm/W)	Freq. (Hz)	Q	Cell constant (Pa·cm/W)
3	170	4.8	997	30.0	8900	974.2	28	13232
6	170	19.2	969	58.5	4600	963.8	54	6552

Table 3.2: Comparison of the performances of the PA cells. Theoretical values have been calculated from equations (3.3), (2.75) and (2.99) and experimental values have been measured using a gas mixture of 5000 ppm CH₄ in N₂.

mm radius by using IM. The experimental cell constant improved by a factor 2 when reducing the resonator radius from 6 mm to 3 mm, as expected from the calculation. The difference between the experimental and calculated cell constant is mainly due to the uncertainty of the sensitivity of the microphone.

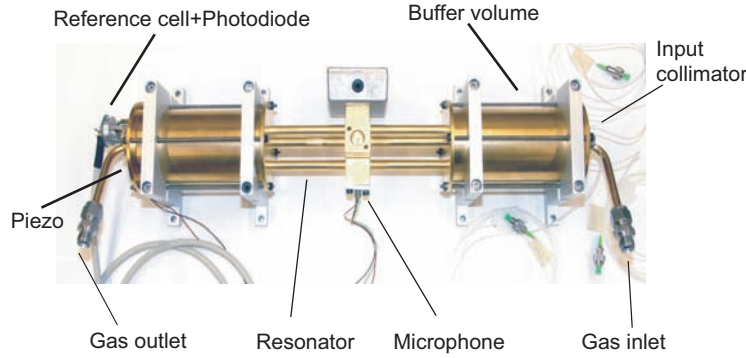


Figure 3.13: Picture of the PA cell consisting of three resonators operated in their first longitudinal mode. Gas reference cells and a piezo transducer allow the stabilisation of the laser wavelength and the tracking of the resonance frequency, respectively.

3.5.2 Improvement of the photoacoustic cell

Since the geometric dimensions of the photoacoustic cell were experimentally optimised, a new cell with fixed dimensions was built. The upgraded version allows multi-gas sensing, active tracking of the resonance frequency and stabilisation of the laser wavelength (tracking of the resonance frequency and stabilisation of the wavelength are described in section 3.6). The new cell is composed of three acoustic resonators of length $L = 170$ mm and radius $R_c = 3$ mm, enabling the possibility to measure up to three different gases (Figure 3.13). The buffer volumes length is kept to a quarter acoustic wavelength ($L_{buff} = 85$ mm) and the diameter was optimised ($d = 50$ mm) to enable the implementation on the outer flange of all required elements, such as windows, loudspeaker and gas inlets. A gold coating was deposited on the internal surface of the cell to reduce adsorption-desorption processes inside the cell for H_2O and HCl [33]. A Teflon coating was deposited for the detection of NH_3 to reduce adsorption-desorption processes as well. A gas reference cell in combination with a photodiode make possible the implementation of an active stabilisation of each laser wavelength, and a piezo-electric transducer is used as a loudspeaker to actively track the resonance frequency.

The resonances of the gold coated PA cell were measured in each tube. The resonance frequencies and the quality factors in each tube were so similar that they could be considered as identical. An example of the resonance and the quality factor measured with 5000 ppm of CH_4 is presented in Figure 3.14. The quality factor is of the same order as in the previous cell, but is however slightly reduced probably due to an imperfect gold deposition inside the resonators and to a reduced impedance mismatch with the buffer volumes due their smaller diameter. The acoustic response of the PA cell to a broad frequency scan (800-10000 Hz) using 5000 ppm of CH_4 is shown in Figure 3.15. According to (2.88), the first longitudinal mode is the most efficiently excited, which is experimentally verified. Odd order longitudinal modes ($(3\ 0\ 0)$, $(5\ 0\ 0)$ and $(7\ 0\ 0)$) are also excited with decreasing amplitude due to the $1/f$ dependence of the PA signal and a reduced overlap integral between the laser beam and higher acoustic modes. Even modes are theoretically not excited for symmetry reasons (see for instance mode $(2\ 0\ 0)$ in Figure 2.7). However, a mode located at about 4 kHz is slightly excited, corresponding to

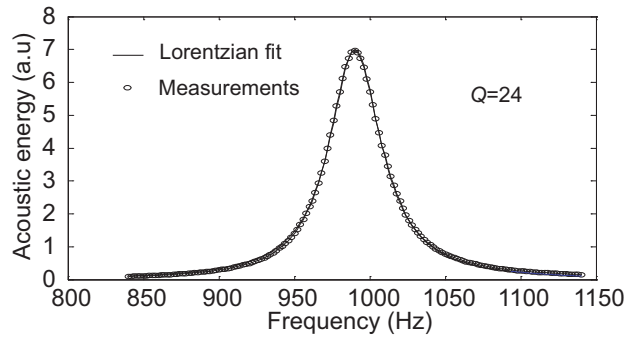


Figure 3.14: First longitudinal resonance of the gold coated PA cell of one of the resonator. The resonator geometric dimensions are $L = 170$ mm and $R_c = 3$ mm.

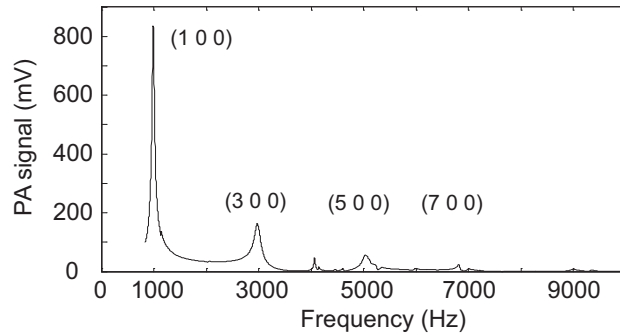


Figure 3.15: Acoustic response of the gold coated PA cell. The longitudinal modes are identified on the resonances of the tube.

the first azimuthal mode of the buffer volume.

The response time of the PA cell is an important parameter that influences trace gas detection. The response time can be determined by applying a step concentration at the entrance of the PA cell and by measuring the corresponding signal variation. Since the gas renewal is directly dependent on the flow rate, a maximum flow rate should be used. However, high flow rates induce acoustic noise in the resonator and are thus limited. In order to determine the critical value, the microphone noise was recorded while no gas passed through the resonator. The flow rate was then increased until the added acoustic noise was significantly higher than the microphone noise (Figure 3.16). Results show that a flow rate up to 1000 sccm (standard cubic centimetre per minute, $1000 \text{ sccm} \equiv 1 \text{ l/min}$) is possible without adding any extra acoustic noise. The response time of the PA cell is then determined by applying a step concentration of CH_4 with a flow rate of 1000 sccm. In order to precisely determine the time decay constant, an exponential fit was used (Figure 3.17). By considering 95% of gas renewal ($1 - 1/e^3$), the response time is equal to 26 s.

Finally, it must be pointed out that the developed cell does not allow simultaneous measurements of the three species, since crosstalk between the distinct resonating tubes is present (see Figure 3.18). The modulation frequency of the laser connected to the beam collimator in tube one, was scanned through the acoustic resonance while the PA signal was recorded in the three tubes.

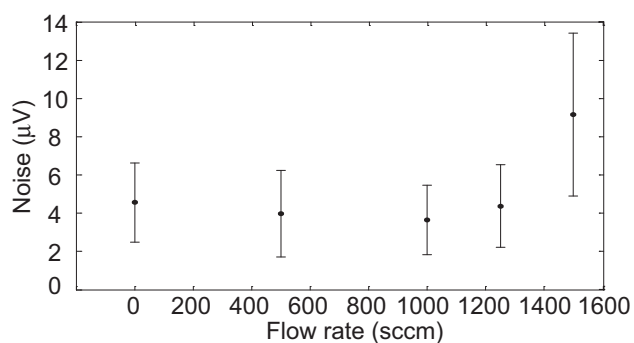


Figure 3.16: Acoustic noise as a function of the flow rate. A flow rate up to 1000 sccm can be used without adding extra noise. *Errorbars* shown on the plot correspond to the standard deviation of the PA signal recorded in a 10-min period with a lock-in integration time of 10 s.

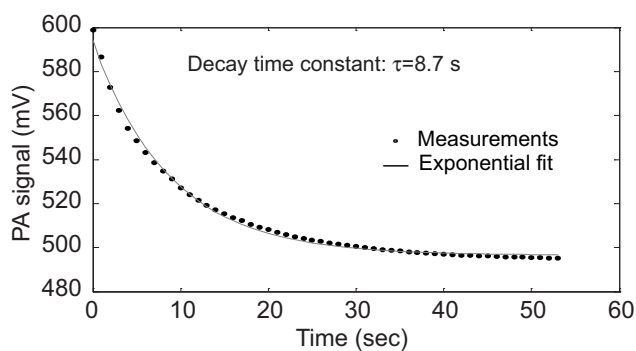


Figure 3.17: Response time of the PA cell to a change of CH_4 concentration. *Circles* are experimental points and the *line* is the result of a fit by an exponential distribution. A response time of 26 s ($=3\tau$) corresponding to 95% of gas renewal is obtained.

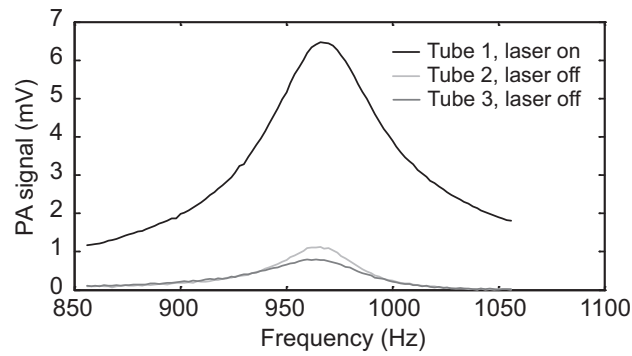


Figure 3.18: Crosstalk between the three resonators. The modulation frequency of the laser connected to the beam collimator in tube one, was scanned through the acoustic resonance while the PA signal was recorded in the three tubes. A crosstalk signal of 17% in tube 2 and 12% in tube 3 with respect to the total PA signal in tube 1 has been observed.

A crosstalk signal of 17% in tube 2 and 12% in tube 3 with respect to the total PA signal in tube 1 has been observed. However, simultaneous detection of three gases is not necessary in applications where only slow variations of concentration are expected and long integration times are used (up to 30 s) as considered in this work (see chapter 4). Cross-talk between the tubes may probably be reduced by increasing the distance between the centre of each tube.

3.6 Resonance frequency tracking and wavelength stabilisation

In order to secure long time and automatic trace gas measurements, an active tracking of the resonance frequency is necessary. Additionally, the laser frequency tends to drift after a few hours of operation and needs to be actively stabilised on the absorption line. These two active tracking and stabilisation are described in the next subsections

3.6.1 Acoustic resonance frequency tracking

The resonance frequency is directly dependent on the sound velocity (c_s), which depends on temperature (T), molar mass of the gas (M) and ratio of the specific heat capacities at constant pressure and volume (γ). According to (2.75) and (2.53), the resonance frequency of the first longitudinal mode is expressed by:

$$f_{res} = c_s \frac{1}{2L_{eff}} = \sqrt{\frac{\gamma RT}{M}} \frac{1}{2L_{eff}} \quad (3.20)$$

where L_{eff} is defined by (3.7) and R is the perfect gas constant.

The amplitude of the PA signal rapidly decreases when the measurement frequency is shifted by a few Hertz off the resonance. Near the resonance frequency ($f = f_{res}(1 + \delta)$, $\delta \ll 1$), the amplitude of the signal is given by [47]:

$$\left| \frac{A(f)}{A(f_{res})} \right| \cong [1 + Q^2(1 - (1 + \delta)^2)^2]^{-1/2} \quad (3.21)$$

A frequency change of 10 Hz produces a reduction of the PA signal of 10% for a Q factor of 28. Variations of tens of Hertz are typical when the buffer gas is changed. A temperature variation of 5°C at room temperature results in a frequency shift of 8.5 Hz, producing a signal loss of 7.5%. In order to secure a long-term operation at the correct frequency, an active stabilisation of the resonance frequency has been implemented using a piezo-electric transducer as a speaker. The tracking is usually achieved by monitoring the response in another mode of the PA cell, since the ratio of the eigenfrequencies of two modes is constant [48] for a fixed PA cell geometry (see Figure 3.19). In this case it was more convenient to use the first longitudinal mode of the second buffer volume for this tracking. An electronic circuit maximises the acoustic signal detected by the microphone and records the corresponding reference frequency. The measurement frequency (f_{meas}) is then obtained by multiplying the tracking frequency (f_{track}) by the constant ratio of the two eigenfrequencies. In order to vary the resonance frequency, a gas mixture composed of oxygen (O_2) and (He) was used. By changing the O_2 percentage in the O_2 -He mixture, the resonance frequency was shifted from 1257 to 1162 Hz. The measurement frequency resulted in a stability of better than 0.4 %.

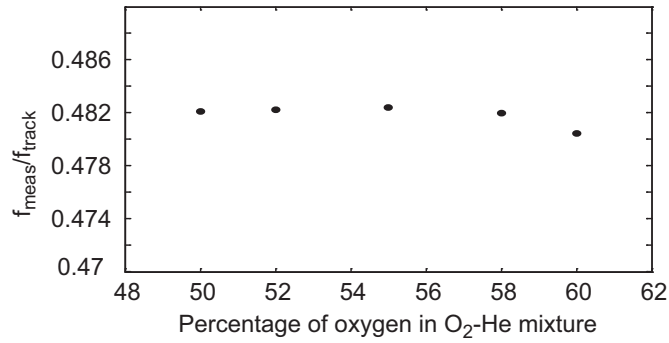


Figure 3.19: Ratio of the measurement frequency (f_{meas}) and the tracking frequency (f_{track}) for different oxygen concentrations in a He-O₂ gas mixture. The PA signal was recorded using a 50 ppm CH₄ concentration.

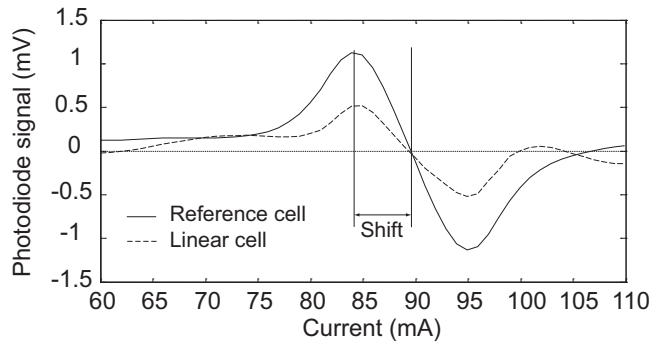


Figure 3.20: Shape of the absorption line measured with the reference (*solid line*) and linear cell (*dashed line*). The maximum of the PA signal is slightly shifted from the centre of the absorption line.

3.6.2 Laser wavelength stabilisation

The stabilisation of the laser frequency is important for long-term unattended operation, since the wavelength must be adjusted at a precise and fixed point to obtain the maximum PA signal. For WM, the maximum does not correspond to the centre of the absorption line, but is slightly shifted (see Figure 3.20).

Although the laser temperature is stabilised to 0.01°C using an appropriate laser diode controller, its frequency tends to slowly drift in time. Figure 3.22 shows the frequency drift for a laser diode emitting at 1651 nm used for methane detection. The stabilisation is performed using a reference cell containing 100% of CH₄ at reduced pressure in combination with a photodiode (see Figure 3.21). The recorded signal is amplified using a lock-in amplifier and demodulated at $1f$. The lineshape looks like a first derivative with an amplitude equal to zero at the centre of the absorption line if the phase of the lock-in detection is correctly adjusted, and varies linearly in the vicinity of this point. This signal is thus used as an error signal in a PI regulation loop and is added as a DC offset to the modulation amplitude. The frequency variation was recorded while the laser was placed in an oven with a starting temperature of 44°C and then let to reach the ambient temperature after several hours (see

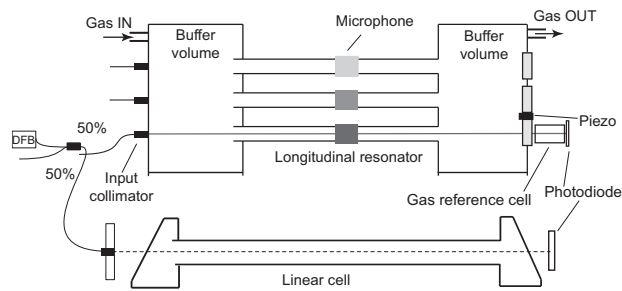


Figure 3.21: Schematic view of the set-up used to actively stabilise the laser wavelength. The reference cell is used as an error signal and the linear cell is used to check the stability.

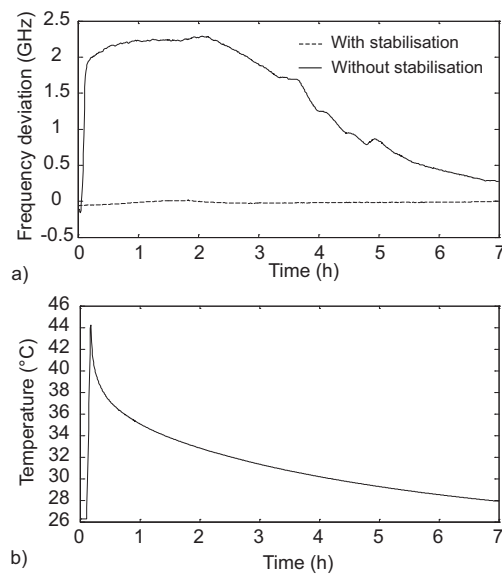


Figure 3.22: a) Frequency drift of a laser diode emitting at 1651 nm over a temperature variation shown in b). An active stabilisation reduces the frequency drift by a factor of about 100 over a temperature variation of 18°C.

Figure 3.22b). Finally, the drift of the laser frequency is recorded using an external linear cell, since the drift cannot be deduced from the error signal. The linear cell is used in combination with a photodiode and wavelength-modulation spectroscopy (see the lineshape in Figure 3.20) [35]. A frequency deviation of this laser corresponding to 2 GHz results in a signal reduction of 54% by considering a Lorentzian absorption line of linewidth 0.062 cm^{-1} at atmospheric pressure in air [49]. In contrast, the frequency shift of a few tens of MHz obtained with the active stabilisation does not result in a significant signal loss.

Bibliography

- [1] A. Miklos, P. Hess, and Z. Bozoki, "Application of acoustic resonators in photoacoustic trace gas analysis and metrology," *Rev. Sci. Instrum.* **72**(4), 1937–1955 (2001).
- [2] I. G. Calasso, V. Funtov, and M. W. Sigrist, "Analysis of isotopic CO₂ mixtures by laser photoacoustic spectroscopy," *Appl. Opt.* **36**(15), 3212–3216 (1997).
- [3] J. Henningsen and N. Melander, "Sensitive measurement of adsorption dynamics with nonresonant gas phase photoacoustics," *Appl. Opt.* **36**(27), 7037–7045 (1997).
- [4] S. Schäfer, A. Miklos, and P. Hess, "Quantitative signal analysis in pulsed resonant photoacoustics," *Appl. Opt.* **36**(15), 3202–3211 (1997).
- [5] S. Schilt, L. Thévenaz, M. Niklès, L. Emmenegger, and C. Hügli, "Ammonia monitoring at trace level using photoacoustic spectroscopy in industrial and environmental applications," *Spectrochim. Acta, Part A* **60**(14), 3259–3268 (2004).
- [6] L. E. Kinsler, A. R. Frey, A. B. Coppens, and J. V. Sanders, *Fundamentals of acoustics* (Wiley, New York, 2001).
- [7] I. S. Gradshteyn and I. M. Ryzhik, *Tables of integrals, series and products* (San Diego, 1996).
- [8] A. Thöny and M. W. Sigrist, "New developments in CO₂-laser photoacoustic monitoring of trace gases," *Infrared Phys. Technol.* **36**(2), 585–615 (1995).
- [9] C. Brand, A. Winkler, P. Hess, M. A., Z. Bozoki, and J. Sneider, "Pulsed-laser excitation of acoustic modes in open high-Q photoacoustic resonators for trace gas monitoring: results for C₂H₄," *Appl. Opt.* **34**(18), 3257–3266 (1995).
- [10] R. Gerlach and N. M. Amer, "Brewster window and windowless resonant spectrophones for intracavity operation," *Appl. Phys.* **23**, 319–326 (1980).
- [11] M. Wolff and H. Harde, "Photoacoustic spectrometer based on a DFB-diode laser," *Infrared Phys. Technol.* **41**, 283–286 (2000).
- [12] A. Petzold and R. Niessner, "Novel design of a resonant photoacoustic spectrophone for elemental carbon mass monitoring," *Appl. Phys. Lett.* **66**(10), 1285–1287 (1995).
- [13] E. Kritchman, S. Shtrikman, and M. Slatkine, "Resonant optoacoustic cells for trace gas analysis," *J. Opt. Soc. Am.* **68**(9), 1257–1271 (1978).
- [14] S. Bernegger and M. W. Sigrist, "CO-laser photoacoustic spectroscopy of gases and vapours for trace gas analysis," *Infrared Phys. Technol.* **30**(5), 375–429 (1990).

- [15] Z. Bozoki, A. Mohacsi, G. Szabo, Z. Bor, M. Erdélyi, W. Chen, and F. K. Tittel, “Near-infrared diode laser based spectroscopic detection of ammonia: a comparative study of photoacoustic and direct optical absorption methods,” *Appl. Spectrosc.* **56**(6), 715–719 (2002).
- [16] A. Boschetti, D. Bassi, E. Iacob, S. Iannotta, L. Ricci, and M. Scotoni, “Resonant photoacoustic simultaneous detection of methane and ethylene by means of a 1.63- μm diode laser,” *Appl. Phys. B* **74**, 273–278 (2002).
- [17] F. G. C. Bijnen, J. Reuss, and J. M. Harren, “Geometrical optimization of a longitudinal resonant photoacoustic cell for sensitive and fast trace gas detection,” *Rev. Sci. Instrum.* **67**(8), 2914–2923 (1996).
- [18] M. Rossi, *Electroacoustique*, vol. XXI of *Traité d’électricité* (Presses polytechniques romandes, Lausanne, 1986).
- [19] O. Nordhaus and J. Pelzl, “Frequency dependence of resonant photoacoustic cells: the extended Helmholtz resonator,” *Appl. Phys. B* **25**, 221–229 (1981).
- [20] J. Pelzl, K. Klein, and O. Nordhaus, “Extended Helmholtz resonator in low-temperature photoacoustic spectroscopy,” *Appl. Opt.* **21**(1), 94–99 (1982).
- [21] V. Zéninari, B. Parvitte, D. Courtois, V. Kapitanov, and Y. Ponomarev, “Methane detection on the sub-ppm level with a near-infrared diode laser photoacoustic sensor,” *Infrared Phys. Technol.* **44**, 253–261 (2003).
- [22] G. Busse and D. Herboeck, “Differential Helmholtz resonator as an optoacoustic detector,” *Appl. Opt.* **18**(23), 3959–3961 (1979).
- [23] V. Zéninari, V. Kapitanov, D. Courtois, and Y. Ponomarev, “Design and characteristics of a differential Helmholtz resonant photoacoustic cell for infrared gas detection,” *Infrared Phys. Technol.* **40**, 1–23 (1999).
- [24] S. Barbieri, J.-P. Pellaux, E. Studemann, and D. Rosset, “Gas detection with quantum cascade lasers: An adapted photoacoustic sensor based on Helmholtz resonance,” *Rev. Sci. Instrum.* **73**(6), 2458–2461 (2002).
- [25] M. Mattiello, M. Niklès, S. Schilt, L. Thévenaz, A. Salhi, D. Barat, A. Vicet, Y. Rouillard, R. Werner, and J. Koeth, “Novel Helmholtz-based photoacoustic sensor for trace gas detection at ppm level using GaInAsSb/GaAlAsSb DFB lasers,” *Spectrochim. Acta, Part A* **63**(5), 952–958 (2006).
- [26] M. Nägele and M. W. Sigrist, “Mobile laser spectrometer with novel resonant multipass photoacoustic cell for trace-gas sensing,” *Appl. Phys. B* **70**(6), 895–901 (2000).
- [27] A. Rossi, R. Buffa, M. Scotoni, D. Bassi, S. Iannotta, and A. Boschetti, “Optical enhancement of diode laser-photoacoustic trace gas detection by means of external Fabry-Perot cavity,” *Appl. Phys. Lett.* **87**, 04,110 (2005).

- [28] J. B. McManus, P. L. Keabian, and M. S. Zahniser, "Astigmatic mirror multipass absorption cells for long-path-length spectroscopy," *Appl. Opt.* **34**(18), 3336–3348 (1995).
- [29] A. A. Kosterev, Y. A. Bakhirkin, R. F. Curl, and F. K. Tittel, "Quartz-enhanced photoacoustic spectroscopy," *Opt. Lett.* **27**(21), 1902–1904 (2002).
- [30] A. A. Kosterev, F. K. Tittel, D. V. Serebryakov, A. L. Malinovsky, and I. V. Morozov, "Applications of quartz tuning forks in spectroscopic gas sensing," *Rev. Sci. Instrum.* **76**(043105) (2005).
- [31] A. A. Kosterev, Y. A. Bakhirkin, and F. K. Tittel, "Ultrasensitive gas detection by quartz-enhanced photoacoustic spectroscopy in the fundamental molecular absorption bands region," *Appl. Phys. B* **80**(1), 133–138 (2005).
- [32] A. Schmohl, A. Miklos, and P. Hess, "Effects of adsorption-desorption processes on the response time and accuracy of photoacoustic detection of ammonia," *Appl. Opt.* **40**(15), 2571–2578 (2001).
- [33] S. M. Beck, "Cell coatings to minimize sample (NH_3 and N_2H_4) adsorption for low-level photoacoustic detection," *Appl. Opt.* **24**(12), 1761–1763 (1985).
- [34] A. Karbach and P. Hess, "High precision acoustic spectroscopy by laser excitation of resonator modes," *J. Chem. Phys.* **83**(3), 1075–1084 (1985).
- [35] S. Schilt, "Mesure de traces de gaz à l'aide de lasers à semi-conducteur," Ph.D. thesis, Swiss Federal Institute of Technology (2002).
- [36] M. J. Kavaya, J. S. Margolis, and M. S. Shumate, "Optoacoustic detection using Stark modulation," *Appl. Opt.* **18**(15), 2602–2606 (1979).
- [37] A. Thöny and M. W. Sigrist, "Novel photoacoustic Stark cell," *Rev. Sci. Instrum.* **66**(1), 227–231 (1995). Part 1.
- [38] A. J. L. Verhage, R. A. Rooth, and L. W. Wouters, "Laser Stark spectrometer for the measurement of ammonia in flue-gas," *Appl. Opt.* **32**(30), 5856–5866 (1993).
- [39] H. Sauren, T. Regts, C. Vanasselt, and D. Bicanic, "Simplifying the laser photoacoustic trace detection of ammonia by effective suppression of water-vapor and of carbon-dioxide as the major absorbing atmospheric constituents," *Environ. Technol.* **12**(8), 719–724 (1991).
- [40] T. J. Bridges and E. G. Burkhardt, "Zeeman spectroscopy of NO with magneto-spectrophone," *Opt. Commun.* **22**(2), 248–250 (1977).
- [41] P. Werle and S. Lechner, "Stark-modulation-enhanced FM-spectroscopy," *Spectrochim. Acta, Part A* **55**(10), 1941–1955 (1999).
- [42] L. S. Rothman, D. Jacquemart, A. Barbe, D. C. Benner, M. Birk, L. R. Brown, M. R. Carleer, C. Chackerian, K. Chance, L. H. Coudert, V. Dana, V. M. Devi, J. M. Flaud, R. R. Gamache, A. Goldman,

- J. M. Hartmann, K. W. Jucks, A. G. Maki, J. Y. Mandin, S. T. Massie, J. Orphal, A. Perrin, C. P. Rinsland, M. A. H. Smith, J. Tennyson, R. N. Tolchenov, R. A. Toth, J. Vander Auwera, P. Varanasi, and G. Wagner, "The HITRAN 2004 molecular spectroscopic database," *J. Quant. Spectrosc. Radiat. Transf.* **96**(2), 139–204 (2005).
- [43] S. Schilt, L. Thévenaz, and P. Robert, "Wavelength modulation spectroscopy: combined frequency and intensity laser modulation," *Appl. Opt.* **42**(33), 6728–6738 (2003).
- [44] S. Schilt and L. Thévenaz, "Wavelength modulation photoacoustic spectroscopy: Theoretical description and experimental results," *Infrared Phys. Technol.* **48**(2), 154–162 (2006).
- [45] P. M. Morse and K. U. Ingard, *Theoretical acoustics* (Princeton university press, Princeton, 1968).
- [46] R. D. Kamm, "Detection of weakly absorbing gases using a resonant optoacoustic method," *J. Appl. Phys.* **47**(8), 3550–3558 (1976).
- [47] C. F. Dewey Jr, *Design of optoacoustic systems*, in optoacoustic spectroscopy and detection, edited by Y-H. Pao (Academic Press, New York, 1977).
- [48] G. Angeli, Z. Bozoki, A. Miklos, A. Lörincz, A. Thöny, and M. Sigrist, "Design and characterization of a windowless resonant photoacoustic chamber equipped with resonance locking circuitry," *Rev. Sci. Instrum.* **62**(3), 810–813 (1990).
- [49] V. Zéninari, B. Parvitte, D. Courtois, V. Kapitanov, and Y. Ponomarev, "Measurements of air and noble-gas broadening and shift coefficients of the methane R3 triplet of the $2\nu_3$ band," *Appl. Phys. B* **72**, 953–959 (2001).

Chapter 4

Trace gas monitoring

4.1 Introduction

This chapter aims at describing two principal applications performed using the developed PA sensor in environments that differ from the laboratory situations. The *in-situ* measurement campaigns made the validation of the system in industrial conditions possible. However, before operating the sensor in off-laboratory circumstances, an extensive test phase in well-controlled conditions has been performed.

After a description of the main issues and objectives of the two applications, an important section is dedicated to laboratory results, starting from the selection of appropriate laser diodes and followed by calibration processes. *In-situ* trace gas monitoring in the life science and in the optical fibre manufacturing process is presented in sections 4.4 and 4.5, respectively.

Finally, a system providing a detection limit at ppb level for ammonia monitoring in ambient air is described in section 4.6.

4.2 Description of the applications

4.2.1 Life science application

Laboratory animal housing systems have recently undergone an important evolution resulting from the development of individually ventilated cages (IVC). The principal advantage of these systems is the efficient limitation of contaminants penetration into the cages. This system maintains over long periods a clean environment from the microbiological point of view and makes an immediate access of the researcher to the animals possible.

The conditions in an animal house are usually controlled and are maintained in strict limits. For the rodents, the temperature is fixed to $22\pm 2^\circ\text{C}$, the relative humidity is kept between 45% and 65%, while the air renewal in the cages is set between 15 to 20 per hour.

The use of a sensitive multi-gas sensor operated in continuous and real-time mode offers new possibilities towards complete monitoring of microclimate parameters in the IVC. For this purpose, the concentration of three physiological gases of interest, namely ammonia (NH_3), carbon dioxide (CO_2) and water vapour (H_2O), has been continuously recorded from the atmosphere of IVC. The measurement campaign was carried out during a complete cycle of the bedding, in order to analyse the microclimate in the cages. The bedding is

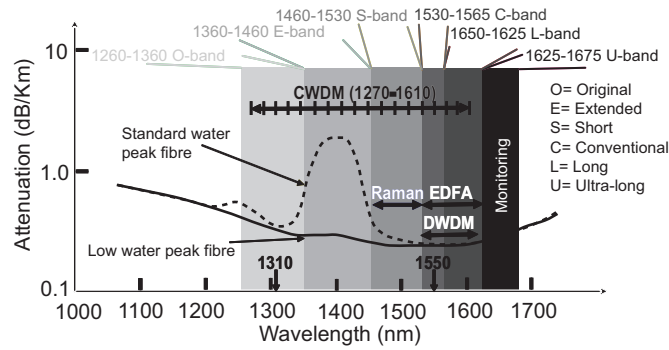


Figure 4.1: Standard and Low-water-peak fibre spectral attenuation. The different telecommunication bands and the coarse wavelength division multiplexing (CWDM) are identified.

regularly changed (usually once per week) in order to secure a high level of hygiene to preserve animals' health. For instance, the threshold limit of NH_3 for human being is fixed at a maximum of 25 ppm in working environments [1].

The concentration level of these gases is relevant for the well being of the laboratory animals, an important contribution to the quality of *in vivo* research. Ammonia, produced by animals' urine, and water vapour, caused by the perspiration of the animals, reflect the quality of bedding and the ventilation rate inside the cage and thus, the level of hygiene. Carbon dioxide is an indicator of the physical activity of living organisms allowing assessment of the circadian activity of the mice in the cages.

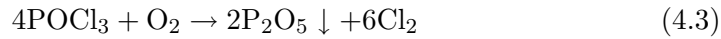
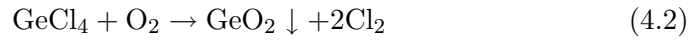
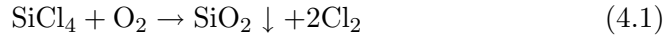
Measurements performed in the animal house were achieved using the PA cell that consists in one resonator. Multi-gas sensing was achieved by using three different laser modulation frequencies within the acoustic resonance frequency. Results of these measurements performed in the animal house are presented in subsection 4.4.2.

4.2.2 Optical fibre manufacturing process application

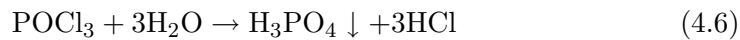
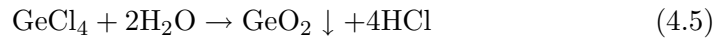
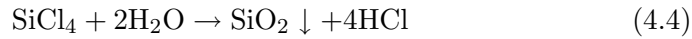
The PA cell described in chapter 3 consisting in three resonators in combination with the laser diodes emitting in the NIR was used to monitor hydrogen chloride (HCl) and water vapour (H_2O) at sub-ppm level for process control in the manufacturing of the novel low-water-peak fibres used in optical telecommunications. Spectral attenuation of a typical standard optical fibre and a low-water-peak fibre is presented in Figure 4.1. The different spectral bands defined for optical telecommunications are also displayed on this figure. This new type of fibres, also called metro fibres or zero-water-peak fibres (ZWPFs), is designed to enable optical transmission in the E-band (1360-1460 nm), so that this window can be opened for implementing cost-effective coarse wavelength division multiplexing (CWDM) technology for current or future network applications [2]. In addition, a lower attenuation in the S-band (1460-1530 nm) makes optical amplification by Raman effect possible instead of the classical use of fibre lasers, the pump being spectrally positioned in the E-band.

The presence of a strong OH^- absorption peak centred at 1383 nm in

standard silica optical fibres is mainly due to moisture contamination that occurs during the manufacturing process of the fibre preform, usually realised in Europe using modified chemical vapour deposition (MCVD). In this process, various gaseous chlorides (SiCl_4 , GeCl_4 , POCl_3) are diluted in a carrier gas that flows through a rotating fused silica tube. The carrier gas mainly contains oxygen (O_2), together with helium (He) at a concentration of a few tens of percent in order to homogenise the gas temperature and therefore to improve the deposition rate of GeO_2 and SiO_2 on the inner wall of the silica tube. Silicon tetrachloride (SiCl_4) and germanium tetrachloride (GeCl_4) are used to create the step index between the core and the inner cladding of the fibre. Phosphoric chloride (POCl_3) is used in the cladding in order to lower the vitrification temperature to avoid mechanical deformation of the tube. The typical gaseous chemical reactions occurring between the chlorides and oxygen during the manufacturing of the preform are the following [3]:



When water contaminations diffuse in the gas mixture, HCl is produced as a result of the strong reactivity between water and chloride compounds:



The measurement of the HCl concentration in the process gas is therefore an excellent indicator of the quantity of water contamination present in the gas mixture. In addition, the residual level of water vapour is monitored in order to quantify the contribution of H_2O in the process. Finally, methane is also an hydrogenated compound that may be an indicator of the gas purity used in the process.

The main source of contamination generally occurs during the replacement of an empty bubbler containing the chlorides. Unfortunately, this change has to be made manually for the POCl_3 container and requires the opening of the gas line, resulting in water ingress into the line. The purge time after the container's exchange is a critical parameter, since it directly influences the production of new preforms by placing the facility in a stand-by situation. The developed PA sensor is therefore used as a diagnostic instrument to monitor the quality of the carrier gas after the replacement of a bubbler.

Calibration of the sensor performed in the laboratory is presented in the next section and *in-situ* measurements are described in subsection 4.5.2.

4.3 Laboratory performances

This section aims at presenting the different selected lasers used in the applications described in the preceding section. Their characteristics are described and discussed in the first subsection. Additionally, the sensor response to various gases and the detection limits obtained for each case are described in details. Finally, the effect of the buffer gas on the photoacoustic signal is explained in subsection 4.3.3.

4.3.1 Laser selection and characteristics

Trace gas monitoring requires extreme performances in terms of sensitivity and selectivity. High sensitivities are necessary to reach detection levels in the part-per-million (ppm) or part-per-billion (ppb) range. Since photoacoustic spectroscopy (PAS) is proportional to the laser power, high laser power is needed to reach these levels of sensitivity. Selectivity makes the detection of one species among many others possible, thus requiring narrow laser linewidths. Various laser sources applied to spectroscopy have been reported in literature. They all present advantages and drawbacks:

- Gas lasers (CO, CO₂) present the main advantage of their high power (several Watts) and make thus possible to reach extreme sensitivities in the ppb level. Unfortunately these lasers are very cumbersome and emit only at discrete frequencies. For instance the CO₂ laser emits lines spaced by 2 cm^{-1} in the $9\text{-}11\ \mu\text{m}$, whereas the spacing of the emission lines of a CO laser is 4 cm^{-1} between 5 and $7\ \mu\text{m}$ [4]. The detection of a particular species is therefore only possible if the absorption line accidentally coincides with an emission line of the laser. Finally, the lifetime of CO₂ lasers is limited due to deterioration of the gas discharge.
- Optical parametric oscillators (OPO) present several advantages in term of power (several hundreds of milliwatts [5]) and tuneability ($0.5\text{-}12\ \mu\text{m}$). The improved quality of nonlinear optical media and the availability of high performance pump lasers have increased the use of OPOs. Extreme sensitivities in the ppb level for CO₂ detection [6] and sub-ppb for ethane [7] were achieved using this kind of sources in conjunction with PA spectroscopy. The main drawback of OPOs is the complexity of the system which rather limits off-laboratory use and make them expensive sources. In addition, the rather broad linewidth (0.25 cm^{-1}) [8] limits the selectivity of the system for sub-ppm detections.
- Quantum cascade lasers (QCL) are recently developed semi-conductor lasers emitting in the middle infrared (MIR) region. These lasers are based on intersubband transitions [9] which is a totally different principle than classical laser diodes based on interband transitions. This offers a great flexibility for designing the emission frequency that must be a fraction of the band gap. Accordingly, these QCLs can be operated at an emission wavelength within the $3\text{-}25\ \mu\text{m}$ range using mature long band gap InP or GaAs technology and therefore virtually spanning the entire MIR spectrum [10]. Additionally, they present good spectral properties, since distributed feedback (DFB) structures enable single frequency emission and mode-hop free operation over a continuous range of a few inverse centimetres. Power of several tens of milliwatts in continuous wave operation at room temperature [11] has been demonstrated. Unfortunately, these devices are not available yet for spectroscopy and must be still operated in continuous mode at low temperature (liquid nitrogen or thermoelectric cooling) or in pulsed mode at ambient temperature. Finally, their use is complex (high current operation requiring a specific electronic supply) and these devices are expensive which hardly satisfies market needs except in some particular applications.

- Tuneable semiconductor laser sources emitting in the IR region are based on different semiconductor materials like lead salt (PbS, PbSe, PbTe) in the 4-30 μm range or antimonide (GaInAsSb, GaAlAsSb, GaSb) in the 2-3 μm range. These lasers are tuneable over a few inverse centimetres (subject to mode hopping) and provide power in the range of 0.1 mW for lead salt lasers and of several tens of milliwatts for antimonide sources [12]. The main disadvantage of these sources (except GaSb) is their operation at low temperature (cryogenic or liquid nitrogen temperature) which requires cumbersome and expensive equipment, thus widely incompatible with cost-effective and *in-situ* monitoring.

In addition to these sources emitting principally in the MIR, semiconductor DFB lasers emitting in the near infrared (NIR) (1-2 μm) region developed for optical telecommunication systems present excellent properties for photoacoustic spectroscopy. Unfortunately absorption in the NIR is one or several orders of magnitude weaker than in the MIR, since fundamental bands occur in the MIR whereas overtones are located in the NIR [13]. However, line intensities located in the NIR combined with the excellent properties of laser diodes and with a carefully PA system design, make sensitivities in the ppm down to the ppb level achievable. The principal properties of these laser diodes are their excellent spectral characteristics (single-mode emission), their tuneability of a few nanometres and their modulation capabilities through the injection current (intensity or wavelength modulation).

The spectral properties of the laser are essential for spectroscopy in order to minimise the influence of interference with other species in the spectral vicinity of the interrogated absorption line. Single-mode emission is thus required to fulfil this condition. Single-mode emission can be obtained by various techniques, that can be divided in three categories: injection locking [14], cavities coupling and selective wavelength reflection. The last category is the most widely used in optical telecommunications (1.3-1.55 μm) and is based on distributed feedback structures¹. The side-mode suppression ratio (SMSR) is usually better than 30 dB for this kind of lasers. The emission line of the laser can be continuously tuned by changing its operating temperature or its injection current. This important property enables to analyse an absorption feature by scanning the laser emission line. However, in order to obtain the correct absorption line profile, the emission linewidth must be much narrower than the absorption linewidth. If this is not the case, the measured profile $g_{meas}(\nu)$ does not exactly represent the absorption line $g_{line}(\nu)$, but rather the convolution with the emission line $g_{laser}(\nu)$.

$$g_{meas}(\nu) = \int_0^{\infty} g_{line}(\nu') g_{laser}(\nu - \nu') d\nu' \quad (4.7)$$

The absorption linewidth is in the order of a few GHz (see subsection 2.2.2) at atmospheric pressure, whereas the laser linewidth is about a few MHz. The condition $\Delta\nu_{laser} \ll \Delta\nu_{line}$ is thus generally always satisfied. A measurement of the linewidth of a typical laser diode emitting in the NIR was performed

¹Laser diodes based on this technique also cover particular wavelengths developed for spectroscopic applications, such as 760 nm for oxygen, 1651 nm for methane, 1742 nm for hydrogen chloride and 2004 nm for carbon dioxide monitoring.

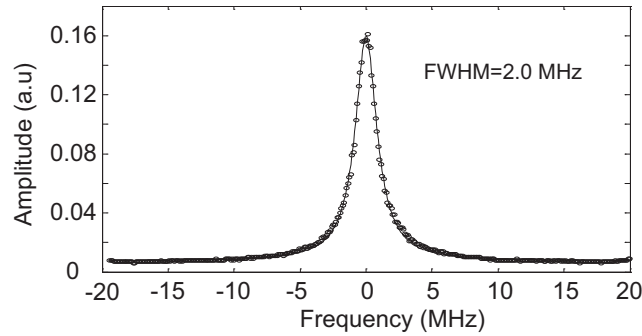


Figure 4.2: Linewidth measurement of a laser emitting at 1532 nm. The linewidth is obtained by the delayed self-heterodyne technique which gives twice the real laser linewidth at half-maximum (autocorrelation spectrum) [15]. The resulting laser linewidth is thus equal to 1.0 MHz (FWHM).

using the delayed self-heterodyne method [15]. Results for a laser diode emitting around 1532 nm is presented in Figure 4.2. A Lorentzian fit applied to the experimental data results in an autocorrelation spectrum of 2.0 MHz linewidth (FWHM) corresponding to twice the laser linewidth. The resulting 1.0 MHz linewidth (FWHM) demonstrates the validity of the above condition.

Another important property of laser diodes is their wavelength tuneability. It enables the possibility to analyse an absorption line profile by scanning the laser emission line or to precisely centre it on the maximum. The laser can be continuously tuned without mode hops by changing the temperature (coarse adjustment) or the injection current (fine tuning). A tuneability of a few nanometres is possible, thus enabling to reach several absorption lines of the same species, or even different species located in the same spectral range.

The selection of the laser diodes has been made in conjunction with the species that had to be investigated in the life science and in the optical fibre manufacturing process applications. Preliminary tests were performed with methane, since this gas has to be monitored for the optical fibre manufacturing application and is, in addition, easy to handle. For instance, CH_4 is non-corrosive and is not a polar molecule that requires any particular cell coating. A strong CH_4 absorption line is located at 1650.96 nm corresponding to the R4 multiplet in the $2\nu_3$ band. Hence, a DFB laser diode operated in this spectral region was selected.

An example of the covered spectral range around 1651 nm is presented in Figure 4.3. The spectral range is 1648-1652 nm when the laser temperature was tuned from 278 K to 313 K. It results in a temperature-tuning coefficient of -12.6 GHz/K and a current-tuning coefficient of -0.81 GHz/mA. The characteristics of this laser are summarised in Table 4.1.

A photoacoustic spectrum of CH_4 has been measured by tuning the laser temperature and by recording the PA signal. This spectrum is shown on Figure 4.4 and is compared with the absorption spectrum calculated from the HITRAN database [16]. A good qualitative agreement between the two spectra is obtained. However, the spectral resolution of the sensor is weaker than the calculated lines, which results in an incomplete resolution of some of the absorption lines. This is due to a large current modulation depth (from

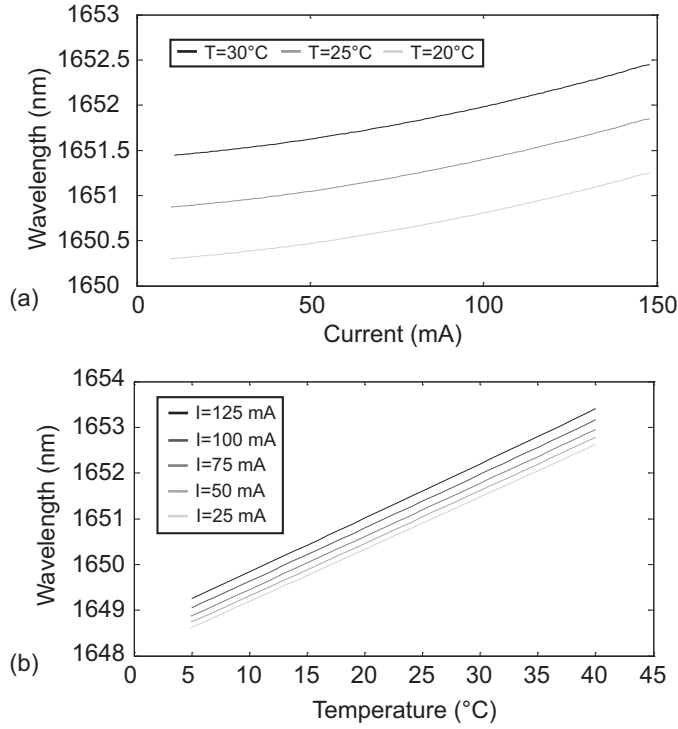


Figure 4.3: Dependence of the laser wavelength as a function of (a) the injection current and (b) the temperature at 1650 nm. The current-tuning coefficient is $0.0074 \text{ nm/mA} = -0.814 \text{ GHz/mA}$ and the temperature-tuning coefficient is $0.114 \text{ nm/K} = -12.55 \text{ GHz/K}$.

Gas	CH ₄	CO ₂	H ₂ O	NH ₃	HCl
Wavelength (nm)	1651.0	1572.3	1368.6	1531.7	1737.9
Spectral range (nm)	1648-1652	1570-1574	1368-1371	1530-1533	1735-1739
Temp. tuning (GHz/K)	-12.6	-13.4	-15.8	-13.9	-12.5
Current tuning (GHz/mA)	-0.81	-0.69	-0.72	-0.85	-0.86
T _{set} (K)	300.1	292.7	286.2	294.1	291.9
I _{set} (mA)	120.5	115.4	117.34	125.1	127.4
Average power (mW)	23	23	22	24	16

Table 4.1: Characteristics of the lasers used for trace gas monitoring. T_{set} and I_{set} are the temperature and current operating point of the corresponding laser, respectively. The average power is obtained for the operating conditions at T_{set} and I_{set}.

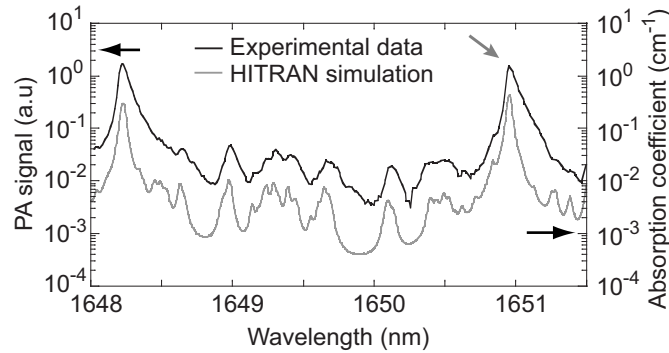


Figure 4.4: PA spectrum of CH_4 . The *Black curve* shows the experimental data and the *grey line* represents the corresponding absorption spectrum calculated from the HITRAN database [16]. The *grey arrow* shows the selected line for CH_4 detection.

threshold to the maximum current rating, corresponding to ± 70 mA), which induces a temperature variation of the laser during the current pulse and thus changes the instantaneous wavelength (chirp). This effect results in a broadening of the apparent linewidth of the laser. Moreover, the temperature variation is not necessary symmetric with the current pulse, which results in a slight asymmetry in the laser linewidth.

The life science application requires the measurement of carbon dioxide, water vapour and ammonia with corresponding wavelength of 1572 nm, 1369 nm and 1532 nm, respectively. The spectra obtained with these three lasers and the PA sensor are presented in Figure 4.5, Figure 4.6 and Figure 4.7. For CO_2 , a good qualitative agreement with the HITRAN database is obtained for the position and the relative intensities of the lines. However, a slight

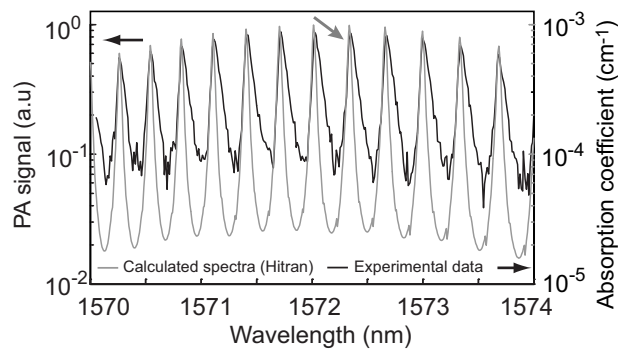


Figure 4.5: PA spectrum of CO_2 . The *Black curve* shows the experimental data and the *grey line* represents the corresponding absorption spectrum calculated from the HITRAN database. The *grey arrow* shows the selected line for CO_2 detection.

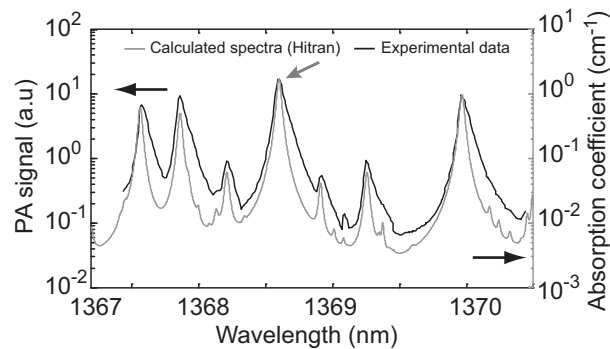


Figure 4.6: PA spectrum of H_2O . The *Black curve* shows the experimental data and the *grey line* represents the corresponding absorption spectrum calculated from the HITRAN database. The *grey arrow* shows the selected line for H_2O detection.

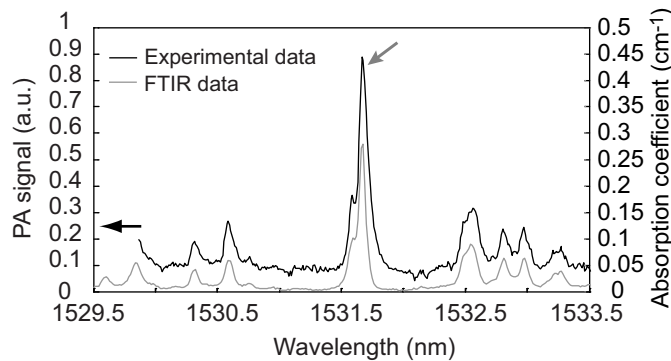


Figure 4.7: PA spectrum of NH_3 . The *Black curve* shows the experimental data and the *grey line* represents the corresponding absorption spectrum measured by FTIR spectroscopy [17]. The *grey arrow* shows the selected line for NH_3 detection.

asymmetry is present on the measured spectrum probably due to the intensity modulation of the laser (see the explanation above for the laser used for the CH_4 spectrum). In addition, since the PA signal is quite weak for the CO_2 concentration used in this measurement (5000 ppm), the noise level is rapidly reached away from the centre of the absorption lines. For water vapour, the two different spectra present a good matching in line position and intensities. Finally, ammonia was not compared with a calculated spectrum, since no data exists in this spectral range. However, it could be compared with a measured spectrum obtained by FTIR spectroscopy [17]. The characteristics of each laser used for the mentioned species are presented in Table 4.1.

Finally, as far as the application of optical fibre manufacturing process is concerned, hydrogen chloride was monitored at 1738 nm, in addition to water vapour. The recorded spectrum is presented in Figure 4.8 and the laser characteristics are summarised in Table 4.1.

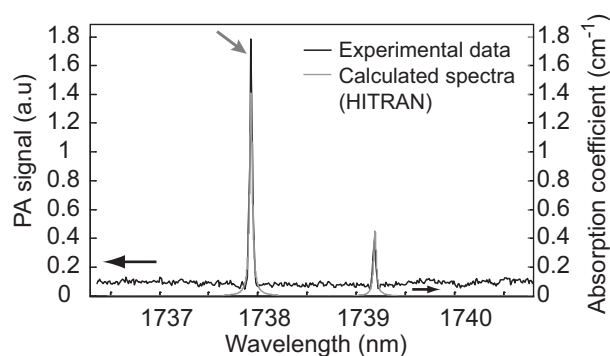


Figure 4.8: PA spectrum of HCl. The *Black curve* shows the experimental data and the *grey line* represents the corresponding absorption spectrum calculated from the HITRAN database. The *grey arrow* shows the selected line for HCl detection.

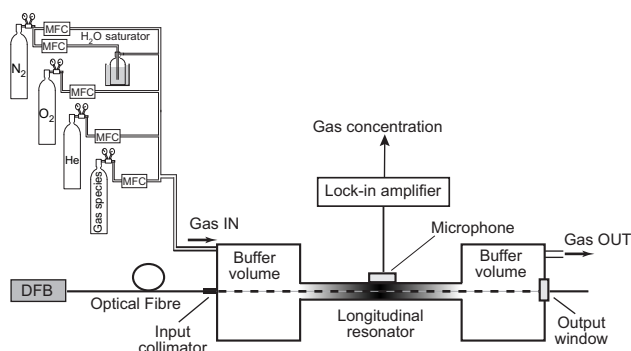


Figure 4.9: Scheme of the experimental set-up including the PA cell and the gas handling system. Mass-flow controllers (MFC) are used to prepare dilutions for calibration purpose.

4.3.2 Calibration and detection limits

In order to investigate the detection limits achievable with the developed system, different certified cylinders containing the gases of interest were used to perform the calibration (see Figure 4.9). Four mass-flow controllers (two 100 sccm, one 500 sccm and one 1000 sccm) and cylinders of pure N₂, O₂ and He were used to prepare precise dilutions. The calibration curves were usually obtained with a flow rate of 1000 sccm and a time constant of 1 s set on the lock-in amplifier. The modulation of the lasers was performed through the injection current (wavelength modulation) and the amplitude was optimised to obtain the largest PA signal (see section 3.4).

A first calibration was carried out using CH₄ diluted in nitrogen. Methane was supplied in a concentration of 5000 ppm buffered in nitrogen and an additional nitrogen cylinder (purity of 99.9999%) was used to extend the dilutions. The response of the sensor to various concentrations of methane in N₂ is shown in Figure 4.10. The sensor response to different methane concentration demonstrates an excellent linearity over four orders of magnitude, starting from 5000 ppm down to 0.5 ppm. The detection limit is defined by considering a signal-to-noise ratio (*SNR*) of 3, where the noise level was recorded during a period

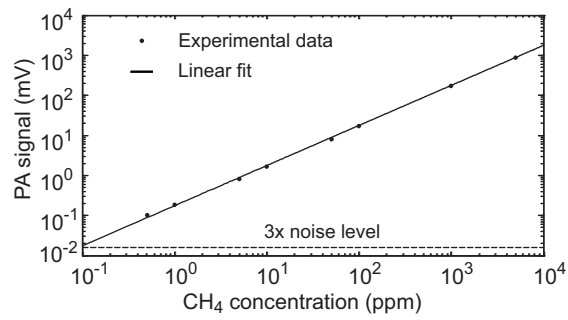


Figure 4.10: Response of the sensor to different CH₄ concentrations diluted in N₂. The detection limit defined for a $SNR = 3$ is 90 ppb.

of 15 minutes and using an integration time fixed on the lock-in of 10 s. This resulted in a average noise of $5.3 \pm 2.3 \mu V^2$, corresponding to a noise equivalent CH₄ concentration of 30 ppb. The detection limit for CH₄ diluted in N₂ is extrapolated from the crossing point of the linear fit and three times the noise level, corresponding to 90 ppb for an average laser power of 23 mW.

²The error corresponds to one standard deviation over the average value.

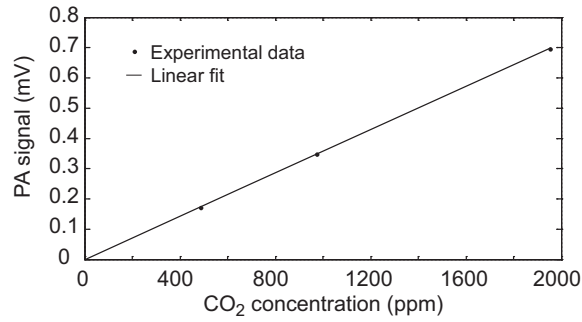


Figure 4.11: Response of the sensor to different CO_2 concentrations diluted in air containing 50% of relative humidity at a temperature of 23°C . The detection limit defined for a $SNR = 3$ is 38 ppm.

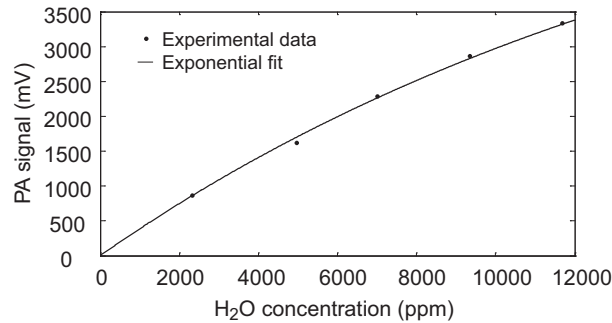


Figure 4.12: Response of the sensor to different H_2O concentrations for the range of ambient humidity levels in air.

4.3.2.1 Gases calibration for the life science application

Calibration curves for CO_2 , H_2O and NH_3 were obtained in a buffer gas similar to the one encountered in the animal house (ambient air at atmospheric pressure). For CO_2 calibration at 1572.3 nm (corresponding to the R18 line of the $(2\ 2^0\ 1)$ band), the buffer gas was composed of 80% N_2 , 20% O_2 and 50% of relative humidity at 23°C and is presented in Figure 4.11. A detection limit of 38 ppm was achieved for an average laser power of 23 mW, obtained using the same method than described above for CH_4 ($SNR = 3$).

Calibration for water vapour was performed at 1368.6 nm , corresponding to the transition $(0\ 0\ 0)_{2,2} \rightarrow (1\ 0\ 1)_{3,3}$, in two different conditions. The first calibration was obtained using dilutions around the ambient water vapour concentration in a buffer gas composed of 80% N_2 and 20% O_2 , since it was the expected range concentration encountered in the animal house (see Figure 4.12). The Beer-Lambert law is poorly approximated by a linear function in this case, since high water vapour concentrations in combination with a high absorption coefficient ($\alpha = 1.72\text{ cm}^{-1}$) are experienced, and an exponential fit is thus required. However, around $55\% \pm 10\%$ of relative humidity, a linear response of the sensor is nevertheless obtained without adding any significant error, and was used for the calibration in the animal house. A detection limit in these conditions is difficult to extrapolate and a response at lower water vapour concentration is required. In order to determine the detection limit for

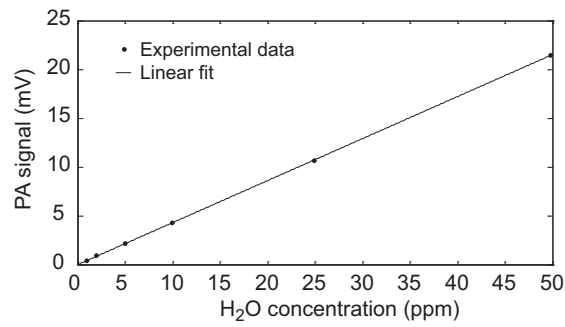


Figure 4.13: Response of the sensor to different H₂O concentrations diluted in nitrogen. The detection limit ($SNR = 3$) is equal to 26 ppb.

water vapour, a certified cylinder of 50 ppm H₂O diluted in nitrogen was used to perform a calibration curve. A crucial issue to achieve this measurement is to secure an air-tight cell sealing. Since a high water vapour concentration is presented in ambient air, minute leaks lead to water ingress into the cell. Additionally, adsorption-desorption processes need to be taken into account [18]. Unfortunately, a residual water concentration of about 5 ppm was still present in the PA cell and in the gas tubes. The contribution of this residual level occurs like an offset on the linear response and was subtracted to the final calibration curve (see Figure 4.13) and a detection limit achieved in these conditions was found to be 26 ppb for an average laser power of 22 mW.

The response of the sensor to ammonia concentrations diluted in nitrogen at 1531.7 nm is presented in Figure 4.14. Stable concentration levels of ammonia are difficult to obtain due to the polarity of the molecule. However, adsorption-desorption processes may be reduced by appropriate cell coating (teflon coating), which was not applied on the prototype cell made of a single tube resonator. A detection limit achieved in these conditions was found to be 0.2 ppm for an average laser power of 24 mW.

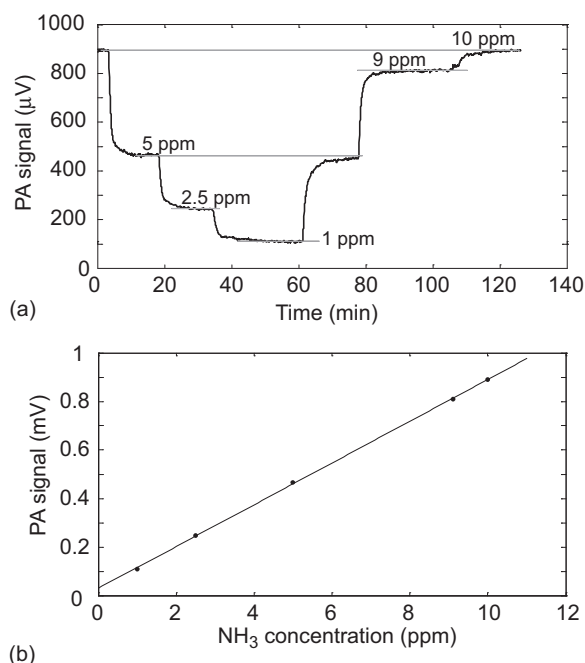


Figure 4.14: (a) Response of the sensor to different NH₃ concentrations diluted in nitrogen. (b) NH₃ calibration curve. A detection limit of 0.2 ppm is obtained ($SNR = 3$).

4.3.2.2 Gases calibration for the optical fibre manufacturing application

Calibration of the PA sensor was performed under similar conditions to those experienced on-site. Different gas mixtures and various concentrations of hydrogenated compounds were obtained from certified cylinders of HCl, H₂O, He and O₂ using mass-flow controllers. The influence of the chloride compounds (SiCl₄, GeCl₄ and POCl₃) was not considered in the calibration phase, as these chemical products are very corrosive, difficult to handle and require a neutralisation process before being rejected into the environment. However, since the concentration of POCl₃ and GeCl₄ did not exceed 3% and SiCl₄ 10.5% in the measured carrier gas (see Table 4.4 in subsection 4.5.1), their influence on the spectroscopic parameters (foreign-gas broadening coefficient of the considered absorption line) is expected to be minor. The effect of the chlorides on the resonance frequency was taken into account, since the gas mixture in the factory was adapted to obtain the same resonance frequency as used for the calibration.

A typical calibration curve for HCl was obtained by diluting a certified mixture of 50 ppm HCl buffered in He, with pure O₂ and He (60% O₂ and 40% He) (Figure 4.15a). The resonance frequency and the quality factor obtained in these conditions were respectively 1137 Hz and 20. Calibration for water vapour at low mixing ratio is delicate owing to the polarity of the molecule and its resulting adsorption-desorption processes problems already mentioned in the preceding section. Therefore, higher H₂O concentrations (up to a few ppm) in combination with a flow of 1000 sccm have been used to determine the calibration slope and to extrapolate the detection limit (Figure

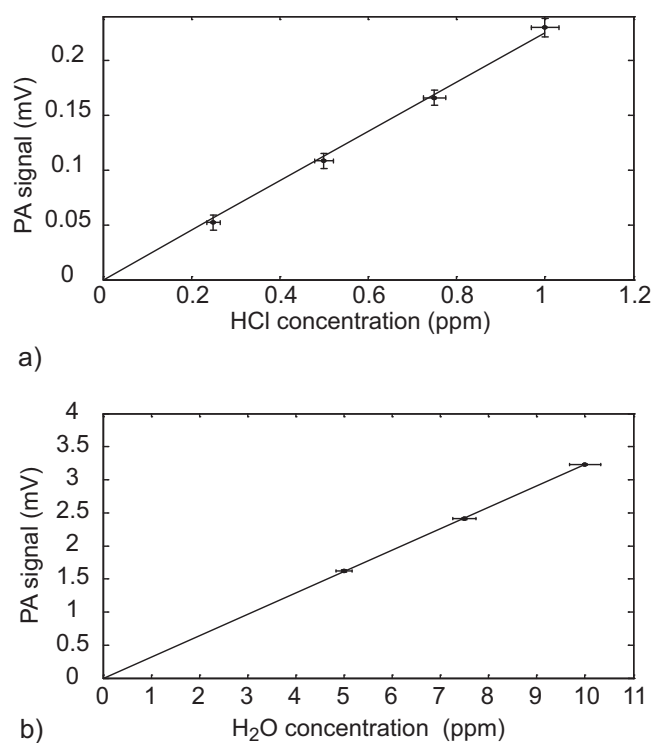


Figure 4.15: Calibration curves for (a) HCl and (b) H₂O in a 60% O₂-40% He mixture. *Error bars* shown on the plot correspond to the uncertainty on HCl and H₂O concentrations generated with the MFCs (horizontal axis) and to the standard deviation of the PA signal recorded in a 5-min period (vertical axis) The integration time was 1 s for HCl and 10 s for H₂O. *Dots* are the measured datapoints and the *line* is the result of a linear fit.

4.15b). The range of H₂O concentrations considered in the calibration (5-10 ppm) is of the same order of magnitude than experienced on-site after the change of the POCl₃ bubbler (0.4-1.8 ppm). Water vapour monitored in GeCl₄ resulted in a lower level down to the 100 ppb range (see section 4.5.2 dedicated to *in-situ* measurements). Results obtained for methane monitoring using the same set-up have shown an excellent linearity over several orders of magnitude (5000-0.5 ppm) and down to a value of a few detection limits, so that it is considered with confidence that the linearity is maintained also for H₂O down to the detection limit. H₂O calibration was performed by diluting a certified mixture of 50 ppm H₂O buffered in nitrogen with O₂ and He, so that a residual of several percents of N₂ was still present in the He-O₂ mixture. A detection limit (defined for a signal-to-noise ratio $SNR = 3$ and with 10 s integration time) of 60 ppb for HCl and 40 ppb for H₂O resulted from these calibration curves.

4.3.3 Influence of the buffer gas

The calibrations performed in the preceding subsection have shown the dependency of the PA signal as a function of the analysed species diluted in various buffer gases. The PA signal does not only depend on the gas to be measured but also on the diluting gas. The influence of the buffer gas on the cell constant is summarised as follow:

- The resonance frequency is directly proportional to the sound velocity, which depends in particular on the molar mass M of the gas:

$$c_s = \sqrt{\frac{\gamma RT}{M}} \quad (4.8)$$

where $R = 8.3144$ J/(mol K) is the constant of perfect gases, T is the temperature and γ is the ratio of the specific heat at constant pressure to the specific heat at constant volume. Resonance frequencies in light molecules gases are much higher than in heavy molecules gases. The inverse behaviour is obtained for the PA signal due to the $1/f$ dependence of the cell constant (see equation (3.3)).

- Some physical constants are strongly different between two buffer gases. These parameters occur in the expression of the quality factor (density ρ_0 , thermal conductivity K , molar mass M , specific heat C_p , viscosity η), and directly in the cell constant (parameter γ). The values of these parameters are listed in Table 3.1 for different gases.
- The buffer gas may also influence the width of the analysed absorption feature, and thus the value of the absorption coefficient on the line centre, as the foreign pressure broadening coefficient can fairly vary between two buffer gases. For example, pressure broadening coefficients of the methane R3 quadruplet in the $2\nu_3$ band measured in the $1.65 \mu\text{m}$ range in different diluting gases have shown a variation as high as 50% between air and helium [19].

In addition to the above mentioned effects, the buffer gas may also have a dramatic influence on the generation of the PA signal in some particular conditions (specific gas mixtures) due to slow molecular relaxation effects. This point is not considered here, but will be addressed in detail in chapter 5.

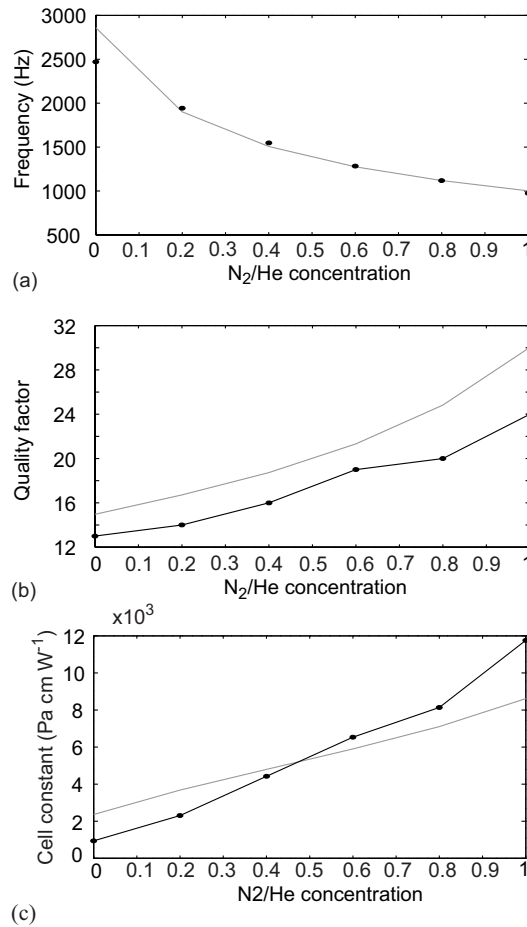


Figure 4.16: Variation of (a) the resonance frequency, (b) the quality factor and (c) the cell constant as a function of the gas composition. *Circles* are experimental data and *grey lines* are theoretical values calculated from (2.75), (2.99) and (3.3), respectively.

The effect of the buffer gas has also been investigated experimentally in the case of CH₄ using the set-up described in the previous section. Gas mixtures made of 100 ppm of CH₄ diluted in different buffer gases have been prepared with mass flow controllers. The first longitudinal resonance of the PA cell has been measured in each diluting gas and a Lorentzian distribution has been fitted on the experimental points through the PA energy³ in order to extract the resonance frequency, the quality factor and the cell constant. Buffer gases made of various compositions of N₂ and He have been used. Figure 4.16 shows the variation of the experimental parameters as a function of the relative concentration of N₂ and He, which is compared with theoretical values.

These results show that the experimental resonance frequency matches very well the calculated value, excepted in the case of pure helium, where the measurements were noisier than in other conditions. This is principally due to the higher frequency (2500 Hz), which directly influences the PA signal ($1/f$ dependence) and reduces the signal accordingly.

³The Lorentzian distribution corresponds to the energy of the PA signal, which is proportional to the square of the PA signal (see equation (2.84)).

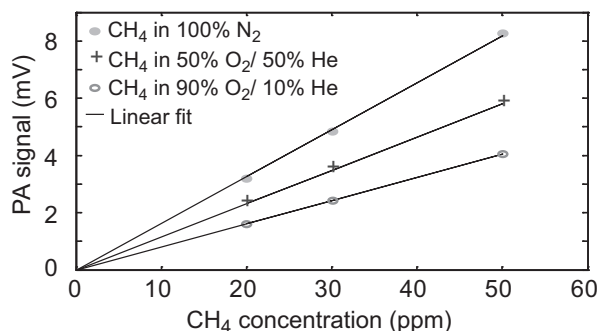


Figure 4.17: Calibration curves for CH₄ in 100% N₂, 50% O₂-50% He and 90% O₂-10%. The PA signal is 30% lower in the 50% O₂-50% He mixture than in pure N₂ and twice weaker in the 90% O₂ -10% He mixture. *Circles* and *crosses* are experimental points and *lines* are the results of linear fits.

The variation of the quality factor shows also a clear tendency, which is in good agreement with the calculation. However, the experimental values are lower (20% for the maximum variation) than the calculated values, probably due to additional losses caused by an imperfect inner surface of the resonator.

The experimental cell constant presents a different value than the predicted values obtained from calculations. The strong difference between N₂ and He results mainly from the high difference in the resonance frequencies obtained in pure N₂ or He (respectively around 1 kHz and 2.5 kHz), but also from the strongly different ($\gamma-1$) parameter occurring in the expression of the PA signal. Additional phenomena may still increase the different behaviour observed between N₂ and He. The lineshape of the measured absorption feature may fairly differ between these two buffer gases, as previously discussed. A possible frequency-dependent response of the microphone may also contribute to this effect, as the resonance frequency is strongly different between N₂ and He. These phenomena may affect the experimental value of the cell constant, but have not been considered in the calculation.

Finally, three calibration curves were performed with CH₄ diluted in 100% N₂, 50% O₂-50% He and 90% O₂-10% He using a constant flow rate of 500 sccm. Methane was provided in a certified gas mixture of 5000 ppm in N₂, which means that a residual of 1% or less of nitrogen was still present in the O₂-He mixtures for CH₄ concentration below 50 ppm. The response of the sensor to methane concentration is presented in Figure 4.17 showing the effect of the buffer gas on the PA signal.

The PA signal is 30% lower in the 50% O₂-50% He mixture than in pure N₂. This is due to the higher resonance frequency (around 1300 Hz) induced by the faster acoustic velocity in He and some other physico-thermal constants of the gas. In the 90% O₂ -10% He mixture, the PA signal is reduced by a factor two compared to pure N₂. The main reason for this is due to molecular relaxation process of methane in presence of large amount of oxygen (see Chapter 5).

All these results confirm that the buffer gas composition is a significant parameter in trace gas monitoring by PAS and has to be carefully investigated for the sensor calibration.

Molecule	λ (nm)	Buffer gas	α^a (cm ⁻¹)	P_0 (mW)	D (ppm)	$\alpha \cdot P_0 \cdot D$ (cm ⁻¹ mW·ppm)
CH ₄	1651.0	100% N ₂	0.44	23	0.09	0.91
CH ₄	1651.0	50% O ₂ -50% He	0.44	23	0.12	1.21
CH ₄	1651.0	90% O ₂ -10% He	0.44	23	0.2	2.02
CO ₂	1572.3	80% N ₂ -20% O ₂	0.002	23	44	2.02
CO ₂	1572.3	80% N ₂ -20% O ₂ + 50% RH	0.002	23	38	1.75
H ₂ O	1368.6	100% N ₂	1.72	22	0.026	0.98
H ₂ O	1368.6	60% O ₂ -40% He	1.72	22	0.040	1.51
NH ₃	1531.7	100% N ₂	0.28	24	0.2	1.34
HCl	1737.9	60% O ₂ -40% He	1.4	16	0.06	1.34

^a α is calculated at 1 atm for air broadening. The effect of the buffer gas on the absorption coefficient is not taken into account.

Table 4.2: Summary of the detection limits obtained for different gases in various buffer gases. λ is the wavelength of the laser, α is the absorption coefficient at line centre, P_0 is the incident laser power and D is the detection limit defined for a $SNR = 3$.

4.3.4 Conclusion

The summary of the different gas species investigated in various buffer gases is presented in Table 4.2. The last column represents the product of the absorption coefficient α by the incident laser power P_0 and the detection limit D . This product is ideally constant for a given PA cell operated in identical measurement conditions. However, as discussed in subsection 4.3.3, the buffer gas strongly influences the PA signal and modifies the detection limit. Moreover, two different PA cells (one with a single resonator and one with three resonators) and different microphones were used to perform these measurements, which makes the comparison of the product $\alpha P_0 D$ difficult. In addition to the difference due to the buffer gas, molecular relaxation effects play an important role on the PA signal (see chapter 5 on page 109).

Finally, sub-ppm detection limits were achieved for most of the species (except CO₂) in the various buffer gases required by the applications, frequently below 100 ppb.

4.4 CO₂, NH₃ and H₂O in-situ monitoring: application to life science

4.4.1 Sensor architecture

Three fibre-coupled DFB laser diodes emitting in the optical telecommunication wavelength range, respectively at 1369 nm for H₂O detection, at 1572 nm for CO₂ and at 1532 nm for NH₃ were chosen for this particular application. The characteristics of the different lasers were presented in Table 4.1. The emissions from the lasers used for CO₂ and H₂O are combined using a fibre coupler that is terminated by a collimator directly mounted on the outer flange of the buffer volume of the PA cell. The average optical power at the laser operating point is 23 mW for the 1572 nm laser (CO₂ detection) and 21 mW for the 1369 nm laser (H₂O), but a very small fraction of this latter power is actually launched into the cell. The reason is the reduced absorption

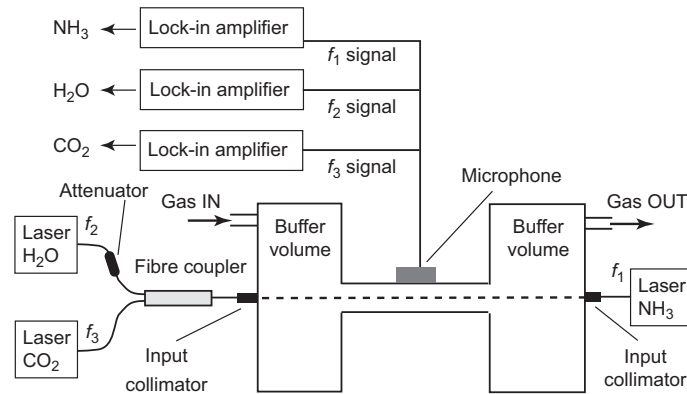


Figure 4.18: Schematic representation of the PA sensor based on three DFB lasers and the PA cell operated in its first longitudinal mode. The lasers are modulated at three different frequencies f_1 , f_2 and f_3 and three lock-in amplifiers extract the corresponding concentration.

of the CO₂ molecules in the spectral range of interest, so that the power from the laser for CO₂ detection must be maximised in the PA cell using a strongly unbalanced (5/95%) directional coupler (see Figure 4.18). The resulting loss of power of the laser for water vapour monitoring does not have any consequence, because a detection limit of 26 ppb is achievable by the sensor using the full laser power (see subsection 4.3.2.1), whereas much higher concentrations (in the percent range) have to be measured in this particular application. An additional optical attenuator was used to further reduce the power of this laser launched into the PA cell in order to obtain a PA signal for water vapour of the same order than for CO₂ and NH₃ to avoid saturation of the lock-in amplifiers.

The fibre from the third laser (NH₃ detection) is also terminated by a collimator that is mounted on the outer flange of the other buffer volume of the PA cell, so that the laser radiation propagates in the opposite direction along the PA cell. This configuration enables to benefit from the entire optical power of this laser (24 mW), thus improving the detection limit of NH₃, which is necessary to detect the low NH₃ concentration expected on-site.

The three laser beams simultaneously propagate along the cell axis in order to efficiently excite the first acoustic longitudinal mode of the resonator. The sound waves generated as a result of molecular absorption are detected using a single electret microphone, located in the centre of the resonator. In order to separate the acoustic signals generated by the different species, the lasers are modulated at three slightly different frequencies, all located in the same resonance peak of the acoustic cavity, as shown in Figure 4.19. The laser for NH₃ detection is modulated at the resonant frequency f_1 in order to benefit from the largest acoustic amplification, where an acoustic quality factor $Q = 28$ is achieved in the resonator. The lasers for H₂O and CO₂ detection are modulated at frequencies $f_2 = f_1 - 5$ Hz and $f_3 = f_1 + 5$ Hz, respectively. With these small differences between the three frequencies, the loss in the acoustic amplification is minor (less than 5%), whereas cross-talk between the corresponding acoustic signals is suppressed through highly selective lock-in detection at frequencies f_1 , f_2 and f_3 , respectively. This

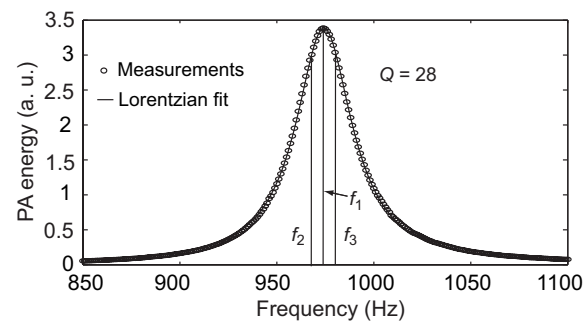


Figure 4.19: Acoustic resonance of the PA cell. *Circles* are experimental points and the *curve* is the result of a Lorentzian fit. The three laser modulation frequencies are represented.

configuration enables the simultaneous and selective measurement of the three gases of interest. Finally, an electronic module controls the laser modulation and processes the data.

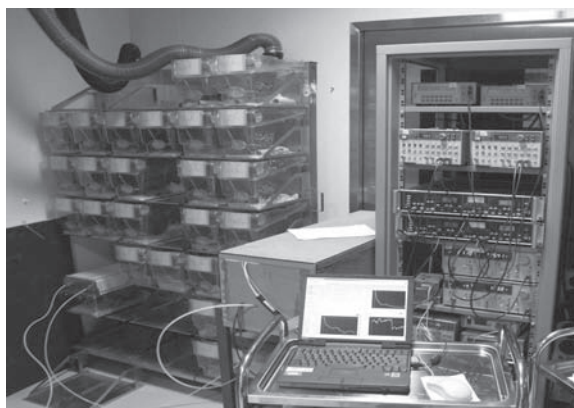


Figure 4.20: Picture of the installation for *in-situ* measurements in the animal house. Air is pumped from the cage into the PA cell and reinjected in the animal cage. The PA cell is hidden by the acoustic surrounding box to ensure low ambient noise.

cage 1	cage 2	cage 3	cage 4	cage 5
6F	2F	3F	1M&2F	6M
cage 6	cage 7	cage 8	cage 9	cage 10
5F	M&F&11P	5M	1F	M&F&7P
cage 11	cage 12	cage 13	cage 14	
M&F&11P	1M&2F	5F	2M	

Table 4.3: Cages description containing mice. M: male, F: female and P: pups.

4.4.2 Experimental results

On-line and real time measurements of ammonia, water vapour and carbon dioxide were performed during a period of two weeks (from day 1 to day 11) in individually ventilated cages housing laboratory mice at the EPFL animal house (see Figure 4.20). Fourteen cages containing a different number of animals ranging from 1 adult to a couple with 11 pups (see details on Table 4.3) have been monitored. For this purpose, air was pumped out from one of the cages into a Teflon tube at a flow rate of 1000 sccm. This flow rate results in a fast response time of the sensor without inducing additional acoustic noise.

The gas passed through the PA cell and the concentration of the three gases was determined. Ammonia concentration was monitored in the different cages on a half-week basis after the bedding cleaning. The average values are shown in Figure 4.21. At Day 7, one cage already exceeds a concentration of 25 ppm, which corresponds to the human threshold limit value for this chemical substance in working environment. After 11 days (date of the next bedding change), a second cage also presented a value over this limit and three others were about to reach it. A high level of ammonia, close to 70 ppm, has been observed in the dirtiest cage. This high level may be dangerous for animals health if it is maintained during several days.

CO₂ and H₂O concentrations monitored continuously during three days in a selected cage are presented in Figure 4.22. CO₂ variations show a 24-hours time period, representing night and day activity. Correlation between water

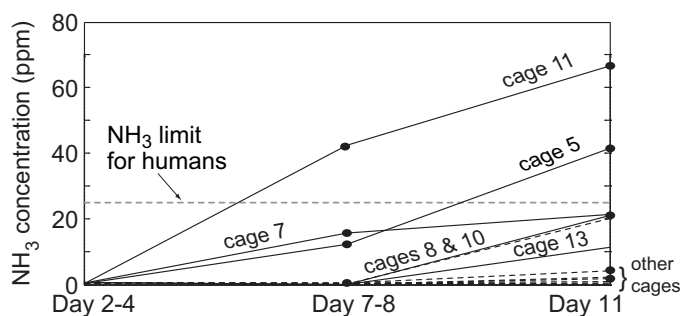


Figure 4.21: Evolution of ammonia concentration from day 2 (after bedding change) to day 11 in different cages.

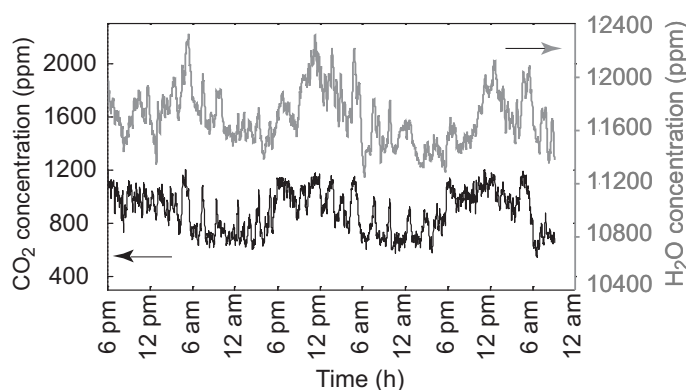


Figure 4.22: Evolution of H₂O and CO₂ levels in a selected cage containing 6 males from day 4 to day 7.

vapour and carbon dioxide cycles are also observed, showing an increase of perspiration of active animals. CO₂ monitoring is also important as it enables the detection of eventual ventilation breakdowns for which an increase of the CO₂ concentration in the cages may be critical for the animals' survival. As an illustration, CO₂ was monitored in cages disconnected from the ventilation (see Figure 4.23). A drastic increase of CO₂ can be immediately observed after the aeration interruption, showing the importance of properly working ventilation. The air renewal flux in the cages has also been measured by injecting a fixed carbon dioxide concentration (5000 ppm) into an empty cage and measuring the CO₂ concentration decay when the injection is stopped (see Figure 4.24). The CO₂ measurement shows an exponentially decaying curve with a time constant of 2 minutes. 95% of CO₂ wash out is obtained after 6 minutes (3 times the decay constant), corresponding to an air flow of 1.63 l/min for a cage of 9.75 litres or 10 cage air renewals per hour.

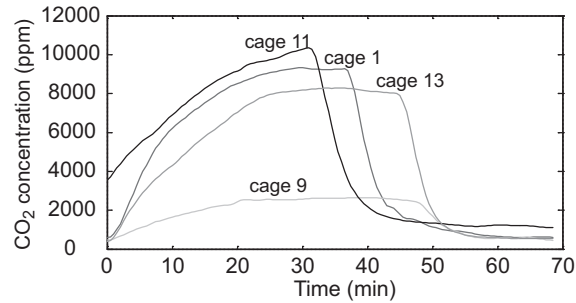


Figure 4.23: CO₂ accumulation in cages disconnected separately from the ventilation. An equilibrium level is reached after 30 to 45 minutes depending on the number of animals.

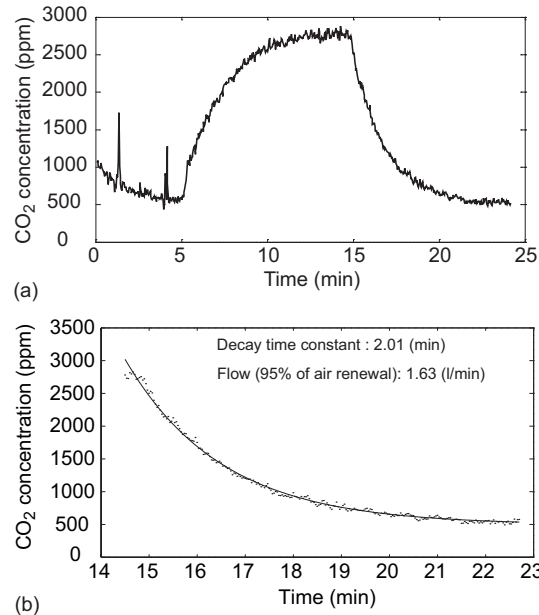


Figure 4.24: Measurement of the ventilation flow of an empty cage. A fixed CO₂ concentration is first injected into the cage. When an equilibrium state is reached, the injection is stopped and the decay of the CO₂ concentration is monitored. The flow is obtained by an exponential fit on the experimental data.

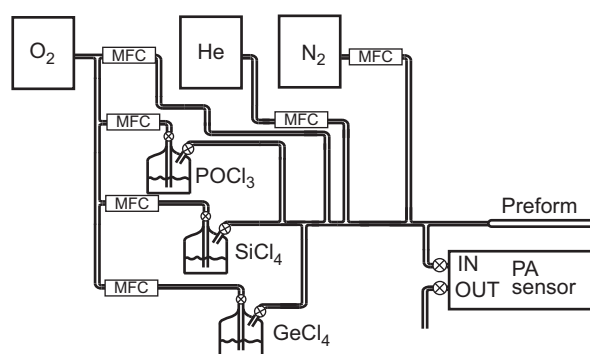


Figure 4.25: Gas distribution system for the preform manufacturing. The PA sensor is inserted in a line parallel to the process line. Mass-flow controllers (MFC) and electro-valves enable dilutions of different gas mixtures.

4.4.3 Conclusion

In-situ application of the sensor has been demonstrated for the monitoring of microclimatic parameters in individually ventilated cages in an animal house which validates the sensor for off-laboratory applications. Continuous measurements have been successfully performed during two weeks and 24 hours a day without any maintenance of the sensor. Simultaneous measurement of NH₃, CO₂ and H₂O has provided a better understanding of the evolution of the bedding conditions in the cages. These results fully demonstrate the suitability of the photoacoustic technique for this application, thanks to its high sensitivity and selectivity and unattended operation. Finally, circadian activity level of animals can also be studied with this technique.

4.5 Multi-hydrogenated compounds monitoring in optical fibre manufacturing process

4.5.1 Experimental details

The PA sensor is based on the 3-resonators cell described in section 3.5.2 (see also Figure 3.13) in combination with semiconductor laser diodes emitting in the near-infrared region. Water vapour was monitored at 1369 nm and HCl at 1738 nm. Methane was finally not monitored, since it was expected that the principal gas pollutant came from water vapour and its transformation into HCl. A gold coating deposited on the inner surface of the cell was used to reduce adsorption-desorption processes. This is an important aspect to achieve accurate measurements of gas traces with a reasonable response time in the case of polar molecules such as HCl and H₂O, which tend to stick on the walls of the cell. Heating of the cell is an alternative technique to reduce this kind of processes [18], which is however difficult to implement in an industrial environment.

In order to monitor HCl and H₂O concentrations in the manufacturing process of the ZWPF, the PA sensor has been inserted in a line parallel to the process line (Figure 4.25). The carrier gas was made of He, O₂ and an additional O₂ flow saturated with either SiCl₄, GeCl₄ or POCl₃. The chloride-saturated gas was generated by bubbling pure O₂ in a container filled with

Chloride	T (°C)	Saturated vapour pressure (mb) [20]	He	O ₂	O ₂ +chloride	Chloride concentration (%)
			(sccm)	(sccm)	(sccm)	
POCl ₃	32	66.5	450	150	400+29	2.79
SiCl ₄	39	534.6	700	200	100+115	10.31
GeCl ₄	39	215.9	500	400	100+28	2.68

Table 4.4: Gas mixtures and chloride concentrations used for HCl and H₂O monitoring.

Chloride	Chloride conc. (%)		H ₂ O conc. (ppm)		HCl conc. (ppm)	
	Meas. gas	Process gas	Meas. gas	Process gas	Meas. gas	Process gas
POCl ₃	2.79	0.088	0.92	0.03	15	0.47
SiCl ₄	10.31	7.85	-	-	2.6	2
GeCl ₄	2.68	2.81	0.095	0.1	0.76	0.8

Table 4.5: Comparison of chlorides, H₂O and HCl concentrations between the buffer gas used for PAS measurements and the process gas used in optical fibre manufacturing.

SiCl₄, GeCl₄ or POCl₃ at fixed temperatures of respectively 39°C, 39°C and 32°C. Measurements were performed in a gas mixture which slightly differed from the carrier gas used in the process (see Table 4.4 and 4.5). The principal reason is that we aimed at quantifying the contribution of each chlorides separately, whereas SiCl₄, GeCl₄ and POCl₃ are mixed together in the process gas. A total flow rate of 1000 sccm has been used in order to secure a fast response time without adding any extra acoustic noise. Electro-valves were used to commute from the preform line to the measurement line, making trace gas monitoring without preform processing possible. The precise gas mixture compositions were chosen in order to have a similar resonance frequency as used in the calibration phase (see subsection 4.3.2.2). The final concentrations and gas mixtures used for HCl and H₂O measurements are summarised in Table 4.4.

Before starting trace gas measurements, the PA cell was continuously purged with nitrogen (N₂) during three days to grant that no impurity was introduced by the sensor. This is particularly important for H₂O due to the sticky nature of this polar molecule [21] and its high natural abundance, since the PA cell has been subject to a H₂O concentration as high as 1%, corresponding to typical humidity content in air.

During the campaign, a continuous N₂ flow of about 1000 sccm passed through the cell when no chloride was flowing through the sensor in order to maintain a clean environment. HCl and H₂O were measured during a 11-day period after the insertion of a new POCl₃ bubbler in order to evaluate the required purge time of the installation. After this time a preform has been manufactured to fulfill the requirements for a low-water-peak fibre. At the end of the campaign, additional measurements were carried out with SiCl₄ and GeCl₄.

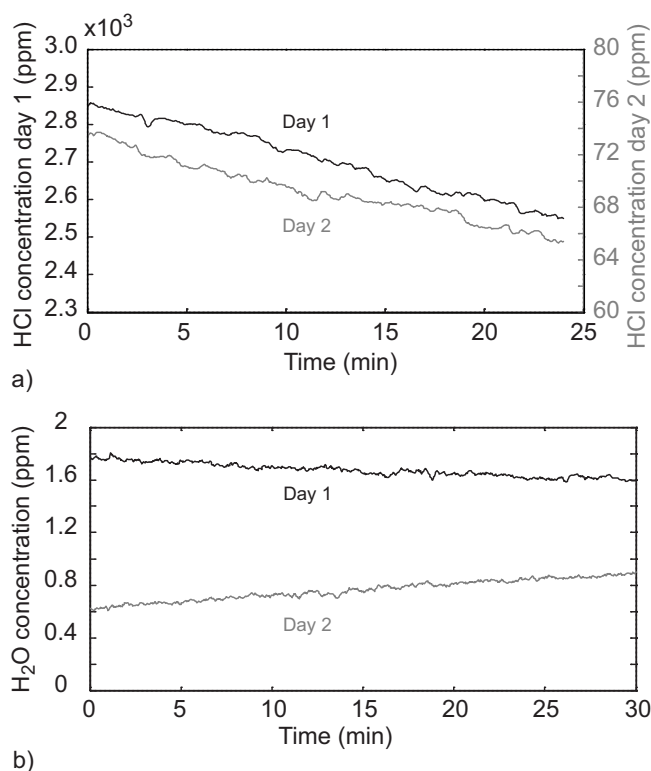


Figure 4.26: Typical concentration measurements over several minutes. (a) HCl and (b) H₂O concentration on day one (*black curve*) and day two (*grey curve*) after the POCl₃ bubbler exchange. The decrease of the concentration of HCl is due to purging of the POCl₃ container by a continuous flow of O₂. H₂O concentration variations originate from two contributions: real water vapour content in the process gas and desorption effects (see text for details).

4.5.2 Results and discussion

Figure 4.26 shows representative measurements of HCl and H₂O performed in the gas mixtures described in Table 4.4 immediately after the change of the POCl₃ bubbler and one day after. A very high concentration of HCl (up to 0.3%) was present at the beginning, showing that the carrier gas was highly contaminated due to the change of the POCl₃ container. In contrast, the water vapour level was in the ppm range due to the fact that most of the water content present in the gas was readily transformed into HCl (see chemical reaction (4.6)). As oxygen was flowing through the POCl₃ bubbler, the HCl concentration decreased along with time due to the purge of the container. The evolution of HCl and H₂O concentrations over 11 days is presented in Figure 4.27 and 4.28.

The variation of the HCl concentration shows a regular decrease during the purge of the container: on day one, the bubbler was changed, producing a high degree of water contamination transformed into HCl and after a continuous purge of the container with O₂ during 49 hours, the concentration decreased to reach a level of 5 ppm. No purging and no measurement were performed the following day (day four) as a result of a machine maintenance. Therefore, a higher HCl concentration of 40 ppm was observed at the beginning of day five

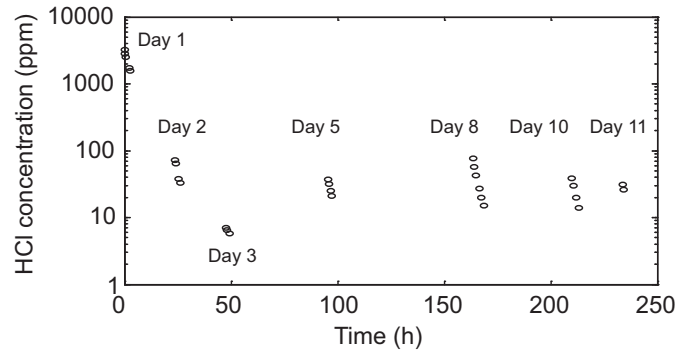


Figure 4.27: HCl concentration level evolution over 11 days. The *grouped circles* represent several measurements performed on the same day during a time period varying from a few tens of minutes up to one hour. Each circle corresponds to one measurement point (integration time of 10s) taken at the beginning or at the end of that period.

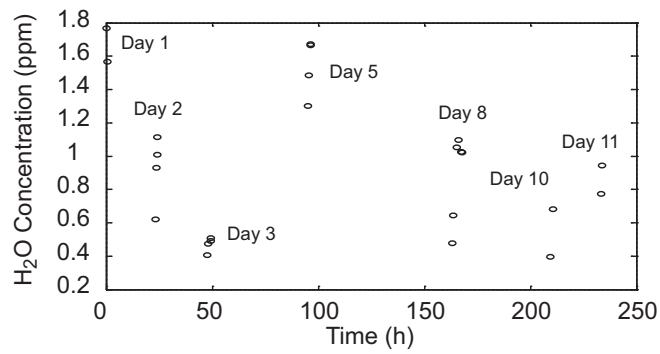


Figure 4.28: H₂O concentration level evolution over 11 days. The *grouped circles* represent several measurements performed on the same day during a time period varying from a few tens of minutes up to one hour. Each circle corresponds to one measurement point (integration time of 10s) taken at the beginning or at the end of that period.

due to water desorption in the teflon head of the container when the O₂ purge was interrupted. The concentration decreased down to 21 ppm after 2 hours of purging. After a new break of two days (week-end), the concentration increased again up to 77 ppm to reach a level of 15 ppm after 5 hours of continuous flow of O₂.

The evolution of the water vapour concentration over these days was quite different as the range of observed variations (from a maximum of 1.8 ppm to a minimum of 0.40 ppm) was much reduced compared to HCl, and the H₂O concentration did not change in a regular way. During the purge, the measured H₂O concentration decreased with time at high HCl levels (day 1 and beginning of day 2), but tended to increase in an intermediate range of HCl concentration of 10-100 ppm (see day 2, 5 or 8).

To explain this behaviour, the measured H₂O signal probably originates from two different contributions. The first one is due to the real water vapour content in the gas that results from residual water introduced in the line during the exchange of the POCl₃ bubbler and not transformed into HCl. This contribution is expected to be dominant in the early phase of the purge and to decrease with the purge time in a similar way as observed for the HCl concentration (see Figure 4.26). A second contribution may result from a process of water desorption from the walls of the cell and possibly from the line. This contribution seems to be significant after a definite purge duration, corresponding to an intermediate range of HCl concentrations of 10-100 ppm. This process is believed to be responsible for an increase of the observed H₂O concentration as illustrated in Figure 4.26b.

It must be emphasised that the concentration of these contaminants is much lower in the real carrier gas used in the preform manufacturing process, since the total carrier gas mixture is different. The POCl₃ concentration in the process is 0.088 % (compared to 2.79% for the measurements) meaning that HCl and H₂O concentrations are reduced accordingly (See Table 4.5). However, the sensitivity of the sensor is sufficient to monitor HCl in the real process gas.

After these eight days of purging, a first preform has been manufactured and a fibre has been drawn in order to analyse its different parameters, in particular the spectral attenuation. To be compliant with the International Telecommunication Union (ITU) recommendation for a low-water-peak fibre [22], the attenuation measured at the maximum of the OH⁻ peak at 1383 nm must be lower than the attenuation at 1310 nm after hydrogen (H₂) ageing [23]. Attenuation curves of the fibre manufactured from the preform processed on day nine is presented in Figure 4.29. A second fibre manufactured seven days later is shown on the same figure. These measurements were carried out after the drawing of the fibre, but without performing H₂ ageing. However, H₂ ageing is not systematically performed and a security margin of 0.02 dB/km is added to the attenuation coefficient to take this effect into account. A maximum of 0.34 dB/km at 1383 nm is acceptable for the fibre to be considered as a low-water-peak fibre. On Figure 4.29, no significant attenuation improvement in the E-band and S-band region can be noticed between the two fibres. In addition, both fibres present an attenuation of 0.320 dB/km (fibre of day eight) and 0.318 dB/km (fibre of day 15) at 1383 nm, which satisfies the criteria defined above.

Finally, HCl and H₂O were monitored in gas mixtures containing GeCl₄

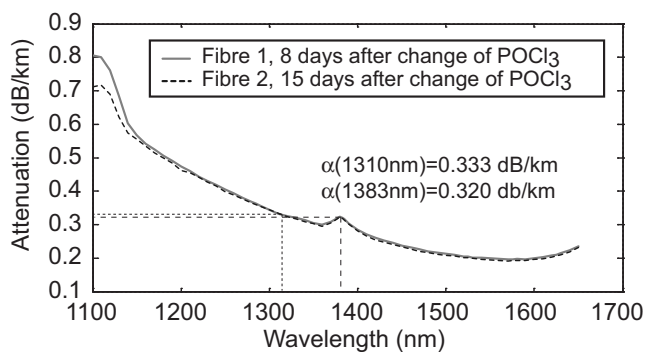


Figure 4.29: Attenuation of the low-water-peak fibres manufactured 8 days (*solid line*) and 15 days (*dashed line*) after the replacement of the POCl_3 container.

and SiCl_4 to identify the contribution of these chloride compounds to the OH^- peak. Figure 4.30 displays the measured concentrations in the case of GeCl_4 for the gas mixtures described in Table 4.4. The measured concentrations were below 1 ppm for HCl and around 0.1 ppm for H_2O . The same measurements using SiCl_4 are presented in Figure 4.31. Unfortunately, H_2O could not be measured due to condensation of the gas owing to the high saturated vapour pressure of SiCl_4 and the large temperature difference between the bubbler (39°C) and the ambient air temperature (20°C). Here again, the gas mixtures used for the evaluation of H_2O and HCl contamination were slightly different from the one used in the process. The GeCl_4 and SiCl_4 concentrations used in the process are 2.81% and 7.85% respectively compared to 2.68% and 10.31% in our measurements, meaning that the measured HCl and H_2O concentration were comparable to the real process concentrations.

In order to compare the different contamination sources, typical chloride concentrations present in the process gas are used to extrapolate HCl and H_2O concentrations from the obtained measurements (see Table 4.5). The substitution of the POCl_3 bubbler results in an HCl concentration of 15 ppm and a H_2O concentration of 0.92 ppm (last measured points before preform manufacturing after eight days of purging) corresponding to 0.47 ppm of HCl and 0.03 ppm of H_2O in the gas mixture used in the process. HCl and H_2O concentrations resulting from the GeCl_4 bubbler correspond to 0.76 ppm and 0.10 ppm in the process gas, respectively. Finally, HCl coming from the SiCl_4 container results in a concentration of 2 ppm. This comparison shows that the principal contamination source comes from the SiCl_4 container, considering that the purge of the POCl_3 bubbler was performed during a sufficient period of time.

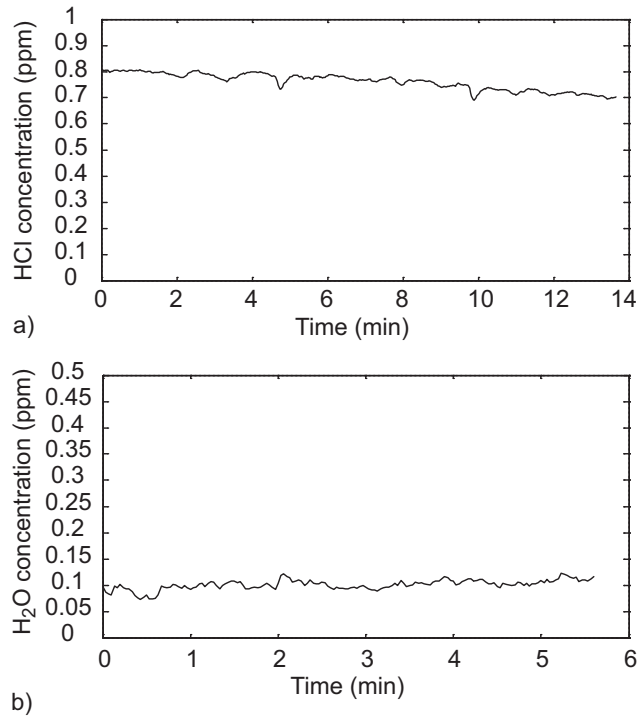


Figure 4.30: HCl (a) and H₂O (b) measurements in a gas mixture of 100 sccm O₂ saturated with GeCl₄, 400 sccm O₂ and 500 sccm He.

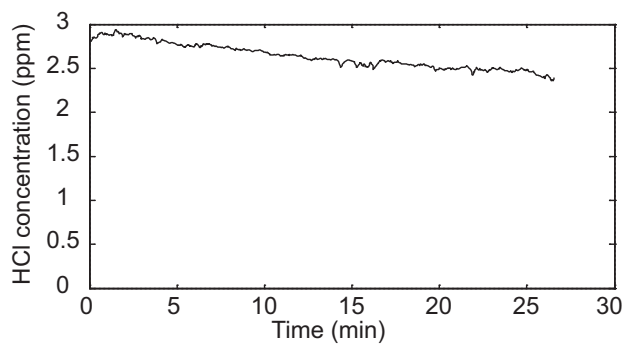


Figure 4.31: HCl (a) and H₂O (b) measurements in a gas mixture of 100 sccm O₂ saturated with SiCl₄, 200 sccm O₂ and 700 sccm He.

4.5.3 Conclusion

Laser diode photoacoustic spectroscopy has demonstrated to be an efficient and reliable measurement technique for trace gas analysis in process gases, especially well adapted to on-line continuous detection and quantification of contamination down to a few tens of ppb. Sensitivity obtained using mW-power laser diodes is sufficient to detect hydrogenated contaminants to a level low enough to secure a ZWPF production. Finally, it was demonstrated that the system can be used in other environment than in atmospheric conditions, such as high purity and highly corrosive gases.

4.6 Ammonia trace measurements at ppb level

4.6.1 Introduction

Sensitive and continuous ammonia monitoring is relevant in various applications, such as DeNO_x processes widely used in power plants and incinerators to reduce NO_x emissions [24], process control in the semiconductor industry, where extremely low levels of NH₃ in clean rooms may drastically deteriorate the performances of lithography process [25], environment monitoring to quantify NH₃ emissions from animal production facilities and automobile traffic [26, 27] or in medicine to analyse NH₃ levels in breath as a diagnostic tool [28]. Whereas detection limits in the parts-per-million or sub-ppm range are sufficient for some of these applications (i.e. DeNO_x process), most of them require much better performances at parts-per-billion level.

Semiconductor distributed feedback lasers emit typical powers of several tens of milliwatts enabling sensitivities in the sub-ppm range for many species (see section 4.3.2), including ammonia [29]. Better detection limits down to ppb level require higher output power generally achieved using gas lasers (CO and CO₂ lasers). However, the use of fibre amplifiers combined with standard telecom diode lasers is an attractive alternative to these cumbersome gas lasers to improve the detection limits towards ppb levels. The first use of an erbium-doped fibre amplifier (EDFA) in combination with PAS was reported by Webber et al. in 2003 for NH₃ detection [30]. Even if these authors reported a detection limit of a few ppb of NH₃, this was extrapolated from higher concentration and no real measurement below 100 ppb is actually shown. Monitoring ammonia at sub-ppm level is a challenging task due to the sticky nature of this polar molecule and the related adsorption-desorption problems [31, 32]. The work reported here aims at presenting ammonia measurements at atmospheric pressure down to a concentration of a few ppb in dry air (80% nitrogen, 20% oxygen) and at evaluating carbon dioxide and water vapour interferences in typical atmospheric conditions.

4.6.2 Sensor design

The photoacoustic sensor is based on the 3-resonators PA cell described in chapter 3 in combination with a laser diode emitting near 1532 nm. For NH₃ measurements, only one resonator with the corresponding laser diode was used, whereas the two other lasers were not connected (Figure 4.32). A special teflon coating was deposited on the inner surface of the resonator in order to reduce adsorption-desorption processes [33]. The PA signal was amplified and

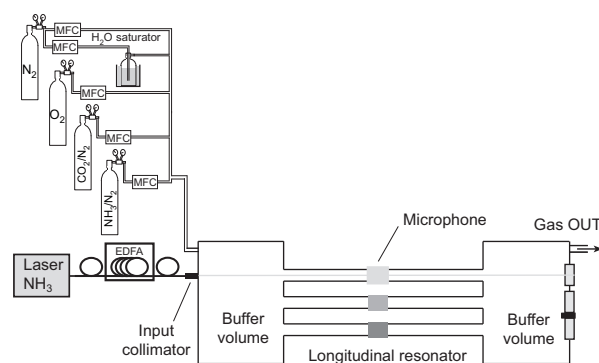


Figure 4.32: Scheme of the experimental set-up including the PA sensor, the erbium-doped fibre amplifier and the gas handling system. Current-modulated light from the DFB laser is amplified and launched into the resonator through a fibre collimator. Mass-flow controllers (MFC) are used to prepare varying low concentrations of NH_3 in dry air (80% N_2 -20% O_2). CO_2 and H_2O (generated by a N_2 flow through a H_2O saturator) can be added to the mixture to study the interference of these species.

measured using a lock-in amplifier with a time constant usually set to 10 s. The PA signals were demodulated at the modulation frequency ($1f$ detection) or at twice the modulation frequency ($2f$ detection) [34]. These two techniques were investigated and compared to determine the optimal configuration to achieve the minimum detection limit

The diode laser is operated in wavelength-modulation mode at either the frequency of the first longitudinal mode of the PA cell ($1f$ demodulation) or at half of the PA cell resonant frequency ($2f$ demodulation). The temperature- and current-tuning coefficients are $-13.9 \text{ GHz}/^\circ\text{C}$ and $-0.85 \text{ GHz}/\text{mA}$. This fibered configuration allows an easy insertion of the EDFA to boost the optical power launched into the PA cell. The optical amplifier was operated in the saturation regime and delivered about 750 mW of amplified power at 1531.67 nm from the 18.5 mW laser, thus providing a 16 dB gain to the laser optical power. The total power of the EDFA including spontaneous emission was about 1 W.

The gas handling system was composed of a certified mixture containing 100 ppm of NH_3 buffered in nitrogen. N_2 and O_2 cylinders were used for dilution and a certified mixture of 5000 ppm of CO_2 was used for quantitative interference measurements. H_2O interference was also investigated by passing part of the flow through a saturator which consists in a water-filled glass cuvette placed in a thermostat bath (see Figure 4.32). The flow exiting the cuvette was saturated in water vapour and the humidity was only dependent on the bath temperature. Dilutions were obtained with mass-flow controllers with a total flow of 1000 sccm in the PA cell. This flow reduces the adsorption-desorption process of ammonia in the PA cell and ensures a fast response time of the sensor without adding any extra acoustic noise. However, low NH_3 concentrations obtained with mass-flow controllers are approximative because of the adsorption-desorption processes.

The actual NH_3 concentrations in the gas stream after the gas mixing system and ahead of the PA cell are measured with an Omnisens TGA300Series trace gas analyzer. The analyzer is based on resonant PAS in combination

with a high power CO₂ laser. Calibration of the instrument has been validated by using continuous gas generator, based on the dynamic evaporation of an aqueous ammonia solution into a continuous N₂ gas stream while being cross-checked with the impinger method (ion chromatography) [35]. The analyzer features online measurements at relatively high flow rates of up to 5000 sccm and short response times. Its wide measurement range (0.1 ppb - 6 ppm) and linearity of $r^2 > 0.9998$ over the measurement range, low detection limit (0.1 ppb) and demonstrated accuracy (0.25 ppb or 1%) makes this analyzer a reference ammonia sensor in the industry and is being used for contamination monitoring in the semiconductor industry and for atmospheric pollution and air quality monitoring applications [35]. The analyser calibration accuracy together with its measurement linearity and range enables precise measurements even at low ppb level and was used throughout the tests as a reference.

4.6.3 Results and discussion

4.6.3.1 Performance of the sensor

In order to quantify adsorption-desorption processes in the system, the sensor response time was investigated. The response time of the sensor was first measured at high ammonia concentration (at ppm level) and then in the ppb range. A concentration step from 1 ppm down to 0.5 ppm at 1000 sccm was applied to the sensor and an exponential fit was used to precisely determine the time decay. By considering 95% of gas renewal ($1 - 1/e^3$), the response time was equal to 95 sec. The same process was then applied at low concentration (step from 40 ppb to 20 ppb NH₃) and a response time of about 6 minutes was obtained. This decay time was compared with the TGA reference instrument and was found to be 85 s. The difference between the two instruments is principally due to the quality of the coating deposited on the inner surface of the PA cell. In addition, the coating deposition inside the resonators and in a short 6 mm stainless steel tube at the inlet of the PA cell could not be properly applied for technical reasons.

Two modulation schemes were investigated in order to achieve the best minimum detectable concentration. Firstly, wavelength-modulation mode with first-harmonic detection ($1f$ detection) was investigated. This modulation scheme yields to a PA signal which is proportional to the first derivative of the absorption feature. The principal drawback of $1f$ detection is the presence of either window or wall noise which contributes to the PA signal [36]. Window and wall noise are due to the residual intensity modulation (IM) associated to wavelength-modulation when the laser current is modulated. The use of an EDFA in the saturation regime reduced the IM index from the laser by almost a factor 10 (Figure 4.33), but a residual noise level was still present. The modulation amplitude was first optimised to maximise the PA signal. However, this configuration was not optimal due to the high noise level associated to the residual IM. The modulation amplitude was therefore rather chosen to maximise the signal-to-noise ratio instead of the PA signal amplitude. In this case, the current modulation amplitude applied to the laser was 6 mA corresponding to 1/4 of the amplitude used to maximise the PA signal.

The detection limit of the PA sensor was determined by measuring NH₃ dilutions in dry air (80% N₂, 20% O₂) from 150 ppb down to 6 ppb and by

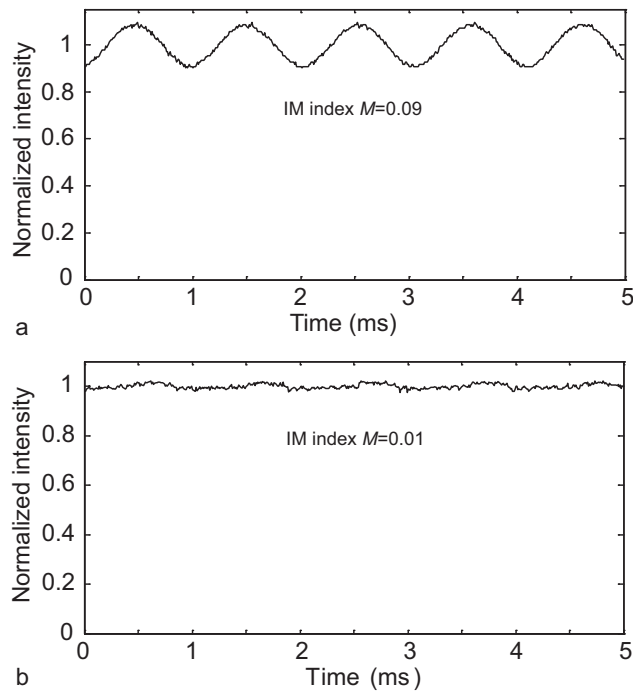


Figure 4.33: Residual intensity modulation of (a) the DFB laser and (b) with the EDFA operated in the saturation regime. The signals are normalised to the DC value and the laser modulation frequency is 1 kHz.

measuring the noise level. Ammonia concentrations were precisely monitored with the commercially available Trace Gas Analyser (TGA) provided by Omnisens SA. NH_3 concentrations obtained from mass-flow controllers differed as much as 30% in comparison with the TGA value (see Table 4.6), thus proving the importance of a properly calibrated instrument. Experimental results obtained with $1f$ detection with respect to NH_3 concentration are shown in Figure 4.34. The minimum detectable concentration is given by the crossing point between the linear fit and the noise level. In the present configuration, the noise level is as high as $20 \mu\text{V}$ (due to wall or window noise) which is about 5 times higher than the microphone noise level. A concentration of 6 ppb NH_3 passed into the sensor could not be detected. In this configuration,

MFC's NH_3 concentrations (ppb)	TGA's NH_3 concentrations (ppb)	Error (%)
100	92	8
50	44	12
25	25	0
12.5	17	36
10	12	20
5	6.5	30

Table 4.6: Comparison of NH_3 concentrations calculated from mass-flow controllers (MFC) adjustment and measured with Omnisens' Trace Gas Analyser (TGA).

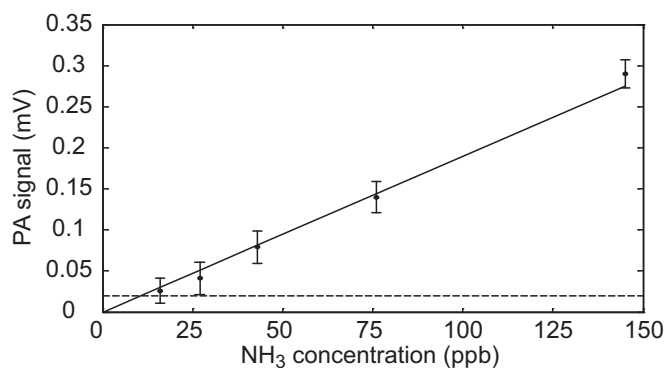


Figure 4.34: PA signal demodulated at $1f$ as a function of ammonia concentration. *Error bars* shown on the plot correspond to one standard deviation of the PA signal recorded in a 5-min period with an integration time of 10 s. The *line* is the result of a linear fit. The *dashed line* is the noise level obtained by the average over 5 minutes of the PA signal recorded with N_2 purge. The noise-equivalent detection limit is about 12 ppb.

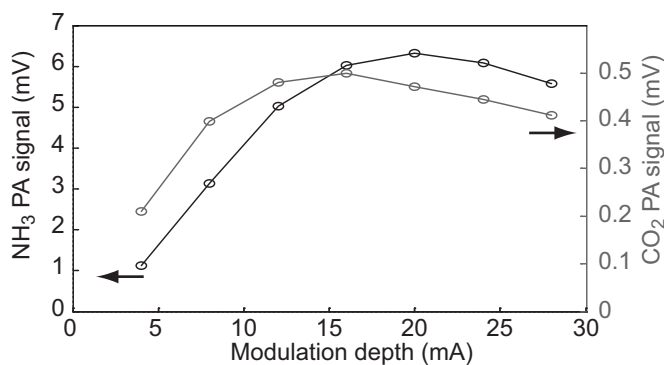


Figure 4.35: Amplitude of the NH_3 and CO_2 PA signals as a function of the laser current modulation depth in the case of a sinusoidal waveform with $2f$ detection. An optimal modulation depth of 20 mA is determined for the detection of ammonia.

the noise-equivalent detection limit is around 12 ppb.

The detection limit may be significantly improved by reducing the noise down to the level of the microphone noise. Since wall noise and window noise result from the residual IM, they mainly occur at the laser modulation frequency and have negligible contribution at higher harmonics. Therefore, a second-harmonic ($2f$) detection scheme was applied to improve the sensor performances. For this purpose, a sinusoidal waveform modulation was applied to the laser at half the resonance frequency. The modulation depth was optimised to maximise the PA signal for NH_3 detection. Results are presented in Figure 4.35, which shows the dependence of the PA signal as a function of the modulation depth for NH_3 , as well as for the neighbouring CO_2 line at 1531.7 nm. An optimal value of 20 mA was obtained for the NH_3 line. The PA signal demodulated at the resonance frequency ($2f$) looks like a second-derivative of the absorption feature. Results obtained with $2f$ detection with respect to NH_3 concentration are presented in Figure 4.36. High concentrations starting from 90 ppb were diluted to achieve low concentrations down to

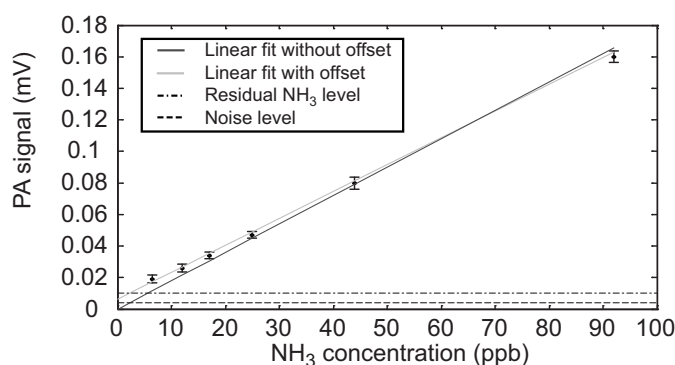


Figure 4.36: PA signal demodulated at $2f$ as a function of ammonia concentration. *Error bars* shown on the plot correspond to standard deviation of the PA signal recorded in a 5-min period with an integration time of 10 s. The *solid lines* are the result of linear fits. The *dot-dashed line* corresponds to the residual level obtained with a N_2 purge. The *dashed line* is the system noise level (average over 5 minutes, 10 s integration) observed after an intensive purge of the sensor with high N_2 flow saturated with water vapour. The noise-equivalent detection limit is 2.4 ppb.

nearly 6 ppb. 6 ppb was the lowest concentration achievable with the available mass-flow controllers. Unfortunately, a residual level of a few ppb of ammonia (dot-dashed line in Figure 4.36) was very difficult to wash out from the cell and the gas line due to the sticky nature of NH_3 and thus contributed to low PA signals. In that case, the sensitivity of the sensor seemed to be limited by this residual level. However, by carefully purging the PA cell during one night with a high air flow saturated with water vapour, the sensor was properly cleaned and the residual level was reduced to the noise of the microphone integrated over 10 s (dashed line in Figure 4.36). This configuration yields to a noise-equivalent detection limit of 2.4 ppb, thus improving the sensitivity by a factor 5 compared to $1f$ detection.

4.6.3.2 CO_2 and H_2O interference with NH_3

In order to identify H_2O and CO_2 interferences with NH_3 , a PA spectrum of these compounds was measured at atmospheric pressure using the EDFA and an external chopper for the modulation of the incident laser beam (Figure 4.37b). For this measurement, a mechanical chopper has been preferred to the direct modulation of the laser injection current in order to produce pure IM. In such conditions, the generated PA spectrum is proportional to the gas absorption coefficient, which makes easier the comparison between experimental and calculated spectra. Concentrations of 1.15% of H_2O (corresponding to 50% of relative humidity at $20^\circ C$), 5000 ppm of CO_2 and 5 ppm of NH_3 were used to record each spectrum separately. The DFB laser diode temperature was tuned between $5^\circ C$ and $40^\circ C$ covering a spectral range from 1530 nm to 1534 nm. CO_2 and H_2O spectra calculated from HITRAN database [16] and a FTIR NH_3 spectrum obtained from the PNNL database [17] are presented in Figure 4.37a. A good agreement between experimental and databases spectra is observed. The strongest NH_3 absorption line is located at 1531.67 nm where H_2O and CO_2 also contribute to the PA signal. Since ammonia detection is performed using a wavelength-modulation scheme in combination with $2f$ de-

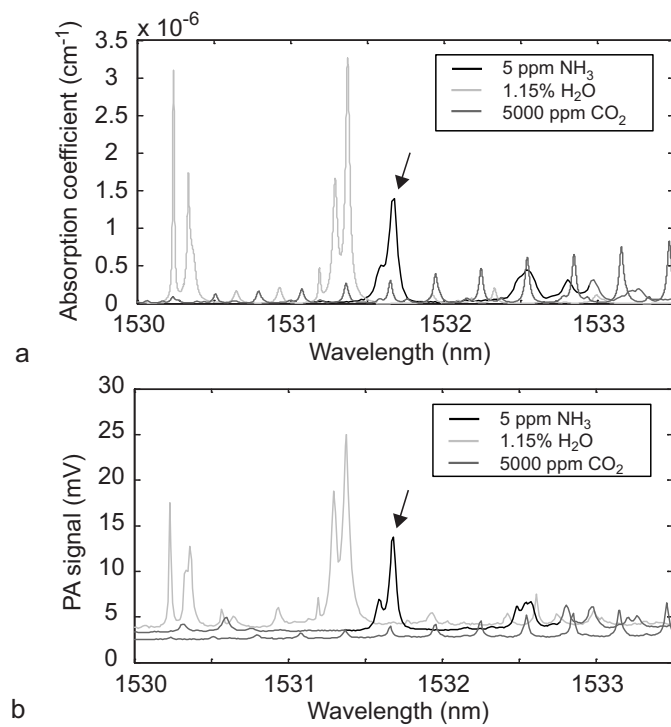


Figure 4.37: a) H₂O and CO₂ spectra calculated from the HITRAN database [16] and NH₃ spectrum obtained from the PNNL database [17] for concentrations of respectively 1.15%, 5000 ppm and 5 ppm. (b) Corresponding PA spectra measured using the EDFA and an external chopper for the same compounds concentrations. The *arrow* shows the selected ammonia line used for measurements.

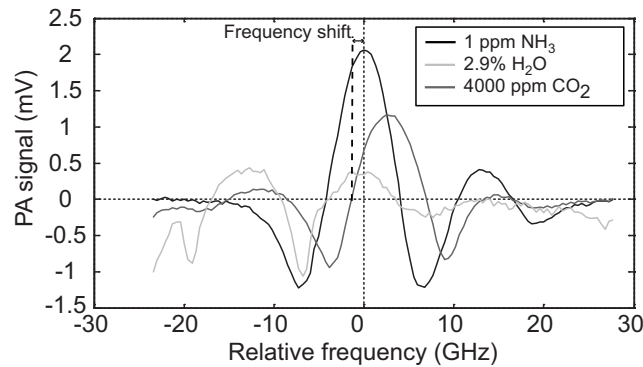


Figure 4.38: NH_3 , CO_2 and H_2O measured spectra at $2f$. Interferences are calculated by measuring the contribution of CO_2 and H_2O at the centre of the ammonia feature (0 GHz). Typical concentrations in air of 1.15% of H_2O (50% of relative humidity at 20°C) and 400 ppm of CO_2 correspond to an ammonia equivalent concentration of 36 and 100 ppb. The frequency shift represents the shift to apply on the laser DC current to obtain a 0 contribution of CO_2 interference.

tection, the same scheme was applied to quantify H_2O and CO_2 interferences. A scan of the absorption lines of 1 ppm NH_3 , 4000 ppm CO_2 and 1.9% H_2O in a balance of dry air (80% of N_2 and 20% of O_2) was carried out by tuning the laser current from 60 mA to 120 mA, corresponding to a frequency scan of 51 GHz (see Figure 4.38). The output power of the EDFA was considered as constant over this scan since the amplifier was used in the saturation regime. In order to determine the equivalent NH_3 concentration due to the contribution of CO_2 and H_2O , an average value of the corresponding PA signals measured at the centre of the NH_3 line was determined over 5 minutes (10 s integration time). Typical CO_2 and H_2O concentrations present in atmosphere were considered to deduce the interference contribution. Thus, it was determined that 400 ppm of CO_2 and 1.15% (50% of relative humidity at 20°C) correspond to 36 ppb and 100 ppb of NH_3 at 1531.67 nm, respectively.

These interferences can be reduced by operating the system at low pressure [30], but operation at atmospheric pressure was nevertheless preferred to maintain a simple configuration. In that case, water vapour contribution can be compensated by measuring the ambient humidity with a commercially available hygrometer or spectroscopically at another wavelength of the laser. In the latter case, an appropriate choice of wavelength, where only water vapour contributes to the absorbed signal, is necessary, for instance at $\lambda = 1530.94$ nm. This contribution may then be subtracted from the overall signal measured on the NH_3 line at 1531.67 nm. For CO_2 interference, the same procedure may be applied with a different wavelength of $\lambda = 1532.25$ nm.

However, a simple and original approach may also be implemented to suppress the interference from ambient CO_2 . The proposed method takes advantage of the slight shift between the centre of the NH_3 and CO_2 absorption lines around 1531.67 nm. The main NH_3 absorption feature located at 1531.67 nm (6528.79 cm^{-1}) is made of two close lines that overlap at atmospheric pressure, whereas the centre of the strongest CO_2 line is shifted by only 0.1 cm^{-1} from the NH_3 feature. As a result of this shift and of the different broadening coef-

Molecule	wavenumber (cm^{-1})	Line strength ($\text{cm}^{-1}/(\text{mol cm}^{-2})$)	γ_{air} (cm^{-1})	γ_{NH_3} (cm^{-1})
NH ₃	6528.76	2.52E-21	0.1	0.45
NH ₃	6528.89	1.34E-21	0.1	0.45
CO ₂	6528.893968	5.19E-25	0.0676	0.0818

Table 4.7: Parameters of the strongest NH₃ and CO₂ lines around 1531.67 nm used in the simulations of the $2f$ -PA signals according to the data from Webber et al. [37] and HITRAN [16]. γ_{air} and γ_{NH_3} are air and self broadening coefficient at atmospheric pressure, respectively.

ficients of these lines (see Table 4.7), the zero-crossing point in the $2f$ signal of the CO₂ line is located only -1.19 GHz (-0.04 cm^{-1}) away from the centre of the NH₃ line in the modulation conditions used in the experimental set-up. By operating the laser at this specific wavelength, the CO₂ contribution to the PA signal may be efficiently reduced, while keeping a strong signal from NH₃. In order to demonstrate the efficiency of this method for the reduction of the CO₂ interference, some simulations of the $2f$ -PA signals from NH₃ and CO₂ have been performed in similar conditions as encountered in the experiment (Figure 4.39). For this purpose, the $2f$ -PA signals corresponding to 1 ppm NH₃ and 4000 ppm CO₂ have been calculated using a theoretical model of the harmonic signals generated in WM-PAS [34]. The laser modulation amplitude has been chosen to maximise the PA signal for NH₃ at atmospheric pressure as in the experiments, thus corresponding to a modulation index (ratio of the frequency modulation amplitude to the width of the target absorption line) $m = 2.2$ for NH₃. The same modulation depth has been considered for CO₂, hence corresponding to a larger modulation index due to the smaller linewidth of the CO₂ line. The effect of the ambient pressure on the CO₂ and NH₃ signals has been considered in order to demonstrate that the proposed CO₂-interference reduction scheme is not pressure sensitive. It can be noticed in Figure 4.39 that the NH₃ signal is reduced by only 10% when the laser is slightly tuned to the zero-crossing point of the CO₂ $2f$ signal compared to the maximum signal achieved at the centre of the NH₃ absorption feature. In the same time, the CO₂ interference is reduced by two orders of magnitude when the laser is slightly frequency shifted to this specific wavelength. The equivalent signal for 4000 ppm of CO₂ is reduced to 4 ppb NH₃ over a pressure range of $\pm 10\%$ around atmospheric pressure, thus corresponding to a sub-ppb interference for a typical atmospheric concentration of 400 ppm CO₂.

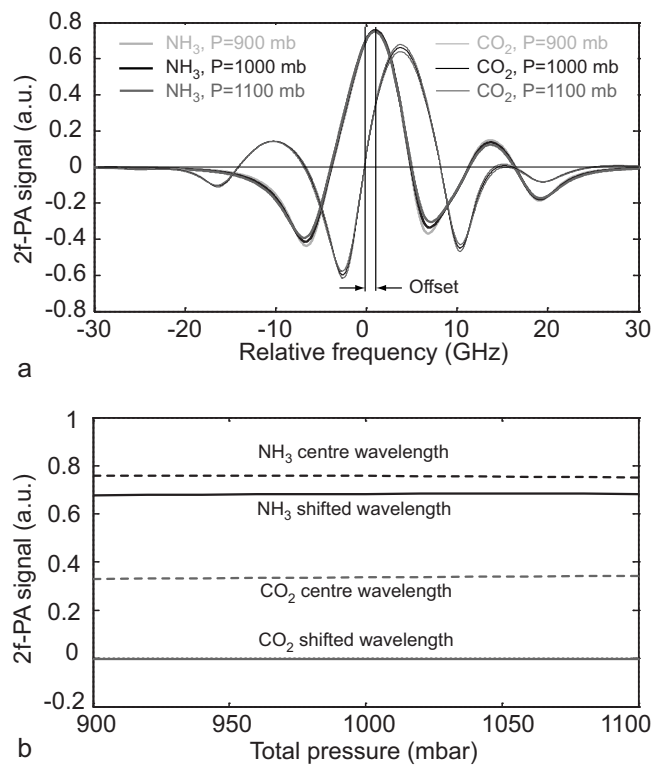


Figure 4.39: (a) Comparison of the simulated $2f$ PA signals for 1 ppm NH₃ and 4000 ppm CO₂ at different pressures. The parameters of the absorption lines have been taken according to Table 4.7 and a modulation depth corresponding to a modulation index $m = 2.2$ for NH₃ at atmospheric pressure has been considered. (b) Comparison of the NH₃ signal and CO₂ interference obtained when the laser is tuned to the centre of the NH₃ absorption feature (*dashed lines*) or slightly shifted -1.19 GHz away (*solid lines*).

4.7 Conclusion

A PA gas sensor was developed to monitor ammonia at ppb level. Since the power of laser diodes is limited to several tens of mW, a configuration using an optical amplifier was investigated to reach such extreme sensitivities. In addition, a well-adapted modulation scheme in combination with an optimised PA cell design are essential to achieve the best signal-to-noise ratio. A carefully designed system results in a powerful sensor capable of measuring a few ppb of ammonia. Finally, interferences from H₂O and CO₂ must be taken into account to measure NH₃ in ambient air. An original method consisting in a wavelength shift of the laser to measure these compounds separately have been proposed to overcome this problem. The robustness of this technique over pressure variations has been validated by simulating $2f$ -PA signals from NH₃ and CO₂.

Bibliography

- [1] M. R. Gamble and G. Clough, "Ammonia build-up in animal boxes and its effect on rat tracheal epithelium," *Lab. Anim.* **10**, 93–104 (1976).
- [2] K. Kincade, "CWDM breathes life into metro, access, and enterprise applications," *Laser Focus World* **39**(3), 97 (2003).
- [3] J. Gowar, *Optical communication systems*, Prentice-Hall international series in optoelectronics (London, 1984).
- [4] C. K. N. Patel, "Laser detection of pollution," *Science* **202**(4364), 157–162 (1978).
- [5] F. Kühnemann, K. Schneider, A. Hecker, A. A. E. Martis, W. Urban, S. Schiller, and J. Mlynek, "Photoacoustic trace-gas detection using a cw single-frequency parametric oscillator," *Appl. Phys. B* **66**(6), 741–745 (1998).
- [6] M. M. J. W. Van Herpen, N. K. Y. Ngai, S. E. Bisson, J. H. P. Hackstein, E. J. Woltering, and F. J. M. Harren, "Optical parametric oscillator-based photoacoustic detection of CO₂ at 4.23 μm allows real-time monitoring of the respiration of small insects," *Appl. Phys. B* **82**(4), 665–669 (2006).
- [7] M. van Herpen, S. C. Li, S. E. Bisson, and F. J. M. Harren, "Photoacoustic trace gas detection of ethane using a continuously tunable, continuous-wave optical parametric oscillator based on periodically poled lithium niobate," *Appl. Phys. Lett.* **81**(7), 1157–1159 (2002).
- [8] M. W. Sigrist, "Trace gas monitoring by laser photoacoustic spectroscopy and related techniques (plenary)," *Rev. Sci. Instrum.* **74**(1), 486–490 (2003).
- [9] J. Faist, F. Capasso, D. L. Sivco, C. Sirtori, A. L. Hutchinson, and A. Y. Cho, "Quantum Cascade Laser," *Science* **264**(5158), 553–556 (1994).
- [10] R. Colombelli, F. Capasso, C. Gmachl, A. L. Hutchinson, D. L. Sivco, A. Tredicucci, M. C. Wanke, A. M. Sergent, and A. Y. Cho, "Far-infrared surface-plasmon quantum-cascade lasers at 21.5 μm and 24 μm wavelengths," *Appl. Phys. Lett.* **78**(18), 2620–2622 (2001).
- [11] D. Hofstetter and J. Faist, "High performance quantum cascade lasers and their applications," in *Solid-State Mid-Infrared Laser Sources*, vol. 89 of *Topics in Applied Physics*, pp. 61–96 (Springer-Verlag, Berlin, 2003).
- [12] M. Sigrist and C. Fischer, "Perspectives of laser-photoacoustic spectroscopy in trace gas sensing," *J. Phys. IV* **125**, 619–625 (2005).
- [13] S. Schilt, "Mesure de traces de gaz à l'aide de lasers à semi-conducteur," Ph.D. thesis, Swiss Federal Institute of Technology (2002).
- [14] H. J. Troger, "Injection locking in semiconductor lasers," Ph.D. thesis, Swiss Federal Institute of Technology (1999).
- [15] D. M. Baney and W. V. Sorin, *Fiber optic test and measurement*, edited by E. Derickson (Prentice Hall, New Jersey, 1998).

- [16] L. S. Rothman, D. Jacquemart, A. Barbe, D. C. Benner, M. Birk, L. R. Brown, M. R. Carleer, C. Chackerian, K. Chance, L. H. Coudert, V. Dana, V. M. Devi, J. M. Flaud, R. R. Gamache, A. Goldman, J. M. Hartmann, K. W. Jucks, A. G. Maki, J. Y. Mandin, S. T. Massie, J. Orphal, A. Perrin, C. P. Rinsland, M. A. H. Smith, J. Tennyson, R. N. Tolchenov, R. A. Toth, J. Vander Auwera, P. Varanasi, and G. Wagner, "The HITRAN 2004 molecular spectroscopic database," *J. Quant. Spectrosc. Radiat. Transf.* **96**(2), 139–204 (2005).
- [17] S. W. Sharpe, T. H. Johnson, R. L. Sams, P. M. Chu, G. C. Rhoderick, and P. A. Johnson, "Gas-phase databases for quantitative infrared spectroscopy," *Appl. Spectrosc.* **58**(12), 1452–1461 (2004).
- [18] A. Schmohl, A. Miklos, and P. Hess, "Effects of adsorption-desorption processes on the response time and accuracy of photoacoustic detection of ammonia," *Appl. Opt.* **40**(15), 2571–2578 (2001).
- [19] V. Zéninari, B. Parvitte, D. Courtois, V. Kapitanov, and Y. Ponomarev, "Measurements of air and noble-gas broadening and shift coefficients of the methane R3 triplet of the $2\nu_3$ band," *Appl. Phys. B* **72**, 953–959 (2001).
- [20] National Institute of Standards and Technology: <http://webbook.nist.gov/chemistry> .
- [21] Z. Bozoki, M. Szakall, A. Mohacsi, G. Szabo, and Z. Bor, "Diode laser based photoacoustic humidity sensors," *Sens. Actuator B-Chem.* **91**(1-3), 219–226 (2003).
- [22] "Characteristics of a single-mode optical fibre and cable," International Telecommunication Union, ITU-T G652 (2003/03).
- [23] "Product specification- sectional specification for class B single mode fiber," International Electrotechnical Commission (IEC), 60793-2-50 (2004-01).
- [24] G. Ramis, L. Yi, and G. Busca, "Ammonia activation over catalysts for the selective catalytic reduction of NO_x and the selective catalytic oxidation of NH_3 . An FT-IR study," *Catal. Today* **28**(4), 373–380 (1996).
- [25] S. MacDonald, N. Clecak, R. Wendt, C. G. Willson, C. Snyder, C. Knors, N. Deyoe, J. Maltabes, J. Morrow, A. McGuire, and S. Holmes, "Airborne chemical contamination of chemically amplified resist," *Proc SPIE* 1466 p. 2 (1991).
- [26] D. Marinov and M. Sigrist, "Monitoring of road-traffic emissions with a mobile photoacoustic system," *Photochem. Photobiol. Sci.* **2**(7), 774–778 (2003).
- [27] M. E. Webber, T. MacDonald, M. B. Pushkarsky, C. K. N. Patel, Y. Zhao, N. Marcillac, and F. M. Mitloehner, "Agricultural ammonia sensor using diode lasers and photoacoustic spectroscopy," *Meas. Sci. Technol.* **16**, 1547–1553 (2005).

- [28] L. R. Narasimhan, W. Goodman, and C. K. N. Patel, "Correlation of breath ammonia with blood urea nitrogen and creatinine during hemodialysis," *PNAS* **98**(8), 4617–4621 (2001).
- [29] A. A. Kosterev and F. K. Tittel, "Ammonia detection by use of quartz-enhanced photoacoustic spectroscopy with a near-IR telecommunication diode laser," *Appl. Opt.* **43**(33), 6213–217 (2004).
- [30] M. E. Webber, M. Pushkarsky, and C. K. N. Patel, "Fiber-amplifier-enhanced photoacoustic spectroscopy with near-infrared tunable diode lasers," *Appl. Opt.* **42**(12), 2119–2126 (2003).
- [31] J. Henningsen and N. Melander, "Sensitive measurement of adsorption dynamics with nonresonant gas phase photoacoustics," *Appl. Opt.* **36**(27), 7037–7045 (1997).
- [32] A. Schmohl, A. Miklos, and P. Hess, "Detection of ammonia by photoacoustic spectroscopy with semiconductor lasers," *Appl. Opt.* **41**(9), 1815–1823 (2002).
- [33] S. M. Beck, "Cell coatings to minimize sample (NH_3 and N_2H_4) adsorption for low-level photoacoustic detection," *Appl. Opt.* **24**(12), 1761–1763 (1985).
- [34] S. Schilt and L. Thévenaz, "Wavelength modulation photoacoustic spectroscopy: Theoretical description and experimental results," *Infrared Phys. Technol.* **48**(2), 154–162 (2006).
- [35] S. Schilt, L. Thévenaz, M. Niklès, L. Emmenegger, and C. Hügli, "Ammonia monitoring at trace level using photoacoustic spectroscopy in industrial and environmental applications," *Spectrochim. Acta, Part A* **60**(14), 3259–3268 (2004).
- [36] C. Brand, A. Winkler, P. Hess, M. A., Z. Bozoki, and J. Sneider, "Pulsed-laser excitation of acoustic modes in open high-Q photoacoustic resonators for trace gas monitoring: results for C_2H_4 ," *Appl. Opt.* **34**(18), 3257–3266 (1995).
- [37] M. E. Webber, D. S. Baer, and R. K. Hanson, "Ammonia monitoring near 1.5 μm with diode-laser absorption sensors," *Appl. Opt.* **40**(12), 2031–2042 (2001).

Chapter 5

Molecular relaxation in photoacoustic spectroscopy

5.1 Introduction

Molecular relaxation is of primary importance in photoacoustic spectroscopy, since the PA signal is the result of molecular absorption of photons and subsequent deactivation of the excited rovibrational state via inelastic collisions¹ with the neighbouring molecules. The PA signal directly depends on the heat production rate that is function of the relaxation time (see equations 2.42 and 2.43). When the condition $\omega\tau \ll 1$ is not fulfilled, the PA signal starts to decrease. This chapter is dedicated to the influence of molecular relaxation in PAS.

Molecular collisions occur through different internal energy transfer of the molecules (translation, vibration or rotation). A theoretical description of elastic collisions in inert gases (see subsection 5.2.1) and inelastic collisions in diatomic molecules (see subsection 5.2.2) is given in section 5.2. Section 5.3 is dedicated to vibration-translation (V-T) energy transfer and section 5.4 deals with vibration-vibration (V-V) energy transfers. Finally, section 5.5 gives a brief overview of rotation-translation (R-T) energy transfers.

Finally, two examples of molecular relaxation are given in section 5.7 and 5.8. The first example treats molecular relaxation in a CH₄-O₂ system, and the second one is dedicated to HCl detection in N₂ and O₂.

5.2 Molecular collisions

Molecules normally gain and lose vibrational and rotational energy in collisions. Radiative lifetimes of molecules excited in the infrared range are very long and can be neglected under most conditions. The nature of the collision process is thus of fundamental importance and will be discussed in this section. A simple model used to describe the collision process between inert gas molecules which have no internal degrees of freedom is first discussed. This model is based on classical kinetic theory of gases without the use of quantum

¹A perfectly elastic collision is defined as one in which there is no loss of kinetic energy in the collision. An inelastic collision is one in which part of the kinetic energy is changed to some other form of energy in the collision (internal energy).

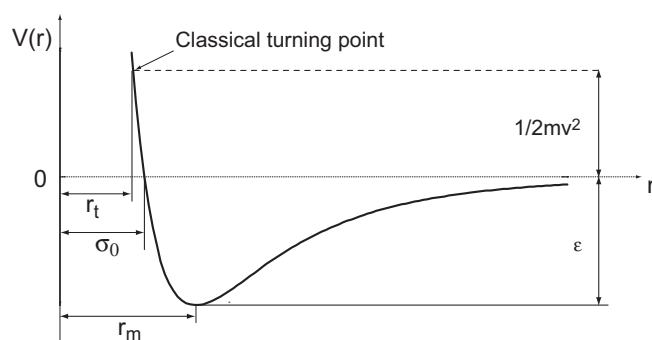


Figure 5.1: The Lennard-Jones intermolecular potential.

theory [1]. The same principle will then be applied to vibrating and rotating diatomic molecules.

5.2.1 Elastic collisions between inert gas molecules

A conventional representation of the intermolecular potential energy curve is given by the Lennard-Jones equation:

$$V(r) = 4\epsilon \left[\left(\frac{\sigma_0}{r} \right)^{12} - \left(\frac{\sigma_0}{r} \right)^6 \right] \quad (5.1)$$

where $V(r)$ is the potential energy at separation r , ϵ is the depth of the potential well at intermolecular distance r_m and σ_0 is the separation at zero energy ($V(r) = 0$). A typical potential energy curve is shown on Figure 5.1. The term $(\sigma_0/r)^6$ represents the long-range attractive forces (London dispersion forces in the case of inert gases), and gives rise to the gentle decrease in $V(r)$ as the molecules first approach. The term $(\sigma_0/r)^{12}$ represents the short-range repulsive forces (due to overlap of electron orbitals), and produces the much steeper rise in $V(r)$ as they approach closer. The total energy remains constant at $1/2mv^2$ (a particle of mass m approaching a fixed molecule from $r = \infty$ at speed v) throughout the collision and is represented on Figure 5.1 by a horizontal dotted line. The particle first accelerates as it runs down the attractive potential to r_m and is then retarded by the steep repulsive potential until it stops at a height $V(r) = 1/2mv^2$. This is known as the classical turning point and corresponds to a separation r_t smaller than σ_0 . Inert gases and simple polyatomic gases give a fair approximation to the Lennard-Jones potential. Some parameters of a few molecules are given in Table 5.1.

Potentials different to the Lennard-Jones often give a better fit for particular systems, but all show the same general characteristics and use values for ϵ , r_m and σ_0 defined similarly. A detailed treatment of the potentials available for both spherical and non-spherical symmetric molecules is given by Hirschfelder, Curtiss and Bird [2].

In any kind of elastic collision, it may be assumed that there is a completely free interchange of translational energy between the collision partners, subject to the laws of conservation of energy and momentum. The rate of transfer of translational energy between molecules is the gas kinetic collision rate, defined

Gas	σ_0 (Å)	ϵ (J/mol)	Z^a (ns ⁻¹)
He	2.576	84.1	9.54
N ₂	3.749	665.3	8.68
O ₂	3.541	732.2	6.35
CH ₄	3.796	1197	10.8
CO ₂	3.996	1582	6.91

Table 5.1: Collision parameters used in the Lennard-Jones potential for different molecules [1].

^aat 273 K and 1atm

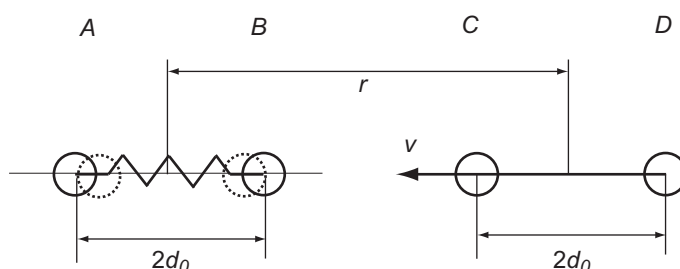


Figure 5.2: Collinear collision between a vibrating molecule and a non-vibrating diatomic molecule.

by the number of collisions made by one molecule per second ²:

$$Z = 4n_m\sigma_0^2\sqrt{\frac{\pi kT}{m}} \quad (5.2)$$

where n_m is the number of molecules in unit volume, m the molecular mass, k is the Boltzmann constant and T is the temperature. Values of Z calculated by (5.2) are given in Table 5.1 .

For mixtures of two gases A and B , the number of collisions per second made by one molecular of species A with molecules of species B becomes:

$$Z_{AB} = 2n_{mB} \left(\frac{\sigma_{0A} + \sigma_{0B}}{2} \right)^2 \sqrt{\frac{2\pi(m_A + m_B)kT}{m_A m_B}} \quad (5.3)$$

5.2.2 Inelastic collisions between diatomic molecules

The simplest model to address is a collinear collision between a vibrating diatomic molecule, AB , and a non-vibrating molecule, CD . This is likely to be the most efficient configuration for energy transfer, and is represented in Figure 5.2. AB is supposed to be a simple harmonic oscillator, for which the equilibrium internuclear distance is $2 \cdot d_0$. CD is a non-vibrating molecule with the same internuclear distance, and r is the distance between the centres of mass of the two molecules.

²For real molecules following the Lennard-Jones type intermolecular potential, it is difficult to precisely define what is considered as a collision. It is convenient to consider both energy transfer and chemical kinetics to define a gas kinetic collision rate, Z as the number of occurrences per second in which the molecular centres approach a certain distance.

Landau and Teller developed an elementary theory of vibrational energy transfer based on that simple molecules model [3, 4]. They assumed that only the repulsive part of the intermolecular potential is steep enough to influence energy transfer, so that the long-range attractive potential can be neglected. If the repulsive potential is represented by a simple exponential decay function:

$$V(r) = V_0 e^{-\alpha r}, \quad (5.4)$$

the probability P_{10} for a vibrational transfer from the first vibrational level to the ground level ($1 \rightarrow 0$) can be calculated by classical time-dependent perturbation theory on the assumption that P is proportional to the square of the Fourier component of the varying force at the oscillator frequency ν . This assumes that all collisions have a translational energy, $\frac{1}{2}m\mathbf{v}^2 \gg h\nu$, and gives P_{10} proportional to $\exp(-4\pi^2\nu/\alpha\mathbf{v})$. The distribution of molecular velocities is given by the Boltzmann distribution, and the proportion of molecules with speed $\geq v$ is $\exp(-mv^2/2kT)$. Integration over the range of possible speeds gives the average probability of deactivation per collision at temperature T as:

$$P_{10} = \exp\left(-3\left(\frac{2\pi^4\mu\nu^2}{\alpha^2kT}\right)^{\frac{1}{3}}\right) \quad (5.5)$$

This model gives the value of P_{10} , the average probability per collision for a ν ($1 \rightarrow 0$) transition to occur. To be able to compare it with experimental results, this value must be related to a transfer rate. The average number of collisions required for a molecule in the $\nu = 1$ state to deactivate to the ground state is:

$$Z_{10} = P_{10}^{-1}, \quad (5.6)$$

The gas kinetic collision rate (5.2) is Z collisions made by one molecule per second. The average time required for a molecule in the state $\nu = 1$ to deactivate is thus:

$$\beta = \frac{Z_{10}}{Z} = \frac{Z_{10}}{4n\sigma_0^2\sqrt{\frac{\pi kT}{m}}} \quad (5.7)$$

β is known as the vibrational relaxation time, and is the characteristic time for reaching the equilibrium between translational motion and intramolecular vibration. Since Z is proportional to the molecular density n , and hence to pressure, β varies inversely with pressure.

Equation (5.7) is an approximation, since it was tacitly assumed that all molecules are in the $\nu = 0$ state except one excited to the $\nu = 1$ state. In fact, the population in the 2 levels corresponds to a Boltzmann distribution. Further, the process is reversible, P_{01} for the reverse transfer must be given by:

$$P_{01} = P_{10} \exp\left(-\frac{h\nu}{kT}\right) \quad (5.8)$$

Taking this into account, the correct form of relation (5.7) for a simple harmonic oscillator is [4]:

$$Z_{10} = Z\beta \left[1 - \exp\left(-\frac{h\nu}{kT}\right)\right] = P_{10}^{-1} \quad (5.9)$$

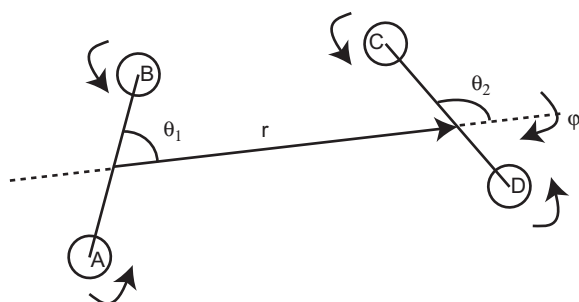


Figure 5.3: Collision between two rotating diatomic molecules.

An alternative way of expressing measurements in terms of a rate constant τ^{-1} for energy transfer, can be defined by the relation:

$$\tau^{-1} = \beta^{-1} p_0^{-1} \quad (5.10)$$

where p_0 is the pressure, and τ^{-1} is usually expressed in $\text{s}^{-1}\text{atm}^{-1}$ or in $\text{s}^{-1}\text{torr}^{-1}$.

Any quantitative treatment for R-T transfer involves complicated geometrical factors, as the varying interactions between all four atoms need to be considered (see Figure 5.3). A further complication arises out of the fact that for most molecules the separation between lower rotational quantum levels is so small that, except at low temperature, a wide range of rotational energy levels are populated under equilibrium conditions. This is in contrast with V-T transfer, where the majority of the molecules are in the $\nu = 0$ level, and only $\nu (0 \rightarrow 1)$ is important. R-T transfer can be treated by a purely classical model, and Parker [5] showed that rotational relaxation can be characterised by a single relaxation time τ_r , involving the whole rotational energy of the molecule, but not to a single rotational transition.

5.3 Vibration-translation energy transfer

The elementary discussion of inelastic collisions in the preceding section has shown the difficulty of setting an exact and rigorous theory of energy transfer. Even if a completely satisfactory theory were available, its quantitative application would be severely limited by the lack of accurate and realistic intermolecular potentials distribution. The theory which has been most widely used for quantitative comparison with experimental measurements of vibrational relaxation is the Schwartz, Slawsky and Herzfeld (SSH) theory [4]. This accounts semi-quantitatively for most of the principal features of vibrational energy transfer, and gives fair quantitative predictions for simple molecules. This theory will be used to provide a basic theoretical framework and to illustrate the relative importance of the various factors that influence the transfer probabilities.

5.3.1 Intermolecular potentials

The first requirement in any theory of energy transfer is to define an intermolecular potential $V(r)$. Analytical solutions of the collision problem require

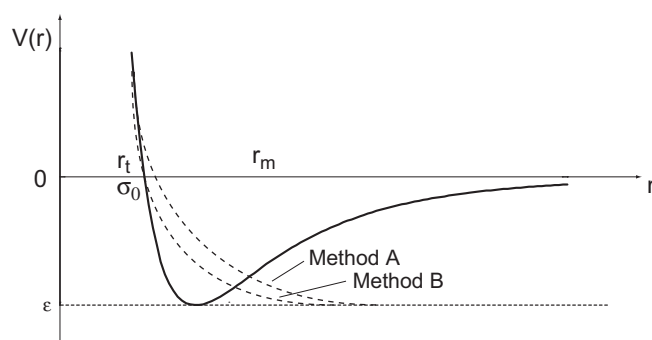


Figure 5.4: Approximation of the Lennard-Jones potential by two different exponential curves.

an exponential potential, as was used in the classical Landau-Teller theory. The potential used by the SSH theory is

$$V(r) = V_0 e^{-\alpha r} - \epsilon \quad (5.11)$$

This is shown diagrammatically in Figure 5.4, where it is compared with the Lennard-Jones potential. It is essentially a repulsive potential, and the attractive forces, represented by $-\epsilon$, are regarded as simply increasing the velocity of relative motion, thereby favouring a higher transition probability.

Molecular collision parameters (see Table 5.1) derived from experimental measurement of transport properties have to be fitted to equation (5.11). Two methods are generally used for doing this [4] (see also Figure 5.4). Both methods equate the two potentials at the classical turning point r_t . Method B also equates the two curves at a second point, σ_0 . Method A makes the exponential curve tangential to the Lennard-Jones curve at the classical turning point. Method B, which gives a larger value of α , is usually found to better agree with experiment. Both r_t and α will vary with the incident velocity, and the value α^* (corresponding to the molecular speed with the highest transition probability, v^*), is used in the calculations. Similar fitting techniques may be applied to potential other than the Lennard-Jones.

5.3.2 Transition probabilities

The probability $P_{k-l(b)}^{i-j(a)}$ that during a binary collision vibrational mode (a) of one molecule changes its quantum state from i to j , while simultaneously a second mode (b) in the other molecule changes its state from k to l , is given by SSH theory as:

$$\begin{aligned} P_{k-l(b)}^{i-j(a)} &= P_0(a)P_0(b) [V^{ij}(a)]^2 [V^{kl}(b)]^2 \times \frac{4\mu}{kT} \\ &\times \exp\left(-\frac{\epsilon}{kT}\right) \left(\frac{8\pi^3\mu\Delta E}{h^2}\right)^2 \int_0^\infty f(\bar{u})d\bar{u} \end{aligned} \quad (5.12)$$

where

$$f(\bar{u}) = \frac{\bar{u}}{\alpha^4} \left(\frac{r_t}{\sigma_0} \right) \exp \left(-\frac{\mu \bar{u}^2}{2kT} \right) \left\{ \frac{\exp(L-L')}{(1-\exp(L-L'))^2} \right\} \quad (5.13)$$

$$L = \frac{4\pi^2 \mu}{\alpha} \bar{u} \quad (5.14)$$

$$L' = \frac{4\pi^2 \mu}{\alpha} \bar{v} \quad (5.15)$$

μ is the reduced mass of the colliding pair of particles mutually approaching with an effective velocity \bar{u} and recede with velocity \bar{v} , P_0 is the steric factor and $[V^{ij}]^2$ is the vibrational factor (see below). The integration is over the thermal distribution at temperature T of the molecular velocities assumed to be Maxwellian. ΔE is the amount of energy exchanged between the vibrational and translational degrees of freedom:

$$-\Delta E = h\nu_a(i-j) + h\nu_b(k-l) = (\bar{v}^2 - \bar{u}^2) \frac{\mu}{2} \quad (5.16)$$

In a simple V-T transition, only mode (a) changes its state, and $k=l$ so that the pre-exponential term $[V^{kl}(b)]^2$ becomes unity. SSH calculations are best performed by making a numerical integration of (5.12).

When ΔE is large, the integration can be solved analytically in terms of α^* to give the formula deduced by Tanczos [6], which is valid for $\Delta E > 200 \text{ cm}^{-1}$ and forms a more convenient basis for discussing the influence of different factors on the transition probability. The Tanczos equation is

$$P_{k-l(b)}^{i-j(a)} = P_0(a)P_0(b) \left(\frac{r_t^*}{\sigma_0} \right)^2 [V^{ij}(a)]^2 [V^{kl}(b)]^2 8 \left(\frac{\pi}{3} \right)^{\frac{1}{2}} \\ \times \left[\frac{8\pi^3 \mu \Delta E}{\alpha^{*2} \hbar^2} \right]^2 \zeta^{\frac{1}{2}} \exp \left[-3\zeta + \frac{\Delta E}{2kT} + \frac{\varepsilon}{kT} \right] \quad (5.17)$$

where

$$\zeta = \frac{\mu u^{*2}}{2kT} = \left(\frac{\Delta E^2 \mu \pi^2}{2\alpha^{*2} \hbar^2 kT} \right)^{\frac{1}{3}} \quad (5.18)$$

The Tanczos equation can be considered in four parts: (1) the geometrical, or steric factors, P_0 ; (2) the collision cross-reference factor $\left(\frac{r_t^*}{\sigma_0} \right)^2$; (3) the vibrational factors $[V]^2$ and (4) the translational factor represented by the remainder of the equation.

1. The steric factors, P_0 , are required to account for the fact that the molecules are not spherically symmetrical and that some collision orientations are more effective than others. They are usually taken as $1/3$ (the average of $\cos^2 \theta$ taken over a sphere) for diatomic molecules and for longitudinal vibrations of polyatomic molecules. For non-linear polyatomic molecules and for bending modes of linear molecules, P_0 is taken as $2/3$. The theory takes no account for rotational transitions, and assumes that the orientation remains constant during a collision. The assumptions are invalid for hydrogen and hydrides³ where a very low moment of inertia is associated with rapid rotation and with wide

³A hydride is a compound of hydrogen with more electropositive elements, like NH_3 or H_2O .

spacing of rotational quantum levels; further discussion of these effects will be given later. The fact that certain orientations will be preferred for collisions involving polar molecules is also ignored, which limits the accuracy of the treatment for these molecules at lower temperatures.

2. The collision cross-reference factor, $\left(\frac{r_t^*}{\sigma_0}\right)^2$, is the ratio of the intermolecular separation at the classical turning point to the separation at zero energy, σ_0 , which is used in calculating the gas kinetic collision number Z . It converts probabilities calculated for a collision cross-section πr_t^2 to the usual elastic cross-section of kinetic theory, $\pi\sigma_0^2$.
3. The vibrational factor, $[V^{ij}(a)]^2$, is the square of the matrix element for the transition between the two vibrational states i, j of molecule (a). It represents the coupling of the initial and final states, i and j , of the oscillator under the influence of the perturbation produced by the collision, and corresponds to the square of the Fourier component of the varying force at the oscillator frequency which is found in classical theory. It depends on the repulsion parameter α and frequency and amplitude of the vibration.
4. The translation factor gives expression to the change in kinetic energy of translation involved in the inelastic collision. The involved parameters are the reduced mass of the colliding molecules, μ , and the temperature T , which together determine the velocity of approach; ΔE , the amount of vibrational energy transferred in the collision, and the intermolecular repulsion parameter α . It must be pointed out that all the terms involve ΔE^2 with the exception of the second exponential term $\exp(-\Delta E/2kT)$. This alone changes sign for the reverse process $P_{l-k(b)}^{j-i(a)}$, and the two probabilities differ by a factor $\exp(-\Delta E/kT)$ in accordance with the principle of detailed balancing (see equation (5.8)).

The exponential term of the translation factor controls the temperature dependence of P , since the whole pre-exponential part of equation (5.17) is only weakly temperature-dependent. The dominant term is usually the negative first exponential term, $\exp(-3\zeta)$. This predicts that $\log P$ will vary with $T^{1/3}$ as in the Landau-Teller expression (5.5). But for cases where the attractive potential (represented by $-\epsilon$) is large, the positive third exponential term $\exp(+\epsilon/kT)$ can become dominant, giving rise to a higher transition probability which vary inversely with T . The SSH theory thus predicts qualitatively the minimum in the Landau-Teller plot ($\log P$ versus $T^{1/3}$) which is observed for strongly polar molecules, and the curvature observed for all other molecules at lower temperatures. Quantitative prediction under these conditions is unsuccessful due to the failure of equation (5.11) to give adequate expression to the effect of the attractive potential, and the SSH theory consistently underestimates P for strongly polar molecules and at lower temperatures.

5.3.3 Modified theories

Two fundamental limitations of the SSH theory have been pointed out in the preceding section:

- Inadequate expression is given for the attractive part of the intermolecular potential. This becomes important for all molecules at low temperatures or for strongly polar molecules at all temperatures.
- The relative orientation of the molecules is regarded as constant during the collision, and the possibility of simultaneous rotational transitions is disregarded. These assumptions are valid for molecules with large moments of inertia, but not for hydrides or deuterides.

Better account may be taken for the attractive forces for non-polar (approximately isotropic) molecules by using the Morse double exponential potential:

$$V(r) = \varepsilon e^{[-\alpha'(r-r_m)]} - 2\varepsilon e^{[-\frac{1}{2}\alpha'(r-r_m)]} \quad (5.19)$$

This allows an analytical solution and leads to an alteration in the exponential factor in equation (5.17) which may be written as [7]

$$P(T) = A(T) \exp \left[-3\zeta + \frac{4}{\pi} \sqrt{\frac{\varepsilon\zeta}{kT}} + \frac{16\varepsilon}{3\pi^2 kT} + \frac{\Delta E}{2kT} \right] \quad (5.20)$$

where $A(T)$ represents the whole, weakly temperature-dependent pre-exponential factor in equation (5.17). This assumes a spherically symmetrical potential and gives a good prediction for the temperature dependence of P for simple non-polar molecules at lower temperatures. This method can only be used when sufficient transport data are available to obtain the force constants for equation (5.19).

For polar molecules, which are strongly anisotropic, the angle dependence of the intermolecular potential must be taken into account, and also the predominance of preferred collisional orientations at lower temperatures. This requires modification of both the pre-exponential and the exponential terms in equation (5.17). Shin has derived the expression [7]:

$$P(T) = \frac{A}{16(a^2 - b^2)} \zeta^{\frac{3}{2}} \exp \left[-3\zeta + \frac{4}{\pi} \sqrt{\frac{\varepsilon\zeta}{kT}} + \frac{16\varepsilon}{3\pi^2 kT} + \frac{\Delta E}{kT} + 2a \right] \quad (5.21)$$

where

$$A = \sqrt{\frac{4\pi}{3}} \left(\frac{4\pi m \alpha \Delta E}{\hbar^2} \right)^2 X^2 \quad (5.22)$$

$$a = \frac{\mu^2}{\varepsilon \sigma_0^3} \left(\frac{\varepsilon^{\frac{3}{4}} \zeta^{\frac{1}{4}}}{(kT)^{\frac{3}{4}}} \right) \quad (5.23)$$

$$b = \left(\frac{\mu Q}{\varepsilon \sigma_0^4} \right) \left(\frac{\varepsilon^{\frac{2}{3}} \zeta^{\frac{1}{3}}}{(kT)^{\frac{2}{3}}} \right) \quad (5.24)$$

where X is the matrix element. This equation takes into account both dipole-dipole and dipole-quadrupole forces (μQ). This expression contains an additional positive exponential term $2a$, which also varies inversely with temperature and will be important for molecules with high dipole moment and small molecule diameter, such as NH_3 . It predicts with fair accuracy the inversion of the temperature dependence of $P(T)$ observed at low temperatures for molecules such as SO_2 [8].

Interaction between molecular vibration and rotation (V-R and V-(T,R)) was proposed by Cottrell *et al.* [9] in order to account for the observation that many deuterides show lower values of P_{10} than the corresponding hydrides, in spite of their substantially lower vibrational frequencies (which in simple SSH theory would correspond to faster relaxation). Cottrell suggested, that since the actual rotational velocity of the hydrogen atoms in most hydrides is larger than the translational velocity of the molecule, vibrational energy transfer into rotation will be more probable than transfer into translation. He produced a quite quantitative theory based on the model of interaction of a classical rotator and quantized oscillator, which was further developed and applied to a wide range of molecules by B. Moore [10]. It gives an expression for P_{10} which formally resembles the SSH expression (5.17), but with the important difference that, since the angular velocity of rotational rather than the translational velocity of the molecules plays the important role, ωd is substituted for the translational velocity and I/d^2 for the reduced mass (ω is the angular velocity, d the bond length of the hydride molecules and I is the moment of inertia). The dominating negative exponential term ζ of the SSH equation (5.17), which may be written in the abbreviated form of equation (5.20) as:

$$P(T) = A(T) \exp(-3\zeta) = A(T) \exp \left[-3 \left(\frac{\Delta E^2 \mu \pi^2}{2\alpha^2 \hbar^2 kT} \right)^{\frac{1}{3}} \right] \quad (5.25)$$

This expression can be replaced by the new terms:

$$P(T) = A(T)'' \exp \left[-3 \left(\frac{2\pi^2 I \Delta E^2}{d^2 \alpha^2 kT} \right)^{\frac{1}{3}} \right] \quad (5.26)$$

This theory, which treats vibrational relaxation as entirely due to V-R transfer, gives good prediction of the deuteride/hydride ratio, but predicts absolute rates which are generally too low.

A classical collision theory for vibrational energy transfer in hydrogen halides (HCl for instance) has been developed by Shin [11]. This solves the classical equations for the collision model of a rotation-averaged oscillator and a rigid rotator in which two hydrogen atoms interact strongly at close-in collisions. It takes into account of the effects of both translational and rotational motion (V-T and V-R transfer occurring simultaneously), and gives a good fit with experimental measurements for HCl, DCl, HBr and HI over a temperature range 800-2000K, where a classical Landau-Teller temperature is predicted and found.

Both the pure semiclassical V-R theory and Shin's classical V-(T,R) theory treat rotational motion of the molecule as classical. This seems to be justified for molecules, such as hydrogen halides, where the quantum vibrational level spacings are very much larger than the quantum rotational level spacings, but it breaks down for polyatomic molecules having much lower vibrational frequencies. If both energy modes are regarded as quantized, two competing factors have to be taken into account. A Δj transition, simultaneous with, and in the opposite direction to a $\delta\nu$ transition, will exert a favourable effect on the transition probability by decreasing ΔE_{int} , the amount of internal energy transferred to translation, since

$$\Delta E_{int} = \Delta E_{vib} - \Delta E_{rot} \quad (5.27)$$

This will tend to favour a large value of ΔJ and of ΔE_{rot} . This effect is balanced by the necessity for conservation of total angular momentum in collision, which favours a small value of ΔJ . Various theoretical calculations have been made, and all predict that a $\Delta\nu = \pm 1$ transfer will normally be accompanied by ΔJ transition with magnitude depending on the mass and moment of inertia of the molecule. For a heavy molecule, such as I_2 , the momentum requirements are more easily met, and ΔJ values up to ± 14 (with an optimum at 6 to 8) are predicted theoretically and confirmed experimentally [12]. For lighter molecules such as O_2 and N_2 , $\Delta J = \pm 2$ is the most probable transition, being 50 % more probable than $\Delta J = 0$, and four orders of magnitude higher than $\Delta J = \pm 4$ [13]. The two major characteristics affecting the comparison between relaxation behaviour of polyatomic gases and of diatomics are:

1. Polyatomic molecules possess several vibrational modes, each of which contributes to the molecular vibrational heat capacity, and can, in principle, relax independently.
2. Polyatomic molecules are structurally flexible and change their effective shape both during vibration, and, more important during collisions.

The first consideration turns out to be relatively undisturbing. The vast majority of polyatomic molecules show a single vibrational relaxation process involving the whole vibrational heat content of the molecule. This is due to rapid intramolecular V-V transfer, which maintains continuous equilibrium of vibrational energy between the active fundamental modes. The whole vibrational heat content of the molecule then relaxes in a single V-T transfer via the lowest mode (which will usually have a higher V-T transfer rate than upper modes). This mechanism is characterised by a single overall relaxation time, β , which may be related to β_1 , the actual relaxation time of the lowest mode, by the equation:

$$\beta_1 = \frac{C_1}{C_s} \beta \quad (5.28)$$

where C_s is the total vibrational heat content and C_1 the contribution to the lowest mode. It has been pointed out [14], that this relation is valid only when the V-V rate is faster than the V-T rate, and when C_1 represents a major part of the vibrational specific heat, which is usually the case. The intramolecular V-V transfer will be discussed in section 5.4.

The consequence of the second argument is much more serious. For most polyatomic molecules even an approximately quantitative description of an elastic collision is currently impossible, while for inelastic collisions, first-order perturbation theory is inadequate. In consequence, the theory discussed in the preceding subsections can only be applied qualitatively for most polyatomic molecules. However, quantitative calculations have been performed for CH_4 , since collision parameters are well known for this spherical symmetry molecule.

It was stated in subsection 5.3.3, that vibrational transitions $\Delta\nu = \pm 1$ in molecules of moderate molecular weight are usually accompanied by simultaneous rotational transitions, $\Delta J = \pm 2$. The amount of internal energy transferred to translation in a V-T, R transfer of this kind will be:

$$\Delta E_{int} = \Delta E_{vib} \pm \Delta E_{rot} \quad (5.29)$$

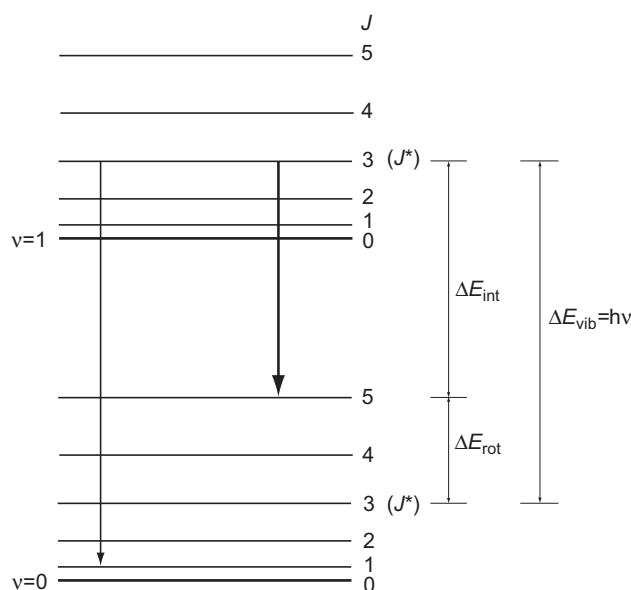


Figure 5.5: Energy-level diagram for simultaneous vibrational and rotational transitions.

If the rotational transition accompanying a $\nu = 1 \rightarrow 0$ vibrational transition is $\Delta j = \pm 2$, the energy-level diagram for a relaxation of a state, $(\nu = 1)(J^*)$ is as shown in Figure 5.5.

The most probable transition is likely to be that involving the smallest transfer to translation, i.e. from $(\nu = 1)(J^*)$ to $(\nu = 0)(J^* + 2)$. For this transition,

$$\Delta E_{int} = \Delta E_{vib} - \Delta E_{rot} = h\nu - B(4J^* + 6), \quad (5.30)$$

so that the magnitude of the effect of the simultaneous rotational transition on the total relaxation process depends critically on $B = h/(8\pi^2cI_B)$, the rotational constant of the molecule. The slow V-(T,R) transfer into the $(\nu = 0)(J^* + 2)$ level is followed by a very rapid thermal equilibration of the rotational level in the $(\nu = 0)$ state: i.e. if J^* is the mostly populated rotational level at the experimental temperature, there is a rapid R-T transfer, predominantly from $(J^* + 2)$ to J^* . The total effective transfer from internal to translational energy is thus ΔE_{vib} , but the rate dominant step is the slower V-(T,R) transfer involving the smaller quantity ΔE_{int} .

5.4 Vibration-vibration energy transfer

5.4.1 The SSH theory for non-resonant and resonant transfer

The SSH expression (5.12) for $P_{k-l}^{i-j(a)}$, the probability that a vibrational mode (a) of one molecule changes its quantum state from i to j , while simultaneously a second mode (b) in the other molecule changes its state from k to l , applies equally to V-T transfer (where $k = l$) and to V-V transfer (where $k \neq l$). For the V-T case, ΔE , the energy exchanged between vibrational and translational degrees of freedom, is

$$\Delta E = h\nu_a(i - j) \quad (5.31)$$

For the V-V case

$$\Delta E = h\nu_a(i - j) - h\nu_b(k - l) \quad (5.32)$$

(cf. subsection 5.3.2). Non-resonant V-V transfers are conveniently handled in terms of the analytical solution of equation (5.12) due to Tanczos (equation (5.17)), which was used as the basis for discussion of V-T transfer in the preceding section, and is valid for values of $\Delta E \geq 200 \text{ cm}^{-1}$. Similar criteria should apply for dependence on vibrational frequency, quantum number, single versus multiple quantum transfer, collision mass, temperature, and intermolecular potential.

For a V-V transfer between different molecular species the additional possibility arises of a resonant transition, where

$$h\nu_a(i - j) = h\nu_b(k - l) \quad (5.33)$$

and $\Delta E = 0$. For resonant and near-resonant transfers a different analytical solution, also due to Tanczos [6], applies for values of $\Delta E \leq 50 \text{ cm}^{-1}$:

$$P_{k-l(b)}^{i-j(a)} = P_0(a)P_0(b) \left[V^{i-j(a)} \cdot V^{k-l(b)} \right]^2 \frac{64\pi^2 \mu kT}{\alpha^2 h^2} \exp[\epsilon/kT] \quad (5.34)$$

Resonant transfers are much faster than non-resonant transfers, and there is no term in ΔE , so that all near-resonant transfers with $\Delta E \leq 50 \text{ cm}^{-1}$ behave as if resonant. Dependence on the frequency of the exchanging modes arises through the pre-exponential term $[V^{i-j(a)} \cdot V^{k-l(b)}]^2$. Since each squared vibration factor for a single-quantum transition, $[V^{(i-l)-i}]^2$, is inversely proportional to frequency, this gives rise to inverse dependence of P on the square of the frequency. Resonant transfers between high frequency modes thus have a collision probability much smaller than unity. This is because, although there is no net transfer of energy from vibration to translation, the change in vibrational quantum state can only be brought about by a time-dependent force [4]. (The same factor also operates for non-resonant transfers (equation (5.17)), but will usually be far outweighed by the exponential dependence on ΔE .) The last pre-exponential term predicts a weak positive dependence on temperature and a weak positive dependence on reduced mass. The only exponential term is that depending on the intermolecular attractive parameter, $\exp[\epsilon/kT]$, so that quite a small value of ϵ will be sufficient to outweigh the pre-exponential term and produce an overall negative temperature dependence for resonant V-V transfer, which will in general be much more sensitive to intermolecular attractive forces than non-resonant transfer. Quantitative treatment of such transfers by SSH theory is again unsatisfactory due to inadequacy of the assumed potential.

5.4.2 Intermode transfer in polyatomic gases

For this subsection, single (V-V) relaxation processes in polyatomic gases are considered. Intramolecular transfer of energy between different vibrational modes can only occur in collision, as the energy difference between the modes must be made up as translational energy. For a molecule with two vibrational modes of frequency ν_1 and ν_2 there are three possible vibrational transitions, which are illustrated on the energy-level diagram in Fig. 5.6 :

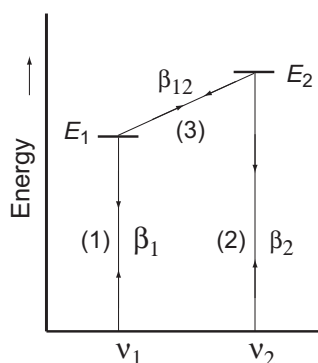
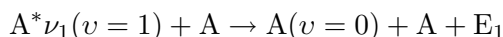
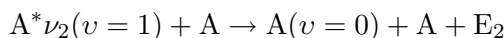


Figure 5.6: Energy level diagram showing transitions for a molecule with two active vibrational modes.

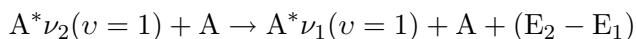
1. Transfer of translational energy from $1 \rightarrow 0$ relaxation of the mode ν_1 , with relaxation time β_1 :



2. Transfer of translational energy from $1 \rightarrow 0$ relaxation of the mode ν_2 , with relaxation time β_2 :



3. The complex transfer of one quantum of vibrational energy from mode ν_2 , to the mode ν_1 , with relaxation time β_{12} :



The values of β_1 , β_2 , and β_{12} may, in principle, be calculated by SSH theory. Since only one molecular species is involved in all three processes, their relative magnitudes are mainly determined by the values of E_1 , E_2 and $E_2 - E_1$. For the model represented in Fig. 5.6 the fastest relaxation process is the complex transfer (3), and the slowest the V-T relaxations of mode ν_2 by process (2). This means that $\beta_2 > \beta_1 > \beta_{12}$. Vibrational energy thus enters the molecule via process (1), which is rate controlling, and rapidly flows in complex collisions via the faster process (3) to the upper mode. Process (2) is too slow to play any role. This is known as a 'series' mechanism and is characterised by a single overall relaxation time β , which can be related to β_1 by $\beta = (C_1/C_s)\beta_1$, where C_1 is the heat capacity contribution due to mode ν_1 alone, and C_s the total vibrational heat capacity.

This kind of behaviour is shown by the vast majority of polyatomic molecules. The most usual pattern of fundamental vibration frequencies is such that the energy gaps between the upper modes are much less than the energy level of the lowest mode. The general picture is that rapid vibration-vibration transfer maintains continuous equilibrium of vibrational energy between the various fundamental modes of the molecule, and that the whole of this energy relaxes in a single vibration-translation transfer process via the lowest mode.

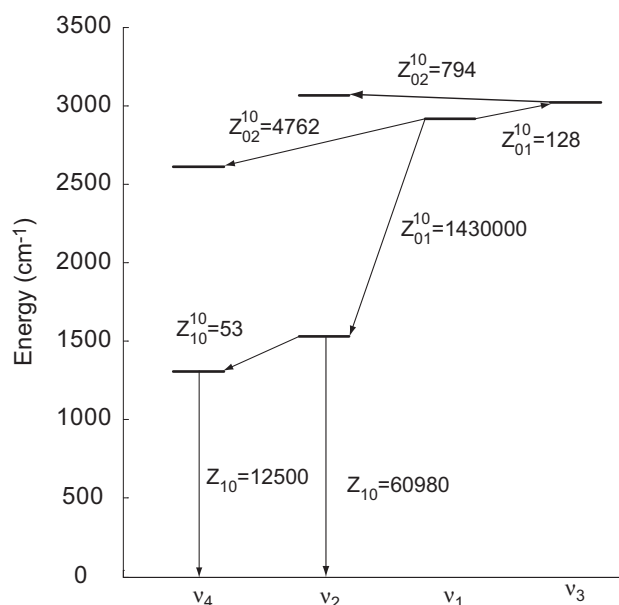
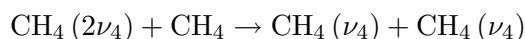


Figure 5.7: Calculated collision numbers for V-V transitions in CH₄ [15].

It is interesting to consider in detail the relaxation processes in an actual polyatomic molecule, CH₄, where SSH calculations for V-T transfer are in fair agreement with acoustic measurements. Collision numbers calculated by SSH theory by Stretton [15] for representative transitions are shown on an energy-level diagram in Fig.5.7. It is clear that each of the upper modes, ν_2 , ν_1 , ν_3 can transfer its energy into the lowest mode, ν_4 , or its first harmonic, much faster than the V-T transfer of ν_4 . The first harmonic of ν_4 relaxes very rapidly to the fundamental level by single-quantum resonant intramolecular V-V transfer:



The overall picture is thus of relaxation of the total vibrational energy via ν_4 with a single relaxation time. Laser fluorescence experiments were made on CH₄ by Yardley and Moore [16], who excited the ν_3 mode by a mechanically chopped He-Ne laser beam $\lambda = 3.39\mu\text{m}$, and obtained the relaxation time for ν_4 by observing the phase shift between the excitation and the fluorescence from both modes over a wide range of chopping frequencies. They found a value $Z_{10} = 14000$ for V-T relaxation of ν_4 , in satisfactory agreement with the theoretical value of $Z_{10} = 12500$ shown in Figure 5.7. The importance of the relaxation process in CH₄ in PAS will be illustrated in section 5.7 in the case of a CH₄-O₂ mixture.

5.5 Rotation-translation energy transfer

The general characteristics of R-T transfer, and how these differ in important respects from those of V-T transfer, were discussed in subsection 5.2.2. Detailed theoretical treatments of rotationally inelastic collisions fall into three classes, quantum mechanical, classical, and semiclassical. The area of application of each method depends on the magnitudes of the rotational and trans-

lational quantum numbers involved. When both rotational and translational quantum numbers are small, as in collisions involving H_2 and He, the quantum method is applicable. For systems specified by low rotational and high translational quantum numbers, e.g. $HCl + Ar$, the semiclassical method may be applied. For the very large number of systems involving heavy molecules with large moments of inertia, where both quantum numbers are large, the classical method is the most suitable. Calculations based on all three methods require an accurate intermolecular potential, $V = V(r, \theta)$, particularly its angular dependence, which is only available for a few simple systems. Reviews of the theoretical treatment R-T transfer have been published by Secret in 1973 [17].

The first classical treatment of rotational transfer was due to Parker [5], who investigated collisions between two homonuclear diatomic molecules, AB and CD . He adopted a potential function

$$V = a \left[e^{(-\alpha r_{AC})} + e^{(-\alpha r_{AD})} + e^{(-\alpha r_{BC})} + e^{(-\alpha r_{BD})} \right] - b \left[e^{(-\frac{1}{2}\alpha R)} \right] \quad (5.35)$$

containing both repulsive and attractive terms, and confined his attention to coplanar encounters with the initial rotational energy zero. Solution of the classical equations of motion showed that rotational relaxation could be characterised by a single relaxation time, β_R , involving the whole of the rotational energy of the molecule. This leads to a rotational collision number, Z_R , given by

$$Z_R = \frac{Z_R^\infty}{\left[1 + \frac{\pi^{\frac{3}{2}}}{2} \left(\frac{T^*}{T} \right)^{\frac{1}{2}} + \left(\frac{\pi^2}{4} + \pi \right) \left(\frac{T^*}{T} \right) \right]} \quad (5.36)$$

where $Z_R^\infty = 1/16(\alpha d/\epsilon)^2$ and $T^* = \epsilon/k$, (α , d (nuclear separation), and ϵ are the intermolecular potential parameters). Equation (5.36) predicts a slight positive temperature-dependence for Z_R (transfer becomes less efficient at higher temperatures and speeds of rotation). The Parker theory has been elaborated by Brau and Jonkman [18].

Widom [19] used a classical 'rough sphere' model for the rotational relaxation of a spherical-top molecule in collision with an inert gas molecule, and found the simple expression

$$Z_R = \frac{3(1+b)^2}{8b} \quad (5.37)$$

where $b = I/\mu a^2$, I being the moment of inertia, μ the reduced mass of the colliding molecules, and a the molecular diameter. Equation (5.37) predicts a minimum value $Z_R = 1.5$ when $I = \mu a^2$ and $b = 1$. This model neglects attractive forces entirely and predicts values of Z_R which are independent of temperature.

The role of rotational excitation in the overall heating and cooling processes of the heavier diatomic and polyatomic gases is unimportant. R-T transfer is very rapid, multiple quantum transitions occur easily, and the rotational population distribution reaches equilibrium almost as quickly as the translational. For H_2 and hydrides the picture is different. R-T transfer is much

slower, also it plays a more important role in the overall heating and cooling processes, as vibrational modes of such molecules do not become active until relatively high temperatures. The rotational excitation process differs fundamentally from the vibrational because of the different ways in which the quantum levels are distributed: the energy gap between successive vibrational levels becomes gradually smaller (owing to anharmonicity) as ν increases, while the gaps between successive rotational levels become rapidly larger as J increases (see Figure 5.5). This means that R-T transitions, $\Delta J = \pm 1$, become progressively less efficient as J and ΔE increase, while R-R transitions, even when involving neighbouring levels, are nearly always non-resonant and inefficient.

5.6 Influence of molecular relaxation in PA spectroscopy

The detection of methane and hydrogen chloride in the application of optical fibre manufacturing process was performed in a buffer gas that was very different to trace gas monitoring in ambient air. As it was explained in subsection 4.3.3, the photoacoustic signal is directly influenced by the composition of the buffer gas. Furthermore, molecular relaxation of the excited rovibrational state into sample heating (i.e. V-T deexcitation) is a key step in the generation of the PA signal. This effect can be considered as instantaneous in most cases, since it is much faster than the period of the laser modulation and has thus no consequence on the PA signal. However, it turns out that this relaxation is much slower in some particular gas mixtures, and the corresponding long relaxation time can strongly influence the generation of the PA signal. Such a phenomenon leads for example to the well-known effect of kinetic cooling of CO₂ observed in the MIR region, which arises when a mixture of CO₂ diluted in N₂ is analysed with a CO₂ laser [20, 21]. In that case, the analysed gas sample is cooled, rather than heated, by the excitation laser beam, which results in a 180 degrees phase lag of the PA signal with respect to the laser modulation. A similar effect has also been recently described in the NIR range, when detecting CO₂ at 1.43- μm using an external cavity laser diode [22]. Molecular relaxation has also been studied in the QEPAS technique (see subsection 3.2.4), since the modulation period is much reduced (30 μs) in comparison to traditional PAS systems (in the millisecond range). In particular, the impact of humidity in HCN detection [23] and molecular relaxation of CO₂ at $\lambda = 2\mu\text{m}$ [24] was described.

The relaxation time of some particular molecules may be orders of magnitude longer [25, 26, 27, 16, 28, 29]. In particular, this is the case for a few diatomic molecules, such as N₂ or O₂ (see Table 5.4), and for collisions with some particular partners (N₂ and O₂, too). Therefore, heat release may be delayed in a gas mixture if the excess energy of the excited molecules can be channeled by collisions, through vibration-to-vibration (V-V) energy transfers, to a long-lifetime transition of the surrounding molecules. As a result, the PA signal is severely damped when the time scale of the V-T processes is comparable to or longer than one period of the laser modulation. Molecular relaxation also occurs in a completely different situation where the relaxation time of the V-T process between the molecule to be detected and the collisional

partner itself is slow (HCN in N₂ [23]).

The dependence of the PA signal with respect to the molecular relaxation time τ is given by (see equation (3.4) with the use of equation (2.43) instead of (2.45) for the heat production rate):

$$S_{PA} = \frac{C_{cell}C\alpha P_0}{\sqrt{1 + (\omega\tau)^2}} \quad (5.38)$$

where C_{cell} is the cell constant defined in equation (3.3), C is the gas concentration, α is the absorption coefficient, P_0 the incident optical power and $\omega = 2\pi f$ is the angular modulation frequency. The phase of the PA signal is given by $\tan \phi = -\omega\tau$. When the relaxation process is fast enough, the condition $\omega\tau \ll 1$ is fulfilled and the PA signal is independent on the relaxation time (see equation (3.4)) and is in phase with the laser modulation ($\phi = 0$). The situation is drastically different when the relaxation process is slow. In that case, $\omega\tau \gg 1$ and the PA signal is phase shifted with respect to the laser modulation ($\phi \neq 0$) and becomes directly linear with the relaxation rate:

$$S_{PA} \cong C_{cell}C \frac{\alpha P_0}{\omega} \tau^{-1}. \quad (5.39)$$

In a gas mixture, the relaxation rate of an excited state of a molecule M is given by a weighted sum of the relaxation rates corresponding to collisions with the different types of surrounding molecules M_i and taking into account the concentration C_i of each species:

$$\tau_M^{-1} = \sum_i C_i \tau_{M-M_i}^{-1} \quad (5.40)$$

5.7 Molecular relaxation in CH₄ detection

The PA cell made of one resonator in combination with a laser diode emitting at 1651 nm⁴ were used to investigate relaxation effects in methane monitoring. Different buffer gases (N₂/O₂ mixtures in different proportions, adjunction of several percents of water vapour or helium) have been used in the experiments in order to study the influence of molecular relaxation on the PA signal. Since the foreign-broadening coefficient of the CH₄ absorption feature of interest changes with the composition of the carrier gas [30], intensity modulation (IM) has been preferred since it is less dependent on the width of the absorption feature than wavelength modulation (WM). For this purpose, the laser current was square-modulated between threshold and a value close to the current limit, in order to achieve complete IM (IM index $M = 1$). However, pure IM was not achieved in these conditions, since residual WM also occurred as a result of the laser chirp induced by the current pulses. But since measurements were performed at atmospheric pressure where the CH₄ absorption feature is several GHz wide, the effect of the residual WM was very weak compared to IM (i.e. the laser chirp was much smaller than the width of the absorption feature) and its influence on the PA signal could be neglected.

⁴The laser diode used in this section was different to the one described in subsection 4.3.1. In particular, the average output power at the operating point was 8 mW, resulting in a detection limit of 0.18 ppm ($SNR = 3$) in dry N₂.

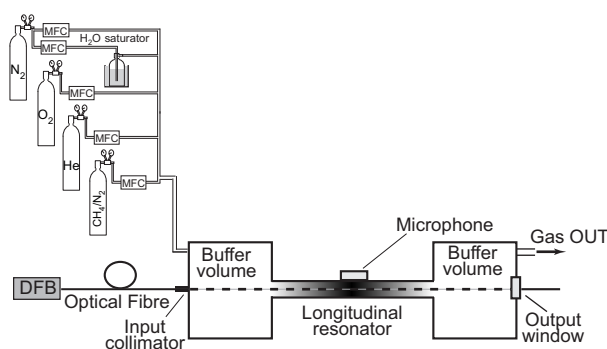


Figure 5.8: Scheme of the experimental set-up including the PA sensor and a gas-mixing system made of four mass-flow controllers to generate different CH₄ concentrations and carrier-gas compositions.

Various CH₄ concentrations and carrier gas compositions have been prepared from certified cylinders using a multi-gas controlling unit and mass flow controllers (5.8). Two cylinders of CH₄ buffered in nitrogen (5000 ppm and 100 ppm) and three pure gases (N₂, O₂ and He) have been used. With four different mass flow controllers, CH₄ concentrations ranging from 5000 ppm down to 0.4 ppm could be generated when N₂ was used as the carrier gas, and from 2000 ppm down to 0.4 ppm in N₂/O₂ mixtures (with a precision on the CH₄ concentration that was dependent on the dilution factor, but always better than 10%). The flow rates in the mass flow controllers were always adjusted in order to have a total gas flow of 500 sccm in the PA cell. The water vapour content in the gas mixture could also be adjusted by passing part of the flow in a saturator, i.e. a water-filled glass cuvette placed into a thermostat bath. The flow exiting the cuvette was saturated in water vapor and the humidity was only dependent on the bath temperature. The humidification of the gas sample was important to study the influence of molecular relaxation effects, as water vapour is usually an efficient catalyst that enhances the vibrational relaxation rate of many species [1].

Relaxation effects were investigated in methane monitoring in different N₂/O₂ mixtures, as well as the effect of various catalysts (H₂O, He) that may promote the vibrational relaxation of the CH₄-O₂ system. As relaxation effects strongly depend on the frequency of the excited acoustic wave, different resonances of the PA cell have been considered. The three first longitudinal modes of odd order - labelled (100), (300) and (500) - have been used, with typical resonance frequencies in air of 1 kHz, 3 kHz and 5 kHz (the even modes cannot be used as they are not excited by the laser beam in this geometry due to symmetry reasons).

5.7.1 Relaxation effects in the CH₄-O₂ system

The variation of the PA response corresponding to 100 ppm of CH₄ in different dry N₂/O₂ mixtures is shown in Figure 5.9. For this measurement, the entire acoustic resonance (amplitude and phase) has been recorded by scanning the laser modulation frequency. The phase measurements do not represent absolute values, as some additional electronic phase shifts may be present even in absence of molecular relaxation effects. However, the reference phase of the

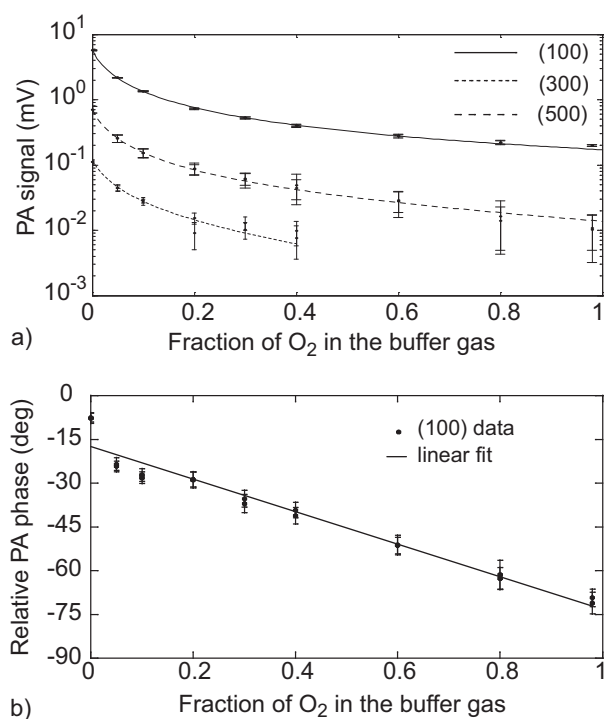


Figure 5.9: Variation of the PA response corresponding to 100 ppm CH₄ as a function of the O₂ fraction in N₂ in the buffer gas. (a) PA amplitude of the three first odd-order longitudinal resonances of the PA cell, labelled (100), (300) and (500); the *line* is the result of a fitting process (see text for details). (b) Phase of the PA signal measured at the first longitudinal resonance; the *solid line* represents a linear fit of the data. *Error bars* shown on the experimental data correspond to the standard deviation of the fitting process used to determine the parameters of the acoustic resonance. Two different measurements are displayed for each experimental condition.

lock-in detection was kept fixed during all the measurements, so that relative phase variations may be attributed to relaxation effects.

The parameters of the resonance (amplitude, central frequency and phase, Q factor) have been extracted from a fitting procedure on the experimental data and the level of uncertainty of each parameter has been determined from the standard deviation of the fitting process. The PA energy (square of the PA amplitude) was fitted by a Lorentzian distribution in order to determine the centre, amplitude and Q factor of the resonance. The phase data were fitted by a fifth order polynomial and the value at the centre of the resonance (given by the Lorentzian fit) was determined.

From these measurements, it turned out that the Q factors were only marginally modified between measurements in pure N₂ and O₂ (for example, it was reduced from $Q \cong 23$ in pure N₂ to $Q \cong 21$ in O₂ for the first longitudinal mode). The PA amplitude in Figure 5.9(a) is reduced by more than one order of magnitude when measured in O₂ in comparison to the case of pure N₂ and the signal is already strongly reduced in N₂/O₂ mixtures containing only a few percents of O₂. The behaviour is similar for the three considered modulation frequencies (1 kHz, 3 kHz and 5 kHz), but the data are less accurate at higher frequency due to a severe reduction in the signal-to-noise ratio, which results from the combination of the $1/f$ dependence of the PA effect and the decrease of the overlap integral between the laser beam and higher order acoustic modes which produces an overall $1/n^2$ dependence (n is the mode number). The phase variation of the PA signal is also shown in Figure 5.9(b) for the first longitudinal mode. A linear change is observed when increasing the O₂ concentration. The strong reduction of the PA signal observed when switching from pure N₂ to O₂ as a carrier gas and the associated phase variation are induced by particular molecular relaxation effects occurring in the CH₄-O₂ system and are almost not influenced by the Q factor of the resonance or by other physical parameters of the buffer gas.

The unexpected experimental results reported in Figure 5.9 about the monitoring of methane in oxygen by PAS are related to singular molecular relaxation effects occurring in the CH₄-O₂ system. They may be explained by considering the deactivation pathway followed by the CH₄ molecules excited by the laser radiation. A complete description of the spectroscopic properties of CH₄ is given in [26] and the rovibrational energy transfer processes in CH₄-N₂/O₂ mixtures are also discussed in a series a papers [26, 27, 31]. The main spectroscopic characteristics of the CH₄ molecule that are essential for the understanding of the experimental results are reminded.

The CH₄ molecule has four vibrational modes: two bending vibrations ν_2 (asymmetric) and ν_4 (symmetric), and two stretching vibrations ν_1 (symmetric) and ν_3 (asymmetric). The first excited bending levels ν_2 and ν_4 are located at 1533 and 1311 cm⁻¹ and the stretching levels ν_1 and ν_3 at 2917 and 3019 cm⁻¹, approximately two times higher in frequency than the two former ones. Consequently, the vibrational energies of methane can be viewed as clusters (called polyads) of states interacting together through Fermi or Coriolis resonances, as shown in Figure 5.10. The spacing between two successive polyads is about 1500 cm⁻¹. Due to the strong interactions existing between the states in a given polyad, the spectroscopic analysis of any vibrational state needs to take into account simultaneously all the states of the polyad to which the level belongs [26].

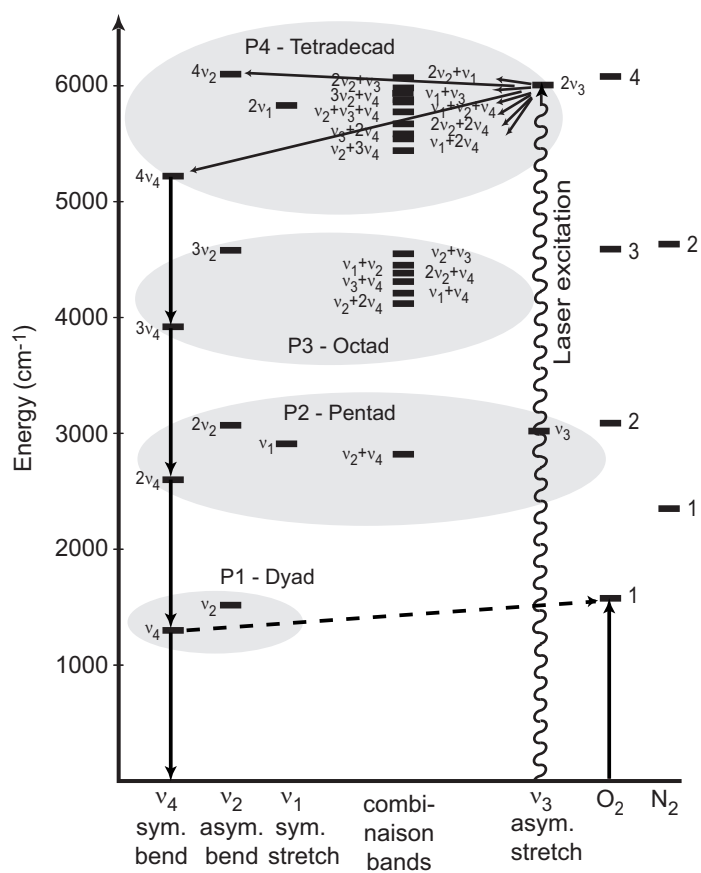


Figure 5.10: Energy levels diagram of CH₄ molecule, showing the laser excitation to the $2\nu_3$ state and the subsequent relaxation scheme with the resonant coupling between CH₄^{*}(ν_4) and O₂^{*}(ν_3) levels (dashed arrow).

Reaction	Rate (s ⁻¹ atm ⁻¹)	Ref.
<i>R</i> ₁ CH ₄ [*] (<i>nν</i> ₄)+CH ₄ → CH ₄ [*] ((<i>n</i> -1) <i>ν</i> ₄)+CH ₄ [*] (<i>ν</i> ₄)	2.7·10 ⁸	[25]
<i>R</i>₂ CH ₄ [*] (<i>nν</i> ₄)+CH ₄ → CH ₄ [*] ((<i>n</i> -1) <i>ν</i> ₄)+CH ₄	8·10 ⁵	[25]
<i>R</i> ₃ CH ₄ [*] (<i>nν</i> ₄)+O ₂ → CH ₄ [*] ((<i>n</i> -1) <i>ν</i> ₄)+O ₂ [*] (<i>ν</i>)	-	
<i>R</i>₄ CH ₄ [*] (<i>nν</i> ₄)+O ₂ → CH ₄ [*] ((<i>n</i> -1) <i>ν</i> ₄)+O ₂	1.3·10 ⁵	[26]
<i>R</i>₅ CH ₄ [*] (<i>nν</i> ₄)+N ₂ → CH ₄ [*] ((<i>n</i> -1) <i>ν</i> ₄)+N ₂	8·10 ⁴	[25]
<i>R</i>₆ N ₂ [*] (<i>ν</i>)+N ₂ → N ₂ +N ₂	1	[27]
<i>R</i>₇ O ₂ [*] (<i>ν</i>)+O ₂ → O ₂ +O ₂	63	[27]
<i>R</i>₈ O ₂ [*] (<i>ν</i>)+N ₂ → O ₂ +N ₂	40	[27]
<i>R</i>₉ O ₂ [*] (<i>ν</i>)+H ₂ O → O ₂ +H ₂ O	1.1·10 ⁶	[28]
<i>R</i> ₁₀ O ₂ [*] (<i>ν</i>)+CH ₄ → O ₂ +CH ₄ [*] (<i>ν</i> ₄)	2·10 ⁷	[16]
<i>R</i>₁₁ O ₂ [*] (<i>ν</i>)+CH ₄ → O ₂ +CH ₄	1·10 ⁶	[28]
<i>R</i>₁₂ O ₂ [*] (<i>ν</i>)+He → O ₂ +He	2.3·10 ⁴	[29]

Table 5.2: Examples of some relaxation rates of some vibrational states of CH₄ with different collisional partners. Reactions labelled in **bold** correspond to V-T processes, the others to V-V processes.

This characteristic is important for the understanding of the collisional relaxation of methane. In particular, very fast energy transfers (in the nanosecond range) occur between the states of the same polyad (intermodal transfer) for both CH₄-CH₄ and CH₄-O₂ collisions. Therefore, the energy transfer between two polyads essentially occurs via the exchange of one *ν*₄ vibrational quantum (see reactions *R*₁ and *R*₃ in Table 5.2), since this is the smallest energy quantum. The relaxation through the *ν*₂ level is less probable, since the relaxation time is much longer than through *ν*₄ (see Figure 5.6 in section 5.4). For CH₄-O₂ collisions, the de-excitation of the CH₄ molecule is accompanied by a resonant excitation of the first vibrational state of oxygen, O₂^{*}(*ν*) located at *ν* = 1556 cm⁻¹, due to its proximity with the CH₄^{*}(*ν*₄) level. For weak CH₄ concentrations, the transfer to the lower polyads occurs predominantly via the resonant process *R*₃ and at each relaxation step, the energy released by CH₄ is transferred to oxygen molecules. As a result, the whole 1.65- μm laser energy initially absorbed in the CH₄^{*}(2*ν*₃) state finally accumulates in the O₂^{*}(*ν*) vibrational state of oxygen. According to Table 5.2, the relaxation time of this state at atmospheric pressure ($\tau_{O_2-O_2} = 1/63$ s) is much longer than one period of the laser modulation (around 1 ms for 1 kHz modulation frequency), so that no PA signal is coherently generated with the laser modulation. This explains the very small PA signal observed when measuring CH₄ in O₂. The situation is totally different for CH₄ diluted in N₂, as the first vibrational state of N₂ has a larger energy than CH₄^{*}(*ν*₄) level, so that no efficient V-V transfer can occur.

In the different N₂/O₂ mixtures considered in Figure 5.9, two different relaxation pathways may be followed by the CH₄ excited molecules. The first one involves CH₄-N₂ collisions that result in the V-T process (reaction *R*₅) that generates a PA signal at all considered modulation frequencies. The second involves CH₄-O₂ collisions that result in the resonant V-V transfer (reaction *R*₃) and in an accumulation of the energy in the O₂^{*}(*ν*) excited state. CH₄-CH₄ collisions may be neglected here since the considered CH₄ concentration is several orders of magnitude smaller than N₂ and O₂ concentrations. In the second relaxation pathway (CH₄-O₂ collisions), the transfer into kinetic energy is limited by the long relaxation time of the excited O₂^{*}(*ν*) state for

both O₂-N₂ and O₂-O₂ collisions according to reactions R_7 and R_8 in Table 5.2. A very high value of the parameter $\omega\tau$ is obtained in this case for each resonance ($\omega\tau \cong 100, 300$ and 500 for modes (100), (003) and (005), respectively). According to equation (5.39), it implies that this energy is almost entirely lost for the generation of the PA signal for the three resonances and only the energy relaxed through CH₄-N₂ collisions contributes to the PA signal. When the O₂ concentration is raised, the amount of energy transferred to O₂ rapidly increases and the PA signal is reduced accordingly, which qualitatively explains the behaviour observed in Figure 5.9(a). The fact that only the V-T process induced by CH₄-N₂ collisions contributes to the PA signal explains the similar behaviour observed for the three considered frequencies. In addition, the phase of the PA signal is also affected when increasing the O₂ concentration, since the relaxation time corresponding to CH₄-N₂ collisions depends on the N₂ concentration. This leads to a linear variation of the phase as qualitatively observed in Figure 5.9(b).

A quantitative model based on the explanations given above was applied to attempt to extract relaxation times (see Appendix A for details of the model). In principle, the relaxation time $\tau_{CH_4-N_2}$ can be obtained by a fitting procedure on the data from Figure 5.9. This fitting requires the value of $\tau_{CH_4-O_2}$ corresponding to the V-V transfer described by reaction R_3 . Unfortunately, this value was not found in the literature, so that the relaxation time $\tau_{CH_4-N_2}$ could not be determined. The fitting process was thus used to obtain a value of $\tau_{CH_4-O_2}$ by taking a value of $\tau_{CH_4-N_2}$ that was reported in reference [25].

Relation (A.10) was used for the fitting process, since the PA signal is proportional to the heat deposition rate. For the first longitudinal frequency, the relaxation rate was $k(100)_{CH_4-O_2} = (1.05 \pm 0.052)10^6 \text{ s}^{-1} \text{ atm}^{-1}$, for the third longitudinal frequency, the relaxation rate was $k(300)_{CH_4-O_2} = (1.16 \pm 0.085)10^6 \text{ s}^{-1} \text{ atm}^{-1}$ and finally for the fifth longitudinal frequency, the relaxation rate was $k(500)_{CH_4-O_2} = (1.33 \pm 0.12)10^6 \text{ s}^{-1} \text{ atm}^{-1}$. The error is given by the standard deviation of the fitting process. All these values are consistent among them, but can unfortunately not directly be compared to other values. However, a rate constant of the transfer O₂-CH₄ was found in [32]. According to the same authors, the ratio $k_{CH_4-O_2}/k_{O_2-CH_4}$ is simply the ratio of the equilibrium populations of level O₂^{*}(ν) to CH₄^{*}(ν_4). Since these two levels are in resonance, their population is assumed to be the same. The corresponding rate constant found in [32] is $k_{O_2-CH_4} = (1.61 \pm 0.3)10^6 \text{ s}^{-1} \text{ atm}^{-1}$, in fair agreement with the experimental values. However, it must be pointed out that the results obtained by the fitting process are highly dependent on the value of $k_{CH_4-N_2}$, so that the product between these parameters is constant. The experimental value obtained in this case is thus an approximation that gives an idea of the order of magnitude of the value.

Due to the strong and very fast coupling between CH₄^{*}(ν_4) and O₂^{*}(ν) states, the negative influence of oxygen on the generation of the methane PA signal is already significant even for small O₂ concentrations (some percents) in the carrier gas. Therefore, such a situation may even be encountered when monitoring CH₄ in ambient air (21% O₂) in relatively dry conditions. In addition, this effect is due to the resonant coupling between the lower CH₄ energy level (ν_4) and the first vibrational mode of O₂ as described herein. It is therefore independent of the upper level of the molecular transition excited by the laser radiation. This has been confirmed by measurements performed

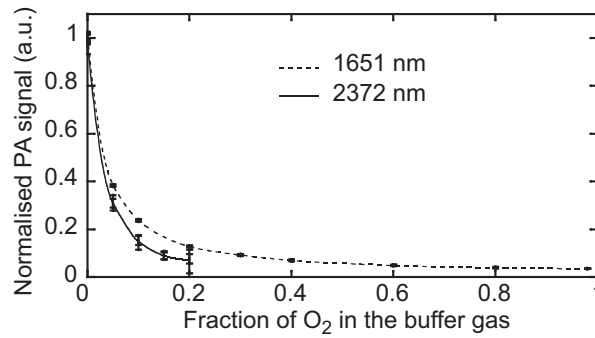


Figure 5.11: Variation of the PA signal (amplitude of the first longitudinal resonance) as a function of the O₂ concentration in the buffer gas for two different excited CH₄ transitions: $2\nu_3$ in polyad P4 ($\lambda = 1651$ nm) and $\nu_1 + \nu_4$ in polyad P3 ($\lambda = 2372$ nm). A CH₄ concentration of 100 ppm was considered and the PA signals were normalised at each wavelength to the value obtained in pure N₂. *Error bars* shown on the experimental data correspond to the standard deviation of the fitting process used to determine the parameters of the acoustic resonance.

in the 2.37 μm range ($\nu_1 + \nu_4$ band belonging to the lower polyad P3) using a new type of GaSb-based semiconductor DFB lasers [33]. It may be noticed in Figure 5.11 that the reduction of the PA signal observed when increasing the O₂ concentration in the carrier gas is comparable between the 1.65- μm and the 2.37- μm absorption bands (it is even slightly more important at 2.37- μm).

A similar behaviour has already been reported for the detection of CH₄ in O₂/N₂ mixtures in the fundamental ν_4 vibrational band [34]. In that case, a 150 deg phase lag of the PA signal was observed and this phenomenon was considered as a kinetic cooling effect, due to its similarity with the CO₂ kinetic cooling. The behaviour reported here for the CH₄-O₂ system is also induced by molecular relaxation effects, but some experimental evidences show it is distinct from a kinetic cooling. Firstly, the CH₄ transition of interest ($2\nu_3$ or $\nu_1 + \nu_4$) does not belong to a hot band, in opposite to the kinetic cooling of CO₂. Furthermore, the observed phase shift of the PA signal is very far from the theoretical value of 180 deg achieved in the case of kinetic cooling. Molecular relaxation effects in the CH₄-O₂ mixture are responsible for a delay in the PA signal generation, but no effective cooling occurs.

5.7.2 Parabolic response of the sensor with respect to CH₄ concentration

The response of the PA sensor to varying methane concentration is shown in Figure 5.12 for different buffer gas compositions: pure N₂, 60% O₂/40% N₂ dry and humidified with 0.15% or 1.1% of water vapor (absolute humidity). For these measurements, both the amplitude and the phase of the PA signal have been continuously recorded at the center of the first resonance during 5 minutes. The average value and the standard deviation of the data have been determined in each case. A mixture containing 60% of O₂ and 40% of N₂ was chosen for the following reasons: (i) in order to be not influenced by other undesirable parameters (variation of the resonance frequency, broadening of

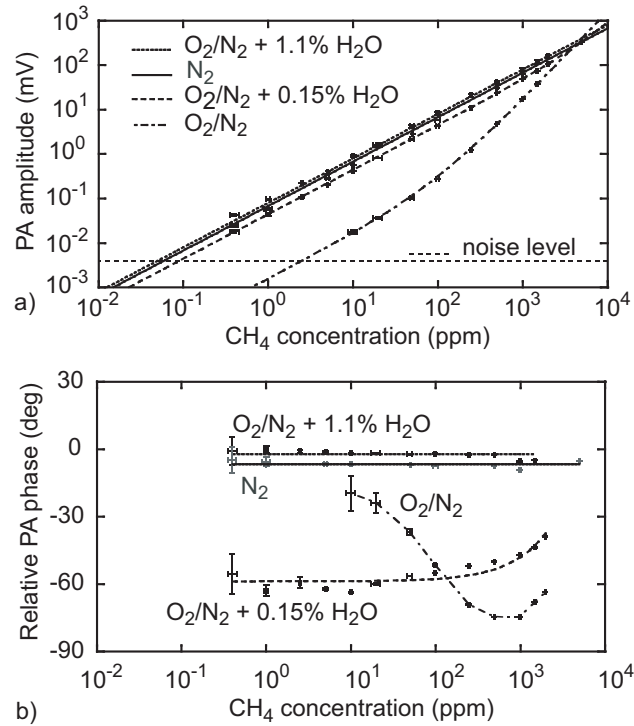


Figure 5.12: Amplitude (a) and phase (b) variation of the PA signal measured at the first longitudinal resonance as a function of the CH₄ concentration for different carrier gases: pure N₂, dry 60% O₂/40% N₂, 60% O₂/40% N₂ humidified with 0.15% and 1.1% H₂O (absolute humidity). *Error bars* shown on the plot correspond to the uncertainty on the CH₄ concentration generated with the MFCs (horizontal axis) and to the standard deviation of the PA signal recorded in a 5-minutes period (vertical axis). *Lines* in (a) are the result of a fit by a linear function (for pure N₂ and O₂/N₂ with 1.1% H₂O) or by the sum of a linear and a quadratic term (for dry O₂/N₂ and O₂/N₂ with 0.15% H₂O). In (b), *lines* correspond to a constant phase for N₂ and O₂/N₂ with 1.1% H₂O and to a linear fit for O₂/N₂ with 0.15% H₂O. For the dry O₂/N₂ mixture, the *line* is just an interpolation between the experimental points.

the absorption line), it was chosen to keep always the same mixing ratio between N₂ and O₂ for all considered CH₄ concentrations; (ii) as the certified cylinders were buffered in N₂, it was not possible to dilute methane in pure O₂; with only 60% of O₂, a wide variety of methane concentrations could be achieved, ranging from 2000 ppm down to 0.4 ppm; (iii) molecular relaxation effects already have a strong influence in a mixture containing 60% of O₂ as shown in Figure 5.9.

Figure 5.12 shows a similar response of the sensor when either pure N₂ or a O₂/N₂ mixture with a high H₂O content (1.1% absolute humidity) is considered. In both cases, a very good linearity ($R > 0.99$) is obtained over more than four orders of magnitude of concentration. The phase of the PA signal also remains constant over the full range of CH₄ concentrations. The CH₄ level resulting in a noise-equivalent signal was found to be 60 ppb for the first longitudinal resonance (for 10 s integration time).

The measured signal was even slightly higher in the humidified O₂/N₂ mixture than in pure N₂, which may suggest that a very small influence of relaxation effects even occurs in pure N₂. This assumption seems to be confirmed by the small phase difference observed between these two carrier gases. The relaxation time may be estimated by the use of the difference in the phase values between these two cases and by using relation (A.11). The phase difference is -5.1° , corresponding to a relaxation time $\tau_{CH_4-N_2}$ of $6 \cdot 10^{-6}$ s at 1 atm or a rate $k_{CH_4-N_2}$ of $16 \cdot 10^4$ s⁻¹atm⁻¹ which is twice the value given in reference [25]. Here again, the experimental value does not exactly match the value given in the literature, but gives a good approximation. The difference between the measured and the experimental value may be due to a small change in the experimental conditions when the phase is measured in humidified O₂/N₂ mixture or in pure N₂. In the two cases, the frequency is slightly different (926 Hz in pure N₂ and 965 Hz in the humidified O₂/N₂ mixture) which directly influences the phase.

A strongly different behaviour was observed when a dry or weakly humidified (0.15% absolute humidity) O₂/N₂ mixture was used as a carrier gas. In these cases, the PA signal was no longer linear, but was expressed as the sum of a linear and a quadratic term (clearly visible for the dry O₂/N₂ mixture). The CH₄ concentration resulting in a noise-equivalent signal was depreciated to 2.5 ppm in dry O₂/N₂ (for 10 s integration time). The phase of the PA signal is also changing as a function of the CH₄ concentration, and the phase variations are larger for the dry O₂/N₂ mixture.

The parabolic response with respect to the CH₄ concentration observed in presence of O₂ is also a clear indication of the importance of relaxation effects in the CH₄-O₂ system. Whereas the collisional V-T relaxation of O₂^{*}(ν) is very slow for O₂-O₂ collisions, it is more than four orders of magnitude faster for O₂-CH₄ collisions (see reaction R₁₁ in Table 5.2). So even for small CH₄ concentrations, the relaxation time of O₂^{*}(ν) state is reduced when increasing the CH₄ concentration. According to equation (5.40), a linear variation of the relaxation rate is obtained for small CH₄ concentrations:

$$\tau_{O_2}^{-1} \cong \tau_{O_2-O_2}^{-1} + C_{CH_4} \tau_{O_2-CH_4}^{-1} \quad (5.41)$$

By combining equations (5.39) and (5.41), the dependence of the PA signal can finally be expressed as the sum of a linear and a quadratic term, which

fully explains the experimental observations:

$$S_{PA} \cong C_{cell} C_{CH_4} \frac{\alpha P_0}{\omega} \left(\tau_{O_2 - O_2}^{-1} + C_{CH_4} \tau_{O_2 - CH_4}^{-1} \right) \quad (5.42)$$

Therefore, the experimentally observed parabolic response results from a double linear dependence of the PA signal to the CH_4 concentration. The first contribution is the usual linear variation on the gas concentration, due to the increasing amount of energy absorbed in the sample. The second is directly induced by the variation of the molecular relaxation rate with the CH_4 concentration as described by equation (5.41).

The phase variation of the PA signal observed in dry or weakly humidified (0.15% H_2O) O_2/N_2 mixtures is more difficult to be quantitatively explained. However, a qualitative interpretation may be given based on the previous argumentation about V-T transfers in a $CH_4/N_2/O_2$ mixture. The phase evolution observed in the dry O_2/N_2 mixture may be qualitatively explained by the characteristics of the relaxation scheme occurring in different ranges of concentration. For low CH_4 concentration, the energy transferred to $O_2^*(\nu)$ via the resonant process R_3 is lost for the PA signal due to the long-lifetime relaxation of $O_2^*(\nu)$. In that case, only V-T process due to CH_4-N_2 collisions (reaction R_5) contributes to the PA signal and the phase of this signal is expected to tend to 0 degree, which seems to correspond to the tendency of the experimental curve at low CH_4 concentration. On the other hand, the $O_2^*(\nu)$ V-T relaxation is strongly fastened at high CH_4 concentrations (reaction R_{11}) and becomes comparable to or faster than one period of the laser modulation. Therefore, the energy transferred to $O_2^*(\nu)$ partially contributes to the PA signal and the phase tends again to 0 degree when the $O_2^*(\nu)$ relaxation is fast enough, i.e. at high CH_4 concentration. In the intermediate range of concentration, the two above mentioned relaxation pathways contribute to the PA signal, with their own amplitude and phase depending on the CH_4 concentration. In particular, the contribution of O_2-CH_4 collisions leads to a phase shift since the factor $\omega\tau$ is non-negligible in the intermediate range of concentration ($\omega\tau \cong 1$). When a small quantity of water vapour (0.15% as in Figure 5.12) is added to the sample, the relaxation of $O_2^*(\nu)$ is promoted and even at very low CH_4 concentration, the energy transferred to $O_2^*(\nu)$ slightly contributes to the PA signal. This contribution increases with the CH_4 concentration due to the associated reduction of the relaxation time (see equation (5.41)). In this case, the phase of the PA signal changes monotonously with the CH_4 concentration as observed in figure 5.12(b).

If the above qualitative arguments allow to explain the observed experimental results, a more detailed analysis reveals large deviation of the measured values from the data calculated by the relaxation rates given in Table 5.2. This discrepancy may result from some erroneous values indicated in Table 5.2, but it may also indicate that the relatively simple relaxation scheme we have considered is incomplete and that other processes may contribute to the relaxation or other physical processes may play a role in the generation of the PA signal. In particular, the rotational energy transfer that contributes to the relaxation scheme of methane was not taken into account.

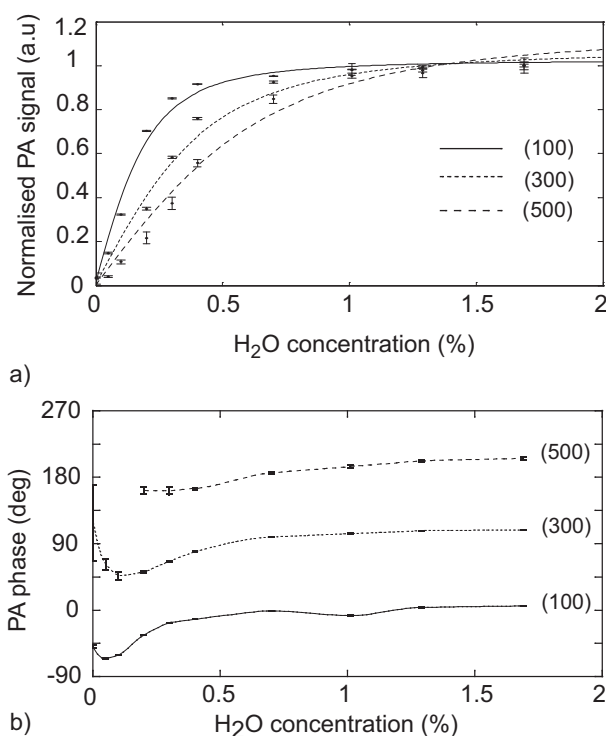


Figure 5.13: Amplitude (a) and phase (b) dependence of the PA signal corresponding to 20 ppm of CH₄ as a function of the H₂O content in the carrier gas (composed of 60% O₂ and 40% N₂) for the three acoustic resonances. *Error bars* shown on the plot correspond to the standard deviation of the PA signal recorded in a 5-minutes period. In (a), the *lines* are the results of a fitting process (see text for details). In (b), the lines are an interpolation between experimental points.

5.7.3 Enhancement of the V-T process rate in CH₄-O₂ mixture using a catalyst

Not only CH₄ is efficient to promote the V-T relaxation of O₂^{*}(ν), but some other species may also act as a catalyst for this relaxation. For example, water vapour is known to promote the vibrational relaxation of several species, including O₂ (see reaction *R*₉ in Table 5.2). This is confirmed by the experimental results shown in Figure 5.13, where the variation of the PA signal (amplitude and phase) corresponding to 20 ppm of CH₄ is displayed as a function of the water content in the 60% O₂/40% N₂ carrier gas. For these measurements, both the amplitude and the phase of the PA signal have been recorded at the centre of the three resonances during 5 minutes and the average value and the standard deviation of the data have been determined. A constant signal amplitude is obtained for water vapour contents higher than 1% (absolute humidity), but a strong reduction of the signal is observed below 1% humidity. Furthermore, measurements performed using different acoustic resonances have shown that the decrease of the PA signal occurs at larger H₂O concentrations for higher frequencies. A similar behaviour is observed on the phase of the PA signal. All these observations qualitatively demonstrate the catalyst effect of water vapour for the relaxation of O₂^{*}(ν).

A quantitative analysis to extract the relaxation time $\tau_{O_2-H_2O}$ was per-

formed by fitting the data obtained in Figure 5.13. This model was based on a simple two level system, where the whole energy is stored in the excited $O_2^*(\nu)$ level and deactivates to the ground level through reactions R_7 , R_8 , R_9 and R_{11} , resulting in a total relaxation rate:

$$\tau^{-1} = C_{O_2}\tau_{O_2-O_2}^{-1} + C_{N_2}\tau_{O_2-N_2}^{-1} + C_{H_2O}\tau_{O_2-H_2O}^{-1} + C_{CH_4}\tau_{O_2-CH_4}^{-1} \quad (5.43)$$

The fitting function applied on the data is given by:

$$S_{PA} = \frac{S_0}{\sqrt{1 + (\omega\tau)^2}} \quad (5.44)$$

where S_0 is the signal obtained when no relaxation effects occurs, i.e. at high H_2O concentrations. The fitting process was applied on each resonance frequency resulting in a relaxation time $\tau_{O_2-H_2O}$ of $4.16 \cdot 10^{-7}$, $2.94 \cdot 10^{-7}$, $2.7 \cdot 10^{-7}$ s at 1 atm for the first, third and fifth longitudinal mode respectively. It results in a relaxation time 1.5 times larger for the first longitudinal mode in comparison with the fifth longitudinal mode. These relaxation times are to be compared with the value given in relation R_9 , resulting in a relaxation time of $9.09 \cdot 10^{-7}$ s atm, which is 2.2 times larger than the value measured in the first longitudinal mode. This difference may be explained by the fact that the direct V-T energy transfer CH_4-H_2O was not considered in the model. Even though no relaxation value was found in literature, the corresponding relaxation time is expected to be small due to the catalyst properties of H_2O . This influence on the measured relaxation times may also explain the difference between the three resonances, since it is not clear how this deactivation path occurs. This discrepancy prevents the development of a precise quantitative description of the relaxation of the considered system based on the relatively simple relaxation scheme that has been proposed and using typical relaxation rates previously published in the literature.

Another species that has demonstrated to efficiently promote the vibrational relaxation of O_2 is helium (see reaction R_{12} in Table 5.2). This is of great importance for the application described in section 4.2.2 (CH_4 monitoring in the manufacturing of ZWPF), as helium is used in large quantities (several tens of percents) in this process. The beneficial influence of helium as a catalyst for the V-T relaxation of $O_2^*(\nu)$ in the generation of the PA signal is illustrated in Figure 5.14.

The amplitude of the PA signal is displayed as a function of the CH_4 concentration in four different carrier gases: N_2 , O_2 , He and a mixture of 90% O_2 and 10% He. Excepted for N_2 , the results displayed in Figure 5.14 were not achieved with pure carrier gases. Since the CH_4 certified cylinders were buffered in nitrogen, a residual of N_2 was always present in the gas mixtures considered in Figure 5.14. However, this N_2 residual was smaller than 2% for CH_4 concentrations below 100 ppm and its influence on the experimental results is estimated to be of minor importance, so that it can be neglected. The signal measured in He is lower than in N_2 due mainly to the much higher resonance frequency (around 2.5 kHz) induced by the faster acoustic velocity in He and to the smaller quality factor of the resonance that results from the difference in some other physico-thermal parameters of the gas, such as the density, viscosity and thermal conductivity. But the difference observed

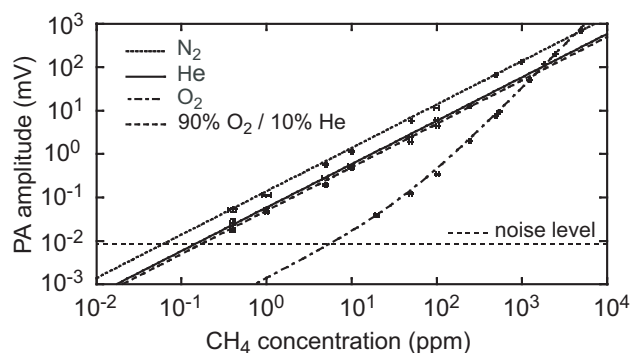


Figure 5.14: Variation of the PA signal corresponding to the first longitudinal resonance as a function of the CH₄ concentration for different carrier gases (N₂, O₂, He and 90% O₂/10% He). A residual of a few percents of N₂ is always present in the gas mixtures since the CH₄ certified cylinders were buffered in nitrogen. *Error bars* shown on the plot correspond to the standard deviation of the PA signal recorded in a 5-minutes period. *Lines* are the result of a fit by a linear function for N₂, He and O₂/He mixture, and by the sum of a linear and a quadratic term for O₂.

between N₂ and He is not at all related to relaxation effects. With the adjunction of only 10% of helium, the signal measured in O₂ reaches almost the same level as in pure He. The O₂^{*}(ν) relaxation rate in an O₂/He mixture may be calculated according to equation (5.40): with 10% of helium, it decreases from 15 ms (in O₂) to 0.4 ms, which becomes smaller than the laser modulation period. Consequently, the absorbed laser energy contributes to the generation of the PA signal and the usual behaviour is again observed (linear variation of the PA signal with the CH₄ concentration). This positive influence of helium makes possible the detection of methane at sub-ppm level for process control in the manufacturing of the ZWPF.

5.7.4 Conclusion

The importance of collisional relaxation processes in the PA signal generation has been demonstrated in the particular case of CH₄ detection in dry O₂ and O₂-N₂ mixtures. A negative influence of molecular relaxation effects has been observed, which resulted in a strongly reduced and phase-shifted PA signal. The origin of this phenomenon lies in the existence of a fast resonant V-V coupling between CH₄^{*}(ν_4) and O₂^{*}(ν) vibrational states, associated to a small V-T relaxation rate of the O₂^{*}(ν) excited state. This effect is independent on the frequency of the excited CH₄ transition and is therefore expected to occur with any laser source used for the detection of CH₄ in O₂/N₂ mixtures by PAS. This has been confirmed by the experimental results obtained on two different NIR absorption bands of methane ($2\nu_3$ at 1.65- μm and $\nu_1 + \nu_4$ at 2.37- μm) using two types of semiconductor DFB lasers.

A qualitative theoretical explanation of the relaxation phenomena involved in the experimental observations has been proposed. However, the relaxation rates calculated from data reported in the literature for different processes connected to the considered system are much smaller than the values estimated from the experimental measurements. This discrepancy shows that the proposed model is only a qualitative description of the observed phenomena and

is not able to predict quantitative data, such as an accurate value of the amplitude or phase of the generated PA signal. Other relaxation processes that were not taken into account probably also contribute to the PA signal. The proposed model is also only a qualitative model of the relaxation phenomena and cannot describe the full process of PA signal generation.

The beneficial effect of several species acting as a catalyst that promotes the V-T relaxation of the CH₄-O₂ system has been demonstrated. Among these substances, methane itself is one of the most efficient. As a result, a unusual parabolic variation of the PA signal with the CH₄ concentration has been observed. A non-linear response with respect to the concentration of the target species has already been reported by other authors in PAS in the case of a gas mixture containing several species diluted in a N₂/O₂ carrier gas. A well-known case occurs for the detection of NH₃ in a sample containing NH₃, CO₂ and H₂O in a N₂/O₂ buffer gas [35]. Although this situation is also induced by relaxation effects (kinetic cooling of CO₂), the non-linear response was produced in that case by the superposition of several PA signals with a different phase. The behaviour reported here is different, as the observed parabolic response occurs for a single species (CH₄) diluted in a N₂/O₂ buffer gas. This parabolic response results from a double linear dependence of entirely different origin. In addition to the usual linear response of the PA signal with respect to the gas concentration (due the increasing amount of energy absorbed in the sample), a second linear variation is induced by relaxation effects. Other species that have shown a beneficial effect on the V-T relaxation of the CH₄-O₂ system are water vapour and helium.

The dramatic reduction of the methane PA signal generated in O₂ and its high dependence on the humidity rate was also observed in O₂/N₂ mixtures containing only a few percents of O₂. Therefore, this phenomenon may also affect the monitoring of methane in ambient air (21% of O₂) by PAS, for example for atmospheric researches or greenhouse gases emission monitoring. This effect must be considered especially when working in relatively dry conditions, which certainly occurs for fields measurement during winter time, or when measurements are performed at reduced pressure (in altitude for example). The positive effect of He also makes the PAS-based sensor suitable for sub-ppm CH₄ detection for process control in the manufacturing of the novel LWPF. Without this beneficial influence, the monitoring of methane by PAS in this application would not be possible, due to the strongly reduced sensitivity induced by relaxation effects.

5.8 Molecular relaxation in HCl detection

Similar measurements were performed with hydrogen chloride to investigate relaxation processes, first in nitrogen and then in oxygen. A certified cylinder of 50 ppm HCl diluted in He was used to make the different dilutions with N₂ or O₂. The variation of the percentage of N₂/He or O₂/He has different effects on the PA signal besides relaxation effects. It was discussed in subsection 4.3.3, that the buffer gas principally influences the resonance frequency, the quality factor and the cell constant, which are all directly related to the PA signal. For instance, the frequency was about 1000 Hz in N₂ and 2700 Hz in He. Moreover, the sensitivity of the microphone is frequency-dependent and the broadening of the considered absorption line is different in helium

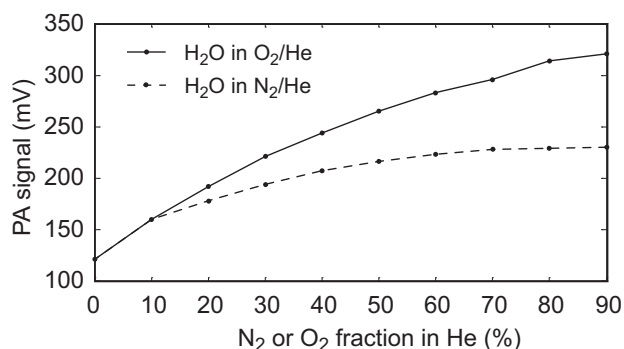


Figure 5.15: Normalisation curves performed in H₂O diluted in a mixture of N₂-He (*dashed curve*) and in a mixture of O₂-He (*solid curve*). The PA signal difference is mainly due to the difference of the line broadening coefficients of H₂O in O₂ and in N₂.

than in oxygen or nitrogen. In order to separate the effects due to molecular relaxation from the other effects, a normalisation curve was performed.

The selected gas used for normalisation was H₂O, since no relaxation effects occur for this substance. The PA signal was recorded in the same gas mixture (N₂/He and O₂/He) than the one used for HCl measurement. A concentration of 1% of H₂O was measured at 1369 nm. Results are presented in Figure 5.15. This normalisation curve takes into account the effects on the quality factor, on the resonance frequency and on the microphone response. However, additional effects due to the broadening of the linewidth were not corrected with this normalisation. For instance, the broadening of the water vapour absorption line is dependent on the buffer gas and is different than for the HCl absorption line. A theoretical investigation through simulations was performed to estimate the error produced by the line broadening.

Wavelength modulation was applied through the laser injection current with a fixed amplitude optimised to maximise the PA signal in air for H₂O and in a 50% O₂-50% He mixture for HCl. This amplitude was then kept fixed during all measurements, whereas the DC current was slightly adjusted to maximise the PA signal.

The pressure broadening of the R3 HCl line in the 2ν band located at 1742.4 nm ⁵ is about 80% larger in O₂ than in He and more than 3 times higher in N₂ than in He (see Table 5.3) [36]. The broadening coefficients for the H₂O absorption line located at 1368.7 nm in He, N₂ and O₂ were not available, so that the parameters were taken from an absorption line located at 1393.5 nm [37]. The differences in the broadening coefficients between these two lines were about 3% and 4% for the air and self broadening coefficients, respectively. It was thus considered that the broadening coefficients in He, N₂ or O₂ mixtures were similar for the two lines.

The simulations were performed for a Lorentzian distribution and for two types of modulation, pure intensity modulation and pure wavelength modulation ⁶. Intensity modulation takes into account the broadening coefficient of

⁵No data was found for the R4 line used in this work, but since the air and self broadening coefficient were similar for the R3 and for the R4 lines (see Table 5.3), the effect of the gas mixture was considered to be the same for the R4 line.

⁶For WM, the phase on the lock-in was adjusted to obtain the maximum of the PA signal.

	Measurements		Simulations	
	H ₂ O	HCl	H ₂ O	HCl
λ (nm)	1368.7	1738.9	1393.5	1742.4
Identification	See ^a	R4	See ^b	R3
Strength (cm ⁻¹ /(mol·cm ⁻²))	1.01·10 ⁻²¹	9.67·10 ⁻²¹	2.72·10 ⁻²²	1.16·10 ⁻²⁰
γ_{air} (cm ⁻¹)	0.093	0.0537	0.0958	0.0624
γ_{self} (cm ⁻¹)	0.51	0.2178	0.488	0.2408
γ_{He} (cm ⁻¹)	-	-	0.0221	0.0221
γ_{N_2} (cm ⁻¹)	-	-	0.1130	0.0753
γ_{O_2} (cm ⁻¹)	-	-	0.0644	0.0401

Table 5.3: Parameters of the line used in the measurements and in the simulations. The broadening coefficients are given at a pressure of 1 atm.

$$^a(0\ 0\ 0)2_{1,2} \rightarrow (1\ 0\ 1)3_{1,3}$$

$$^b(0\ 0\ 0)3_{2,2} \rightarrow (1\ 0\ 1)3_{0,3}$$

the line, whereas the effect of the modulation depth does not contribute. For WM, the signal depends on the normalised WM index m given by [38]

$$m = \frac{\Delta\nu}{\Delta\nu_r} \quad (5.45)$$

where $\Delta\nu$ is the frequency deviation of the optical carrier and $\Delta\nu_r$ is the absorption line width. m is thus dependent on the gas composition, since the broadening of the line changes and produces a variation of the PA signal.

Results of the simulations performed in a He-N₂ mixture are presented in Figure 5.16. For IM modulation, the ratio of the absorption coefficients varies from 0.168 in 100% N₂ to 0.135 in He, resulting in a change of 20%. For WM, the ratio of the PA signals changes by less than 25%. In consequence, the residual error produced by the normalisation curve is estimated to be about 25%.

Identical simulations were performed in a He-O₂ mixture whose results are shown in Figure 5.17. For IM modulation, the ratio of the amplitudes varies from 0.187 in 100% O₂ to 0.135 in He, resulting in a change of 28%. For WM, the ratio changes by about 7%. In consequence, the maximum residual error produced by the normalisation curve in a mixture of O₂-He is estimated to be less than 10%. The variation of the ratio HCl/H₂O is smaller for WM than for IM, probably due to the fact that the effect of the line broadening on m is partially compensated by the variation of the absorption coefficient in the centre of the line.

Finally, this normalisation curve has been realised with a laser that was different to the one used to measure HCl concentration resulting in a difference in the modulation parameters. In particular, the ratio $\Delta\nu/\Delta i$, where $\Delta\nu$ is defined above and Δi is the modulation current, changes with the modulation frequency [39] and is laser dependent. However, since the lasers were provided by the same manufacturer and that the operating points were similar, this effect was neglected.

HCl is a polar diatomic molecule with one vibrational mode whose first energy level ($\nu = 1$) is located at 2886 cm⁻¹. The spectroscopic properties of HCl required to understand the relaxation effects are described in [40, 41, 42, 43] and rovibrational energy transfer processes in HCl-O₂/N₂/He are also

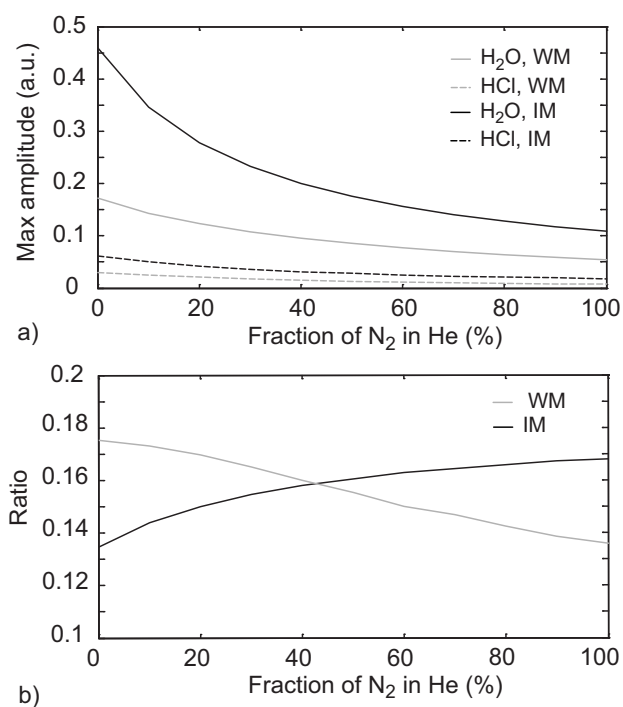


Figure 5.16: (a) Simulation of the maximum of the absorption coefficient (IM) and the corresponding $1f$ signal (WM) as a function of the N_2 fraction in the buffer gas for H_2O and HCl . (b) The variation of the ratio of HCl to H_2O gives the error in the measurement.

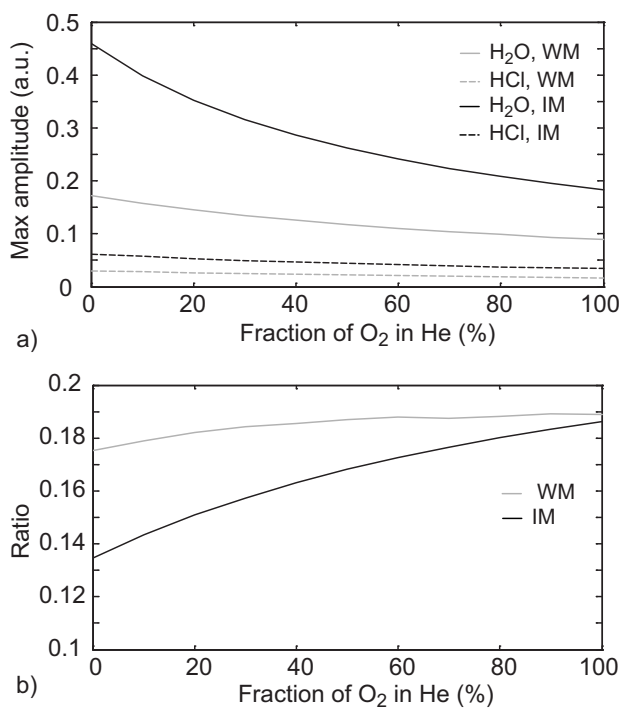


Figure 5.17: (a) Simulation of the maximum of the absorption coefficient (IM) and the corresponding $1f$ signal (WM) as a function of the O_2 fraction in the buffer gas for H_2O and HCl . (b) The variation of the ratio of HCl to H_2O gives the error in the measurement.

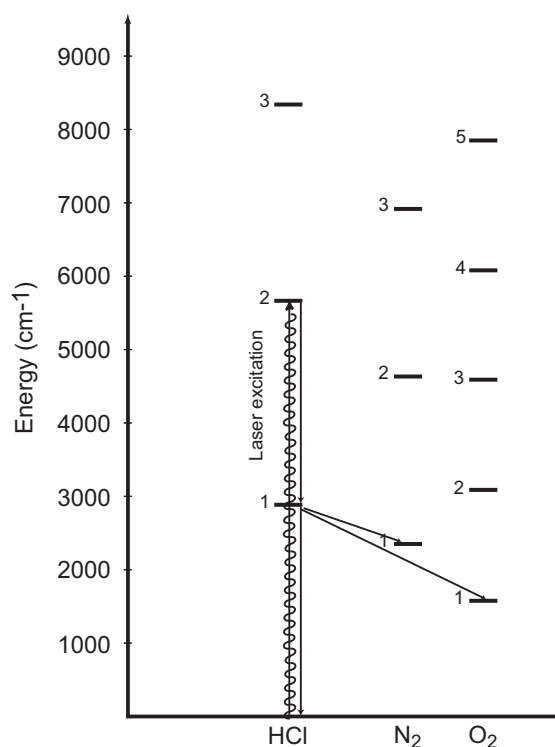


Figure 5.18: Energy level diagram of HCl, showing the laser excitation to the $\nu = 2$ state and the subsequent relaxation scheme through V-V transfer to N₂ or O₂.

discussed in a series of papers [44, 45, 46, 47]. In addition, the relaxation rates for different reactions are summarised in Table 5.4.

5.8.1 Relaxation effects in the HCl-He-N₂ system

In order to investigate molecular effects of HCl in a He-N₂ mixture, the response of the sensor to 5 ppm HCl in different ratios of He-N₂ was measured. Results are shown in Figure 5.19. A rapid decrease of the PA signal occurs when N₂ is added in the gas mixture due to relaxation effects. For a concentration of N₂ larger than 70%, the PA signal is almost stable and reaches a value reduced by 75% in 90% of N₂ compared to the pure He mixture. These results may be explained by considering the deactivation pathway followed by HCl molecules excited by the laser radiation and the energy levels of HCl and N₂ in combination with the corresponding rate constants (see Figure 5.18 and Table 5.4).

The principal properties are described in the following paragraph to understand, at least qualitatively, the effects of relaxation in an HCl/He/N₂ mixture. Since the laser diode emits at 1738 nm corresponding to the vibrational state ($\nu = 2$) of HCl, this level is highly populated and rapid subsequent deactivation to the lower level ($\nu = 1$) occurs through collisions with N₂ and He. This transition is the most probable, since it corresponds to the smallest energy quantum. HCl molecules in the ($\nu = 1$) level deactivate through collisions with He and N₂ (HCl-HCl collisions were neglected due to the low HCl concentration (<50 ppm)). The deactivation from level ($\nu = 2$) and from level ($\nu = 1$) occurs identically through two different pathways, one through

Reaction	Rate ($\text{s}^{-1}\text{atm}^{-1}$)	Ref.
R₁ $\text{HCl}^*(\nu = 1) + \text{HCl} \rightarrow \text{HCl}(\nu = 0) + \text{HCl}$	$6.3 \cdot 10^5$	[47]
R₂ $\text{HCl}^*(\nu = 1) + \text{He} \rightarrow \text{HCl}(\nu = 0) + \text{He}$	$1.5 \cdot 10^3$	[44]
R₃ $\text{HCl}^*(\nu = 1) + \text{H}_2\text{O} \rightarrow \text{HCl}(\nu = 0) + \text{H}_2\text{O}$	$3.8 \cdot 10^8$	[47]
<i>R₄</i> $\text{HCl}^*(\nu = 2) + \text{HCl} \rightarrow \text{HCl}^*(\nu = 1) + \text{HCl}^*(\nu = 1)$	$7.2 \cdot 10^7$	[40]
<i>R₅</i> $\text{HCl}^*(\nu = 1) + \text{O}_2 \rightarrow \text{HCl}(\nu = 0) + \text{O}_2^*(\nu = 1)$	$8.1 \cdot 10^4$	[44]
<i>R₆</i> $\text{HCl}^*(\nu = 1) + \text{N}_2 \rightarrow \text{HCl}(\nu = 0) + \text{N}_2^*(\nu = 1)$	$6.6 \cdot 10^5$	[47]
R₇ $\text{N}_2^*(\nu = 1) + \text{N}_2 \rightarrow \text{N}_2(\nu = 0) + \text{N}_2$	1	[27]
R₈ $\text{N}_2^*(\nu = 1) + \text{He} \rightarrow \text{N}_2(\nu = 0) + \text{He}$	$1.45 \cdot 10^2$	[48]
R₉ $\text{N}_2^*(\nu = 1) + \text{H}_2\text{O} \rightarrow \text{N}_2(\nu = 0) + \text{H}_2\text{O}$	$1.1 \cdot 10^5$	[27]
R₁₀ $\text{O}_2^*(\nu = 1) + \text{O}_2 \rightarrow \text{O}_2(\nu = 0) + \text{O}_2$	63	[27]
R₁₁ $\text{O}_2^*(\nu = 1) + \text{He} \rightarrow \text{O}_2(\nu = 0) + \text{He}$	$2.3 \cdot 10^4$	[29]
R₁₂ $\text{O}_2^*(\nu = 1) + \text{H}_2\text{O} \rightarrow \text{O}_2(\nu = 0) + \text{H}_2\text{O}$	$1.1 \cdot 10^6$	[28]

Table 5.4: Examples of some relaxation rates of some vibrational states of HCl with different collisional partners. Reactions labelled in **bold** correspond to V-T processes, the others to V-V processes.

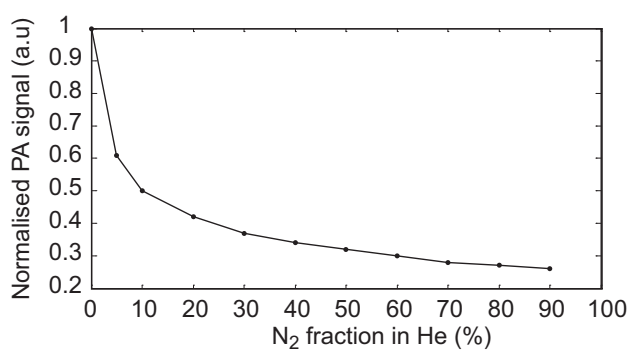


Figure 5.19: Variation of the PA signal amplitude corresponding to 5 ppm HCl as a function of N₂ fraction in He. The PA signal is normalised by the PA signal recorded for H₂O and normalised to the value obtained in pure helium.

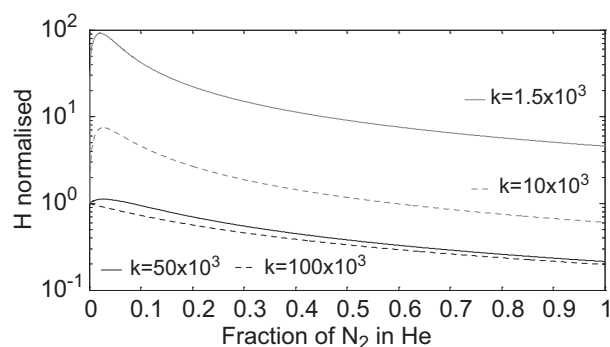


Figure 5.20: Simulation of H based on equation (A.15) and normalised by $H(C_{N_2} = 0)$ for different values of k_{HCl-He} (in $s^{-1}atm^{-1}$).

He collisions and one through N_2 collisions. Collisions with He molecules occur via relation R_2 , which is a direct V-T transfer that contributes to the PA signal. However, a relaxation time found in [44], $\tau_{HCl-He} = 6.7 \cdot 10^{-4}$ s at a pressure of 1 atm is not short enough to ensure $\omega\tau \ll 1$ (in this case, $\omega\tau = 12$), so that the PA signal is already expected to be reduced in He.

When N_2 is added to the gas mixture, according to the energy diagram, part of the energy released is transferred to the first level of N_2 ($\nu = 1$, $\tilde{\nu}_{N_2} = 2330$ cm^{-1}) through V-V process, which is the most probable energy transfer (see section 5.4). The path through N_2 is much more efficient (400 times) than through He (see reactions R_2 and R_6), so that part of the energy transfers to N_2 . In this case, the energy transfer is not resonant (in contrast with CH_4 deactivation in O_2) and only the part of the energy $\Delta E = \tilde{\nu}_{HCl} - \tilde{\nu}_{N_2} = 555$ cm^{-1} contributes to the PA signal. The reason for this, is that the deactivation of the excited level of N_2 to the ground state via V-T transfer is very slow ($\tau = 1$ s at 1 atm), so that $\omega\tau \gg 1$ and no PA signal is coherently generated with the laser modulation. The percentage of energy stored in the first excited level of N_2 ($\nu = 1$) is 80%, corresponding to $\tilde{\nu}_{N_2}/\tilde{\nu}_{HCl}$. The presence of He in this case does not improve the situation, since the relaxation time of the V-T transfer N_2 -He is not small enough ($\tau_{N_2-He} = 6.9 \cdot 10^{-3}$ s at 1 atm, reaction R_8) to obtain the condition $\omega\tau \ll 1$ and to recover part of the PA signal.

A more quantitative analysis based on the model described in Appendix A was attempted. Simulations of relation (A.15) for different rate k_{HCl-He} are presented in Figure 5.20. These simulations show that the heat production rate H is strongly dependent on the parameter k_{HCl-He} and that the behaviour of the signal is completely different for the considered k values. A fair matching between experimental results and the simulation is obtained for a very high value of $k_{HCl-He} = 100 \cdot 10^3$ $s^{-1}atm^{-1}$, which is two orders of magnitude higher than the value given in reference [44]. It must be pointed out, that the parameter k_{HCl-He} is again dependent on the value of k_{HCl-N_2} and that the product between these two rates is almost constant. However, the value of k given in reference [44] seems to be underestimated, since the PA signal would already be reduced by a factor 12 in pure He, which is in disagreement with the experimental results shown in Figure 5.19.

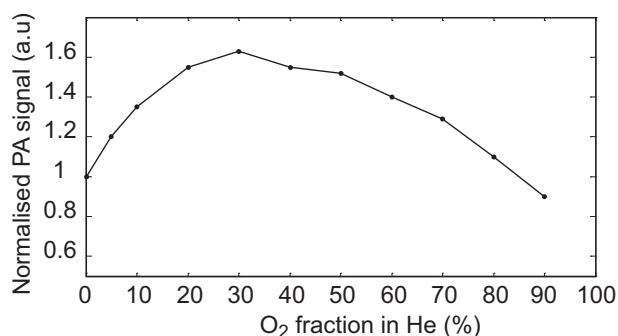


Figure 5.21: Variation of the PA signal amplitude corresponding to 5 ppm HCl as a function of O₂ fraction in He. The PA signal is normalised by the PA signal recorded for H₂O and normalised to the value obtained in pure helium.

5.8.2 Relaxation effects in the HCl-He-O₂ system

The variation of the PA response of 5 ppm HCl in different dry mixtures of He-O₂ is shown in Figure 5.21. An increase of the PA signal is obtained until the concentration of O₂ reaches 30%. From that point, the PA signal starts to decrease and reaches, in 90% of O₂, a value close to the one in pure He. These experimental results may be explained by considering the deactivation pathway followed by HCl molecules excited by the laser radiation. The deactivation of HCl from level ($\nu = 2$) to ($\nu = 1$) and ($\nu = 1$) to ($\nu = 0$) is the same than explained in the preceding section, N₂ partner being replaced by O₂ molecules. From the ($\nu = 1$) level, collisions with He are also the same than mentioned in the HCl/He/N₂ system.

When O₂ is added to the gas mixture, a second pathway is opened, so that molecules deactivate through O₂ as well. According to the energy diagram, part of the energy released is transferred to the first level of O₂ ($\nu = 1$, $\tilde{\nu}_{O_2} = 1556 \text{ cm}^{-1}$) through V-V process, which is the most probable energy transfer (see section 5.4). In this case, the energy transfer is not resonant (in contrast with CH₄ in O₂ deactivation) and only the part of the energy $\Delta E = \tilde{\nu}_{HCl} - \tilde{\nu}_{O_2} = 1330 \text{ cm}^{-1}$ that is not transferred in the first level of O₂ contributes to the PA signal. Here again, the deactivation of this level to the ground level does not contribute to the PA signal when no He is present, since the relaxation time is very long ($\tau = 1/63 \text{ s}$ at 1 atm). In Figure 5.21, the PA signal increases after a few percent of O₂ which can be explained as follow: the relaxation of HCl is about 50 times more efficient with O₂ collisions than with He (see reactions R_2 and R_5), so that the V-V process given by R_5 is the preferred. In this process, only part of the energy ($\tilde{\nu}_{HCl} - \tilde{\nu}_{O_2}$) is transformed into kinetic energy contributing to the PA signal, the remaining being transferred into internal energy of O₂, which has a long relaxation time in the case of collisions with O₂. However, the presence of He plays the role of a catalyst for this relaxation (as already described for the case of CH₄), which drastically reduces the time decay of the O₂ excited state (see reaction R_{11}). Therefore, the energy stored in the O₂ ($\nu = 1$) level deactivates fast enough to contribute to the PA signal. This 2-step relaxation pathway is more efficient than the V-T process due to HCl-He collisions, which explains the initial increase of the PA signal observed when adding O₂ to He. However,

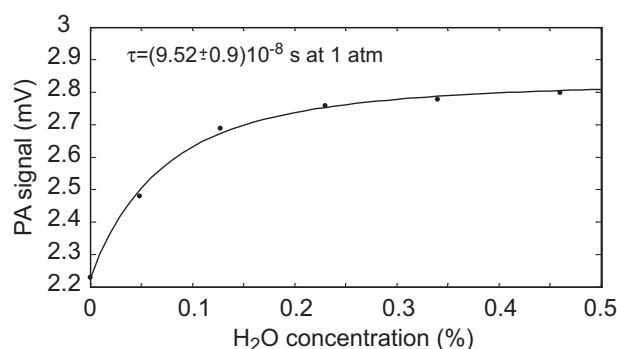


Figure 5.22: Amplitude dependence of the PA signal corresponding to 5 ppm HCl as a function of the H₂O content in the carrier gas composed of 50% O₂ and 50% He. *Dots* represents the measurement points and the *line* is the result of a fitting procedure (see text for details).

when the percentage of O₂ increases, the concentration of He is insufficient to reduce the relaxation time and the PA signal starts to decrease.

Finally, the PA signal in 90% O₂ is more important than in 90% N₂, since the part of the energy that is transferred into internal energy (to O₂ or N₂) and that is lost for the PA signal (long relaxation time) is weaker because $\tilde{\nu}_{O_2} < \tilde{\nu}_{N_2}$.

No quantitative model is proposed for this situation since this case is even more complicated than the one experienced before. The model should include a supplementary effect coming from He that plays the role of a catalyst and allow the deactivation of the first excited state of O₂ to the ground state.

5.8.3 Improvement of V-T transfers by the use of a catalyst

The role of water vapour as a catalyst was demonstrated in subsection 5.7.3 for the CH₄-O₂ system. The same procedure was applied to the HCl-He-O₂ and HCl-He-N₂ systems. Figure 5.22 shows the PA signal for a concentration of 5 ppm HCl and a varying water vapour concentration in a mixture of 50% He-50% O₂. The water-vapour content in the gas mixture was adjusted by passing part of the flow through a saturator, i.e. a water-filled glass cuvette placed in a thermostat bath. The flow exiting the cuvette was saturated in water vapour and the humidity was dependent only on the bath temperature. The H₂O concentration was then varied by changing the ratio dry O₂/(O₂+H₂O). The water vapour concentration was continuously recorded with a commercially available hygrometre to ensure the correct concentration. The PA signal increases as soon as a fraction of percent of H₂O is added to the mixture. The effect of H₂O on the deactivation of the first level of O₂ is immediate, since the relaxation time is drastically reduced (see reaction R₁₂) which improves the generation of the acoustic wave.

A quantitative relaxation time $\tau_{O_2-H_2O}$ is obtained by applying a fit corresponding to the equation:

$$S_{PA} = S_{off} + \frac{S_0 - S_{off}}{\sqrt{(1 + (\omega\tau)^2)}} \quad (5.46)$$

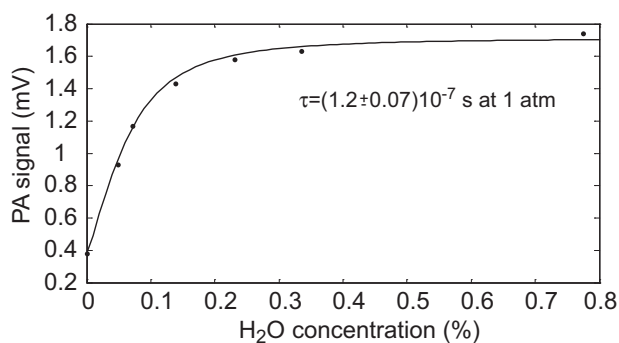


Figure 5.23: Amplitude dependence of the PA signal corresponding to 5 ppm HCl as a function of the H₂O content in the carrier gas composed of 50% N₂ and 50% He. *Dots* represents the measurement points and the *line* is the result of a fitting procedure (see text for details).

where S_{off} is the value obtained for the dry O₂-He mixture (0% H₂O), S_0 is the full PA signal obtained in absence of relaxation effects, ω is the angular modulation frequency and $\tau^{-1} = C_{H_2O}\tau_{O_2-H_2O}^{-1} + C_{O_2}\tau_{O_2-O_2}^{-1} + C_{He}\tau_{O_2-He}^{-1}$ is the overall relaxation time. This fit results in a relaxation time $\tau = (9.52 \pm 0.9)10^{-8}$ s at 1 atm ⁷ which is a factor 10 lower than the value given by reaction R_{12} ($\tau = 9.1 \cdot 10^{-7}$ s at 1 atm).

The same procedure was applied in the HCl-He-N₂ system (50% He-50% N₂) whose results are presented in Figure 5.23. An increase of a factor 4 of the PA signal is obtained after the addition of 0.8% of H₂O in the He-N₂ mixture. Here again, the deactivation of the first N₂ excited level is efficiently achieved due to the catalyst effect of H₂O (see reaction R_9). The effect is even more efficient in the N₂-He mixture than in O₂-He, since He does not act as a catalyst for N₂. A quantitative relaxation time was extracted by the same fitting procedure than described for the He-O₂ system resulting in a relaxation time of $\tau = (1.2 \pm 0.07)10^{-7}$ s at 1 atm which is a factor 70 smaller than the value given by reaction R_9 ($\tau = 9.1 \cdot 10^{-6}$ s at 1 atm).

The extracted relaxation times were in both cases smaller than the value given in reference [27], probably due to the fact, that the (V-T) relaxation process HCl-H₂O (see reaction R_3) was not considered. The very efficient corresponding rate in combination with a small fraction of water vapour can thus not be neglected for the determination of $\tau_{N_2-H_2O}$ or $\tau_{O_2-H_2O}$.

5.9 Conclusion

Relaxation effects have been studied experimentally and theoretically for CH₄ in an oxygen-nitrogen system and for hydrogen chloride in an oxygen/nitrogen-helium system. The influence of molecular relaxation has demonstrated a dramatic impact on the detection of these two species in particular conditions. The qualitative behaviour of the presented systems has been well understood: energy transfers through V-T or V-V processes were identified and explained and the role of catalysts (like H₂O or helium) on the PA signal has also been described in details.

⁷The error is the standard deviation given by the fitting process.

Theoretical models were proposed to understand quantitatively these complex processes. Unfortunately, these models fail to give a coherent quantitative analysis, probably due to two principal reasons.

The first reason find its origin in the experimental measurement of relaxation times. Neither in CH_4 , nor in HCl , the relaxation effects were entirely dissociated from other effects. For instance, in CH_4 monitoring the influence of the slight change in frequency was neglected, which probably influences the relaxation time derived from phase measurements. Moreover, line broadening effects in the different gas mixtures were not taken into account, which modifies the amplitude of the PA signal in different mixtures. In HCl , a normalisation curve was performed to try to get rid of external contributions. The frequency, quality factor and response of the microphone were normalised, but the influence on the PA signal of the line broadening and the modulation parameters of two different lasers were not taken into account by the normalisation.

The second reason is due to the difficulty to find reliable relaxation times published in the literature. In the worst case, no values were found and in other cases the order of magnitude seemed to be incoherent compared to the experimental observations.

Nevertheless, all these relaxation measurements contribute to the understanding of the generation of the PA signal and how they influence the response of the sensor.

Bibliography

- [1] J. D. Lambert, *Vibrational and rotational relaxation in gases* (Clarendon Press, Oxford, 1977).
- [2] J. O. Hirschfelder, C. F. Curtiss, and R. B. Bird, *Molecular theory of gases and liquids* (Wiley, New York, 1954).
- [3] L. Landau and E. Teller, "Zur Theorie der Schalldispersion," *Phys. Z. Sowj. Un.* **10**, 34 (1936).
- [4] K. F. Herzfeld and T. A. Litovitz, *Absorption and dispersion of ultrasonic waves* (Academic Press, New York, 1959).
- [5] J. G. Parker, "Rotational and vibrational relaxation in diatomic gases," *Phys. Fluids* **2**(4), 449–462 (1959).
- [6] F. I. Tanczos, "Calculation of vibrational relaxation times of the chloromethanes," *J. Chem. Phys.* **25**(3), 439–447 (1956).
- [7] H. K. Shin, "Temperature dependence of intermolecular energy transfer in polar molecules," *J. Am. Chem. Soc.* **90**(12), 3029–3039 (1968).
- [8] J. D. Lambert and R. Salter, "Ultrasonic Dispersion in Gaseous Sulphur Dioxide," *Proc. R. Soc. of London A* **243**(1232) (1957).
- [9] T. L. Cottrell, A. W. Read, J. McLain, and R. C. Dobbie, "Transition probabilities in molecular encounters .7. Further evidence for vibrational-rotational energy transfer. Relaxation in $\text{AsH}_3 + \text{AsD}_3$," *Trans. Faraday Soc.* **60**(4942), 241–247 (1964).
- [10] C. B. Moore, "Vibration-rotation energy transfer," *J. Chem. Phys.* **43**(9), 2979–2986 (1965).
- [11] H. K. Shin, "Deexcitation of molecular vibration on collision - vibration-to-rotation energy transfer in hydrogen halides," *J. Phys. Chem.* **75**(8), 1079– (1971).
- [12] R. B. Kurzel, J. I. Steinfeld, D. A. Hatzenbuehler, and G. E. Leroi, "Energy-transfer processes in monochromatically excited iodine molecules. V. Rotational energy transfer in argon-excited I_2 ," *J. Chem. Phys.* **55**(10), 4822–4832 (1971).
- [13] C. F. Hansen and W. E. Pearson, "3-dimensional model of collision-induced vibrational transitions in homonuclear diatomic molecules," *J. Chem. Phys.* **53**(9), 3557–3567 (1970).
- [14] F. D. Shields, "On obtaining transition rates from sound absorption and dispersion curves," *J. Acoust. Soc. Am.* **47**(5), 1262–1268 (1970).
- [15] J. L. Stretton, "Calculation of vibrational relaxation times in polyatomic gases," *Trans. Faraday Soc.* **61**, 1053–1067 (1965).
- [16] J. T. Yardley and C. B. Moore, "Vibrational energy transfer in methane," *J. Chem. Phys.* **49**(3), 1111–1125 (1968).

- [17] D. Secrest, "Theory of rotational and vibrational energy-transfer in molecules," *Annu. Rev. Phys. Chem.* **24**, 379–406 (1973).
- [18] C. A. Brau and R. M. Jonkman, "Classical theory of rotational relaxation in diatomic gases," *J. Chem. Phys.* **52**(2), 477–484 (1970).
- [19] B. Widom, "Rotational relaxation of rough spheres," *J. Chem. Phys.* **32**(3), 913–923 (1960).
- [20] A. D. Wood, M. Camac, and E. T. Gerry, "Effects of 10.6 μm laser induced air chemistry on the atmospheric refractive index," *Appl. Opt.* **10**(8), 1877–1884 (1971).
- [21] M. Hammerich, A. Olafsson, and J. Henningsen, "Photoacoustic study of kinetic cooling," *Chem. Phys.* **163**, 173–178 (1992).
- [22] A. Veres, Z. Bozoki, A. Mohacsi, M. Szakall, and G. Szabo, "External cavity diode laser based photoacoustic detection of CO_2 at 1.43 μm : The effect of molecular relaxation," *Appl. Spectrosc.* **57**(8), 900–905 (2003).
- [23] A. A. Kosterev, T. S. Mosely, and F. K. Tittel, "Impact of humidity on quartz-enhanced photoacoustic spectroscopy base detection of HCN," *Appl. Phys. B* **85**, 295–300 (2006).
- [24] G. Wysocki, A. A. Kosterev, and F. K. Tittel, "Spectroscopic trace-gas sensor with rapidly scanned wavelengths of a pulsed quantum cascade laser for in situ NO monitoring of industrial exhaust systems," *Appl. Phys. B* **80**, 617–625 (2005).
- [25] C. Boursier, J. Menard, L. Doyennette, and F. Menard-Bourcin, "Rovibrational relaxation of methane in $\text{CH}_4\text{-N}_2$ mixtures: Time-resolved IR-IR double-resonance measurements at 193 K and kinetic Modeling," *J. Phys. Chem. A* **107**(27), 5280–5290 (2003).
- [26] L. Doyennette, F. Menard-Bourcin, J. Menard, C. Boursier, and C. Camy-Peyret, "Vibrational energy transfer in methane excited to $2\nu_3$ in $\text{CH}_4\text{-N}_2/\text{O}_2$ mixtures from laser-induced fluorescence measurements," *J. Phys. Chem. A* **102**(22), 3849–3855 (1998).
- [27] H. E. Bass and H.-J. Bauer, "Kinetic model for thermal blooming in the atmosphere," *Appl. Opt.* **12**(7), 1506–1510 (1973).
- [28] D. R. White, "Vibrational relaxation of oxygen by methane, acetylene, and ethylene," *J. Chem. Phys.* **42**(6), 2028–2032 (1965).
- [29] D. R. White and R. C. Millikan, "Oxygen vibrational relaxation in $\text{O}_2\text{-He}$ and $\text{O}_2\text{-Ar}$ mixtures," *J. Chem. Phys.* **39**(7), 1807–1808 (1963).
- [30] V. Zéninari, B. Parvitte, D. Courtois, V. Kapitanov, and Y. Ponomarev, "Measurements of air and noble-gas broadening and shift coefficients of the methane R3 triplet of the $2\nu_3$ band," *Appl. Phys. B* **72**, 953–959 (2001).

- [31] F. Menard-Bourcin, C. Boursier, L. Doyennette, and J. Menard, "Rovibrational energy transfer in methane excited to $2\nu_3$ in $\text{CH}_4\text{-N}_2$ mixtures from double-resonance measurements," *J. Phys. Chem. A* **105**(51), 11,446–11,454 (2001).
- [32] J. T. Yardley and C. B. Moore, "Vibration \rightarrow vibration and vibration \rightarrow translation energy transfer in methane-oxygen mixtures," *J. Chem. Phys.* **48**, 14–17 (1968).
- [33] S. Schilt, A. Vicet, R. Werner, M. Mattiello, L. Thévenaz, A. Salhi, Y. Rouillard, and J. Koeth, "Application of antimonide diode lasers in photoacoustic spectroscopy," *Spectrochim. Acta, Part A* **60**(14), 3431–3436 (2004).
- [34] F. G. C. Bijnen, F. J. M. Harren, J. H. P. Hackstein, and J. Reuss, "Intracavity CO laser photoacoustic trace gas detection: cyclic CH_4 , H_2O and CO_2 emission by cockroaches and scarab beetles," *Appl. Opt.* **35**(27), 5357–5368 (1996).
- [35] R. A. Rooth, A. J. L. Verhage, and W. Wouters, "Photoacoustic measurement of ammonia in the atmosphere: influence of water vapor and carbon dioxide," *Appl. Opt.* **29**(25), 3643–3653 (1990).
- [36] M. De Rosa, C. Nardini, C. Piccolo, C. Corsi, and F. D'amato, "Pressure broadening and shift of transitions of the first overtone of HCl," *Appl. Phys. B* **72**, 245–248 (2001).
- [37] V. Zéninari, B. Parvitte, D. Courtois, N. N. Lavrentieva, Y. N. Ponomarev, and G. Durry, "Pressure broadening and shift coefficients of H_2O due to perturbation by N_2 , O_2 , H_2 and He in the $1.39\ \mu\text{m}$ region: experiment and calculations," *Mol. Phys.* **102**(16-17), 1697–1706 (2004).
- [38] S. Schilt and L. Thévenaz, "Wavelength modulation photoacoustic spectroscopy: Theoretical description and experimental results," *Infrared Phys. Technol.* **48**(2), 154–162 (2006).
- [39] S. Schilt, "Mesure de traces de gaz à l'aide de lasers à semi-conducteur," Ph.D. thesis, Swiss Federal Institute of Technology (2002).
- [40] C. J. Dasch and C. B. Moore, "Single quantum vibrational energy-transfer from HCl ($\nu = 2$) and HBr($\nu = 2$)," *J. Chem. Phys.* **72**(7), 4117–4122 (1980).
- [41] S. R. Leone and C. B. Moore, "V \rightarrow V Energy-Transfer in HCl with tunable optical parametric oscillator excitation," *Chem. Phys. Lett.* **19**(3), 340–344 (1973).
- [42] M. M. Hopkins and H.-L. Chen, "Vibrational excitation and relaxation of HCl ($\nu = 2$) state," *J. Chem. Phys.* **57**(9), 3816–3821 (1972).
- [43] H. L. Chen and C. B. Moore, "Vibration \rightarrow rotation energy transfer in hydrogen chloride," *J. Chem. Phys.* **54**(9), 4072–4080 (1971).
- [44] P. F. Zittel and C. B. Moore, "V \rightarrow T,R and V \rightarrow V relaxation in DCl systems," *J. Chem. Phys.* **58**(7), 2922–2928 (1973).

-
- [45] F. Al Adel, L. Doyennette, M. Margottin-Maclou, and L. Henry, "Vibrational relaxation of HCl ($\nu = 1$) by CO, NO, and O₂ and of HBr ($\nu = 1$) by CO," *J. Chem. Phys.* **77**(6), 3003–3010 (1982).
- [46] D. J. Seery, "Vibrational relaxation of HCl with inert gas collision partners," *J. Chem. Phys.* **58**(5), 1796–1799 (1973).
- [47] H. L. Chen and C. B. Moore, "Vibration→vibration energy transfer in hydrogen chloride mixtures," *J. Chem. Phys.* **54**(9), 4080–4084 (1971).
- [48] R. Frey, J. Lukasik, and J. Ducuing, "Tunable Raman excitation and vibrational relaxation in diatomic-molecules," *Chem. Phys. Lett.* **14**(4), 514–517 (1972).

Chapter 6

Conclusion

Laser photoacoustic (PA) spectroscopy is the core topic of this thesis and is a specific technique particularly well adapted for multi-gas sensing from the sub-ppm range down to the ppb level. The essential contribution of this work has been to demonstrate that the use of semiconductor lasers in combination with a carefully designed photoacoustic sensor makes trace gas detection in industrial applications possible. In addition, two methods have been developed to perform multi-gas sensing using a single instrument. The first method consisted in the use of a single resonator in combination with frequency multiplexing whereas the second technique was based in a 3-tube configuration.

The design of the PA cell has been carried out on the basis of simulations in order to optimise the configuration of the acoustic resonator. The selection of a resonant configuration based on the first longitudinal acoustic mode opened possibilities towards multi-species detection in one single sensor with low (sub-ppm) to ultra-low (ppb) detection limits for various gases of interest. An original design of a PA cell made out of three acoustic resonators makes the whole sensor compact and portable. In addition, the design of the PA cell was oriented to be optimised for DFB semiconductor lasers emitting in the NIR. Their reliability, their single-frequency emission and their optical power in the mW range (typically 10 to 25 mW) made these sources ideal candidates to fulfil the severe requirements of a sensor to be used in industrial environments.

A first application in the life science field was investigated to test the sensor in off-laboratory conditions. Three different gases (CO_2 , NH_3 and H_2O) relevant to the well-being of rodents in individually ventilated cages were continuously and simultaneously monitored during a period of two weeks. Original results concerning the circadian activity of mice and important parameters concerning the animal house system (air renewal in cages, air ventilation breakdown simulations, change of the bedding) were obtained during this measurement campaign.

The second application addressed the manufacturing of the novel low-water-peak fibre in industrial environment. Hydrogenated compounds (mainly HCl and H_2O) were monitored at sub-ppm level during a period of eleven days. Original results concerning the identification and the contribution of the different contamination sources were obtained. These important results gave information about the purity level of the carrier gas that was reached after the change of chloride containers. Moreover, the stand-by time before a new preform could be manufactured was estimated, thus reducing the number of preforms that would not comply with the severe requirements of low-water-

peak fibres.

This industrial application faced very different conditions than those experienced in trace gas monitoring in ambient air, particularly concerning the buffer gas. Careful calibration of the sensor in similar conditions than those experienced on site was carried out in the laboratory. This investigation led to unexpected results originating from molecular relaxation. This phenomenon was addressed in details for CH_4 and HCl in mixtures of N_2 and O_2 . This effect has shown a drastic decrease of the sensor sensitivity making the sub-ppm detection limit unattainable. However, substances acting as catalysts (H_2O , He) improved significantly the performance of the sensor. Moreover, these original results showed that this effect may become important for methane detection in ambient air (21% of O_2) if relatively dry conditions are experienced.

Finally, the possibility to reach extreme detection limits (ppb level) by the use of an erbium-doped amplifier was demonstrated for ammonia detection. The contribution of interferences from other species (CO_2 , H_2O) at this low concentration levels was investigated. An original method to reduce this effect has been developed and successfully validated through simulations and then using test gases.

Perspectives

PA spectroscopy is a powerful technique particularly well adapted to on-site measurements. The overall compact and simple set-up is a key advantage in comparison with standard absorption spectroscopy techniques, which require long absorption paths to reach equivalent sensitivity. Development of PA towards isotope monitoring in medicine, earth science or biology applications is a challenging task. In particular, the stability of the signals has to be carefully controlled in order to obtain a very high precision on the isotope ratio.

The continuous development of new light sources and improvements in terms of optical power are a key issues to increase the sensitivity of the sensors. The use of currently developed quantum-cascade lasers opens new spectral regions in the MIR where stronger absorption lines occur and where no light amplification is possible. Sensitivities towards ppb levels in the MIR seem reasonable to achieve for species with high absorbing cross-section.

In the future, PA spectroscopy can be seen with confidence as playing a key role in trace gas sensing, in the view of a progress through optimisation of the production tools and of a more secure environment.

Appendix A

Modelling molecular relaxation

In order to understand quantitatively the effects in molecular relaxation, a model based on multi-levels deexcitation processes is proposed. The simple 2 level model described in subsection 2.4.1 is not appropriate for CH₄ and HCl deexcitation, since the deactivation path goes through 4 steps for CH₄ and through 2 steps for HCl. Figure A.1 shows the general energy diagram used in the model. The model also includes a collisional partner M_c , like N₂ or O₂. The upper level population ($\nu = 4$) is obtained by solving equation (see equation 2.37):

$$\frac{dN_4}{dt} = N\sigma\phi_0(1 + e^{i\omega t}) - \frac{N_4}{\tau} \quad (\text{A.1})$$

where only the time dependent term contributes. The solution of this differential equation is of type:

$$N_4 = N_{04}e^{i\omega t} \quad (\text{A.2})$$

with (see also equation 2.40)

$$N_{04} = \frac{N\sigma\phi_0\tau}{1 + (\omega\tau)^2}(1 - i\omega\tau) \quad (\text{A.3})$$

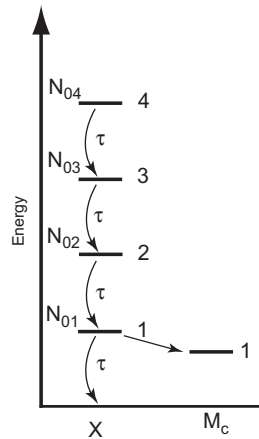


Figure A.1: Energy diagram used for modelling molecular relaxation.

For the third level, the rate equation is given by (where the source term has been replaced by N_4/τ):

$$\frac{dN_3}{\tau} = \frac{N_4}{\tau} - \frac{N_3}{\tau} \quad (\text{A.4})$$

Solving this equation by the same way than for the level ($\nu = 4$), N_{03} is found:

$$N_{03} = \frac{N_{04}}{1 + (\omega\tau)^2} (1 - i\omega\tau) \quad (\text{A.5})$$

The same procedure is applied for the population of level 2 and 1:

$$N_{02} = \frac{N_{03}}{1 + (\omega\tau)^2} (1 - i\omega\tau) \quad (\text{A.6})$$

$$N_{01} = \frac{N_{02}}{1 + (\omega\tau)^2} (1 - i\omega\tau) \quad (\text{A.7})$$

CH₄ in a N₂-O₂ mixture

For the case of CH₄ in O₂, the laser is excited to the $2\nu_3$ and the corresponding energy transfer occurs via the exchange of one ν_4 quantum (see details in section 5.7). This deexcitation is accompanied by a resonant excitation of the first vibrational excited state of oxygen. As was already discussed in subsection 5.7.1, the entire energy that is stored in this level does not contribute to the PA signal due to the long relaxation time of O₂^{*}($\nu = 1$) to deactivate to the ground level.

The heat deposition rate of level i is obtained by considering the ways of deactivation. In particular, the probability that the transfer occurs with one of the colliding partner (in this case N₂) has to be taken into account. For instance, the heat deposition rate for level i is given by (see equation (2.41)):

$$H_i = \frac{hc\tilde{\nu}_4}{\tau_{CH_4-N_2}} N_{0i} C_{N_2} \frac{\tau}{\tau_{CH_4-N_2}} \quad (\text{A.8})$$

where C_{N_2} is the concentration of N₂, τ is the relaxation time that includes all possible paths to deactivate (through N₂, via V-T transfer and through O₂ via resonant V-V transfer):

$$\begin{aligned} \tau^{-1} &= C_{N_2} \tau_{CH_4-N_2}^{-1} (V - T) + C_{O_2} \tau_{CH_4-O_2}^{-1} (V - V) \\ &= \tau_{CH_4-N_2}^{-1} + C_{O_2} \left(\tau_{CH_4-O_2}^{-1} - \tau_{CH_4-N_2}^{-1} \right) \end{aligned} \quad (\text{A.9})$$

The term $C_{N_2} \tau / \tau_{CH_4-N_2}$ represents the probability that the transfer occurs through N₂ collisions.

The total heat deposition rate is given by:

$$\begin{aligned} H_{tot} &= H_1 + H_2 + H_3 + H_4 = \\ &= \frac{hc\tilde{\nu}_4}{\tau_{CH_4-N_2}} C_{N_2} \frac{\tau}{\tau_{CH_4-N_2}} \frac{N\sigma\phi_0\tau}{[1 + (\omega\tau)^2]^4} \\ &\times \left[4 - 4(\omega\tau)^2 - i \left(10\omega\tau + 5(\omega\tau)^3 + 4(\omega\tau)^5 + (\omega\tau)^7 \right) \right] \end{aligned} \quad (\text{A.10})$$

The phase of this expression is given by (it is considered that $\omega\tau$ is small, so that only the first order term contributes):

$$\tan \varphi = -\frac{5}{2} \omega\tau \quad (\text{A.11})$$

The factor 5/2 obtained for the phase is due to the multiple level deactivation. For the first step (level 4 to level 3), the deactivation occurs through τ . For the second step (level 3 to 2), the deactivation also occurs through τ , thus from level 4 to level 2, the total relaxation time is the sum of the two. The same procedure can be applied for the next levels, resulting in a total relaxation time for level 4 to level 0 of 10τ (1+2+3+4), so that the mean time measured corresponds to $10/4$, 4 being the number of levels.

HCl in a N₂-He mixture

The case for HCl is similar to the one described above, concerning the multiple level deactivation. In this case, only two levels participate to the deactivation since the laser excited the second level of HCl. However, the deactivation through N₂ (V-V process) is not resonant, as it was the case for the CH₄-O₂ system.

HCl relaxes by two possible ways at each step:

- V-T transfer through helium with a probability of $C_{He} \frac{\tau}{\tau_{HCl-He}}$
- V-V transfer through N₂ with a probability of $C_{N_2} \frac{\tau}{\tau_{HCl-N_2}}$

where C_{He} and C_{N_2} are the concentration of He and N₂, respectively, and τ is

$$\begin{aligned} \tau^{-1} = & C_{He} \tau_{HCl-He}^{-1} (V - T) + C_{N_2} \tau_{HCl-N_2}^{-1} (V - T) \\ & + C_{N_2} \tau_{HCl-N_2}^{-1} (V - V) \end{aligned} \quad (A.12)$$

The deactivation of HCl through N₂ is probably mainly dominated by the (V-V) process [1], so that the (V-T) transfer can be neglected:

$$\tau^{-1} = C_{He} \tau_{HCl-He}^{-1} (V - T) + C_{N_2} \tau_{HCl-N_2}^{-1} (V - V) \quad (A.13)$$

The heat production rate for level 2 and level 1 is given by:

$$\begin{aligned} H_2 = & N_{02} \left[\frac{hc\tilde{\nu}_{HCl}}{\tau_{HCl-He}} C_{He} \frac{\tau}{\tau_{HCl-He}} + \frac{hc(\tilde{\nu}_{HCl} - \tilde{\nu}_{N_2})}{\tau_{HCl-N_2}} C_{N_2} \frac{\tau}{\tau_{HCl-N_2}} \right] \\ H_1 = & N_{01} \left[\frac{hc\tilde{\nu}_{HCl}}{\tau_{HCl-He}} C_{He} \frac{\tau}{\tau_{HCl-He}} + \frac{hc\tilde{\nu}_{HCl}}{\tau_{HCl-N_2}} C_{N_2} \frac{\tau}{\tau_{HCl-N_2}} \right] \end{aligned} \quad (A.14)$$

The second term on the right-hand side of these equations represents the energy that contributes to the PA signal, since the energy transfer to N₂ is not a resonant (V-V) transfer.

The total heat rate and the population of N_{01} and N_{02} are obtained by the method explained above:

$$H_{tot} = \frac{N\sigma\phi_0 hc\tau^2}{[1 + (\omega\tau)^2]^2} \left[\frac{\tilde{\nu}_{HCl}}{\tau_{HCl-He}^2} C_{He} + \frac{\tilde{\nu}_{HCl} - \tilde{\nu}_{N_2}}{\tau_{HCl-N_2}^2} C_{N_2} \right] \left[2 - i \left(3\omega\tau + (\omega\tau)^3 \right) \right] \quad (A.15)$$

The phase is given by:

$$\tan \varphi = -\frac{3}{2}\omega\tau \quad (A.16)$$

which is consistent with the explanation given above.

Bibliography

- [1] J. F. Bott and N. Cohen, "Vibrational-Relaxation of HCl($\nu = 1$) in presence of several diatomic-molecules at 295-750 k," J. Chem. Phys. **63**(4), 1518-1524 (1975).

Publications

- [1] J.-P. Besson, S. Schilt, and L. Thévenaz, “Multi-gas sensing based on photoacoustic spectroscopy using tunable laser diodes,” *Spectrochim. Acta, Part A* **60**(14), 3449–3456 (2004).
- [2] J.-P. Besson, S. Schilt, and L. Thévenaz, “Sub-ppm multi-gas photoacoustic,” *Spectrochim. Acta, Part A* **63**(5), 899–904 (2006).
- [3] J. P. Besson, S. Schilt, F. Sauser, E. Rochat, P. Hamel, F. Sandoz, M. Niklès, and L. Thévenaz, “Multi-hydrogenated compounds monitoring in optical fibre manufacturing process by photoacoustic spectroscopy,” *Appl. Phys. B* **85**, 343–348 (2006).
- [4] J. P. Besson, S. Schilt, E. Rochat, and L. Thévenaz, “Ammonia trace measurements at ppb level based on near-IR photoacoustic spectroscopy,” *Appl. Phys. B* **85**, 323–328 (2006).
- [5] S. Schilt, J. P. Besson, and L. Thévenaz, “Methane monitoring by near infrared photoacoustic spectroscopy: The importance of relaxation phenomena,” *J. Phys. IV* **125**, 7–10 (2005).
- [6] S. Schilt, J.-P. Besson, and L. Thévenaz, “Near-infrared laser photoacoustic detection of methane: the impact of molecular relaxation,” *Appl. Phys. B* **82**(2), 319–329 (2006).
- [7] J. P. Besson, M. Gyger, S. Schilt, and L. Thévenaz, “Individually ventilated cages microclimate monitoring using photoacoustic spectroscopy,” in *4. Konferenz über Optische Analysenmesstechnik in Industrie und Umwelt*, vol. 1863 of *VDI Berichte*, pp. 99–106 (2004).
- [8] J. P. Besson, S. Schilt, and L. Thévenaz, “Sub-ppm multi gas sensing based on photoacoustic spectroscopy using DFB laser diodes,” in *4. Konferenz über Optische Analysenmesstechnik in Industrie und Umwelt*, vol. 1863 of *VDI Berichte*, pp. 189–196 (2004).
- [9] J. P. Besson, S. Schilt, and L. Thévenaz, “Sub-ppb ammonia detection based on photoacoustic spectroscopy,” in *17th International Conference on Optical Fibre Sensor*, M. Voet, R. Willsch, W. Ecke, J. Jones, and B. Culshaw, eds., vol. 5855 of *Proceedings of SPIE*, pp. 415–418 (Bellingham, WA, 2005).

- [10] S. Schilt, J.-P. Besson, and L. Thévenaz, “Fiber-coupled photoacoustic sensor fo sub-ppm methane monitoring,” in *Second European Workshop on Optical Fiber Sensors*, J. M. López-Higuera and B. Culshaw, eds., vol. 5502, pp. 317–320 (SPIE, Bellingham, WA, 2004).
- [11] S. Schilt, J. P. Besson, L. Thévenaz, and M. Gyger, “Continuous and simultaneous multigas monitoring using a highly sensitive and selective photoacoustic sensor,” in *CLEO/QELS and PhAST* (2005).

Nomenclature

List of symbols

α	Absorption coefficient
α_{mn}	n^{th} root of the equation involving the m^{th} order Bessel function
β	Vibrational relaxation time
β_T	Coefficient of thermal expansion
$\Delta\omega_j$	Half-width of the acoustic resonance of mode j
$\Delta\tilde{\nu}_V$	Voigt halfwidth (HWHM)
$\Delta\tilde{\nu}_L$	Collision halfwidth (HWHM)
$\Delta\tilde{\nu}_D$	Doppler halfwidth (HWHM)
$\Delta\tilde{\nu}_{nat}$	Natural halfwidth (HWHM)
ΔE	Amount of energy between two transitions
ϵ	Depth of potential well
η	Coefficient of shear viscosity
η_b	Coefficient of bulk viscosity (or volume viscosity)
γ	Ratio of the specific heat at constant pressure to the specific heat at constant volume
κ_T	Isothermal compressibility
Λ	Acoustic wavelength
μ	Reduced mass of the colliding pair
ν	Frequency of the lightwave
ω	Angular modulation frequency
ω_j	Angular frequency of mode j
ϕ	Photon flux
ρ_0	Equilibrium value of density
ρ_a	Density fluctuations

σ	Cross section of the molecules
σ_0	Distance at zero energy
σ_m	Symmetry factor of the molecule
σ_{max}	Maximum cross-section of the molecule
τ	Relaxation time
τ_n	Nonradiative relaxation time
τ_r	Radiative relaxation time
τ_{coll}	Mean time between collisions
$\tilde{\nu}_0$	Line centre frequency
$\tilde{\nu}$	Wavenumber
$\tilde{\nu}_a$	Doppler frequency shift
$\tilde{\nu}_i$	i^{th} vibrational normal mode
φ	Phase lag between the number density N' of the excited state and the photon flux ϕ
\bar{u}	Incident velocity
\bar{v}	Receding velocity
a	Beam radius
A_c	Cross-section of the capillary (Helmholtz resonator)
A_j	Pressure amplitude of mode j
A_m	Rotational frequency of the molecule
a_m	Absorbance of the medium
A_{nm}	Einstein coefficient due to spontaneous emission
B_m	Rotational frequency of the molecule
B_{nm}	Einstein coefficient due to stimulated emission
C	Concentration of the gas
c	Speed of light in vacuum
C_j	Cell constant of mode j
C_m	Rotational frequency of the molecule
C_p	Heat capacity at constant pressure
c_s	Speed of sound
C_v	Heat capacity at constant volume

d_i	Degeneracy of the normal mode $\tilde{\nu}_i$
$d_{\eta,j}$	Thickness of the viscous boundary layer of mode j
$d_{th,j}$	Thickness of the thermal boundary layer of mode j
E_J	Rotational energy
E_j	Acoustic energy of mode j
E_m	Upper energy level
E_n	Lower energy level
E_ν	Vibrational energy
g	Broadening coefficient
$g(\tilde{\nu})$	Absorption line shape
g_D	Gaussian distribution
g_L	Lorentzian distribution
g_n	Degeneracy of the lower state
g_V	Voigt distribution
g_{air}	Air-broadening coefficient
g_{self}	Self-broadening coefficient
H	Heat production rate (by volume and unit time)
h	Planck's constant
I	Transmitted light intensity
I_0	Incident light intensity
I_j	Overlap integral of mode j
J	Rotational quantum number
J_m	Bessel function of the first kind
K	Thermal conductivity
k	Boltzmann constant
L	Length of a cylindrical cavity
l	Length of the absorbing media
L_{eff}	Effective length of the cylindrical cavity
M	Molar mass
m	Molecular mass
N	Gas density

n	Temperature coefficient
N'	Gas density of the excited state
N_L	Loschmidt number
n_m	Number of molecules in unit volume
N_n	Population in the lower quantum state
N_{tot}	Total density of molecules
p	Pressure fluctuations
P_0	Average optical power, steric factor in SSH theory
p_0	Equilibrium value of pressure
p_j	Normalisation coefficient of mode j
$p_j(\mathbf{r}, \omega)$	Pressure distribution of mode j
P_{ij}	Probability of transition from state i to state j in a collision
$P_{k-l(b)}^{i-j(a)}$	Probability of simultaneous transitions, $i - j$ and $k - l$
p_{self}	Partial pressure
Q	Quality factor
Q_J	Rotational partition function
Q_n	Nuclear partition function
Q_ν	Vibrational partition function
Q_{int}	Total internal partition function
R	Perfect gas constant
R_c	Radius of a cylindrical cavity
r_m	Intermolecular distance
r_t	Separation at classical turning point
R_{nm}	Matrix element of the dipolar moment
S	Linestrength
T	Temperature
T_0	Equilibrium value of temperature
T_a	Temperature fluctuations
T_{ref}	Reference temperature
V	Intermolecular energy potential
V'	Effective volume (Helmholtz resonator)

v_a	Velocity of the molecule
V_c	Volume of the cell
Y_m	Bessel function of the second kind
Z	Number of collisions per second
v_l	Longitudinal component of \boldsymbol{v}
v_t	Transverse component of \boldsymbol{v}
\boldsymbol{v}	Particle velocity vector

List of acronyms

CWDM	Coarse wavelength division multiplexing
DFB	Distributed feedback
EDFA	Erbium-doped fibre amplifier
FTIR	Fourier transform infrared spectroscopy
FWHM	Full-width at half-maximum
HWHM	Half-width at half-maximum
IM	Intensity modulation
ITU	International Telecommunication Union
IVC	Individually ventilated cages
MCVD	Modified chemical vapour deposition
MFC	Mass-flow controllers
MIR	Mid infrared
NIR	Near infrared
OPO	Optical parametric oscillator
PA	Photoacoustic
PAS	Photoacoustic spectroscopy
PNNL	Pacific Northwest National Laboratory
ppb	Part-per-billion
PPLN	Periodically poled lithium niobate
ppm	Part-per-million
QCL	Quantum cascade lasers
QEPAS	Quartz-enhanced photoacoustic spectroscopy
sccm	Standard cubic centimetre per minute

SMSR	Side-mode suppression ration
SNR	Signal-to-noise ratio
SSH	Schwartz, Slawsky, Herzfeld
TGA	Trace Gas Analyser
WM	Wavelength modulation
ZWPF	Zero-water-peak fibre

BESSON Jean-Philippe

Chemin de la Cocarde 1B
1024 Ecublens
Phone : 021 624 98 82
E-mail : Jean-Philippe.Besson@epfl.ch

Swiss
Date of birth: 26th October 1976
Married, 1 child

EDUCATION

- 2002-2006: PhD student**
Swiss Federal Institute of Technology, Lausanne (EPFL)
Nanophotonics and Metrology Laboratory
Research domain: Laser spectroscopy
- 1996-2002 Degree in Electrical Engineering**
Swiss Federal Institute of Technology, Lausanne (EPFL)
Semester projects:
- Study and realization of a fiber polarization controller
- Realization of an high frequency amplifier (2.45 GHz)
Diploma project :
- Fiber index profile measurement
- 1992-1996 Certificat de maturité cantonale, scientifique**
Gymnase français de Bienne (BE), Switzerland

PROFESSIONAL EXPERIENCE

- 2002-2006 Research Assistant:**
Swiss Federal Institute of Technology, Lausanne (EPFL)
- Responsible of the photoacoustic-based sensors project
- Author of scientific publications
- Teaching Assistant:**
- Supervision of four undergraduate projects
- 2001 Traineeship of 10 weeks at the Institute for Fundamental Metrology (DFM) in Denmark**
Field : Measurement of homogeneity of photodetectors
- 2001 EPFL, Assistant of electronics and Lab View for students' laboratories**

LANGUAGES

French	Mother tongue
English	Fluent : Cambridge Certificate in Advanced English
German	Fluent
Swiss German	Spoken : fluent

COMPUTER KNOWLEDGE

Software	Word, Excel, Power Point, Matlab, Labview, Latex, Advanced Design System, LabWindows
Programming Languages	Pascal, Java
Environments	Windows, UNIX

NON PROFESSIONAL ACTIVITIES

Sports	Running, ski, cycling, basketball
Music	Member of the University choir of Lausanne, responsible for the logistic part